DEVELOPMENT AND CHARACTERIZATION OF ACTIVATED BIOCHAR AS ELECTRODE MATERIAL FOR CAPACITIVE DEIONIZATION

by

Amir Mehdi Dehkhoda

M.A.Sc., The University of British Columbia, 2010

B.Sc., Sharif University of Technology, 2008

A THESIS SUBMITTED IN PARTIAL FULFILLMENT OF

THE REQUIREMENTS FOR THE DEGREE OF

DOCTOR OF PHILOSOPHY

in

THE FACULTY OF GRADUATE AND POSTDOCTORAL STUDIES

(Chemical and Biological Engineering)

THE UNIVERSITY OF BRITISH COLUMBIA

(Vancouver)

April 2016

Abstract

Biochar, a by-product of biomass pyrolysis, was investigated as a carbon-based electrode material for a water treatment method based on electrostatic adsorption/desorption of ions in electric double layers (EDLs) formed on the charged electrodes (capacitive deionization, CDI). Surface area, porous structure, and functional groups of biochar were developed, and corresponding effects on EDL capacitive performance were studied. A novel method was explored to tailor the micro- and meso-porous structures of activated biochar by exploiting the interaction between pre-carbonization drying conditions and carbonization temperature (475–1000°C) in a thermo-chemical process (KOH chemical activation). The mechanism of porosity development was investigated; results suggest that the conversion of KOH to K_2CO_3 under different drying conditions has a major role in tailoring the structure. The resultant surface area, micro- and meso-pore volumes were: 488–2670 $m^2\ g^{-1}$, 0.04–0.72 $cm^3\ g^{-1}$, and 0.05–1.70 $cm^3\ g^{-1}$, respectively.

Tailored biochar samples were investigated using physico-chemical surface characterization and electrochemical methods. For electrochemical testing, activated biochar was sprayed onto Ni mesh current collectors using Nafion® as binder. The majorly microporous activated biochar showed promising capacitances between 220 and 245 F g^{-1} when 0.1 mol L^{-1} NaCl/NaOH was used as the electrolyte. Addition of mesoporous structure resulted in significantly reduced electrode resistance (up to 80%) and improved capacitive behaviour due to enhanced ion transport within the pores.

CDI of NaCl and $ZnCl_2$ solutions was investigated in a batch-mode unit through the use of tailored biochar electrodes. For NaCl removal, all samples showed promising capacity (up to 5.13 mg NaCl g^{-1}) and durability through four consecutive cycles. In contrast, in the case of

$ZnCl_2$, the microporous sample showed a considerable drop in removal capacity (>75%) from cycle 1 to 4, whereas the combined micro- and mesoporous sample exhibited relatively small electrosorption capacity. Interestingly, the sample with mostly mesoporous structure has shown the highest removal capacity (1.15 mg $ZnCl_2$ g^{-1}) and durability for Zn^{2+} removal. These results emphasize the importance of tailoring the porous structure of biochar as a function of the specific size of adsorbate ions to improve the CDI performance.

Preface

All of the research work presented in this dissertation including framing research questions, literature review, research proposal, design and conducting of the experiments, data collection and interpretations, as well as drafting and preparation of the thesis dissertation and three research articles along with conference presentations are completed by the author, Amir Mehdi Dehkhoda, under direct supervision of Professors Naoko Ellis and Előd Gyenge in the Department of Chemical & Biological Engineering at The University of British Columbia, Vancouver, BC, Canada.

The work presented in the thesis has been published in the peer-reviewed journals listed as follows:

- A version of Chapter 4 was published in the Journal of Applied Electrochemistry: Dehkhoda A.M., Ellis N., Gyenge E., "Electrosorption on activated biochar: effect of thermo-chemical activation treatment on the electric double layer capacitance". *J Appl Electrochem 2014; 44:141–157. doi:10.1007/s10800-013-0616-4.*

- A version of Chapter 5 was published in the journal *Biomass and Bioenergy*: Dehkhoda A.M., Gyenge E., Ellis N., "A novel method to tailor the porous structure of KOH-activated biochar and its application in capacitive deionization and energy storage". *Biomass Bioenergy* 2016; 87:107–121. *doi:10.1016/j.biombioe.2016.02.023.*

- A version of Chapter 6 was published in the journal *Microporous and Mesoporous Materials*: Dehkhoda A.M., Ellis N., Gyenge E., "Effect of activated biochar porous structure on the capacitive deionization of NaCl and $ZnCl_2$ solutions". *Microporous Mesoporous Mater 2016; 224:217–228. doi:10.1016/j.micromeso.2015.11.041.*

The primary experimentation, data collection, and results' analyses were conducted by Amir Mehdi Dehkhoda. The manuscript was written by Amir Mehdi Dehkhoda and co-authored by Profs. Előd Gyenge and Naoko Ellis.

Additionally, the following list summarizes the published work from this dissertation in proceedings of various international conferences:

- A.M. Dehkhoda, E. Gyenge, N. Ellis, (2015) "Activated biochar with tailored porosity and its application in water treatment and energy storage", published in the proceedings of *The World Conference on Carbon: "Carbon 2015: Innovation with carbon materials"*, Dresden, Germany.
- Dehkhoda, A.M., Ellis, N., and Gyenge E., (2013) "Activated Biochar: a green and low-cost electrode material for capacitor applications", published in the proceedings of *224th ECS meeting: Energy Technology Division*, San Francisco, CA, USA
- Dehkhoda, A.M**.,** Ellis, N., and Gyenge E., (2013) "Development of Biochar as a Promising Carbon-Based Candidate in Electric Double Layer Applications" published in the proceedings of *American Institute of Chemical Engineers* (*AIChE) 13th annual meeting: global challenges for engineering a sustainable future*, San Francisco, CA, USA.

Table of contents

List of tables

List of figures

List of symbols and abbreviations

Symbol	Definition	Unit
$	Dollar	—
£	Pound sterling	—
$C_{j,x}$	Concentration of electrolyte at specific distance (x) from electrode	mol L^{-1}
C_{bulk}	Electrolyte bulk concentration	mol L^{-1}
Z_j	Ionic charge number	—
V_T	Thermal voltage	Volts
R	Universal gas constant	J mol K^{-1}
F	Faraday's constant	C mol^{-1}
J	Ionic strength	mol L^{-1}
T	Temperature	K
C_{dl}	Double layer capacity	F m^{-2}
C_{st}	Stern layer capacity	F m^{-2}
$C_{st,vol}$	Volumetric Stern layer capacity	F m^{-3}
C_d	Diffuse layer capacity	F m^{-2}
d	Stern layer thickness	Å
w	Salt adsorption surface density	mol m^{-2}
a	Specific electrode area	m^2 g^{-1}
V_{cell}	Cell voltage	Volts
$C_{j,mi}$	Concentration of ion (j) in micropores	mol m^{-3}
$C_{ions,mi}$	Total ion density in micropores	mol m^{-3}
$C_{anion,mi}$	Total anion density in micropores	mol m^{-3}
$C_{cation,mi}$	Total cation density in micropores	mol m^{-3}
$C^0_{anion,mi}$	Density of salt adsorption at zero applied voltage	mol m^{-3}
u_i	Ionic mobility	m^2 V^{-1} s^{-1}

Greek symbol	Definition	Unit
$\phi(x)$	Potential distribution at distance (x) from the electrode divided by thermal voltage	Dimensionless
λ_d	Debye Length	Å
ε	Dielectric permittivity	C V^{-1} m^{-1}
ε_0	Electric permittivity of vacuum	C V^{-1} m^{-1}
ε_D	Dielectric constant of water	Dimensionless
$\Delta\phi_d$	Potential difference over diffuse layer divided by thermal voltage	Dimensionless
$\Delta\phi_D$	Donnan potential difference over the diffuse layer divided by thermal voltage	Dimensionless
$\Delta\phi_{st}$	Potential difference over Stern layer divided by thermal voltage	Dimensionless
σ	Surface charge density	mol m^{-2}
Λ	Charge efficiency	Dimensionless
Λ_i	Molar conductivity	S m^2 mol^{-1}
Γ_{salt}	Amount of removed salt upon applying the cell voltage	mol g^{-1}
$\sum$	Total transferred charge to the surface of electrode	mol g^{-1}
μ_{att}	Chemical attraction energy between ions and carbon micropores (divided by RT)	Dimensionless
σ_{mi}	Local volumetric ionic charge density in the micropores	mol m^{-3}
ρ_{mi}	Electrode density (mass per unit total electrode volume)	g m^{-3}
p_{mi}	Micropore volume relative to the total electrode volume	Dimensionless

Abbreviation	Definition
AC	Activated Carbon
ACC	Activated Carbon Cloth
AEM	Anion Exchange Membrane
Biochar-AR	As received biochar
Biochar-675-0, 5, 30	Electrodes made with 0, 5, or 30 wt.% Nafion using activated biochar at 675°C with 2 h dwell time.
Biochar-1000-0, 5, 30	Electrodes made with 0, 5, or 30 wt.% Nafion using activated biochar at 1000°C with 5 h dwell time.
Biochar-675-SD	Activated biochar at 675°C with 2 h dwell time prepared from Short Dried (SD) impregnated sample (12 h drying under air)
B675-SD-HNO3-150, 450C	Electrodes made with 5 wt.% Nafion using activated biochar at 675°C treated in nitric acid followed by calcination at 150°C or 450°C.
B-KOH-SD, LD, LLD-15h,140h,280h-Air, N2	Impregnated biochar with KOH dried at different lengths (SD: 15 h, LD: 140 h, and LLD: 280 h) and atmosphere (air or Nitrogen) without carbonization.
B475, 675, 875-ND, SD, LD, LLD-15h,140h,280h-Air, N2	Activated biochar at different carbonization temperatures (475°C, 675°C, 875°C) using dried impregnated biochar with KOH at different lengths (ND: 0 h, SD: 15 h, LD: 140 h, and LLD: 280 h) and atmosphere (air or Nitrogen).
B675,875-ND, MD, LD-Air	Activated biochar at different carbonization temperatures (675°C or 875°C) using impregnated biochar and KOH dried under different lengths (ND: 0 h, MD: 65 h, and LD: 140 h) under air.
BET	Brunauer-Emmet-Teller
BJH	Barrett-Joyner-Halenda
CB	Carbon Black
CCD	Central Composite Design
CDC	Carbide Derived Carbon

Abbreviation	Definition
CDI	Capacitive Deionization
CEM	Cation Exchange Membrane
CNF	Carbon Nanofiber
CNT	Carbon Nanotube
CV	Cyclic Voltammetry
EC	Electrical Conductivity
ED	Electrodialysis
EDL	Electric Double Layer
EIS	Electrochemical Impedance Spectroscopy
FAO	Food and Agriculture Organization
FCDI	Flow Electrode Capacitive Deionization
FESEM	Field Emission Scanning Electron Microscopy
FT	Fischer-Tropsch
FT-IR	Fourier Transform Infra-Red
GCD	Galvanostatic Charge Discharge
GCS	Gouy-Chapman-Stern
HCDI	Hybrid Capacitive Deionization
HK	Horvath Kawazoe
h	Hours
IRR	Investment Rate of Return
IUPAC	International Union of Pure and Applied Chemistry
K	Kilo
LSV	Linear Sweep Voltammetry
M	Million

Abbreviation	Definition
MCDI	Membrane Capacitive Deionization
mD	Modified Donnan
MED	Multi-effect Distillation
min	Minute
MSF	Multi-stage Flash Distillation
NOM	Natural Organic Material
nr.	Number
OCM	Ordered Mesoporous Carbon
RO	Reverse Osmosis
TEM	Transmission Electron Microscopy
Wt.%	Weight Percentage
XRD	X-ray Diffraction

Acknowledgements

I would like to express my sincere gratitude to all who have helped me through completing this degree, those who truly believed in my potential and supported me unconditionally during this journey.

There are no proper words to convey my profound gratitude and respect to my supervisors, Professors Naoko Ellis and Előd Gyenge, for creating a friendly and supportive environment in which my capabilities as a research scientist have prospered during my doctoral work. They enriched my learning by sharing their unparalleled wealth of knowledge, sound advice, and enthusiasm toward exploring new ideas. They have inspired me to become an independent researcher by developing my analytical and critical reasoning. I am also deeply indebted for their unconditional support, patience, and confidence in me during the times that I needed them most.

I am also grateful to my PhD committee members, Dr. Peter Fransham and Professor Marek Pawlik, for their constructive guidance and cooperation in the completion of this work. Peter went beyond the call of duty by providing industrial insight and support. Marek has kindly given me the opportunity to work in his laboratory to complete the surface charge characterization. My appreciation also extends to Professor Kevin Smith for his scientific guidance and generosity in allowing me to use his laboratories for surface area and porosity characterization.

I would also like to thank all the individuals who have helped me with their technical knowledge and expertise in characterization analyses conducted in this work: Dr. Jophat Engwayu for Zeta potential measurements; Anita Lam for XRD analysis; Timothy Ma and Paula Parkinson for atomic absorption tests; Derrick Horne and Bradford Ross for HRTEM and SEM imaging; Dr. Ken Wong and Dr. Philip Wong for conducting XPS and Raman investigations, and Clare Maloney for elemental analyses. I am also grateful to the staff of our department,

especially Richard Ryoo, Ivan Leversage, Ken Wong, Helsa Leong, Lori Tanaka, and Marlene Chow.

During completion of my PhD, I have received a great deal of technical and emotional support from my research colleagues, who have also been very good friends with me. My appreciation goes to Dr. Mehdi Bazri, Dr. Nima Mohseni, Amin Taheri, Pooya Hosseini, Dr. Anna Ignaszak, Dr. Rahman Gholami, Dr. Alireza Bagherzadeh, and Dr. Amin Aziznia. My gratitude extends to my best friends, Alireza Rashidian, Ali Kalantarnia, and Arash Saghafi; I am greatly indebted for their help and friendship along with their care and presence at the best and worst moments of my life. To me, the word "best friend" is defined by memories of Maziar Salahi; I am sure he is smiling with me now.

Enough thanks cannot be expressed to my family, especially my mother, Vajiheh, my father, Mahmoud, my sister, Parisa, and my brother-in-law, Hamid. Despite their being continents away, their unconditional love, support, and patience have warmed my heart and strengthened my will each and every day. I would like to express my debt of gratitude to my father, who has always inspired me to develop my vision in life and encouraged me to think and act beyond the limits. I would also like to acknowledge the impact of my grandfather, Rahim J. Sadeghian, in my professional and personal life. He is a role model to me, symbolizing that with strong will and determination you can achieve any goal.

Last but not least, I would like to acknowledge the Government of Canada for giving me the opportunity to pursue my higher education and the generous financial support of the Natural Sciences and Engineering Research Council of Canada (NSERC) Discovery and Discovery Accelerator Supplement grant program. Also, the financial support of the Rio Tinto Alcan Canada Fund in the form of a Graduate Student Fellowship is greatly appreciated.

To my beloved parents and sister,

Mahmoud, Vajiheh, and Parisa,

To my grandfather, Rahim J. Sadeghian

"What you get by achieving your goals is not as important as what you become by achieving your goals."

Henry David Thoreau

Chapter 1: Introduction

1.1 Background

1.1.1 What is biochar?

Biochar is a carbon-rich solid material produced by thermal decomposition of organic material in the presence of limited oxygen and at relatively low temperatures (<700°C) [1]. The thermal decomposition process is called pyrolysis, and it dates back to ancient Egypt where it was used to produce tar and certain embalming agents.

Pyrolysis of biomass (biological material derived from living or recently living organisms) is established as a process of producing energy from renewable sources [2]. Three different products are obtained from biomass pyrolysis: bio-oil, combustible gases, and biochar. The first two products are used for producing energy (i.e., power/heat generation and transportation fuel) while the third product, i.e., biochar, is a chemical feedstock (e.g., as a soil amendment product) [3], [4]. The product composition of pyrolysis is dependent not only on the initial biomass source but also on reaction conditions such as heating rate, retention time, and maximum heat treatment temperature. There are two pyrolysis processes based on the reaction conditions: slow and fast. In the former one (traditionally used to produce charcoal) the biomass is heated slowly (1–20°C min^{-1}) to about 500°C in the absence of air with the product residence time between minutes and hours. However, in the fast pyrolysis process, the heating rate, maximum heating temperature, and residence time of products are ~1000°C min^{-1}, 450–600°C, and 1–5 s, respectively [3], [5], [6]. Generally, 15–25 wt.% of the initial biomass converts to residual biochar upon completion of the fast pyrolysis process, whereas this amount is increased to about 50 wt.% for the slow pyrolysis process [2].

The major market for biochar is currently soil conditioning; this dates back to 450 B.C., as evidenced by Terra Preta sites throughout the central Amazon area [1], [6], [7]. Utilization of biochar for soil amendments is reported as a means of abating climate changes by sequestering carbon (i.e., storage in soil) while simultaneously increasing crop yields and producing energy [8]. Recently, further applications of biochar as a carbon-rich candidate in carbon sequestration, organic and inorganic remediation, and catalysis have been reported [1], [9]–[11].

As a carbon-rich material with various acidic and basic functional groups, biochar showed promising results (i.e., 2–200 mg g^{-1} adsorption capacity) in organic and inorganic contamination removal from water (e.g., phenol, methylene blue, Cu^{2+}, Cd^{3+}, Pb^{2+}, and Zn^{2+}) [10], [12]. Biochar samples prepared from different feedstocks (e.g., bamboo, peanut straw, oak wood, hard wood, corn straw, cow manure, and rice husk) and pyrolysis conditions have been used in treating drinking water, ground water, and synthetic and actual wastewater. However, the stripping of pollutants/contaminants from biochar and the potential reusing capability of biochar adsorbents have been poorly reviewed in the literature [10], [12].

Biochar has also been reviewed as a precursor for activated carbon production [13], [14]. Owing to the extensive emissions of organic and inorganic pollutants to the environment in the past few decades, purifications by adsorption processes (e.g., by activated carbon assisted processes) have become attractive, especially in wastewater treatment and air pollution control [15]. Activated carbon has a long history in adsorptive applications of colour, odour, and taste. Ancient Egyptians used activated carbon for purification of water. The main advantages of using activated carbon in adsorption applications are the ease of operation, simplicity of design, insensitivity to toxic substances, and complete removal of desired ions even at low

concentrations [16], [17]. Meanwhile, the main disadvantages include high cost for industrial applications along with regeneration difficulties such as reduced capacities by attrition.

1.1.2 Water scarcity and the necessity for a promising treatment method

There is a rapidly rising global demand for potable water and water for agricultural and industrial use due to population growth and exhaustion of natural resources. According to the Food and Agriculture Organization (FAO) report, 1.8 billion people will be facing severe water scarcity[1] by 2025, and two-thirds of the world population could be under water stress[2] conditions [18]. Currently, about 2.6 billion people have little or no access to water for sanitation purposes, and millions of people die annually (3900 children a day) from water-borne diseases [19]. Water related problems are expected to grow even worse in the coming decades because of scarcity occurring in the regions that are currently considered as water rich [20].

About 98% of the world's water is either brackish (1000–30,000 ppm of salt concentration) or seawater (35,000 ppm of salt concentration) and requires treatment processes to provide fresh water sources for human needs. In addition to desalination of brackish water and seawater, minimizing freshwater use and maximizing the reuse of wastewater by different industries are the long-term approaches to addressing the global water challenges. As depicted in Figure 1.1, the majority of the water is used in industrial sectors in high-income countries [21].

[1] Defined when the annual water supply is <1000 m^3 per person per year.
[2] Defined when the annual water supply is between 1000 to 1700 m^3 per person per year.

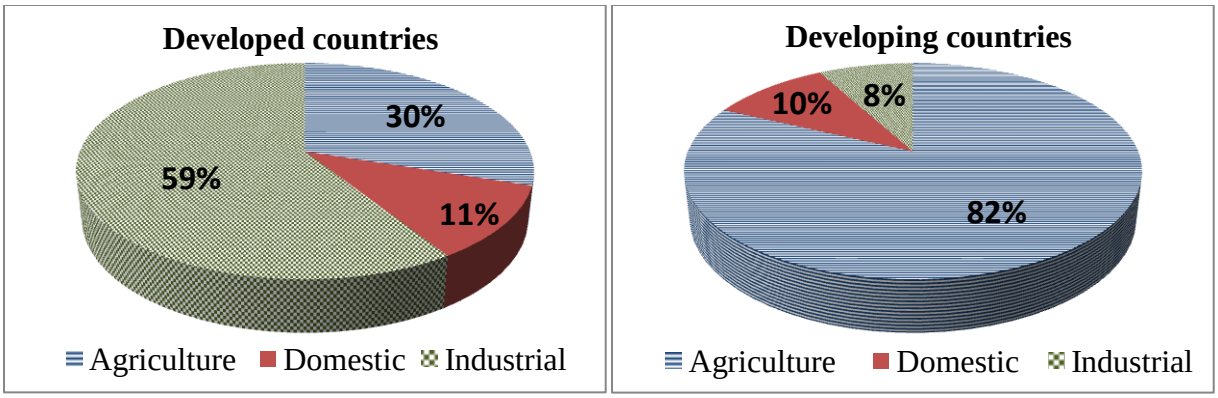

Figure 1.1 Amount of water used by different sectors in high-income and developing countries (adapted from [5]).

There is a significant amount of water contaminated by different industries such as mining, oil and gas, food production, and pharmaceutical during processes associated with manufacturing, heating, cooling, and carrying raw or waste material. According to Environment Canada, over 30 billion cubic metres of untreated or undertreated wastewater were discharged in surface freshwater bodies, groundwater, and municipal sewers from different industries in 2009 [22]. Proper treatment of these wastewaters for reuse or disposal purposes is crucial for industries. Additionally, according to the stringent environmental regulations set by governments, industries are obligated to make appropriate treatment processes prior to disposal in the environment or reuse of wastewater in their processes [23]. Hence, acquiring effective wastewater treatment methods is one of the major challenges of industrial countries.

1.1.2.1 Challenges of common water treatment methods

The most common water treatment methods used for brackish/seawater desalination or industrial wastewater treatment include membrane separation processes such as reverse osmosis (RO) or electrodialysis (ED) and thermal separation processes such as multi-effect distillation (MED) and multi-stage flash distillation (MSF). Further operational details of the water treatment methods mentioned are provided in Section 2.1.

According to Borsani and Rebagliati, about 90% of desalination and water treatment plants worldwide use either RO or MSF systems [24]. Thermal separation methods are generally more effective than membrane systems owing to their higher efficiency in desalination of highly saline seawater. However, they are more expensive, which is attributed to their higher energy consumption; they require large quantities of fuel to vaporize the salt water. Borsani and Rebagliati reported a thorough comparison among RO, MSF, and MED, estimating the cost of water desalination for each of these treatment methods [24]. The largest difference between various types of estimated costs corresponded to the thermal energy requirement, i.e., US$105 million in MED and MSF vs. zero in RO. On the other hand, RO showed a higher estimated cost of required electric power as opposed to MED and MSF: US$114 million vs. US$76 and US$92 million, respectively. For desalination of brackish water, the membrane systems (namely RO) replaced the thermal methods owing to their lower costs. Nonetheless, the membrane replacement cost of RO systems still makes them less economically favoured in desalination of seawater, especially in regions with low energy prices (e.g., Middle East). However, recent developments of RO technology have made this system comparable to thermal methods, even in seawater desalination in regions with high energy prices [25], [26].

Despite the commonality of RO and MSF systems in desalination and wastewater treatment plants, there are significant disadvantages associated with these methods. The major disadvantages of these RO and MSF techniques include inefficient energy usage (2.9–4 kWh per cubic metre of treated seawater), secondary environmental contaminations (from added chemicals during pre- and post-treatment processes as well as regeneration of membranes), corrosion, and large capital/operational costs (Table 1.1) [20], [27], [28].

Table 1.1 Breakdown of the annual operation and maintenance costs of a seawater desalination plant (170,000 m^3 per day capacity) [24].

Type of cost	MSF (US$ × 10^3)	MED (US$ × 10^3)	RO (US$ × 10^3)
Operational chemicals	50	100	250
Chemicals for cleaning	1500	1000	2500
Membranes	NA	NA	2000
Wages for operations staff	400	600	500
Wages for maintenance staff	100	175	100
Other maintenance costs (e.g., spare parts)	300	200	250

In addition to the type of treatment method, the desalination cost is also dependent on the type of saline water (brackish or seawater) and capacity of the plant [25]. The cost of seawater desalination through conventional processes is estimated to range between US$0.5 and US$3.75 m^{-3}, depending on the plant capacity, while brackish water desalination costs almost half [25], [26], [28]. Karagiannis et al. have reviewed the reported literature estimating the water desalination costs of RO and MSF [25]. Their study shows that RO systems are getting more attention as opposed to thermal separation methods because of their lower costs in both brackish and seawater desalination due to the recent developments in membranes technology [25].

1.1.3 Water treatment through electrochemical adsorption: Capacitive deionization (CDI)

Conventional water treatment methods can address many of the water problems; however, they are usually operationally, chemically, and energetically intensive processes requiring considerable capital, engineering expertise, and infrastructure that could burden their implementation in most parts of the world [20]. A considerable amount of research has been

conducted to identify cheaper water treatment methods with less energy used while minimizing the impact of the use of chemicals on the environment. Developing a novel and cost- and energy-efficient water treatment method can considerably alleviate water management challenges by increasing the cost-effectiveness and efficiency of the process.

Recently, water desalination based on electrochemical adsorption/desorption, e.g., capacitive deionization (CDI), gained attention as a cost-effective and energy-efficient method [27]–[31]. In short, CDI (sometimes referred to as "electrosorption") is an electric potential induced adsorption process on the surface of electrodes. The fundamental CDI process is based on the formation of electrical double layers (EDLs) in the proximity of electrodes as a result of applying an electric potential. The ions are electrostatically adsorbed on the EDLs and can be desorbed by removing the applied potential. More details of the EDL theory and concept are covered in Section 2.2.

The CDI process was first introduced by Caudle et al. in 1966 [32]. They used porous activated carbon as an electrode for electrochemical adsorption in the desalination process. In 1970, Johnson's group extended Caudle's work in studying the theory basis of CDI and investigated different electrode materials, and conducted preliminary cost evaluation studies [33]. They have reported a comprehensive study on ion adsorption within a porous electrode. This technology has gained attention in the desalination and wastewater treatment community since the 1970s. Following the works of Caudle and Johnson, an enormous amount of research has been conducted on different porous electrode materials in CDI through understanding the basics of this technology and designing small- and semipilot-sized units for desalination of brackish water.

The CDI process has two major steps: (a) electrostatic adsorption on the EDLs, where charged ions in electrolyte solutions are forced to migrate toward oppositely charged electrodes by low imposed constant voltage or current (i.e., <1 V and ±1 A) and (b) regeneration, where removing or reversing the applied potential (or current) results in desorption of ions and consequently regeneration of electrodes (Figure 1.2).

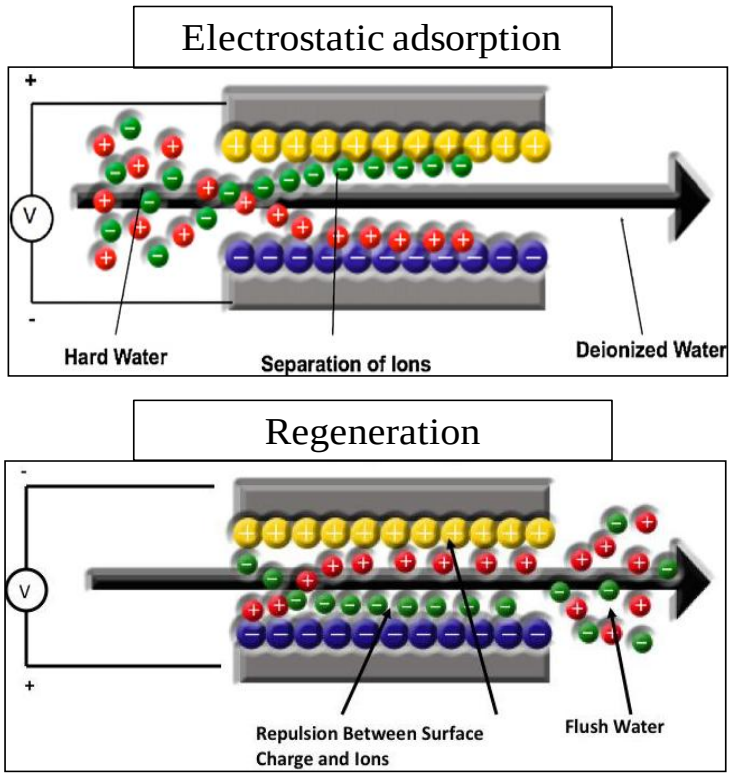

Figure 1.2 Diagram of CDI process adapted from [4].

CDI can be applied to purify water streams containing ions such as Na^+, Cl^-, SO_4^{2-}, Ca^{2+}, and NO_3^- for desalination and water softening applications or to remove a variety of heavy and transitional metal ions (e.g., Zn^{2+}, Cu^{2+}, Mn^{2+}, Cd^{2+}, Cr^{3+}, and Cr^{6+}) in industrial wastewater treatment. CDI has been previously employed in brackish and seawater desalination [34], [35], wastewater remediation [36], and also water softening applications [37].

A CDI unit consists of two pairs of oppositely charged porous electrodes that could be further assembled into CDI stacks with multiple electrodes. A direct comparison of the operation

and production costs between CDI and other commonly used water treatment methods cannot be made because of the lack of CDI commercialization. However, based on the fundamental concept of CDI and the studies reporting on the pilot-scale units, the required energy and cost of the process have been estimated [28], [38], [39]. The amount of energy required in CDI of brackish/seawater or industrial wastewater ranged between 0.2 and 1 kWh m^{-3}, which is significantly lower than that required in RO and distillation methods [28], [30]. The energy efficiency of the CDI process (e.g., in <10,000 ppm) is attributed to the separation of the minority compound of saline water (i.e., salt ions) from the majority compound (i.e., water) unlike in other conventional methods where the majority compound is being separated from the minority. Additionally, based on the fundamentals of CDI technology (i.e., EDL phenomenon), energy is released during the regeneration of electrodes due to desorption of ions from the electrodes. This released energy could be used to charge a neighbouring electrode in the electrosorption step, resulting in potential energy recovery during the CDI process. Further details of EDL theory are explained in Chapter 2.

Ease of electrode regeneration, cost and energy efficiency, high adsorption capacity, and waste minimization are among the most important advantages of the CDI technique compared with commonly used purification methods of RO and MSF. Particularly, the main advantages of CDI as compared with RO are the elimination of high pressure pumps and membranes, reduction in the amount of operational equipment such as piping, and a significant decrease in energy consumption (Table 1.1) [27]. Additionally, unlike distillation methods (e.g., MED and MSF), CDI does not require heat sources and high pressure pumps, thus allowing for easy system scaling. The absence of cation and anion exchange membranes in CDI is advantageous over electrodialysis (ED) [28]. When compared with ion exchange methods, reducing and elimination

of secondary waste streams (e.g., strong acid and base streams required for regeneration) and exclusion of periodic interruptions of the deionization process are among the most important advantages of CDI systems [40]. Moreover, the CDI process shares a similar concept (i.e., reversible electrostatic adsorption on the surface of electrodes) with electrochemical capacitors (known as supercapacitors); thus, CDI has a unique ability to simultaneously store energy while treating water, i.e., "desalination with a supercapacitor" [30].

1.1.4 CDI technology developments

The development of CDI technology from early 1960 to the present day can be categorized into three groups: conceptual and theoretical studies, engineering advancements, and material development. In the early ages of CDI development (1960–1980), most of the technology advancements included theoretical and conceptual investigations with some engineering aspects around 1980. Since 1995, the major development of CDI technology has been based on electrode material development. The classic use of activated carbon was replaced with the introduction of monolithic high surface area carbon aerogel material by Farmer et al. [39]. Following their work and up to the present day, researchers have focused on different forms of carbon-based material to optimize the CDI performance.

1.1.4.1 Electrode material

The correct choice of electrode material is a major factor affecting the performance of a CDI system. Carbon-based materials gained significant attention because of their electrochemical stability, variety of forms and porosity, and relatively low cost. Carbon-based electrodes of several compositional, structural. and electrode configuration types were reported for both electrosorption and supercapacitor applications.

The most important factors of carbon materials that affect the CDI performance can be summarized as follows:

1. Large ion-accessible surface area
    - Larger surface area results in larger EDLs and increased capacitance; however, not all of the surface area is accessible for ions with a specific size.
2. Fast ionic accessibility and small mass transfer limitation within the pore network
    - In addition to large surface area, the accessibility of ions within the pores of the electrode material greatly affects the CDI performance.
    - Both intra-particle porosity (pore size of carbon material) and inter-particle porosity (e.g., electrode thickness) affect the ionic accessibility.
3. High electrochemical stability over the range of pH and voltage used
    - To ensure the stability and durability of the electrodes
4. Large electrical conductivity
    - To ensure the entire electrode is charged with limited gradient
5. Low contact resistance between the current collector and the electrode material
    - To avoid a large voltage drop from the current collector to the electrode material
6. Acceptable wetting behaviour
    - To ensure the accessibility of the electrolyte within the entire pore network
7. Low-cost and scalability potential
8. Ease of processability to provide a variety of electrode forms for different CDI systems
9. Low environmental concerns associated with preparation and large (natural) abundance of precursor

Based on the summarized characteristics, combining a large surface area with high ionic mobility has significant importance in developing an effective electrode material. However, this is difficult to accomplish, since high surface area is attributed to a high number of small pores and consequently transport limitations. On the other hand, larger pores provide improved transport pathways for the ions but at the cost of decreasing the total surface area.

The classic electrode material in CDI applications includes mainly activated carbon and carbon aerogel [33], [34], [39], [41]. However, in the past decade novel materials were proposed for CDI, including carbon nanotubes (CNTs) [42]–[44], carbide-derived carbons [45], [46], mesoporous carbon [47]–[50], hierarchical carbon aerogel [51], [52], graphene-based materials [53]–[55], consolidated amorphous carbon [56], and various composite electrodes (e.g., carbon-metal and different carbon forms) [44], [57], [58]. Further details regarding the physico-chemical characteristics and preparation methods of different carbon-based material are provided in Section 2.4.

1.1.4.2 Challenges of carbon-based materials in CDI

In order for CDI technology to grow successfully as a commercial water treatment method, electrodes should be coupled into pairs, stacks, and modules (Figure 1.3) [28]. Despite the advancements made in the field of electrode material development, there are still some basic challenges to be addressed: irregular pore size distribution and combination of high capacity (through increasing micropore content) in addition to fast ionic transfer within the pores. Moreover, development of large-scale CDI units (e.g., producing millions of gallon per day) currently suffers from the high cost of electrodes and environmental issues arising from preparation steps [28]. About 60–70% of the total cost of carbon-based EDL capacitors is attributed to the electrode material, while the organic electrolyte and the salts added to provide

the ions in the electrolyte are the remaining major contributors to the total cost of carbon-based EDL capacitors [59]. Most of the reported mesoporous carbon materials (e.g., OMC, CNT, modified carbon aerogel) require preparation methods associated with complicated polymerization steps and expensive polymeric substrates, resulting in high cost of electrodes as well as secondary environmental pollution [59], [60]. Thus, there still remains a chasm between performance and feasibility for practical implementation. In other words, some of the highest capacitance carbon electrodes might not be cost effective, especially for technologies that compete with more established non-electrochemical processes (e.g., in the case of desalination), or carbons that may be cost effective yet do not possess electrochemical characteristics superior to other technologies. In addition to the intrinsic physico-chemical and structural properties of the carbons, the design of efficient EDL devices imposes engineering constraints, such as high electrical conductivity of the porous carbon electrode, high solid-liquid mass transfer capacity, and low pressure drop for electrolyte flow. Efforts to optimize a cost-effective and energy-efficient electrode material along with promising electrode design are crucial in development of CDI technology.

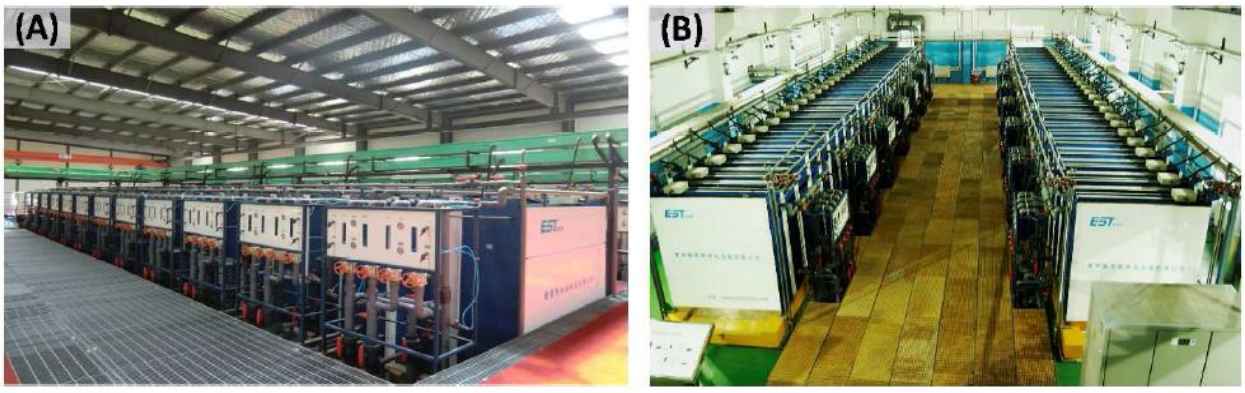

Figure 1.3 Large-scale CDI desalination units in China (EST Water & Technologies): (A) 60,000 m^3 day^{-1} desalination plant for municipal wastewater reuse; and, (B) 5000 m^3 day^{-1} coal mine wastewater remediation plant [16].

Producing porous carbon from low-cost biomass residues (e.g., wood, tree barks, crop residues, and fruit bunches) has gained attention in the past few years [61]. In addition to the favourable economics of these materials, their renewability and minimal secondary environmental impacts make them more attractive candidates compared with the synthesized carbon from polymeric substrates, e.g., carbide-derived carbon.

Biochar can be used as a renewable and potentially low-cost carbon-based electrode material in CDI. Using biochar as a valued-added electrode material for CDI broadens its application as a renewable material in different processes and also increases product utilization of the pyrolysis process.

1.2 Research questions and objectives

The main research questions can be summarized as follows:

- Can biochar be used as a promising carbon-based material for electric double layer (EDL) applications? If so, what are the main parameters affecting EDL performance?
- What are the effects of surface area, pore size, and surface chemical groups on the performance of biochar as an EDL material? As well, how can these parameters be optimized to improve the performance?
- What are the properties of biochar that affect the removal of different ions through CDI?

The strategic objective of this research is to develop a renewable biochar material as an electrode candidate for CDI technology to remove unwanted ions from aqueous electrolytes. The specific research objectives can be divided into three phases as follows:

Phase I: Initial studies on using biochar in EDL applications:

a. To investigate the effect of surface area and porosity on EDL behaviour of biochar electrodes.

b. To study the effect of surface functional group modifications on EDL performance.

Phase II: To optimize the performance of biochar as an EDL electrode material:

a. To optimize the surface area and porosity (via KOH chemical activation) through tailoring the structure of biochar.
b. To understand the mechanism of porous structure tailoring.
c. To study the effect of controlled porosity on EDL performance.

Phase III: To study the optimized biochar electrodes for potential CDI application:

a. To build a CDI testing unit.
b. To study the CDI performance including durability and regeneration.
c. To compare the effects of differently prepared biochar materials in CDI of two ions with different sizes.

1.3 Thesis layout

The thesis is organized in seven chapters. The flow diagram of the thesis is shown in Figure 1.4. Chapter 1 includes an introduction to the thesis, disclosing problem definition, framing research questions, and proposing objectives. Based on Chapter 1, a thorough investigation of the literature related to the field of study is provided in Chapter 2. Chapter 3 covers material preparation and characterization methods. Chapter 4 deals with **Phase I** of the research, which is mainly initial studies of the effect of biochar properties such as surface area, pore size, and electrical conductivity on the EDL performance. Upon identification of the major parameters affecting the EDL performance, further research is conducted, as described in Chapter 5, focusing on the optimization of these parameters towards development of biochar as an EDL electrode (**Phase II**). Further investigations to control the surface area and porous structure of biochar (through modified KOH activation) and its effect on EDL performance are included. **Phase III** of the research, described in Chapter 6, focuses on the best biochar candidates studied as electrode material in a small-sized CDI unit treating NaCl and $ZnCl_2$. The correlation between

the porous structure and adsorption/desorption performance is also studied. Chapter 7 summarizes the core findings and conclusions of the thesis in addition to recommendations for future work.

Research findings and investigations of the present thesis project contribute to the introduction of a novel generation of renewable carbon-based material from a low-cost by-product precursor for CDI technology. This can potentially advance the development of CDI as a cost- and energy-efficient treatment method to alleviate the upcoming water crisis in the next few decades.

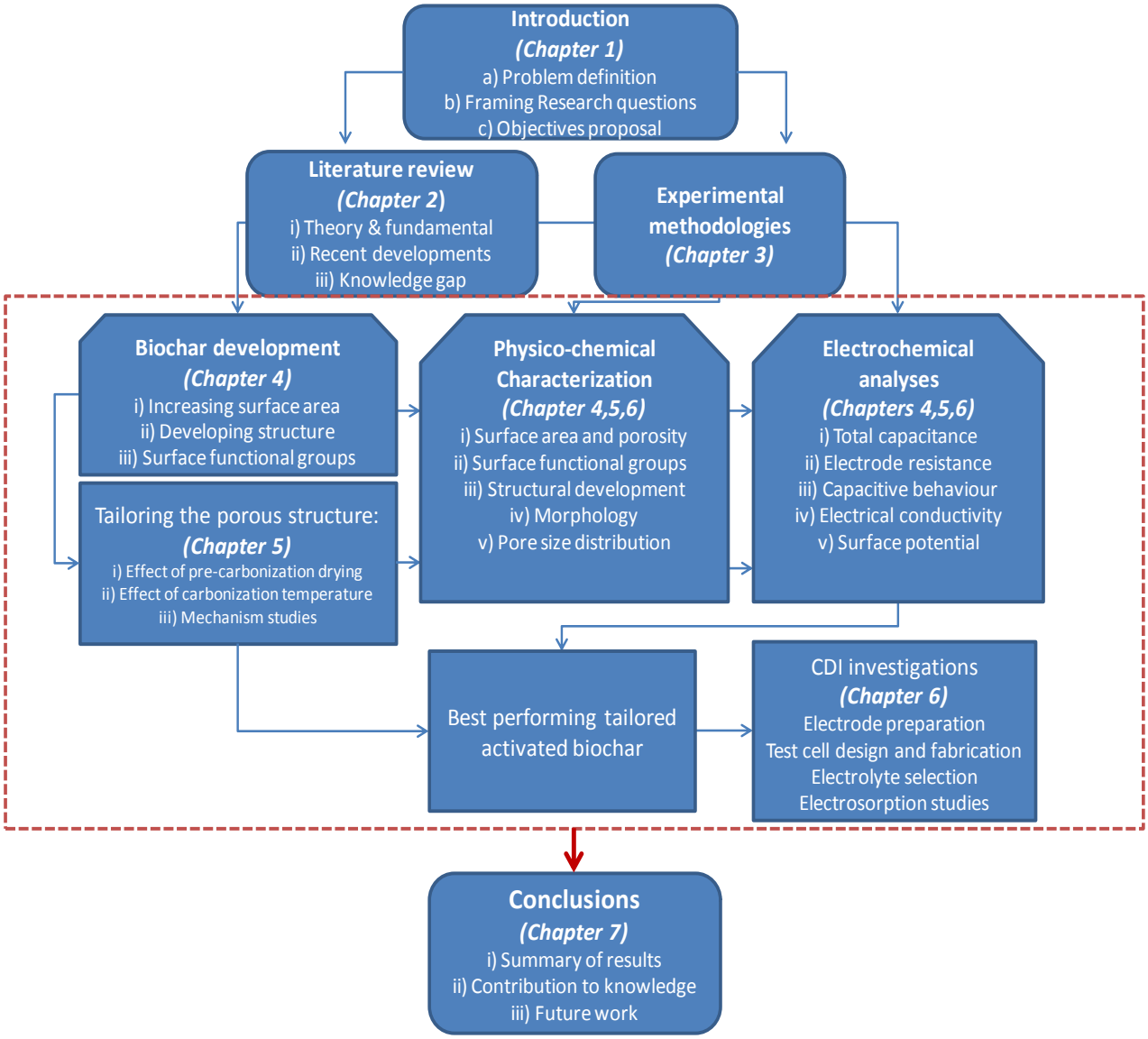

Figure 1.4 Flow diagram of thesis (red dotted square represents the origin of results constituting the Conclusion chapter).

Chapter 2: Literature review

2.1 Commonly used water treatment methods

2.1.1 Thermal separation

The fundamentals of the thermal treatment processes are based on separation of salts through evaporation and condensation. Multi-effect and multi-stage distillations are the two main thermal separation methods used in ~80% of desalination plants [28].

Multi-effect distillation (MED) is the oldest thermal separation method used for desalination of seawater with references and patents existing since 1840 [62]. The process consists of multiple stages (a.k.a., effects) with different temperature and pressure. The heated feed water flows in consecutive stages with decreasing temperature and pressure. Continuous evaporation and condensation at different stages leads to separate the salts from feed water. Comparing to the other thermal separation methods, MED is the most energy-efficient method due to the energy reuse between the multiple stages [63].

Multi-Stage Flash distillation (MSF) is the most common thermal separation method frequently used in the Middle East where it benefits from low energy prices [25], [26]. Similar to the MED method, MSF is also consisted of multiple stages. The principle of this method is based on the evaporation of heated feed water at lower temperature/pressure of consecutive stages.

2.1.2 Membrane separation

In membrane treatment systems, e.g., nano-filtration, electrodialysis (ED), ultra-filtration and reverse osmosis (RO), salts are retained, while water diffuses through the membrane. About 86% of the membrane desalination plants use reverse osmosis (RO) method [28]. In addition to desalination applications, RO is also widely used in industrial wastewater treatment [64]. Comparing to the thermal separation method, RO has smaller energy consumption for

desalination, making it more frequently used in regions with high energy costs such as Europe [26]. The RO is based on a property of certain polymers called semi-permeability: low permeability for dissolved species while being significantly permeable for water. High pressure (i.e., 10–40 and 55–68 bars for brackish and seawater, respectively) should be applied to feed water to overcome the osmotic pressure of the solution and permeate the water through membrane. The RO systems usually include pre-treatment (e.g., adding chemicals to prevent fouling, adjusting the pH of feed water, and particulate matter removal) and post-treatment (e.g., disinfection and re-mineralize) processes.

Another membrane system competing with RO in desalination of brackish water is electrodialysis (ED). This treatment method is based on the movement of charged species in an electric field through a stack of polymeric anion and cation exchange membranes with an alternating sequence. By applying the electrical potential between the electrodes, the cations start moving toward cathodes (negative electrode) and anions toward anodes (positive electrodes). The cations can migrate through the cation exchange membranes (CEM), while being retained by anion exchange membranes (AEM). Similar trend occurs for the anions except with the opposite order: passing through AEM and being retained by CEM. The ion movement results in the rise of concentration in some compartments (i.e., brine) and consequently decreased concentration in adjacent compartment (i.e., dilute) (Figure 2.1). In the first and last ED stack (i.e., adjacent to cathode and anode electrodes) the electrochemical reactions may occur depending on the applied potential and pH of the feed water producing H_2, O_2, or Cl_2 gases. According to Fritzmann et al., ED systems are economically favourable over RO in low ion concentration (<3000 ppm) feed water, e.g., in chemical and petrochemical industries [26].

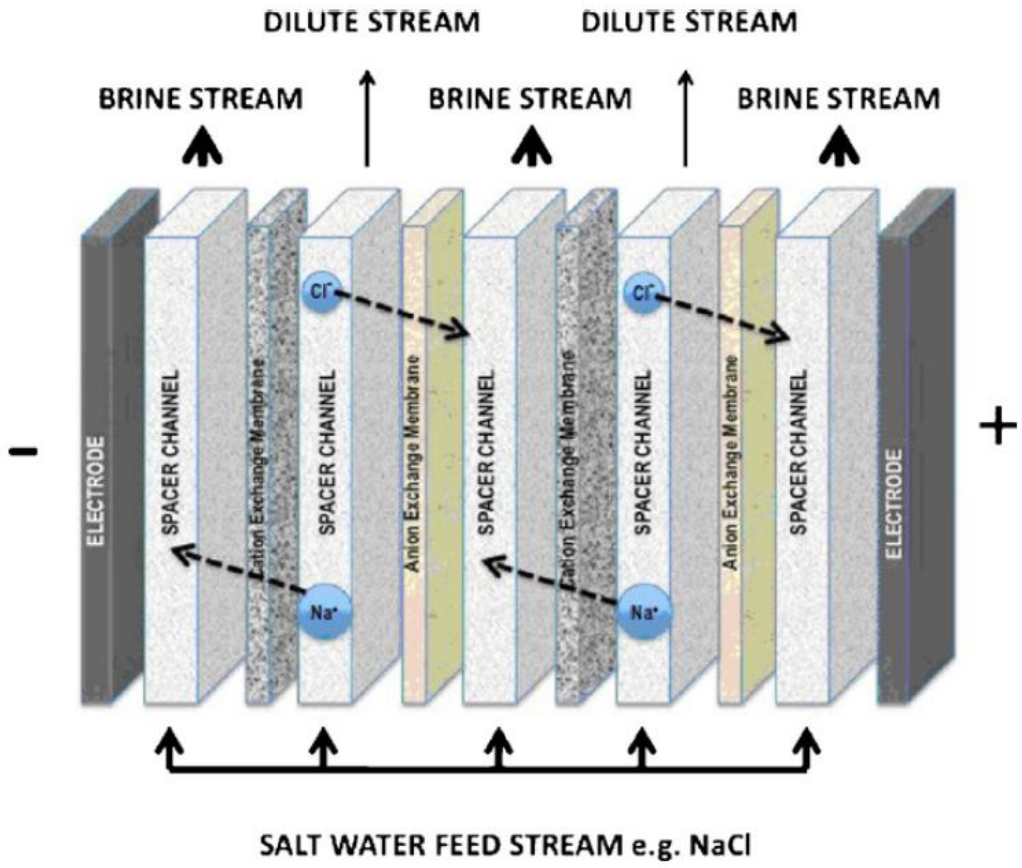

Figure 2.1 Schematic diagram of electrodialysis treatment method; source: [4].

2.2 Theory and concept of CDI: electric double layer

The electric double layer (EDL) model basically describes a charge separation across a charged interface in an electrolyte. The charge neutrality exists between the excess electronic charge in one phase (e.g., electronic charge of carbon material) and the ionic charge on the other phase (e.g., ions in the electrolyte-filled pores). The charge of the two phases sum up to zero, making the EDL neutral as a whole.

The main theory of electric double layer was established by Herman Von Helmholtz in 1879, followed by Gouy-Chapman model in 1913 [17]. Von Helmholtz expressed an electric double layer as a simple capacitor in which one layer of ions is adsorbed on the surface of a

charged electrode (Figure 2.2). The Helmholtz-model cannot sufficiently describe the EDL structure in porous material; where, the ions do not adsorb in the plane right next to the surface, but remain distributed in a layer near the surface (Gouy-Chapman or diffuse Layer). Louis Georges Gouy and David Chapman have introduced an exponential decrease of potential from the surface of electrode to the bulk of electrolyte [65]. Yet, the complete theory was established by Stern in which both Helmholtz and Gouy-Chapman models were combined with an addition of a layer in between the electrode and the diffuse layer. In this model there are two main layers (i.e., double layer) generated on the electrolyte side: the Stern (or Helmholtz) layer having comparable thickness to the hydrated radius of adsorbate ions bearing no charge; and, the diffuse layer (a.k.a., Gouy-Chapman layer) (Figure 2.2) [66]. Ideally, at the start of the diffuse layer (i.e., Stern *plane*) there is an excess of ions surrounded by their hydration shell that are electrostatically adsorbed as shown in Figure 2.2. In the diffuse layer, on the other hand, the ion concentration decays with increasing distance from the surface of the electrode (x) following the Boltzmann distribution as functions of potential and temperature, Equation (2.1).

$$C_{j,x} = C_{bulk}.\exp\left(-Z_j.\phi(x)\right) \tag{2.1}$$

where $C_{j,x}$ is the concentration at specific distance from electrode, C_{bulk} is the bulk concentration, $\phi(x)$ is the potential distribution at distance (x) from the electrode divided by thermal voltage (V_T)[1], and Z_j is the ionic charge number.

The thickness of the Stern layer is similar to the hydrated radius of the adsorbate ions (~1–30 Å). There is no precise width reported for the diffuse layer; however, it can be approximated by a characteristic length at which the potential and counter-ion concentration (i.e., ions of the

[1] V_T=RT/F where F, R, and T are the Faraday's constant, the universal gas constant, and temperature, respectively.

opposite charge as that of the surface) decay by a factor of e (~2.7) known as Debye length, Equation (2.2) [38].

$$\lambda_d = \left[\frac{\varepsilon_0 \varepsilon_D . RT}{F^2 . \sum Z_j^2 C_j}\right]^{0.5} = \left[\frac{\varepsilon_0 \varepsilon_D . RT}{2F^2 . J}\right]^{0.5} \quad (2.2)$$

where ε_0, ε_D and J are electric permittivity of vacuum (=8.85 × 10^{-12} C V^{-1} m^{-1}), dielectric constant of water (=78.5 at 25°C), and ionic strength of the electrolyte, respectively. Hence, the Debye length is proportional to the ionic strength of the electrolyte, i.e., ~3–300 Å for a typical 1:1 electrolyte such as NaCl at 1 and 10^{-4} mol L^{-1} concentration.

In the double layer theory, the potential at the Stern plane is assumed to be equal to Zeta potential, i.e., one of the important surface electrical characteristics. The amount of Zeta potential is based on the surface chemistry of each particle and the pH of the solution in which the particles are dispersed. The Zeta potential can be utilized as an important surface charge characteristic value for the particles in an emulsion. The characteristics of iso-electric point (i.e., at which there are no charge on the Stern plane and Zeta potential equals zero) can also be determined by knowing the Zeta potential variations versus pH of the solution [16].

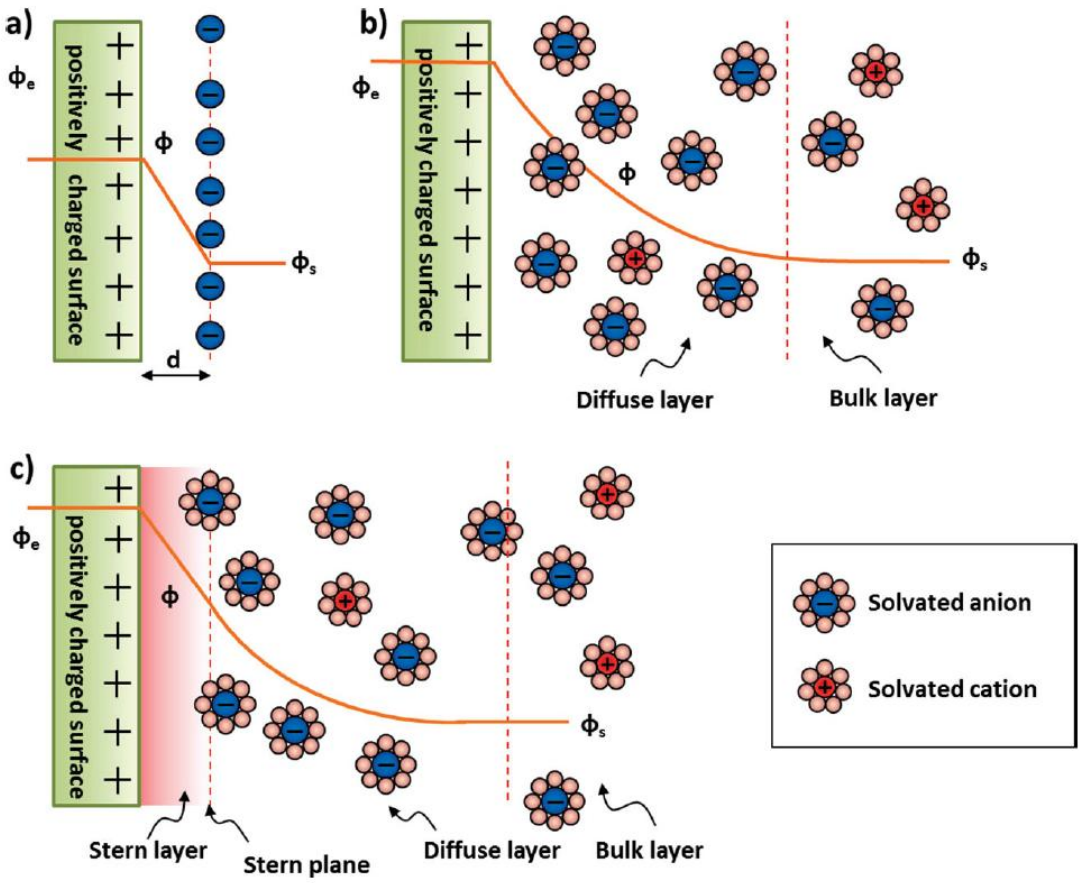

Figure 2.2 Development of EDL theory: (a) Helmholtz; (b) Gouy-Chapman; and (c) Stern models. The electrical potential (ϕ) decays as transitioning from electrode (ϕ_e) to the solution bulk (ϕ_s) infinite away from the electrode surface [53].

The total capacitance of a double layer (C_{dl}) can be estimated by two imaginary capacitors connected in series, Equation (2.3): one being equivalent to the Stern layer (also known as compact layer), C_{st}; while, the other one is corresponding to the Gouy-Chapman (i.e., diffuse) layer, C_d [27].

$$\frac{1}{C_{dl}} = \frac{1}{C_{st}} + \frac{1}{C_d} \tag{2.3}$$

Various models are proposed to estimate the Stern layer capacitance as either constant or a function of electrode potential [67], [68]. The following equation is reported assuming constant capacitance for symmetric ions:

$$C_{st} = \frac{\varepsilon}{4\pi d} \tag{2.4}$$

where d is the Stern layer thickness (i.e., the closest distance of ions to the electrode surface) and ε is the dielectric permittivity in C V^{-1} m^{-1}. Thus, the Stern capacity is only dependent on the Stern layer thickness (i.e., approximately is equal to the hydrated radius of the ions).

To calculate the C_d (based on Gouy-Chapman-Stern theory) the amount of charge stored in the diffuse layer should be divided by the potential difference over the diffuse layer. Calculation of the charge density over diffuse layer is discussed in Section 2.2.1.1. For a single symmetric 1:1 electrolyte (e.g., NaCl) the following equation describes the diffuse layer capacitance [67]:

$$C_d = \frac{\varepsilon}{\lambda_d}.\cosh\left(\frac{Z.\Delta\phi_d}{2}\right) \tag{2.5}$$

where $\Delta\phi_d$ is the dimensionless potential difference over diffuse layer[1] and λ_d is the Debye length from Equation (2.2). Equation (2.5) suggests an increase in capacitance by decreasing the Debye length (e.g., increasing the concentration of the electrolyte). Moreover, plotting the capacitance vs. $\Delta\phi_d$ yields an inverted parabola where the capacitance is minimum at $\Delta\phi_d$ = 0 (a.k.a., iso-electric point).

2.2.1 Electric double layer models for porous structures

Numerous models have been reported in the literature describing the structure of EDL at both planar surfaces and in the porous structure of charged material. Reviewing the existing literature is beyond the scope of this work; however, based on Porada's critical review [38], two important models are summarized with respect to the pore size of the electrode material and EDL structure. In the first model the typical pore size of material is much larger than Debye length where, Gouy-Chapman-Stern (GCS) theory was utilized; and in the second model, the pore size

[1] The potential difference between the Stern plane and the bulk (can be assumed as zero) divided by the thermal voltage V_T=RT/F; where R, T, and F are universal ideal gas constant, temperature, and Faraday's constant.

is small relative to the Debye length where EDL overlap is expected and modified Donnan approach was used.

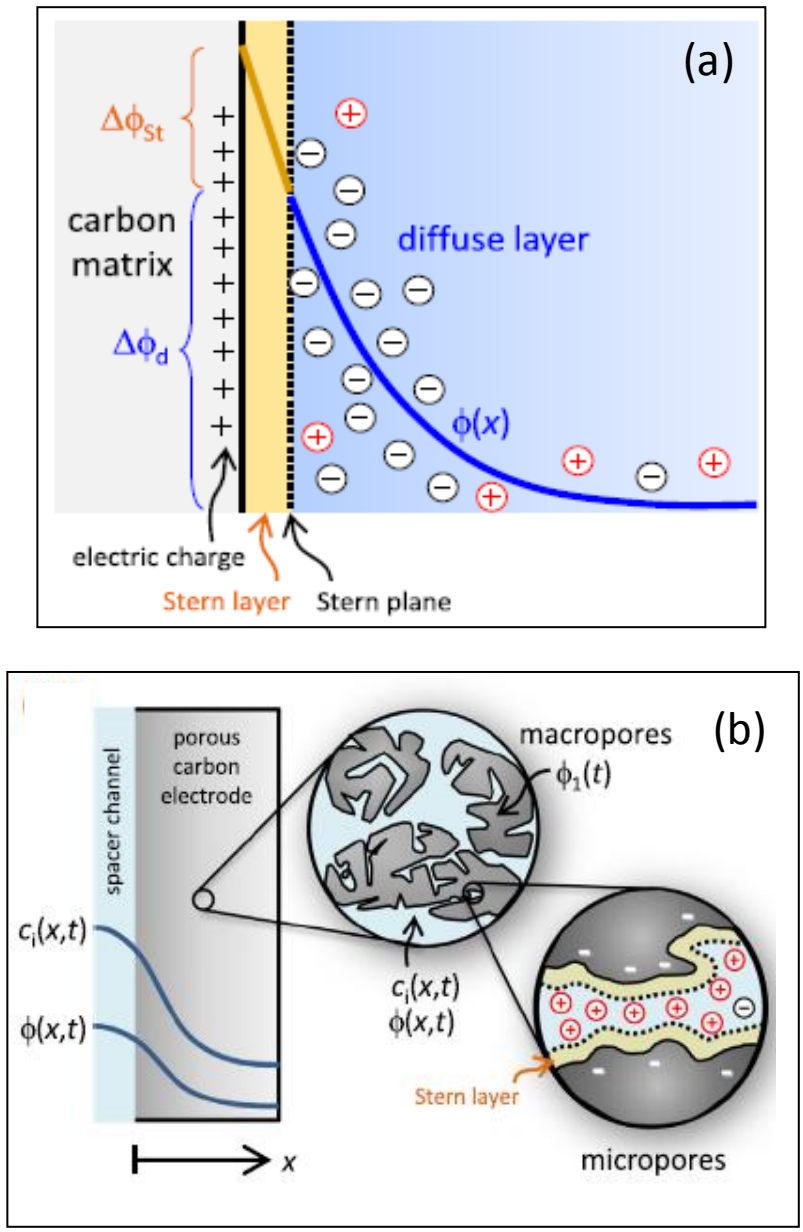

Figure 2.3 Two proposed models for charge and ion storage in CDI using porous carbon electrodes [23]: (a) Gouy-Chapman-Stern model for a planar non-overlapping EDL; (b) Two-porosity model (micro- and macropores) assuming locally averaged ion concentrations (in the micropores described by Donnan model).

2.2.1.1 Gouy-Chapman-Stern (GCS) model

For the pore sizes larger than the Debye length, a fair assumption can be made that the EDLs do not overlap and thus, the classical Gouy-Chapman-Stern (GCS) theory can be developed for a single porous electrode (Figure 2.3 a). The assumption holds valid at either highly concentrated solutions (i.e., short Debye length based on Equation (2.2)) or, very large pores (>10 nm). The dimensionless[1] potential difference over the Stern and diffuse layers are referred to as: $\Delta\phi_{st}$ and $\Delta\phi_{d}$, respectively. Equation (2.1) (Boltzman distribution) gives the ion concentration at position (x) from the electrode (carbon) surface. Integration of Equation (2.1) across the diffuse layer can be made to obtain the surface charge density, σ, in mol m^{-2} for a symmetric 1:1 electrolyte (e.g., NaCl) [69]:

$$\sigma = 4\lambda_d C_{bulk}.\sinh\left({}^{\Delta\phi_d}/_{2}\right) \tag{2.6}$$

where λ_D is the Debye length (from Equation (2.2)) and $\Delta\phi_d$ is the dimensionless potential difference over the diffuse layer. The surface charge density is defined as moles of charge per unit area of electrode surface and can be multiplied by Faraday's number (96,485 Coulombs per mol) to obtain the surface charge density in Coulombs per unit area (C m^{-2}).

The excess concentration of ions stored in the EDL (i.e., salt adsorption surface density) can also be obtained by Equation (2.1) [70], [71]:

$$w = 8\lambda_d C_{bulk}.Sinh^2\left({}^{\Delta\phi_d}/_{4}\right) \tag{2.7}$$

An important characteristic parameter to study the CDI performance (e.g., energy requirement) is charge efficiency, Λ, defined as the equilibrium ratio of salt removal vs. charge in a two-electrode setup [70]. The importance of this parameter is related to one of the key

[1] To convert the units in dimensional voltage, the values should be multiplied by Thermal Voltage, i.e., V_T=RT/F.

predictions of Gouy-Chapman theory for the diffuse layer charge compensation. Two phenomena are considered for charge compensation in the diffuse layer: a) counter-ion adsorption and b) co-ion (ions with the same charge as that of the surface) desorption. The latter implies that ions in the proximity of the surface (prior to applying the charge) start to be expelled due to the same charge sign as the surface charge builds up. This type of charge compensation is not favourable in CDI processes because, for each electron transferred between the two electrodes only a portion is contributing to the ion adsorption. The charge efficiency is defined as [70], [71]:

$$\Lambda = {\Gamma_{salt}}/{\sum} \tag{2.8}$$

where Γ_{salt} is the amount of removed salt upon applying the cell voltage (e.g., moles per mass of all electrodes, mol g^{-1}) and $\sum$ is the total transferred charge to the surface of electrode (in mol g^{-1}) calculated from $\sum_F$ (obtained from integrating current over time, in C g^{-1} units) divided by Faraday's number. The charge efficiency can be estimated by both experimental and theoretical methods. The theoretical values of Γ_{salt} and $\sum$ can be calculated based on Equations (2.7) and (2.6), respectively. Assuming two identical electrodes with the same magnitude of the diffuse layer potential ($\Delta\phi_d$), the following equations can be obtained: $\Gamma_{salt} = w.a$; and $\sum = \sigma.a$, where (a) is the specific electrode surface area in m^2 g^{-1}. Combining these equations with Equations (2.6) – (2.8) results in:

$$\Lambda = \tanh\left({\Delta\phi_d}/{4}\right) \tag{2.9}$$

Thus, according to the GCS model, the charge efficiency is only dependent on the potential difference in the diffuse layer, $\Delta\phi_d$. To complete the calculation of the GCS model, the applied cell voltage should be related to potential difference over diffuse ($\Delta\phi_d$) and Stern ($\Delta\phi_{st}$) layers.

Assuming symmetric electrodes, the following equation can be used to relate cell voltage to double layer potential differences:

$$V_{cell}/_{(2.V_T)} = |\Delta\phi_d + \Delta\phi_{st}| \tag{2.10}$$

The potential difference over the Stern layer ($\Delta\phi_{st}$) is directly related to (σ) according to Gauss's law [70]:

$$\Delta\phi_{st}.C_{st}.V_T = \sigma.F \tag{2.11}$$

With C_{st} the Stern layer capacity (F m^{-2}) and V_T is the thermal potential (= RT/F). The mentioned calculations are valid for symmetric electrodes with non-overlapping EDLs.

2.2.1.2 Modified Donnan model for overlapping EDL in micropores

In the previous section the Gouy-Chapman-Stern model was discussed for a planar, non-overlapping EDL structure. However, literature suggests that this model fails to properly predict the situation in which the Debye length is of the order of, or larger than the average pore size due to EDL-overlapping [70]. To resolve this issue, another model (modified Donnan, mD) is proposed to describe salt adsorption and charge storage in the limit of strongly overlapped EDLs [72]–[76]. According to the mD model, the EDLs in the micropores are strongly overlapping to the point that the electrical potential of electrolyte inside the micropores can be assumed to be constant and does not vary with position. The assumption holds valid when the Debye length is much larger than the micropore size (i.e., typically ~1–2 nm). The detailed structure of the EDL and ion distribution in microporous carbons is described in [77], [78]. In the mD model, two modifications are made to the basic Donnan approach [77]: 1) including Stern layer between the carbon matrix (location of electronic charge) and the ion in the electrolyte-filled micropores and 2) assuming a non-electrostatic chemical attraction energy when the ion transfers from electrolyte to inside the carbon particle, μ_{att}. This chemical attraction energy is observed

experimentally in [79]. Based on these two modifications the mD model is described by the following equation [45], [72], [74], [75]:

$$C_{j,mi} = C_{bulk}.\exp\left(-Z_j.\Delta\phi_D + \mu_{att}\right) \tag{2.12}$$

where subscript "mi" stands for micropores inside a carbon particle and $\Delta\phi_D$ is the Donnan electrostatic potential difference between micro- and macropores (i.e., large pores being transport pathways outside the particle, Figure 2.3 b). Equation (2.12) is very similar to Equation (2.1) except for the replacement of $\Delta\phi_D$ with $\phi\ (x)$ and the addition of chemical attraction energy term, μ_{att}. Also it should be noted that Equation (2.1) is used to describe the ion concentration at distance (x) from the electrode surface and was integrated to obtain charge- and salt-voltage relationships in Equations (2.6) and (2.7). However, Equation (2.12) can be used for the whole micropore volume and integration is not necessary as summing up for both ions (cation and anion) results in total ion density in the pores (e.g., for NaCl):

$$C_{ions,mi} = C_{cation,mi} + C_{anion,mi} = 2.C_{bulk}.\exp(\mu_{att}).\cosh\left(\Delta\phi_D\right) \tag{2.13}$$

The local volumetric ionic charge density in the micropores, σ_{mi} in (mol m^{-3}) units, can be also calculated based on Equation (2.12) as:

$$\sigma_{mi} = C_{cation,mi} - C_{anion,mi} = -2.C_{bulk}.\exp(\mu_{att}).\sinh\left(\Delta\phi_D\right) \tag{2.14}$$

The ionic charge density can be related to Stern layer potential difference, $\Delta\phi_{st}$, based on a similar relationship shown in Equation (2.11) as:

$$\sigma_{mi}.F = \Delta\phi_{st}.C_{st,vol}.V_T \tag{2.15}$$

where $C_{st,vol}$ is the volumetric Stern layer capacity (F m^{-3}).

For a symmetric CDI cell, the equilibrium charge $\sum_F$ and salt adsorption Γ_{salt} (relative to the amount of salt adsorption at zero applied voltage) per total mass of electrodes can be related to σ_{mi} and $C_{ions,mi}$ as follows [45], [72], [74], [75]:

$$\Gamma_{salt} = \frac{1}{2}.\frac{p_{mi}}{\rho_{mi}}.(C_{ions,mi} - C^{0}_{anion,mi}); \sum_{F} = -\frac{1}{2}.F.\frac{p_{mi}}{\rho_{mi}}.\sigma_{mi} \quad (2.16)$$

where ρ_{mi} and p_{mi} are the electrode density (mass per unit total electrode volume) and the micropore volume relative to the total electrode volume, respectively. The ratio of p_{mi}/ρ_{mi} is equal to the micropore volume per mass of carbon powder (can be measured using nitrogen adsorption) times the mass fraction of carbon relative to the total electrode mass (e.g., 90%). The charge efficiency in the mD model can then be defined similar to the Equation (2.8). Finally, similar to the GCS model, the relation between applied cell voltage (V_{cell}) and potential difference over Stern and Donnan layers can be obtained by: ${}^{V_{cell}}/_{(2.V_T)} = |\Delta\phi_D + \Delta\phi_{st}|$.

2.3 History background of CDI

Figure 2.4 summarizes a timeline of CDI technology development [38]. Between 1960 and 1978 the majority of the scientific development resulted from theoretical studies of Blair, Murphy and coworkers [32], [80], [81]. It was assumed that ions can only be removed from the water based on the specific chemical groups of the electrode material taking part in oxidation and reduction reactions. A few years later, the concept of "electrochemical demineralization" was studied by Evans and Hamilton based on Coulometric and mass balance analysis [82]. According to their study, Faradaic reactions on the surface of electrodes were responsible for ionization of the surface chemical groups resulting in ion removal [82].

The first introduction of the capacitive mechanism in electrochemical demineralization was made in 1967 by Murphy and Caudle [32]. They reported the first detailed mathematical analysis of ion concentration in a CDI system based on capacitive mechanism [32]. In 1968, Reid et al. reported the long term operation of a demineralization unit without loss of capacity over time [83]. More importantly, they showed that ions other than sodium and chloride (e.g., calcium,

magnesium, nitrate, sulfate, and phosphate) can be effectively removed by electrochemical demineralization.

A breakthrough in the concept of electrochemical demineralization was made in early 1970s by Johnson's studies [84]. The first concept of "potential modulated ion sorption" (i.e., EDL) was identified as the main responsible mechanism for the ion removal. Their study also revealed that the Faradic reactions on the surface of electrodes lead to degradation and thus, they are not essential from the long term performance efficiency perspective [84]. Further study was made by Johnson and Newman toward development of porous electrode material (i.e., activated carbon) and to investigate the correlation between ion adsorption and charge-voltage dependency [33]. Following to the introduction of EDL concept in CDI processes, extensive work was conducted by Soffer, Oren and coworkers on the EDL theory and development of CDI technology (e.g., engineering enhancement aspects), that still continues to the present day [27], [85], [86].

After a time gap in CDI technology development between 1978 and 1995, an increasing number of studies in CDI were focused on electrode material development. In 1995, Farmer et al. reported on a carbon-based material known as carbon aerogel that gained significant attention due to its monolithic structure with high surface area and electrical conductivity in CDI applications [39]. It is clear from Figure 2.4 that the majority of the scientific development of CDI technology directed toward material development from 1995 to 2012. Detailed descriptions of the material advancements for CDI process are provided in Section 2.4.

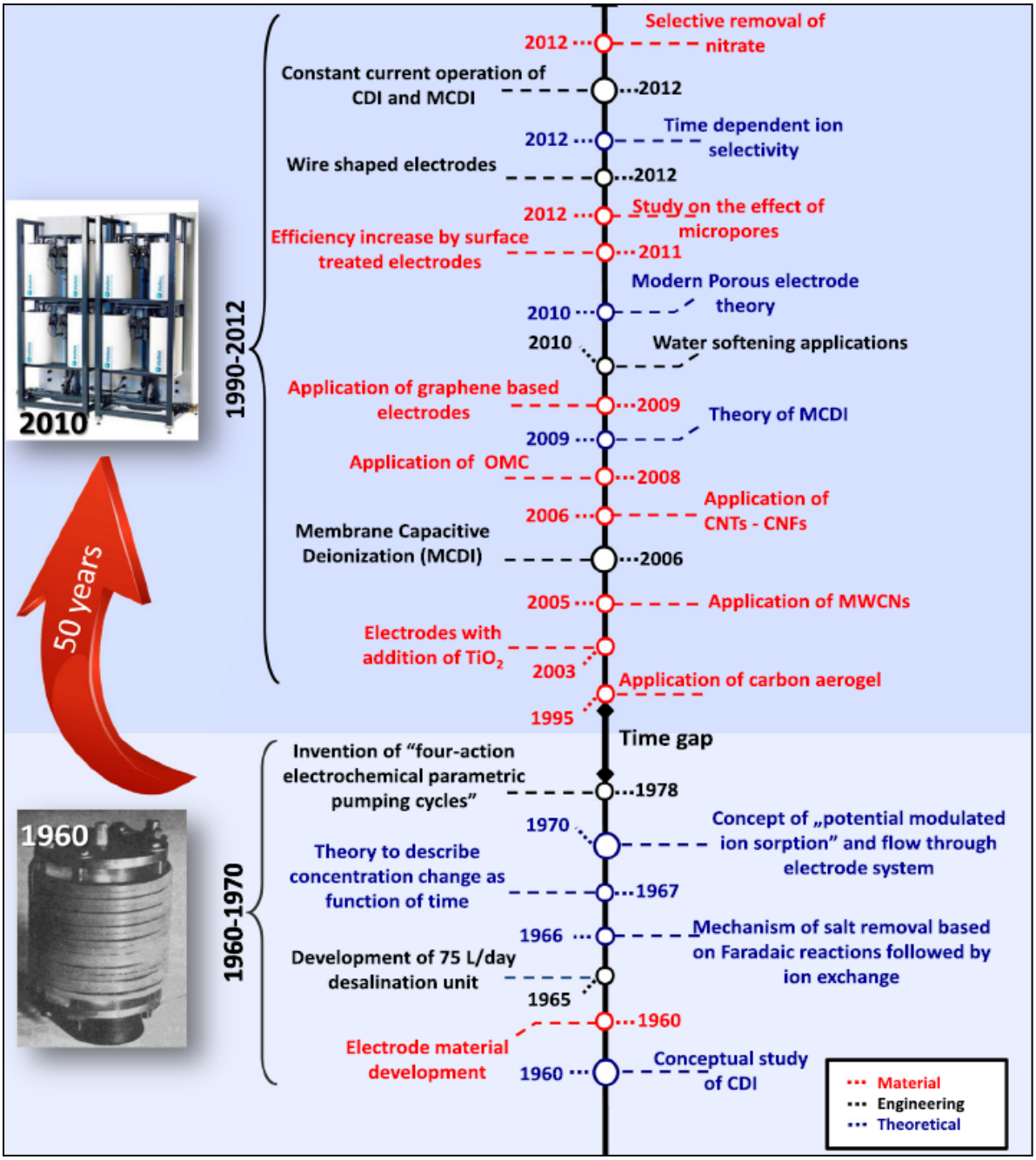

Figure 2.4 Scientific advancement of CDI between 1960 and 2012 [23].

2.4 Electrode material development of CDI

Since 1990s, a growing number of publications are directed toward development of effective carbon-based electrodes for EDL-based applications such as CDI and energy storage. Most of the CDI electrodes are made from a mixture of carbon particles (powder form), polymeric binders,

and usually a conductive additive (e.g., carbon black). The mixture is spread on current collectors (e.g., metal planes, graphite sheets) using physical methods such as pasting and drying to produce film electrodes made from individual carbon particles. In order to avoid using polymeric binders, other structured electrodes were reported using porous monoliths [87], carbon felts and fabrics [88], [89], or an interwoven array of porous fibers [90]. However, these electrode structures are associated with higher preparation costs comparing to the film electrodes. Recently, impregnated electrodes containing noble metals (in addition to binder and electrical conductive additives) have also been reported for capacitive deionization [91].

Significant efforts in CDI research have been made so far to exploit carbon-based electrodes: activated carbon [17], [49], [61]; carbon aerogels [34], [57], [60]; ordered mesoporous activated carbon (OMCs) [40], [47]; carbon nanotubes [42]–[44]; microporous carbide-derived carbons [45], [46]; modified activated carbon cloth [92], [93]; activated carbon nano-fiber web [94]; graphene-based material [53]; and carbon black [95]. The most important characteristics of an effective electrode material are: surface area; total pore volume; pore size distribution; electrochemical stability; electrical conductivity; and last but not least cost considerations. In the following sections, the properties of different carbon-based material (notably porous structure) and their effect on CDI performance is described.

Prior to further discussing the carbon-based material, it is important to define the different types of intra-particle porosity in porous material. According to the definition of the International Union of Pure and Applied Chemistry (IUPAC), pores can be categorized based on their size as follows:

- Macropores: > 50 nm
- Mesopores: Between 2 and 50 nm

- Micropores: < 2 nm

2.4.1 Activated carbon

Activated carbons (ACs) are by far the most commonly used commercial form of material in CDI from the early stages of 1970s. ACs usually have surface areas of 500–3000 m^2 g^{-1} [96]. ACs can be produced from different carbonaceous precursors including wood, coal, starch, coconut shells as well as synthetic sources such as resins. Among different AC precursors, lignin, hard wood, softwood, peat, coal and coconut shell have gained industrial attention due to their low price, sustainable supply, and ease of collection and transportation. These carbon materials are mostly in the form of micrometre-sized powders; however, other forms (e.g., fibers, beads, or monoliths) can be prepared using resin-derived precursors. One of the major disadvantages of ACs is the broad distribution of pore sizes comparing to other carbon-based material (e.g., template-produced carbons, nanotubes, and carbide-derived carbons) which will be discussed further in the following sections.

Different precursors and synthesis conditions result in a great variety of porous structure, pore size distribution, surface area, and chemical groups of AC. Detailed characterization of these parameters is important for a comprehensive comparison of AC material with other carbon-based electrode material for CDI.

Ban et al. has studied the electrosorption of hydrophobic, differently charged model substances (such as naphthalene-sulfonic acid ions, benzyl alcohol, and naphthoic acid anions) on a packed bed of granular activated carbon [97]. Jung et al. investigated the adsorption of uranium ions from lagoon sludge by applying a negative electrical potential to activated carbon fibres in a fixed bed reactor in a pH controlled environment [98]. Above 99% of Uranium ions were selectively removed from 100 mg L^{-1} influent and more than 99% of the adsorbed ions

were desorbed by applying a positive potential of 1.2 V and pH 3. The influential parameters on electrosorption performance in their report include surface acidic groups, applied voltage, and pH of the solution. Zou et al. reported a detailed study on CDI of brackish water using activated carbon electrodes [40]. They employed secondary surface treatment methods on ACs to improve the electrosorption capacity including the treatment with 3 mol L^{-1} KOH at 80°C, or the deposition of TiO_2. Both of these modifications increased the electrosorption capacity by 5 and 10%, respectively, due to enlarging the pore size, surface area, and reducing the Faradaic reactions on the surface of AC due to bonding of TiO_2 molecules with polar groups of carbon [40].

There are other studies in the literature reporting on the incorporation of different functional groups (e.g., metal oxide groups) to improve the performance of AC electrodes. Ahn et al. reported on the improved performance due to charge transfer of the surface functional groups [99]. Ryoo et al. investigated the modification of activated carbon cloth (ACC) with Ti-O groups upon loading with titanium (IV)-butoxide [93]. They reported increased electrosorption capacity due to change of the oxidation state of titanium and additional charge transfer. Other researchers reported on addition of other functionalities by incorporating nano particles such as ZnO, SiO_2, and Al_2O_3 resulted in improved capacities [100], [101]. In spite of the reported advantages, the long-term stability of these types of electrodes is questionable due to the degradation of functional groups over time.

An alternative surface modification method to metal-oxide coating is to oxidize the surface of AC with HNO_3 or KOH or reduction by hydrogen annealing [92], [102]. Oh et al. studied ACC electrodes treated by KOH or HNO_3, resulting in decreasing the specific surface area by 16 and 5%, respectively, while maintaining the average pore size unchanged [92]. Higher observed

electrosorption capacity was attributed to the opening of the closed pores (due to activation of carbon) [92].

2.4.2 Carbon aerogels

Another group of commonly used carbon-based material in CDI is carbon aerogel. Carbon aerogels showed promising CDI results mainly attributable to their high electrical conductivity (25–100 S cm^{-1}), high surface area (400–1100 m^2 g^{-1}), unique monolithic structure (interconnected particles with 3 to 30 nm in diameter with interstitial pores) and controllable pore size (<50 nm) [27], [34], [57], [103], [104]. The carbon aerogels have been synthesized in different forms such as powder, thin films, monoliths and small beads. Carbon aerogel was first introduced, characterized and tested by Pekala et al. for electrochemical separations [104]. These material are prepared by pyrolyzing the organic aerogel (constituted by polymerization of monomers in the form of cross linked wet polymer gels) at temperatures between 800 and 1100°C under inert atmosphere. Farmer et al. in a series of patents and reports have investigated the utilization of carbon aerogel for the removal of Na_2SO_4, Na_2CO_3, Na_3PO_4 from aqueous solutions [27], [39]. They found that the electro-conductivity of carbon aerogel is greatly influenced by pyrolysis parameters such as temperature and time.

As a result of low bulk density, carbon aerogels have low mechanical stability. Thus, the preparation of carbon aerogels was modified by addition of silica to carbon matrix to improve wettability, mechanical characteristics and ease of production of electrodes. The addition of silica increased the electrosorption capacity by 28% mainly due to the increased wettability. Gabelich et al. have also studied the adsorption of inorganic salts from their solutions in CDI system using carbon aerogels [34]. Effect of ion properties (e.g., radii, charge, mass, and size),

carbon aerogel preparation method, applied voltage, and content of Natural Organic Matters (NOM) on the electrosorption capacity and inorganic salt removal was studied.

2.4.3 Ordered mesoporous carbon (OMCs)

As previously mentioned, transport of ions within the carbon matrix affect the performance of CDI significantly. Efforts have been made in the literature to produce carbon material with large ordered mesopore content, i.e., ordered mesoporous carbon (OCM). OCMs are prepared through hard or soft templating methods [105], [106]. The hard templating method is involved with addition of a carbon precursor to templates such as zeolite or ordered mesoporous silica followed by carbonization. In the final step, the template is removed by chemicals such as hydrofluoric acid. In the soft templating method, a self-assembly of tri-block copolymers is carbonized to produce OCM. Depending on the preparation steps, the surface areas of OMCs are typically between 750 and 1500 $m^2\ g^{-1}$ which is comparable to that of many ACs. However, due to the completely different pore arrangement, reports suggested superior performance for OMCs compared to ACs [50], [107]. The possible disordered arrangement of micropores in ACs hinders the fast ion transport, thus a certain percentage of the high surface area is not effective for CDI performance. Zou et al. suggested a pore size around 3 nm as particularly effective size in removal of NaCl [107]. These results stress the importance of porous structure on the development of CDI performance.

2.4.4 Carbide-derived carbons

Carbide derived carbons (CDCs) have majorly microporous structure with extremely narrow distribution. The narrow micropore distribution and negligible mesopore volume of CDCs distinguish them significantly from ACs and OMCs, respectively. CDCs are prepared by etching of carbide powders at high temperatures (200–1200°C) in dry chlorine gas. Following to the

chlorine treatment, the samples are annealed under hydrogen to remove the residual chlorine compounds. The typical surface area of CDCs samples are between 1200 and 2000 $m^2 g^{-1}$ which can further develop to 3000 $m^2 g^{-1}$ when combined with activation [108].

Recent studies using CDCs as electrode material suggested an increase in capacity in sub nanometre micropores due to the distorted hydration shell of adsorbate ions [45], [46], [109]. This is in contrast to the commonly held view of micropores as a limitation for ion transport. Porada et al. studied differently prepared CDC materials and reported the effective behaviour of these carbon-based material in CDI of NaCl [45]. Fundamental aspects of the anomalous increase of capacitance in sub-nanometre micropores have also been studied [46], [109]. These results further confirm the importance of sub-nanometre micropores in increasing the CDI performance.

2.4.5 Graphene and carbon nanotubes

Carbon nanotubes (CNTs; tubular cylinders of carbon atoms) and graphene (two dimensional planar sheet of carbon atoms) are two other forms of advanced carbon material gained significant attention in various applications including CDI and energy storage. These carbon material possessed unique properties such as high electrical and thermal conductivity, high surface area, high mechanical stability, and mesoporous structure. The accessible surface area of CNTs and graphene is considered to be the exterior of the material in contrast to AC, where almost the whole surface area is within the material (i.e., slit-shaped pores). However, these nano-materials can also have significant intraparticle porosity when composed as electrodes for electrochemical applications such as CDI. For examples, the graphene sheet might be bent or wrinkled to produce slit-shape pores even within one sheet.

CNTs are produced by catalytic decompositions of certain hydrocarbons [110]. The surface area of CNTs is typically from 129 to 500 $m^2 g^{-1}$. However, studies also suggested increasing the surface area through KOH activation for improved EDL performance [111], [112]. Both single wall and multi-wall CNTs have been reported as electrode material in CDI and energy storage applications. Zhang et al. reported different multi-wall CNTs produced from catalytic decomposition of methane [113]. The surface area of samples ranged from 50 to 129 $m^2 g^{-1}$ with the largest CDI capacity obtained from the highest surface area sample. According to the literature, the relatively small surface area of CNTs (e.g., compared to ACs), resulted in smaller CDI capacitance compared to the carbon material with higher surface area [114]. Studies also investigated the mixture of CNT and AC to increase the surface area and improve the CDI capacitance. For example, Dai et al. studied the CDI performance of different mixtures of CNT/AC electrodes (from 1:0 to 0:1 ratios) for the removal of NaCl [115]. They observed that increasing the CNT content resulted in reducing the capacity continuously. However, the energy efficiency of the electrodes with high content of CNT was increased due to the improved electrical conductivity [115]. Gao et al. developed a new type of cost-effective large area CNT electrodes (i.e., CNT and carbon nano fiber, CNF) for electrosorption from NaCl, $CuCl_2$, $ZnCl_2$, and $FeCl_3$ solutions [44]. The CNT-CNF films are prepared on a graphite substrate by low temperature and low pressure thermal chemical vapour deposition of acetylene. The effect of different ion properties such as charge, ionic radii, and hydrated radii on the electrosorption performance was studied, suggesting that CNF-CNT films have the preference to adsorb multivalent cations. Additionally, for cations with the same ionic charge, the one with the smaller hydrated radius would be more effectively adsorbed [44]. Despite of the reported advantageous behaviour of using CNT in either pure or composite forms, the main disadvantage

is the presence of metal catalyst in the CNT structure which may reduce the electrochemical stability and result in unwanted parasitic side-reactions [38], [110].

Electrodes made from pure or composite graphene were also studied [53], [55], [116], [117]. Li et al. reported higher CDI capacitance of treated graphene electrodes (i.e., surface area <50 m^2 g^{-1}) compared with AC (i.e., surface area 990 m^2 g^{-1}) [53]. Zhang et al. studied the performance of AC, mesoporous carbon, and mesoporous carbon/graphene composite electrodes [116]. The mesoporous carbon/graphene composite showed the highest removal capacity and ionic transfer rates (i.e., lowest electrode resistance). The graphene nano-sheets were prepared through thermal exfoliation of graphite-oxide. The mesoporous carbon/graphene composite was then prepared through direct triblock-copolymer templating method using graphene with subsequent carbonization [116].

2.4.6 Carbon black

Carbon blacks (CBs) are fine powders (typically between 20 and 200 nm in average diameter) produced by thermal decomposition or partial combustion of hydrocarbons (e.g., oils and gases) [118]. These carbon materials have near spherical particles and are well known for their high electrical conductivity (0.1 to 100 S cm^{-1}) [118]. CBs are typically used in electrode preparation as highly conductive additives. The surface area of CBs has a wide range between <10 and 1500 m^2 g^{-1} [119], [120]. Panic et al. have studied the capacitive behaviour of two carbon black samples with different surface area and porous structure [95]. The effect of micro- and macropore (i.e., originated from the large agglomerates of particles) structures on the total capacitance of different carbon black samples was studied and the sample with more micropore content (and higher surface area) showed larger capacitance.

2.5 Applications and cell configurations

Besides the development of electrode material, various technological advancements were made during the past few years in CDI process compared to the classical work of the 20th century including: addition of ion-exchange membrane barriers in combination to electrodes [35], [36], [121], [122]; constant current condition [72]; salt release at reversed voltage [122]; optimized operational modes (e.g., stop-flow operation) [123]; energy recovery from electrode regeneration [124], [125]; and flow carbon suspension electrodes [35].

In addition to developing an effective material to be used as electrodes, various cell configurations have also been studied in the literature. One of the classic and most-widely utilized cell configuration of CDI consists of two electrodes separated by a space in which the electrolyte flows, a.k.a., flow-by (or flow-between) system (Figure 2.5 a) [39], [80], [85]. This type of cell configuration have been used in various applications from salt removal of different feed waters [60] to investigating the CDI performance of novel electrode material [45], [55] or fundamental studies of CDI concept [122], [126]. Another classic CDI cell type is called flow-through system in which the electrolyte is flowing perpendicular to the electrodes (through electrodes) (Figure 2.5 b). Avraham et al. studied the flow-through CDI systems for fundamental investigations of process parameters, e.g., charge efficiency [51]. They reported faster charging rate of electrodes in flow-through setup compared to flow-by systems. Additionally this cell-type eliminates the space between the electrodes (as required in flow-by systems), thus, minimizing the cell thickness (from 200–500 μm to ~10 μm) allowing more compact cells with lower ionic resistance [51], [52].

A significant variation of the basic CDI cell configuration was introduced in 2006 by Lee et al. [36]: addition of ion exchange membranes on the separator side of each electrode (Figure 2.5

c) similar to anion and cation exchange membranes (AEM and CEM) in electrodialysis (Figure 2.1). This cell-type is commonly known as membrane CDI (MCDI). The addition of membranes on the electrodes can be either as free-standing [38], or coated on the electrode material (to minimize the electrode thickness) [127]. Addition of membranes in CDI can improve the performance through increasing the charge efficiency (ratio of salt adsorption to charge per cycle) by blocking the counter-ions from carrying parasitic current [122]. Moreover, the membranes can be potentially tailored to selectively remove the desired ions from the electrolyte [128], [129]. The development of MCDI systems has been intensively investigated in the recent years in terms of membrane materials, fabrication methods, and theoretical understanding [37], [122], [127].

Another recent development in the CDI cell configuration was reported in 2013, where slurry of carbon electrode material and electrolyte is pumped through cell compartments [35]. The concept of flow electrode CDI (FCDI) is similar to that of electrochemical-flow capacitors in energy storage applications [130]. As the carbon electrode and saline water slurry flow between the charging compartments, the carbon particles are charged and the ions can be adsorbed on the EDLs (Figure 2.5) [131]. Carbon with the adsorbed ions is then separated (via sieving filters of ~100 μm size) to produce clean water. Two major advantages of flow-electrode CDI systems compared to static electrode CDI are: first, continuous desalination of effluent without interruptions for cell regeneration as the CDI process in not limited by reaching the capacity of the active material requiring intermittent regeneration and, second, the desalination capability of higher concentrations by continuous addition of the uncharged carbon particle slurries in the system [35]. Figure 2.5 shows different cell architectures for flow electrode CDI.

Moreover, recently another novel development in cell configuration was reported combining a battery electrode (sodium manganese oxide) and a capacitive porous carbon electrode in one desalination cell, a.k.a., Hybrid CDI (HCDI) (Figure 2.5 d) [132]. The sodium ions are removed (captured) by faradaic reaction in sodium manganese oxide electrode; while, the chlorine ions are electrostatically adsorbed on the porous carbon electrode. The maximum removal capacity (31.2 mg g^{-1}) was significantly higher than reported values for CDI units (1–13 mg g^{-1}). Additionally, rapid ion removal rate and significant stability were reported for the HCDI system [132]. To the best knowledge of the author, cation exchange membrane HCDI systems are not reported in the literature thus far.

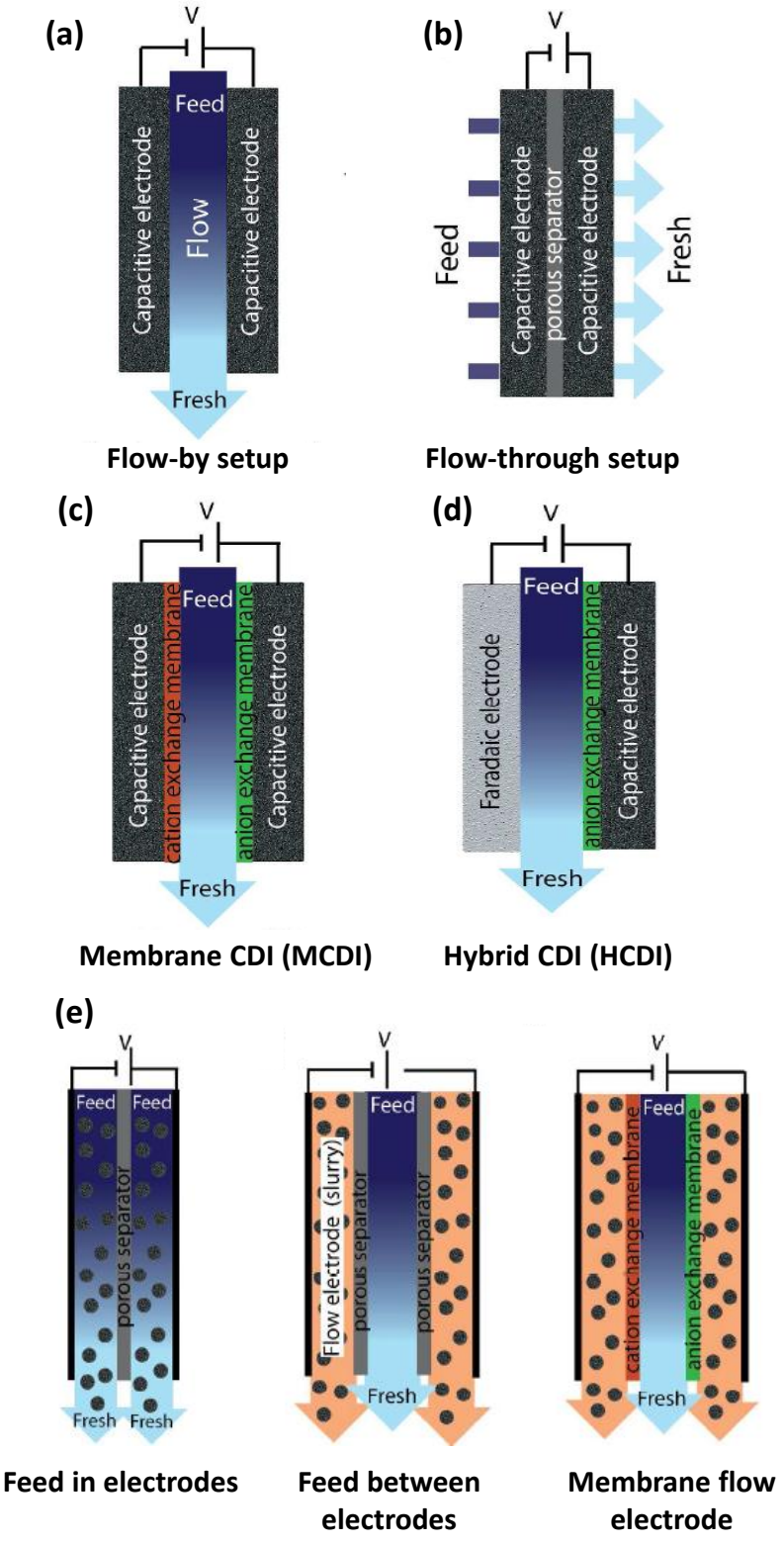

Figure 2.5 Different CDI cell configurations: (a) flow-by (flow-between); (b) flow-through; (c) Membrane CDI; (d) Hybrid CDI; and, (e) flow electrode CDI, adapted from [16].

2.6 Biochar: a renewable cost-effective carbon rich precursor

As discussed in Section 1.1.1, biochar is a by-product of the pyrolysis process (i.e., thermal decomposition in the absence or limited presence of oxygen) converting biomass into valuable products such as chemicals and fuel [1], [8], [133]. The main elemental composition of biochar is carbon, oxygen, nitrogen and non-combustible inorganic material known as ash. Based on the pyrolysis parameters (e.g., time and temperature) and the feedstock, the carbon content of biochar is varied between 30% and 60%.

2.6.1 Surface chemistry and elemental composition of biochar

The surface chemistry of biochar is highly dependent on the biomass feedstock and pyrolysis conditions (e.g., heating rate, temperature, and time) resulting in different hydrophilic, hydrophobic, acidic, and basic properties. According to the International Biochar Initiative, there are three classes of biochar based on the carbon content: class 1 with >60 wt.% or more; class 2 with 30–60 wt.%; and class 3 with <30 wt.% [10]. Additionally, O, H, N, S and P are the main heteroatoms in the aromatic rings of biochar carbon sheets. These heteroatoms result in surface chemical heterogeneity and different acidic and basic groups. Carboxylic, phenolic, and carbonyls are the main acidic groups; while, chromenes and pyrones are basic functionalities.

Besides carbon and heteroatom content, biochar also includes minerals in form of ash such as Al (Al_2O_3), Ca (CaO), Mn, Fe (Fe_2O_3), Si (SiO_2), and some heavy and transitional metals (Cd, Co, Li, Ni and Zn). Similar to carbon and heteroatoms, the composition and content of ash in biochar is varied (10–50 wt.%) based on feedstock and process conditions [7]. The presence of ash content in biochar structure can affect the traditional char applications such as adsorption and combustion properties as well as structural development during pyrolysis [1], [6].

2.6.2 Structure of biochar

Biochar is a non-graphitic/non-graphitizable carbon material basically constituted of amorphous carbon sheets [1]. One of the major differences between biochar and other organic matter is the large content of aromatic carbon especially fused aromatic structures, i.e., the arrangement of monocyclic carbon rings sharing connecting bonds [7]. Depending on the pyrolysis temperature, the fused aromatic structure can be varied with majorly amorphous structure at lower temperatures (<450°C) and turbostratic structure at higher temperatures (500–900°C). Despite of the general amorphous nature of biochar, some local crystalline structure of highly conjugated aromatic compounds (fused aromatic C) was observed [1]. These crystalline areas are visualized as flat aromatic carbon sheets (similar to small graphene layers) cross-linked randomly by weak Van der Waals bonds (Figure 2.6). These graphite-like micro-crystallites are known to be responsible for the electrical conductivity of biochar material as "conducting phase" [1]. The other component of biochar carbon matrix is the aromatic-aliphatic organic compounds with complex structures including residual volatiles generated during thermal biomass decomposition (i.e., tars) [134], [135]. These compounds can fill and block the pores of biochar as well as occluding mineral content in the pores.

As shown in Figure 2.6, increasing the carbonization temperature contributes to structural development through enlarging the graphite-like micro-crystallites and generating more order between the sheets (i.e., turbostratic structure[1]). Moreover, increasing the temperature further develops the surface area of biochar (up to 500 $m^2\ g^{-1}$) by evolution of volatiles (e.g., tars and other amorphous decomposition products) and consequently enhancing the pore development [1].

[1] Carbon sheets might be parallel and equisidant but they are rotated in respect to each other. Moreover, the spacing between the layers is larger than that of graphite structure.

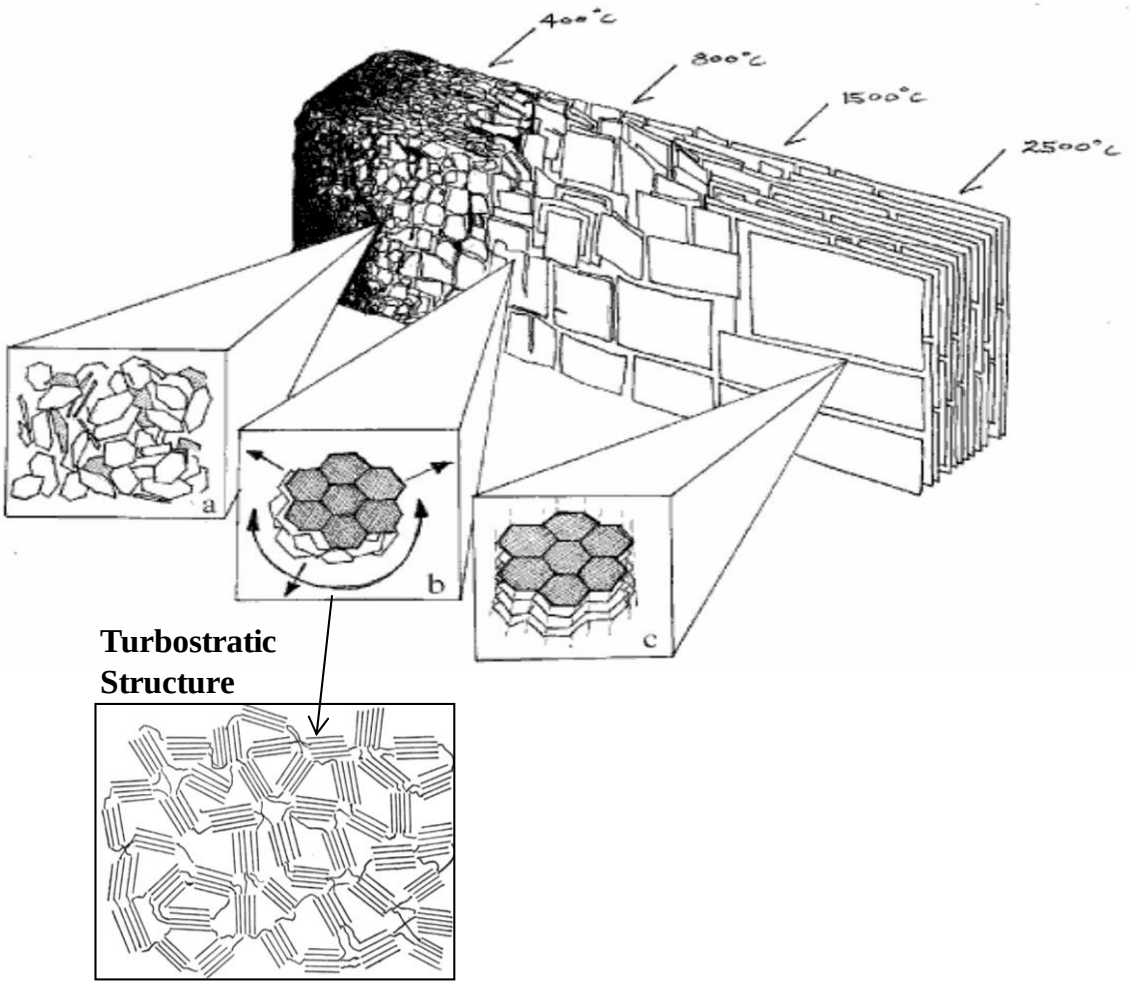

Figure 2.6 Carbon structure in biochar: a) aromatic carbon sheets in a random disordered structure; b) growing carbon sheets with developing turbostratic structure; c) graphitic structure with order in third dimension at high temperatures (>1700°C) [44].

2.6.3 Cost of biochar

Cost estimation of biochar produced from different precursors is not frequently reported in the literature. There are a number of different variables affecting the cost of biochar such as availability of precursor, pyrolysis conditions, processing requirements, and region (country) of production [10]. One of the major contributors to the cost of biochar is the cost of biomass including transportation costs to the pyrolysis site [2], [136]. An alternative way to alleviate the

transportation costs of biomass is to use mobile pyrolyzers that could be transferred to the biomass sources [137], [138]. The mobile pyrolysis can be applied to different types of biomass including forestry and agricultural waste to produce energy.

The market value of biochar is dependent on whether it is the main product or other value-added products are obtained. Based on pyrolysis conditions, biochar could be the main targeted product or a by-product in case of bio-refineries. Manganaro and Lawal studied the Fischer-Tropsch liquid fuel production from crop residues including fast pyrolysis, auto thermal reforming, and FT synthesis processes [139]. The fast pyrolysis char by-product was estimated US$500 t^{-1} for soil enhancement applications [139]. Another study by Brown et al. investigated the profitability of fast pyrolysis vs. slow pyrolysis of corn stover based on the projected sequestrated carbon and energy prices until 2030 [140]. The investment's rate of return (IRR) was estimated based on the price of corn stover from US$0 to US$83 per metric ton. The fast pyrolysis IRR ranged between 29% and 37% for zero cost feedstock and between 15% and 26% for the more realistic corn stover price of US$83 t^{-1}. However, the slow pyrolysis showed IRR between 8% and 17% at zero cost of corn stover and not profitable when corn stover costs US$83 t^{-1}. The main reason was attributed to the low value of biochar even with sequestrated carbon is priced US$20 to US$55 per metric ton CO_2-e. Thus, producing biochar as the main product in slow pyrolysis (i.e., if used as a carbon sequestrating product) is unlikely to be profitable. However, the fast pyrolysis process majorly producing gas and transportation fuel with biochar as a by-product (and carbon sequestrating reagent) showed a relatively attractive economics based on the estimated prices of gasoline fuel and sequestrated carbon in the coming years [140].

Shackley et al. reported a comprehensive study on the cost of producing biochar in UK [136]. They have estimated the cost based on type of feedstock (fresh or waste biomass), operating costs, production size, storage and transport of feedstock. They also incorporated the income from electricity generation (from produced gases) and "Renewable Obligation Certificate", i.e., certificate given to the electricity producing plants from renewable sources to meet obligations set by the UK government. These certificates can be traded between different parties. The cost of biochar estimated between –148 and 389 £ t^{-1} (–US$222 to US$584 t^{-1}) with negative value showing biochar as a product at a profit. Moreover, their study suggested 60–90% reduction in cost of biochar production using waste biomass as opposed to fresh biomass sources (in a medium-scale unit using 16,000 dry tons of feedstock per year). This was attributed to the gatefee revenues available for the waste biomass feedstock compared to fresh feedstock [136].

2.6.4 Developing biochar as activated carbon

The worldwide demand for Activated Carbon (AC) is rising rapidly with a 10% increase per year due to diverse applications ranging from pollution abatement to energy storage [141]. Producing AC from waste and by-products gained attention since availability of low-cost precursors is necessary for the economic feasibility of large-scale AC production [13], [142], [143]. Ioannidou and Zabaniotou have done a critical review of using different agricultural residues to produce activated carbon [5]. They discussed the effect of various activating conditions, physical and chemical, on the properties of produced ACs.

Biochar can be used as a renewable and low-cost precursor for AC production [13]. Using biochar as a valued-added AC broadens its application in different processes also increasing the product utilization of pyrolysis process. Activated biochar (i.e., activated carbon) has shown potential capabilities for the removal of organic and inorganic contaminations (e.g., Cu^{2+}, Zn^{2+},

and Pb^{2+} ions) from wastewater with adsorption capacities up to 200 mg g^{-1} [10]. As explained in Section 2.6.2, based on the feedstock and pyrolysis conditions (specifically heating temperature), biochar can show a wide range of surface area between 1 and 500 m^2 g^{-1}. The porous structure of biochar samples (specifically those prepared at low pyrolysis temperatures in fast pyrolysis process, i.e., <450°C) is partially or fully blocked by tars. For biochar samples to be used as activated carbon (AC), the surface area and pore structure need to be enhanced.

The conventional methods of increasing the surface area of carbonaceous material is physical or chemical activation widely studied in the literature. Effect of different reaction parameters on the properties of AC produced from both physical and chemical activation methods are studies extensively in the literature [13], [144]–[149]. Basically there are two main steps in producing activated carbon material: carbonization of the raw material in the absence of air below 800°C (i.e., pyrolysis); followed by the activation through either physical or chemical methods [5].

Physical activation is carried out most frequently in industrial applications [1]. This process contains two stages: pyrolysis and activation. Upon pyrolysis of the carbonaceous precursor, the carbonized material is subjected to partial gasification in the presence of oxidizing gases such as CO_2, steam, air or a combination of these gases at high temperatures typically >900°C. Development of porosity is mainly attributed to the oxidation and burn off of carbon during gasification. According to the literature, CO_2 contributes to opening the closed pores while also widening the existing pores by activation [150]. Steam, on the other hand, promotes the removal of volatiles (through partial devolatilization) and also enhances crystalline carbon formation [151].

Chemical activation is involved with addition of chemical reagents (e.g., H_3PO_4, $ZnCl_2$ and alkali metal hydroxides or salts) to carbon precursors followed by carbonization at high temperatures (500–900°C). One of the major advantages of chemical activation over physical activation is the combination of both carbonization and activation stages in one step. The exact mechanism of chemical activation is not well understood [152], [153]; however, according to some literature, the general reaction (using alkalis) includes the hydroxide reduction and carbon oxidation to generate porosity [152]. CO, CO_2 and H_2 are generated during the reaction and the chemically activating agent is eliminated by washing with acid/base and water [153]. Further description of the mechanism is explored in Phase II, Chapter 5.

There has been a growing focus on chemical activation as opposed to physical activation, due to higher surface area, narrower pore size distribution, and lower carbon burn-off, as well as operational advantages such as shorter reaction time and lower carbonization temperatures [13], [145], [146]. However, chemical activation methods are not as common as physical activation due to the possibility of generating secondary environmental pollution during disposal [154]. Nevertheless, alkali metal hydroxides/salts (e.g., KOH, NaOH, K_2CO_3) showed promising results in porosity development of carbonaceous precursors while having less environmental concerns for end-use applications, e.g., pharmaceutical and food processing, compared to other activation reagents [147], [148], [155]. Despite of numerous reports studying effects of different chemical activation process conditions on the properties of produced ACs (e.g., critical review of Ioannidou and Zabaniotou), some operational parameters are yet overlooked in the literature.

Similar to other carbonaceous raw material in the literature [13], [156]–[159], biochar can be activated through chemical or physical activation method [13], [160], [161]. Azargohar and Dalai have studied the production of activated carbon from fast pyrolysis biochar (with 10 $m^2\ g^{-1}$

surface area) through physical (steam) and chemical (KOH) methods [13]. They have studied the effects of activation parameters (e.g., mass ratio of KOH and steam to biochar, nitrogen flow rate, and carbonization temperature) on the surface area and the yield of activated biochar through Central Composite Design (CCD). The optimum conditions for each activation method were reported based on the highest values of surface area and reaction yield. Chemical activation method showed higher BET surface area (783 vs. 643 m^2 g^{-1}) and better yield (i.e., 75% vs. 57%) compared to physical activation upon optimum conditions applied. Also, the majority of the pores in chemically activated biochar were microporous with average pore size of 13–15 Å; while, physical activation resulted in a broader distribution of pores between 13 and 26 Å.

2.7 Significance and novelty

One of the major challenges for the CDI technology to function as a large-scale water treatment method is the development of electrode material. Many of the promising materials reported in the literature are associated with costly and complicated preparation methods as well as potential secondary environmental pollutions associated with preparation steps. The present work investigates the application of biochar as a low-cost by-product carbon precursor for EDL-based applications namely CDI. Physico-chemical properties are developed and their corresponding effects on the EDL performance are studied. Moreover, a novel variant of chemical activation was proposed as a simple method to control the porous structure of activated biochar to be potentially utilized in adsorption-specific applications. The activated biochar electrodes with tailored porous structure could introduce a new generation of renewable electrodes for CDI technology. Additionally, the application of biochar could be broadened as a novel renewable carbon-based candidate for pollution abatement and energy storage applications.

Chapter 3: Experimental procedures and methodologies

3.1 Material preparation

In this chapter the experimental methods used for preparation of samples and their physical, chemical, and electrochemical characterizations are presented.

The as-received biochar samples used in this work were prepared through fast pyrolysis of whitewood (Spruce) at 600°C. The samples were provided by Dynamotive Energy Systems (Vancouver, BC, Canada). With respect to the properties of biochars, it is presumed that there is variability between samples produced from different species. Yet, the source of biochar used throughout this project remained constant. Prior to using the biochar, samples were dried in oven at 120°C for at least 72 h. The Vulcan XC-72 (carbon black) was obtained from Cabot Corporation (US). Nafion® (5 wt.% solution in a mixture of lower aliphatic alcohols and water) was purchased from Sigma Aldrich and used as such. Isopropanol (ACS reagent), HCl solution (37 wt.% concentration), and HNO_3 (63 wt.% concentration) were all purchased from Fisher Scientific. KOH pellets (>90% purity) was purchased from Sigma Aldrich. NaCl (certified ACS ≥99.99%) and $ZnCl_2$ (99.99% trace metals basis) were purchased from Fisher Scientific and Sigma-Aldrich, respectively. Acid-Resistant Nickel mesh (Monel® alloy with 150 × 150 mesh size per square inch with 0.066 mm wire diameter; McMaster Carr) and carbon cloth (uncompressed thickness of 380 μm; ElectroChem Inc.) were utilized as current collectors.

3.1.1 Chemical activation

The overall chemical activation procedure was followed by the method reported by Azargohar and Dalai [162]. Dried as-received biochar was first ground (using a ceramic mortar and pestle) and sieved between 50 and 180 μm mesh size. The ground biochar powder (~20 g) was then mixed with a specific amount of 7 mol L^{-1} KOH solution such that the mass ratio of

pure KOH to biochar was 3.55 (i.e., optimum mass ratio yielded the highest surface area as reported by Azargohar and Dalai [162]). After stirring this mixture at room temperature for 2 h in a beaker with a magnetic stirrer (to ensure the accessibility of KOH to biochar), the mixture was filtered via either filter papers (for the samples studied in Chapter 4) or centrifuging (for the samples used in Chapters 5 and 6). Centrifuging the samples (at 10,000 rpm for 5 min) provided better separation compared to filtration since using filter papers led to shrinkage as a result of exposure to highly concentrated KOH solution and problematic separation.

Upon separating the impregnated biochar with KOH, the pre-carbonization drying step carried out and the samples were dried at 110°C for varied lengths of time (0, 15, 140, and 280[1] h) under different atmospheres (N_2 or air). Air drying was done in a typical low-temperature laboratory oven, while drying under nitrogen was done in a tube furnace with 80 mL min^{-1} flow of ultra-pure nitrogen.

The dried KOH-treated samples were then ground to powder using a ceramic mortar and pestle to make relatively consistent particle size and placed in a tube furnace (Thermo Scientific Inc.) under nitrogen flow (258 mL min^{-1}) for carbonization between 475°C and 1000°C. The samples were initially heated to 300°C for 60 min (3°C min^{-1} rate) to ensure the complete removal of water. Afterwards, the activated samples were further heated (3°C min^{-1} rate) to the desired temperatures (between 475°C and 1000°C) with different dwell time (0.5–5 h). The samples were then left to cool to room temperature under nitrogen flow followed by washing with distilled water until the pH of wash water became neutral (measured by pH-indicator strips). The washed samples were then mixed with 250 mL of 0.1 mol L^{-1} HCL and stirred at room temperature for an hour for demineralization and complete removal of KOH. A final washing

[1] The longest drying time of 280 hrs was conducted to investigate the extent of drying effect, and not necessarily meant to be practical from large-scale production perspective.

step with distilled water was conducted after HCl treatment until the wash water became neutral (via pH-indicator strips). The washed treated biochar was dried overnight at 110°C.

3.1.2 Working electrode preparation

The carbon-based samples (e.g., untreated biochar, activated biochar, and Vulcan XC-72) were ground and sieved between 40 and -150 μm mesh sizes. The powder samples (~40 mg) were then mixed with 2–10 mL isopropanol (99.9% assay; Fisher Scientific) and in some cases with Nafion® solution (as binder) to prepare the ink composition for spraying onto different current collectors: Ni mesh, carbon cloth, and graphite felt (details provided in Appendix A). Having the carbon material deposited on a mechanically flexible, thin and electronically conductive substrates is advantageous, as it allows the design of cells with various configurations, e.g., stacked or rolled screens. Different ink solutions were prepared based on various weight percentages of Nafion®, i.e., 0, 5, 10, and 30 wt.%, to study the adherence of the activated biochar particles to the current collectors. The prepared ink solutions were sonicated for 2 h in an ultra-sonicator to ensure high dispersion of particles in the solution. To prepare relatively homogeneous electrodes, the sonicated ink solutions were sprayed onto current collectors using either automatic or manual spraying methods.

In the automatic spraying method, a moving stainless steel plate controlled by numerical computation (CNC) was equipped with IWATA® air-brusher (50 mL capacity) for homogeneous spraying (further details in Appendix A). The Ni mesh current collector was placed on a heated stainless steel plate (40°C) to improve the spraying and prevent flooding of the substrate by the ink. Automatic spraying utilized to prepare electrodes on Ni mesh with the coated material loading between 10 and 30 mg. The electrodes studied in Chapters 4 and 5 are prepared based on this method.

In the manual spraying method, similar heated stainless steel plate (40°C) was used in a static position while manual spraying was performed using Mastercraft® air-powered gravity-feed spray gun. Carbon cloth was used as current collector and to increase the wettability, the cloth was treated in 60°C HNO_3 (1 mol L^{-1}) for 75 min followed by extensive washing with deionized water prior to spraying. The manual spraying was performed to increase the material loading and decreasing the spraying time for the electrodes requiring larger masses (~0.027 g cm^{-2}). The manually sprayed electrodes used for Chapter 6 analyses. Further specifications of the electrodes are described in each corresponding chapter.

3.2 Physical and chemical characterization of the carbons

3.2.1 Surface area and porosity

The surface area and porosity of activated biochar samples were studied using N_2 adsorption isotherms at –196°C. Surface area, micropore volume, and mesopore volume of each sample were measured by Brunauer-Emmet-Teller (BET), t-plot, and Barrett-Joyner-Halenda (BJH) methods, respectively, using a Micromeritics ASAP 2020 Accelerated Surface Area and Porosimetry Analyzer[1]. The instrument variability is within ±3% of the reported values. Calculations corresponding to each characterization method are reported by Webb and Orr [163]. Prior to each experiment, about 90 mg of sample was vacuum degassed (at 10 μm Hg and 120°C) for 5 h in the built-in degas port of the instrument. The N_2 adsorption isotherms for all samples showed either type I or IV according to IUPAC classification characteristic of microporous and mesoporous structures, respectively.

To further study the micropore distribution and cumulative volume, samples were characterized by Horvath Kawazoe (HK) method using N_2 as adsorbing gas at significantly low

[1] Available in lab 5.06 in Department of Chemical & Biological Engineering at the University of British Columbia.

P/P° relative pressures (i.e., 5×10^{-7} to 5×10^{-2}). Samples were vacuum degassed at 300°C for 8 h prior to the HK analysis.

3.2.2 Structure and morphology

3.2.2.1 FESEM and TEM

The morphology and structure of the activated biochar samples were studied through Field Emission Scanning Electron Microscopy (FESEM) and Transmission Electron Microscopy (TEM), respectively. For FESEM imaging, the powder samples were first diluted in isopropanol and sonicated for 5 min. About 20 μL of the diluted samples were then transferred onto stainless steel stubs and dried in oven. FESEM images were taken using Hitachi S-4700 at 3–30 kV[1]. For TEM analysis, the samples were diluted in reagent grade ethanol (99.5%, Extra Dry; Fisher Scientific) and 5 μL of the diluted powder samples was placed on TEM grid to provide facile evaporation and product visibility during imaging. TEM images were obtained using Tecnai G2 microscope at acceleration voltages of 20–200 kV[2].

3.2.2.2 Raman spectroscopy

The Raman spectra were recorded at an excitation wavelength of 632 nm via a LabRAM ARAMIS microscope with an argon-ion laser source[3]. The deposited samples on aluminum substrate were exposed to the laser beam (1 μm diameter at the focus; exposure time 1 s) at room temperature. To ensure the consistency of the results, data collected from three to five different regions of each sample.

[1] Available in Bio-Imaging facility in Department of Botany at the University of British Columbia.
[2] Available in Bio-Imaging facility in Department of Botany at the University of British Columbia.
[3] Available in room 344 in Advanced Materials & Process Engineering Building at the University of British Columbia.

3.2.2.3 X-ray diffraction (XRD) analysis

The crystallographic structure of each carbon-based sample was investigated using X-ray Diffraction analysis (XRD) on a Bruker AXS D8 Advance X-ray Diffractometer (in Bragg-Brentano configuration) equipped with a Lynxeye ID silicon strip detector[1]. A Ni filter was used to strip out the Cu Kβ radiation thus leaving Cu Kα1,2 radiation generated at 40 kV and 40 mA. Custom-made sample holder with a shallow well was used for sample mounting. EVA 10.0.1.0 software was used for data interpretation.

3.2.3 Elemental and ash content analyses

The elemental composition of the samples was measured by Canadian Microanalytical Services (Delta, BC, Canada). The C, H, and N elemental content of samples were characterized by measuring the combustion gases (CO_2, N_2 and H_2O) obtained upon exposing the samples to oxygen flow at 1800°C. To measure the oxygen content of each sample (organic content), pyrolysis in the absence of air was done followed by measuring the CO content using gas chromatography. About 100 mg of each sample was used for elemental analysis and the experiments were conducted in triplicates.

The ash content of the samples was measured by Exova Labs (Surrey, BC, Canada). Samples were heated at 900°C under air and the remaining mass was reported as the ash content (Lost On Ignition; LOI-900 method). Inductively coupled plasma atomic emission spectroscopy (ICP-AES) were utilized to quantify the ash elemental composition.

The elemental composition of biochar is shown in Table 3.1. The majority of the ash content is consisted of SiO_2 (60%), Al_2O_3 and CaO (~8% each). Further details are provided in Table B1, Appendix B.

[1] Available in Structural Chemistry Facility in Chemistry Department at the University of British Columbia.

Table 3.1 Elemental analysis (wt.%) and ash content of the dried as-received biochar

Sample	C (%)	H (%)	N (%)	O[1] (%)	Ash (%)
As-received biochar	64.65	2.23	0.13	23.03	13.6

3.2.4 Surface chemistry

Surface functional groups were investigated using Fourier Transform Infra-Red (FT-IR) spectroscopy using a Varian 3100 FT-IR Excalibur Series spectrometer with attenuated total reflectance (ATR): Pike MIRacle™ATR with ZnSe crystal[2]. Scan speed of 2.5 kHz with aperture setting of 4 cm^{-1} over a wave number range of 4000–650 cm^{-1} were applied for spectra collection. For each sample 64 scans were co-added to improve the signal-to-noise ratio.

3.3 Electrochemical characterization

Cyclic Voltammetry (CV), Galvanostatic Charge Discharge (GCD) and Impedance Spectroscopy (EIS) analyses were conducted in a three-electrode configuration at room temperature with Pt mesh as counter electrode and mercury/mercury oxide (Hg/HgO/KOH 0.1 mol L^{-1}) as reference electrode. The electrolyte was composed of 0.1 mol L^{-1} NaCl in 0.1 mol L^{-1} NaOH (using deionized water) to relate the results to the potential applicability of activated biochar electrodes for both water desalination through CDI (e.g., in chlor-alkali industry) and supercapacitor fabrication (e.g., using alkali electrolyte). Also, the basic electrolyte was chosen to ensure that there is no contribution from Faradaic reactions of current collector (i.e., based on Pourbaix diagram of Nickel) in electrochemical analyses.

3.3.1 Cyclic voltammetry (CV)

Cyclic Voltammetry is one of the major electrochemical analyses to study the EDL behaviour of different material. Constant potential rate (in V s^{-1}) is applied to the working

[1] Organic content of oxygen
[2] Available in lab 5.18 in Department of Chemical & Biological Engineering at the University of British Columbia.

electrode in a specified potential window while the current response is measured. A plot of current versus potential is constructed, i.e., voltammogram. An ideal EDL capacitor is supposed to show a rectangular shaped voltammogram in which the sign of current is reversed immediately upon reversal of the potential sweep [103], [110]. In this process the produced current is purely electrostatic and is independent from potential.

The total capacitance of an electrode can be quantified using the cyclic voltammogram by dividing the anodic and cathodic current differences ($\Delta I = I_a - |I_c|$) at the EDL plateau region with the corresponding sweep rate based on Equation (3.1) [54], [164], [165].

$$I = C \, . \, (^{dV}/_{dt}) \tag{3.1}$$

The investigated electrodes were first electrochemically conditioned by performing 150 cycles at sweep rate of 50 mV s^{-1} between –0.4 and +0.4 V vs. Hg/HgO, generating reproducible voltammograms. After the conditioning step, the electric double layer behaviour of the electrodes was studied by cyclic voltammetry and charge/discharge experiments, respectively. The cyclic voltammetry (CV) potential scanning was conducted at different sweep rates between 0.5 and 50 mV s^{-1} using the 1100A Series Electrochemical Analyzer (CH Instruments, USA)[1].

3.3.2 Galvanostatic charge/discharge (GCD)

Galvanostatic charge/discharge experiments were performed using the Solartron 1470E potentiostat[2]. Constant 0.25 and –0.25 mA cm^{-2} current densities were applied as charge and discharge currents at equal time intervals (varied between 10 and 150 s). The maximum potential was set to 0.07 V cm^{-2}. The Ohmic potential drop (IR-Drop) of each electrode was also measured using the sudden drop of the potential while switching between the charging and

[1] Available in lab 6.08 in Department of Chemical & Biological Engineering at the University of British Columbia.
[2] Available in lab 6.18 in Department of Chemical & Biological Engineering at the University of British Columbia.

discharging currents (values were obtained from data points at the end of charging section and the beginning of the discharge) [165].

3.3.3 Electrochemical impedance spectroscopy (EIS) analysis

The alternating current (AC) impedance spectroscopy (EIS) was performed using Solartron 1470E and the spectrum was analyzed using Multistat® software[1]. The AC potential amplitude was 10 mV and the frequency ranged between 10^{-2} and 10^{5} Hz.

3.3.4 Electrical conductivity (EC)

The Electrical Conductivity (EC) of the activated biochar powder was measured using linear sweep voltammetry (LSV). About 20 mg of dried and sieved powders (10–50 μm mesh size; dried 2 h at 120°C) placed between ultra conductive Cu plates (alloy 101; McMaster-Carr) with 2 mm distance (Figure C1, Appendix C). Constant potential sweep (20 mV s^{-1}) was applied to the test cell and the potential was plotted against current. The experiments were repeated at least three times. The slope of the diagram was obtained (i.e., representative of Ohmic resistance) and used for electrical conductivity (EC) measurement.

3.3.5 Capacitive deionization (CDI) and electrosorption

Capacitive deionization of Na^{+} and Zn^{2+} in their corresponding solutions of NaCl and $ZnCl_2$ has been studied. The NaCl was chosen to relate the results to desalination purposes; while, $ZnCl_2$ is one of the toxic pollutants in metal mining effluents (e.g., Rio Tinto Alcan[2]) with high degree of toxicity reported by the National Recommended Water Quality Criteria and is also on the Priority List of Hazardous Substances of Comprehensive Environmental Response, Compensation, and Liability Act [166], [167].

[1] Available in lab 6.18 in Department of Chemical & Biological Engineering at the University of British Columbia.
[2] http://www.riotinto.com/documents/_Energy/Appendix%20H.pdf

Capacitive deionization of 10 mmol L^{-1} NaCl (>99.0 % Certified ACS; Fisher Scientific) was conducted in a batch-mode 200 mL acrylic test cell (Figure 3.1). The biochar electrodes were mounted on acrylic plates and placed with 9 mm distance in the test cell. The identical electrodes (0.21–0.25 g) were then connected to a potentiostat (Princeton Applied Research; BES 263A[1]) and charged at constant current density of 0.22 mA cm^{-2} for 4500 s. The CDI tests have been conducted at natural pH of 5.7. The schematic representation of the CDI test cell is shown in Figure 3.1. No stirring has been done during the CDI experiments. Upon completion of the charging, the electrodes were regenerated at 0 mA in 1 mmol L^{-1} NaCl for 6800 s followed by further discharging in deionized water overnight (17 h). The regenerated electrodes were then used for three additional CDI cycles under identical conditions to study the durability. The reversed current method was not used for regeneration of electrodes since no ion exchange membranes were used in producing electrodes. Thus, by reversing the current the electrodes start to adsorb the counter ions rather than being regenerated.

To measure the removal capacity of the electrodes, samples were taken in triplicates from test-cell electrolyte (i.e., 10 mmol L^{-1} NaCl) at the beginning and the end of the charging cycle and the amount of Na^+ ion was measured by Atomic Absorption Spectrometer (Varian SpectrAA) using sodium Hallow Cathode Lamp (Fisher Scientific) at 589 nm wavelength[2]. The difference between initial and final amount of Na^+ was normalized per volume of the test-cell and the amount of activated biochar on each electrode and reported as removal capacity in mg g^{-1} L^{-1}.

Upon completion of the NaCl CDI experiments, the electrodes were further tested for electrosorption of Zn^{2+} from 10 mmol L^{-1} $ZnCl_2$ (99.99% trace metal basis; Sigma Aldrich)

[1] Available in lab 6.08 in Department of Chemical & Biological Engineering at the University of British Columbia.
[2] Available in Environmental Engineering Lab in Department of Civil Engineering at the University of British Columbia.

solution (pH 5.7) under similar constant current conditions (i.e., 2 mA) for four consecutive cycles. Regeneration of the electrodes was similarly conducted between each cycle in 1 mmol L^{-} [1] $ZnCl_2$ at 0 mA followed by discharging in deionized water overnight (17 h). The amount of Zn^{2+} removal was measured using Atomic Absorption Spectrometer with Zn^{2+} Hallow Cathode Lamp (Westinghouse) at 213.9 nm wavelength[1]. The Zn^{2+} removal capacity was calculated through the similar method as Na^{+} removal capacity.

3.3.6 Zeta potential and surface charge characterization

The surface charge characterization at different pH values was studied by measuring the Zeta potential using a ZetaView® Nanoparticle Tracking Analyzer (Particlemetrix, Meerbusch, Germany)[2]. A suspension of 100 ppm activated biochar sample was prepared by mixing in 0.01 mol L^{-1} NaCl. The suspension was then sonicated for 1 min and mixed with a magnetic stirrer for 10 min at the desired pH value. The pH was adjusted (between 2.0 and 11) using 5% and 1% NaOH or HCl solutions, respectively. The sample was left to stand for 1 minute prior to analysis. An aliquot was then drawn for Zeta potential analysis using a glass syringe and injected into the ZetaView® electrophoresis cell. The results are reported as average Zeta potential calculated from the electrophoretic mobility using the Smoluchowski equation and plotted vs. pH.

[1] Available in Environmental Engineering Lab in Department of Civil Engineering at the University of British Columbia.
[2] Available in lab 517 in Norman B Keevil Institute of Mining Engineering at the University of British Columbia.

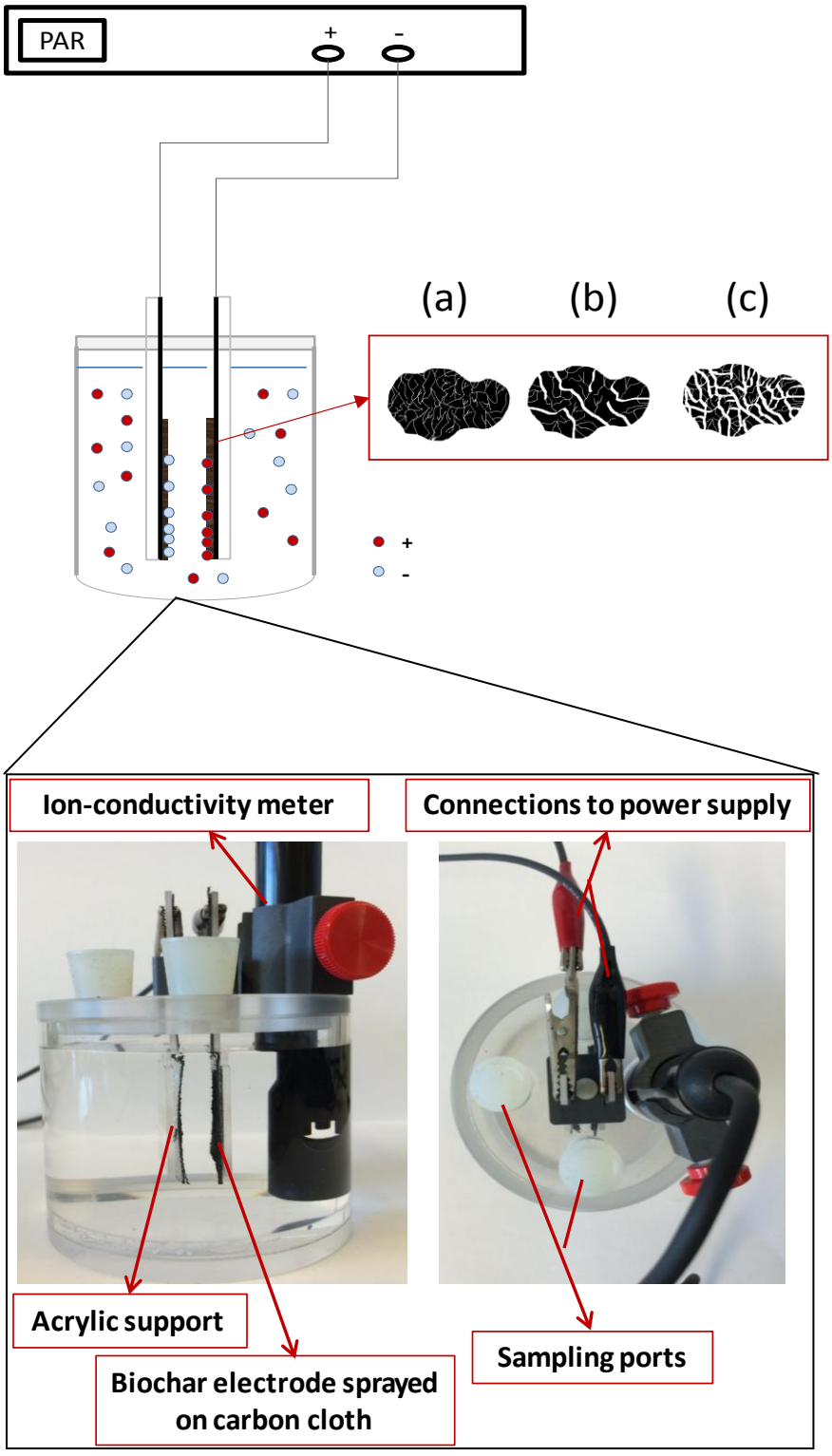

Figure 3.1 Schematic representation and setup of CDI unit using activated biochar electrodes with: (a) microporous; (b) mixed micro- and mesoporous; and (c) mixed micro- and mesoporous with the majority of the latter.

Chapter 4: Phase I - Initial studies on biochar as EDL electrodes[1]

4.1 Introduction

In this chapter, primary investigation is conducted to study the electric double layer (EDL) behaviour of biochar. The effects of surface area and porosity enhancement as well as surface functional groups are studied.

The first step in producing potential material for CDI application is to study the EDL behaviour. EDL performance characterization of several forms of carbon-based electrodes were reported, including different activated carbon blacks, various carbon cloths, papers and felts, carbon nanotubes, carbon aerogels and graphene [34], [39]–[44], [54], [57], [97], [168]–[170]. The main reported factors affecting the EDL performance were surface area and chemical functional groups.

With respect to biochar, to the knowledge of the authors, the cause-effect relationship involving activation variables, the resulting porous structural characteristics, surface functional modification, and EDL capacitance have not been extensively explored. To contribute to this area, using biochar treated with 7 mol L^{-1} KOH, here we report the effect of activation temperature and dwell time (675°C with 2 h or 1000°C with 5 h) on the structural features and EDL performance.

Moreover, the effect of surface functional group modifications on the EDL performance was studied. Selected biochar sample was oxidized with 1 mol L^{-1} HNO_3 followed by calcination at different temperatures (i.e., 150 or 450°C) and investigated for EDL-based applications. As electrolyte, 0.1 mol L^{-1} NaCl in 0.1 mol L^{-1} NaOH was employed. The results presented here are

[1] A version of this chapter has been published:
Dehkhoda AM, Ellis N, Gyenge E. Electrosorption on activated biochar: effect of thermo-chemical activation treatment on the electric double layer capacitance. *J Appl Electrochem* 2014;44:141–57. doi:10.1007/s10800-013-0616-4.

relevant to the capacitive deionization of alkaline NaCl solutions, which could have practical applicability for waste water treatment in the chlor-alkali industry.

4.2 Results and discussion

4.2.1 Effect of physical and structural properties on EDL performance

4.2.1.1 Surface area, porosity, and morphology

One the most important characteristic of a carbon-based electrode in EDL-based applications is high surface area and porosity, with the caveat that micropores could be less useful due to overlapping EDLs [16], [95], [171]. EDL-overlap happens when the diffuse layers of two nearby surfaces (i.e., containing countercharge ions) overlap. This results in the removal of capacitive behaviour within the micropores of porous electrode material. In the present study, as described in detail in Sections 3.1.1, chemical (i.e., KOH) activation using KOH combined with heat treatment was applied to develop the surface area and porosity of the biochar. Two different activated biochar samples were produced using carbonization processes at different temperatures (675 and 1000°C) and dwell times (2 and 5 h). The activation conditions, i.e., 675°C (with 2 h dwell time) and 1000°C (with 5 h dwell time), were chosen to prepare and investigate biochar samples with the high surface area [162], and graphite-like structure [172], respectively. Prior to carbonization at respective temperatures, the impregnated biochar samples were dried under air for 72 h. The activated biochar prepared at 675°C with 2 h dwell time is referred to as Biochar-675, whereas the activated biochar prepared at 1000°C with 5 h dwell time is referred to as Biochar-1000. The as-received biochar is referred to as Biochar-AR. More details of the activation procedure are presented in Section 3.1.1.

The effect of activation process on the surface area and porosity of the biochar is presented in Table 4.2. Moreover, the surface area and porosity of Vulcan XC-72 were also measured and are shown for comparison.

The as-received biochar material (referred to Biochar-AR from here on) has a very low surface area (<2 m^2 g^{-1}) due to blockage of its pores (i.e., empty volumes between the crumpled and randomly cross linked carbon sheets) by the tarry material evolved during the pyrolysis. The removal of tarry material through chemical activation with KOH increased the surface area and porosity of Biochar-AR as shown in Table 4.1. Moreover, the surface area and porosity of the activated biochar samples are considerably higher than that of Vulcan XC-72. The latter is well-known as an effective carbon material in a variety of electrochemical and EDL capacitive applications [95].

Comparing the surface areas of Biochar-675 to Biochar-1000, a significant decrease is observed with increasing the activation temperature and dwell time (Table 4.1). This may be attributed to: a potential collapse and burn-off of the micropore walls of biochar during higher activation temperature and longer dwell time, [15]; and/or, the development of localized graphite-like structure in the biochar matrix. Since the graphite structure does not possess any porosity, formation of this structure could possibly reduce the total surface area of Biohar-1000 sample [173]. Comparing the porous structures of Biochar-675 and Biochar-1000 reveals a large difference between micropore content (0.31 vs. 0.03 cm^3 g^{-1}), while showing almost similar mesopore volume (0.59 vs. 0.63 cm^3 g^{-1}) (Table 4.1), further supporting the phenomenon of burn-off and collapse of micropore walls at high carbonization temperature and longer dwell time. Moreover, the possibility of developing graphite-like structure during the chemical

activation at 1000°C was also confirmed by TEM images as well as FT-IR, XRD, and Elemental Analyses. Results are discussed further in Sections 4.2.1.2 to 4.2.1.4.

Table 4.1 Surface area and porosity of carbon-based samples

Sample	BET surface area ($m^2 g^{-1}$)	Average pore size (nm)	t-plot micropore volume ($cm^3 g^{-1}$)	BJH mesopore volume ($cm^3 g^{-1}$)	Total pore volume ($cm^3 g^{-1}$)
Biochar-AR	1.66	—	—	—	—
Biochar-675	990	3.20	0.31	0.59	0.90
Biochar-1000	614	3.88	0.03	0.63	0.66
Vulcan XC-72	200	5.05	0.03	0.31	0.34

The surface morphology of Biochar-675 and Biochar-1000 were investigated using SEM (Figure 4.1) and TEM (Figure 4.2). Both Biochar-675 and Biochar-1000 showed small flakes in their structures. Furthermore, the TEM images in Figure 4.2 indicated localized crystalline structure in the Biochar-1000 sample, namely, more graphite-like structures were present. The TEM images of Biochar-675 did not present any crystalline structure. These results confirm the phenomenon of developing more graphite-like structure within the biochar matrix by increasing the carbonization temperature and during longer dwell times [172], [174]. Further discussions regarding biochar structure are provided in Section 2.6.2.

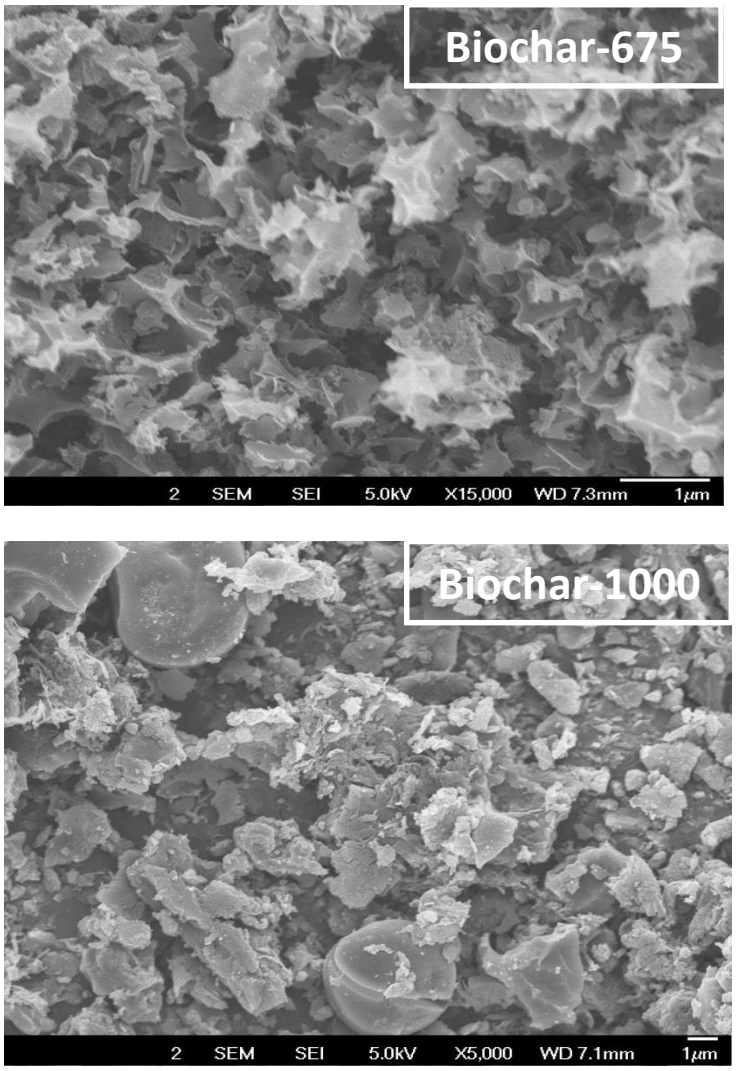

Figure 4.1 SEM images of Biochar-675 and Biochar-1000 samples.

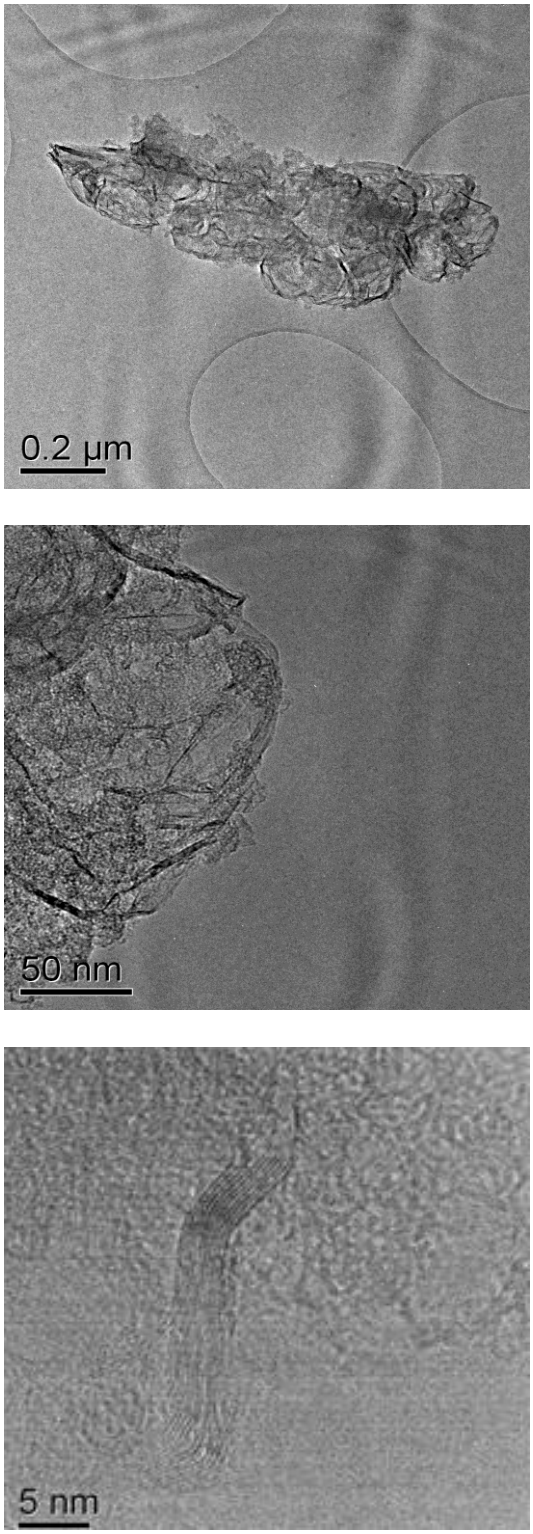

Figure 4.2 TEM images of Biochar-1000.

4.2.1.2 Elemental analysis

The C, H, O and N elemental content of the investigated samples is presented in Table 4.2. Other residual elements such as K and Si are not detectable by the method employed, i.e., combustion (or pyrolysis) combined with gas chromatography (see Chapter 3 for further details). These additional elements make up the weight percentage differences to 100% in Table 4.2.

According to the literature, biochar has a number of oxygen-containing functional groups such as carboxylic, phenolic, and lactonic groups, that contribute to physical adsorption and potentially pseudo-capacitance [172]. This is confirmed here by the high weight percentage of oxygen in the as-received biochar sample (Biochar-AR). The chemical and thermal activation procedures used to produce Biochar-675 and Biochar-1000, reduced the O/C and H/C weight ratios (Table 4.2) due to partial removal of oxygen and hydrogen, respectively.

Table 4.2 Elemental composition (as wt.%) of the carbon-based samples

Sample	C	H	N	O[1]	H/C ratio	O/C ratio
Biochar-AR	63.36	2.41	<0.3	24.46	0.038	0.39
Biochar-675	80.62	0.87	<0.3	11.96	0.011	0.15
Biochar-1000	59.09	0.87	<0.3	5.16	0.015	0.087
Vulcan-XC 72	97.39	<0.3	<0.3	0.63	<0.003	6.5×10^{-3}

4.2.1.3 FT-IR spectroscopy

The surface functional groups of all carbon-based samples have been characterized by FT-IR spectroscopy (Figure 4.3). The Biochar-AR showed a distinctive peak at 740–764 cm^{-1}, i.e., peak (1), corresponding to the out-of-plane bending of ring CH bonds of heteroatomic and aromatic compounds [172], [175]. Additional peaks at 910, 1020, 1210, and 1370 cm^{-1}, i.e., peaks (2), (3),

[1] Organic oxygen content

(4), and (5), were observed characterizing OH bend in carboxylic acid, C-O stretch in carboxylic acid, Ar-OH groups and CH in alkanes, respectively. Also, sharp peaks at 1580 and 1700 cm^{-1}, i.e., peaks (7) and (8), are attributed to C=C stretch in ring mode and aromatic acidic groups (i.e., C=O in carboxylic groups) [6]. Peaks around 2300 cm^{-1} correspond to the adsorbed water in the analyzed sample; while, peaks at 2850 and 2900 cm^{-1}, i.e., peaks (9) and (10), show aromatic CH bonds [6]. Finally a broad peak in the 3200–3500 cm^{-1} region is assigned to either phenolic OH groups or adsorbed water on the sample that most probably are overlapped. The spectra of Biochar-AR sample suggested a structure containing aromatic carbon rings bearing acidic groups which is also in accordance with Elemental Analyses and similar reports in the literature [172].

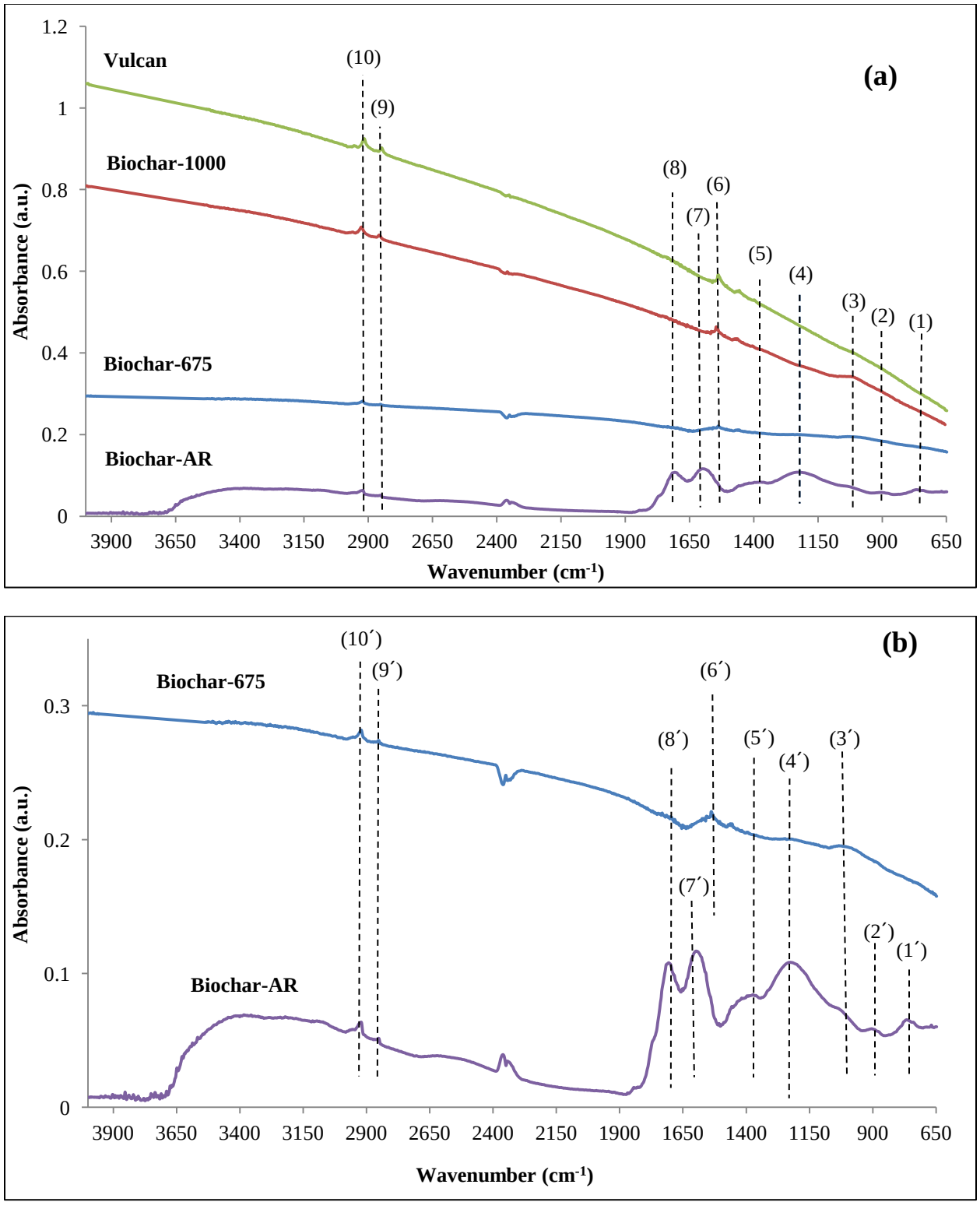

Figure 4.3 FT-IR spectra of: (a) all carbon-based samples; (b) Biochar-AR and Biochar-675 samples (peak numbers are used for better identification in Results and Discussions).

The Biochar-675 spectra (Figure 4.3 b) indicate peaks at 1020 and 1530 cm^{-1}, i.e., peaks (3´) and (6´), which are attributed to C-O stretch in carboxylic acid and aromatic C=C bonds, respectively. Also, peaks at 2850 and 2900 cm^{-1}, i.e., (9´) and (10´), are attributed to aromatic CH bonds. Comparing to Biochar-AR spectra, peaks at 1210, 1370, 1580, and 1700 cm^{-1}, i.e., peaks (4´), (5´), (7´) and (8´), were noticeably absent or weak in the Biochar-675 spectra (Figure 4.3 b). This can be attributed to the development of more ordered structure within Biochar-675 as a result of chemical activation through removal of some heteroatoms and developing more C=C bonds within the carbon sheets [175]. Absence of peaks in the region of 740–764 cm^{-1} and 1370 cm^{-1} wavenumbers, i.e., peaks (1´) and (5´), confirm removal of heteroatoms (e.g., oxygen and hydrogen) from which is also in agreement with Elemental Analyses results. Moreover, an extra peak at 1530 cm^{-1}, i.e., peak (6´), in the Biochar-675 spectra was observed attributed to the development of additional C=C bonds within the carbon sheets as a result of chemical activation in Biochar-675 versus Biochar-AR [172], [174].

The Biochar-1000 and Vulcan samples showed very similar spectra except for the presence of a small bump at 1020 cm^{-1}, i.e., peak (3), in the former sample characterizing the presence of C-O bonds in the form of carboxylic acid.

Comparing the Biochar-1000 and Biochar-675 spectra suggest stronger peaks at 1530, 2850, and 2900 cm^{-1} for the Biochar-1000 confirming the development of more graphite-like structure as well as extended content of C=C and C-H aromatic bonds. The development of graphite-like structure in Biochar-1000 sample has also been shown in TEM images (Figure 4.2).

These results suggest that the surface functional groups and the structure of Biochar-AR were changed significantly via chemical activation through development of graphite-like structures. Additionally, the Biochar-675 sample has more oxygen containing groups in the form

of carboxylic and phenolic groups as compared to Biochar-1000 and Vulcan samples, which could be potentially favourable in EDL capacitance through increasing the pseudocapacitance and wettability of the electrode [176], [177]. Further discussion is provided in Section 4.2.2.

4.2.1.4 X-ray diffraction (XRD) analysis

The structural changes between the biochar samples were further investigated through XRD analyses (Figure 4.4). The broad peak in the region of 2θ = 15–30° is indexed as C(002) diffraction peak indicating amorphous carbon structure with randomly oriented aromatic sheets of Biochar-AR. Sharp peaks around 2θ = 21, 22, 26, 30.5, and 49° correspond to the miscellaneous inorganic components mainly constituted of quartz, within the structure of Biochar-AR [178], [179]. Additional sharp peaks at 2θ = 24 and 37° can also be indexed as whewellite [$Ca(C_2O_4).H_2O$] compounds [179]; while, further peaks at 2θ = 36 and 39° can be attributed to calcite compounds [178], [179]. All these various peaks correspond to the ash content and tarry materials trapped within the pores of as-received biochar sample. Upon chemical activation at 675°C all of these sharp peaks have been eliminated except for the ones at 2θ = 21° and 26° confirming the removal of the majority of ash content within the pores of biochar. Moreover, the broad C(002) peak in the region of 2θ = 15–30° became narrower indicating development of more ordered between the randomly oriented carbon sheets. This has been confirmed further by the presence of another broad diffraction peak of graphite C(100) at 2θ = 40–50° which is observed in ordered turbostratic carbon crystallites [14], [175], [180]. These broad peaks (i.e., in the regions of 2θ = 15–30° and 2θ = 40–50°) got narrower in the Biochar-1000 XRD pattern confirming the formation of more graphite-like structure as previously observed in TEM and FT-IR results. Moreover, a further bump at C(004) plane around 2θ = 53° corresponding to the lateral growth of graphene sheets can be observed in

Biochar-1000 sample. All Biochar-AR, Biochar-675 and Biochar-1000 samples showed similar peak at around 2θ = 28° attributed to the turbostratic crystalline nature of biochar [180].

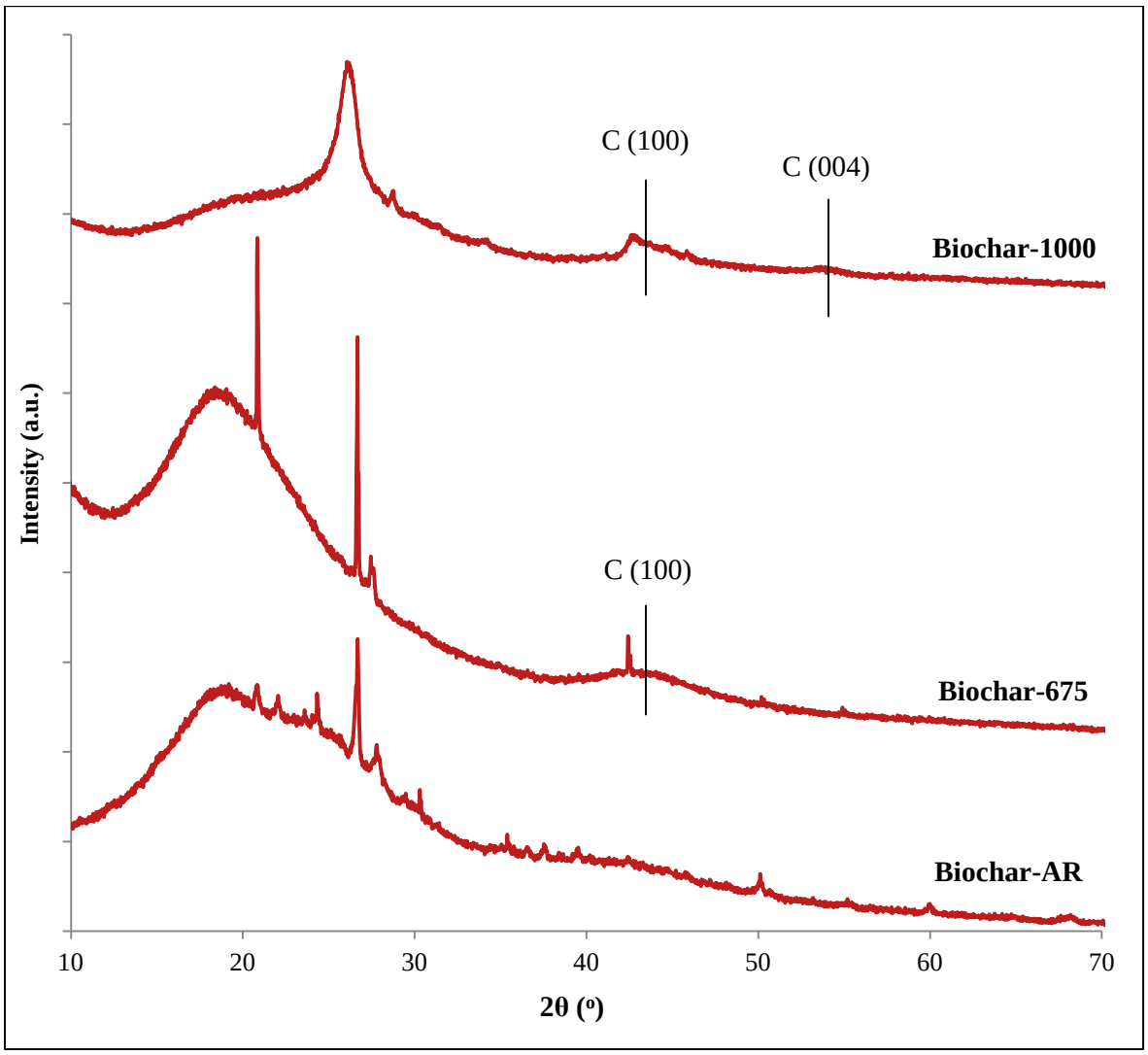

Figure 4.4 XRD patterns of activated biochar samples.

4.2.1.5 Electrical conductivity

One of the important characteristics of an electrode material is electrical conductivity. The electrical conductivity of carbon materials is strongly dependant on the content of heteroatoms, hybridization, thermal treatment, and microstructure [171]. Additionally, many variables are affecting the electrical conductivity of carbonaceous powders including the shape of grains, size of grains, and the amount of compression in the test cell [181]. Thus, the measurements reported

in the literature in many cases are very specific to the conditions used and they can be best used for comparisons within the samples reported in the same study.

Table 4.3 summarizes the measured electrical conductivities of the powder carbon-based samples in this study. The Vulcan sample was also tested in the same setup as a highly conductive reference material in electrochemical applications. Comparing Biochar-AR with Biochar-675 and Biochar-1000 the electrical conductivity was significantly increased upon chemical activation. Moreover, the Biochar-1000 sample showed much higher electrical conductivity than Biochar-675. This can be attributed to the generation of more graphite-like structure along with lower content of heteroatoms (as evidenced by Elemental Analyses, TEM images, FT-IR, and XRD results) resulting in fewer barriers for electrons to be transferred within microcrystalline units [110], [175]. Thus, by changing the structure of biochar through chemical activation (i.e., developing more graphite-like structure) the electrical conductivity can be significantly increased reaching values comparable to that of Vulcan-XC 72.

Table 4.3 Electrical conductivity of the carbon-based samples

Sample	Electrical conductivity (S cm^{-1} g^{-1})
Biochar-AR	7.0×10^{-9}
Biochar-675	0.046
Biochar-1000	0.424
Vulcan-XC 72	2.79

4.2.1.6 Cyclic voltammetry (CV) analysis of biochar electrodes

Three types of electrodes were prepared and comparatively investigated: i) as-received biochar (non-activated); ii) activated biochar (Biochar-675 and Biochar-1000, respectively); and iii) as-received Vulcan XC-72 utilized as a reference carbon sample. For each carbon material,

three different inks were produced based on increasing weight percentages of Nafion®, i.e., 0, 5 and 30 wt.%. The working electrode was the carbon-deposited Ni mesh with a geometric area of 7.09 ± 0.35 cm^2. The carbon-based ink and the electrode preparation procedure involving spraying of the carbon-Nafion ink on a Ni mesh current collector are described in detail in Section 3.1.2. Increasing the amount of Nafion® mixed with the carbon improved the attachment of the carbon particles to the current collector as reflected by the increased carbon coating yield (Table 4.4). The Nafion® content of each electrode in wt.% is referred to in the last digit of electrode's name, e.g., Biochar-AR-0 and Biochar-675-5 refer to biochar electrodes prepared using as-received biochar and activated biochar (at 675°C and 2 h dwell time) with 0 and 5 wt.% Nafion®.

Table 4.4 Prepared electrodes and coating efficiency characteristics of the Ni mesh current collector

Sample	Nafion® (wt.%)	Total mass of coated material (mg) [a]	Mass of coated carbon-based material (mg)	Coating yield (%) [b]
Biochar-AR-0	0	8.2	8.2	5.1
Biochar-AR -5	5	15.9	15.1	12.5[1]
Biochar-AR -30	30	13.9	9.7	24.2
Biochar-675-0	0	7.3	7.3	5.2
Biochar-675-5	5	18.9	17.9	8.9
Biochar-675-30	30	31.9	22.3	18.5
Biochar-1000-0	0	7.6	7.6	12.6
Biochar-1000-5	5	21	19.9	16.5
Biochar-1000-30	30	31.2	21.8	27.2
Vulcan-0	0	33.5	33.5	33.5
Vulcan-5	5	25.4	24.1	40.1
Vulcan-30	30	32.1	22.4	56

a Includes the carbon-based material and dry Nafion weight (where applicable)
b Coating yield = mass of carbon coated/total mass of carbon sprayed as ink solution

CV analysis of the activated biochar and Vulcan XC-72 electrodes was conducted in a three-electrode set-up using 0.1 mol L^{-1} NaCl in 0.1 mol L^{-1} NaOH as electrolyte. All electrodes were investigated at different potential sweep rates ranging between 5 and 50 mV s^{-1}. The CV of the pure Ni mesh current collector was also recorded to offset any potential contributions to the current generated by the carbon electrodes. The contribution of the Ni mesh was found to be negligible in the explored potential range (e.g., at 50 mV s^{-1} the current was lower than 0.2 mA; Figure A4 in Appendix A). Furthermore, the Biochar-AR electrodes (i.e., as-received without

[1] Standard deviation (from triplicate experiments) is within ± 5% of the reported values.

thermo-chemical activation) showed virtually negligible EDL behaviour (Figure A5, Appendix A) as expected based on the very low surface area (i.e., 1.66 m^2 g^{-1}, Table 4.1). Hence, the activated biochar electrodes, Biochar-675 and Biochar-1000 were studied in detail and compared to the Vulcan XC-72 electrodes (Figures 4.6 and 4.7).

Vulcan XC-72 is used in EDL-based applications due to its high surface area and electrical conductivity [95], [171]. The CV diagrams in Figure 4.5 for the Vulcan electrodes show typical EDL behaviour between –0.5 V and + 0.5 V vs. Hg/HgO with one reduction wave between –0.2 and –0.4 V corresponding to the reduction of oxygen-containing functional groups such as ketone and quinone groups as well as reduction of the dissolved oxygen in the electrolyte (Figure 4.5) [95], [182].

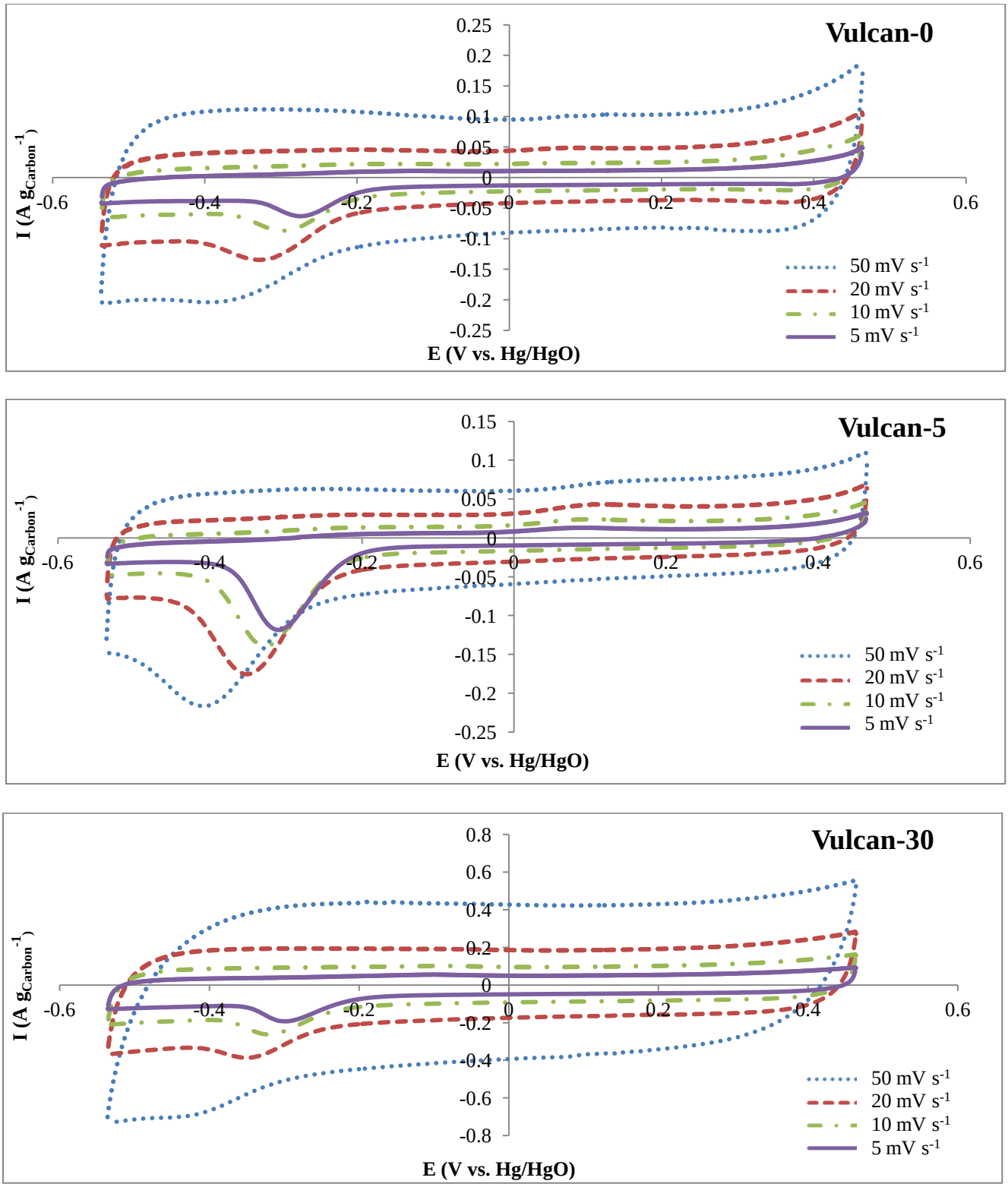

Figure 4.5 Cyclic voltammograms of Vulcan XC-72 electrodes at different sweep rates with 0, 5 and 30 wt.% Nafion content using 0.1 mol L^{-1} NaCl in 0.1 mol L^{-1} NaOH electrolyte.

The CV behaviour of the electrodes prepared with Biochar-675 with three different Nafion contents (i.e., Biochar-675-0, Biochar-675-5, and Biochar-675-30) is shown in Figure 4.6. The voltammograms obtained at slower sweep rates (<20 mV s^{-1}) have a shape that is closer to the ideal EDL capacitive response (i.e., more rectangular-like), hence, confirming similar reports in the literature [54], [183], [184]. This is mostly attributed to the longer time available for ions to access the micropore content of Biochar-675 (Table 4.1) at slower sweep rates. Panić et al. reported a similar observation in their study using a carbon black electrode [95]. The addition of 5 and 30 wt.% Nafion® to Biochar-675 resulted in some shape deformation of the voltammograms at faster sweep rates (e.g., 20 and 50 mV s^{-1}). One reason could be the hampered access of the ions to the surface sites in case of high Nafion polymer loading (e.g., 30 wt.%) during the short time available during fast potential sweep rates. Additionally, especially at high Nafion loading, the ohmic potential drop (or IR-drop) must be also considered (further discussions are provided in Section 4.2.1.7)

The electrodes prepared with Biochar-1000 revealed also typical EDL behaviour in CV tests, i.e., rectangular-shaped voltammogram (Figure 4.7). However, two differences are noted when comparing the voltammograms of Biochar-1000 and Biochar-675 electrodes (Figures 4.7 and 4.6, respectively). First, the Biochar-1000 voltammograms are somewhat more rectangular in shape (i.e., closer to the ideal capacitive EDL behaviour) particularly at high sweep rates (such as 20, and 50 mV s^{-1}); and second, the addition of Nafion (5 and 30 wt.%) caused minimal shape distortion in case of Biochar-1000. The high mesopore content and negligible micropore content of Biochar-1000 compared to Biochar-675 (Table 4.1) is beneficial because the mesopores are less prone to blockage by Nafion agglomerates. Further comparing the voltammograms of activated biochar with Vulcan (Figure 4.5) suggests the absence of oxygen group reduction peak

for biochar samples. This can be due to the different type of oxygen containing groups (e.g., phenolic and carboxylic) in the biochar samples as opposed to the Vulcan sample (containing quinone-type functional groups that are involved in the redox catalysis of O_2 reduction).

The total capacitance of an electrode can be quantified using the cyclic voltammogram by dividing the anodic and cathodic current differences ($\Delta I = I_a - |I_c|$) at the EDL plateau region with the corresponding sweep rate [54], [164], [165]. Thus, plotting the current differences obtained from Figures 4.5–4.7 at the plateau of each CV (i.e., at 0 V) versus the potential sweep rate should yield a linear function, with the slope representing the total capacitance per unit carbon mass of each investigated electrode (Figure D1, Appendix D). For all electrodes the current difference at 0 V versus potential sweep rate showed excellent linear fit, allowing therefore, the calculation of the total capacitance as a function of carbon-material and Nafion content (Appendix D).

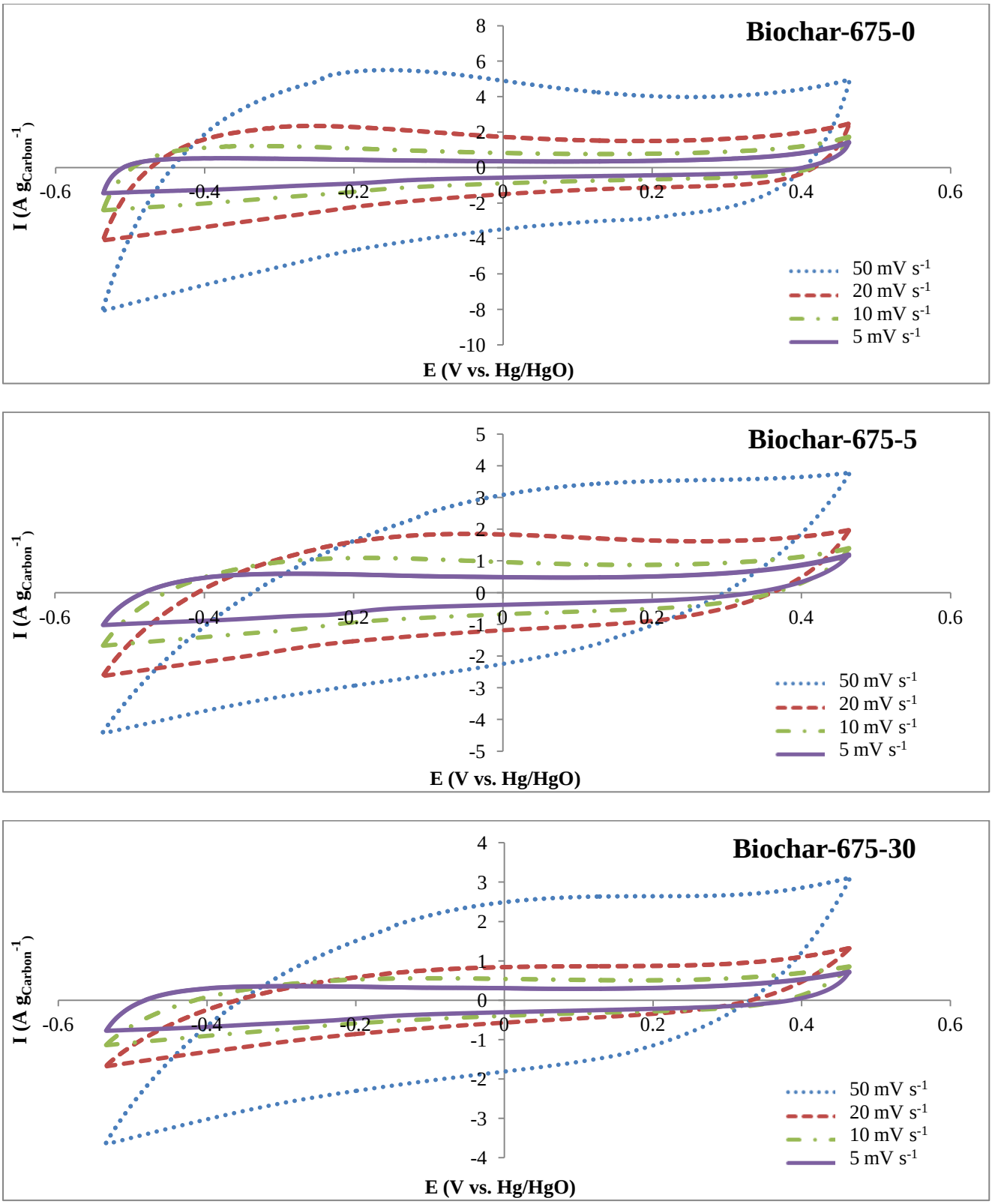

Figure 4.6 CV diagrams of Biochar-675 electrodes at different sweep rates with 0, 5, and 30 wt.% Nafion content using 0.1 mol L^{-1} NaCl in 0.1 mol L^{-1} NaOH electrolyte.

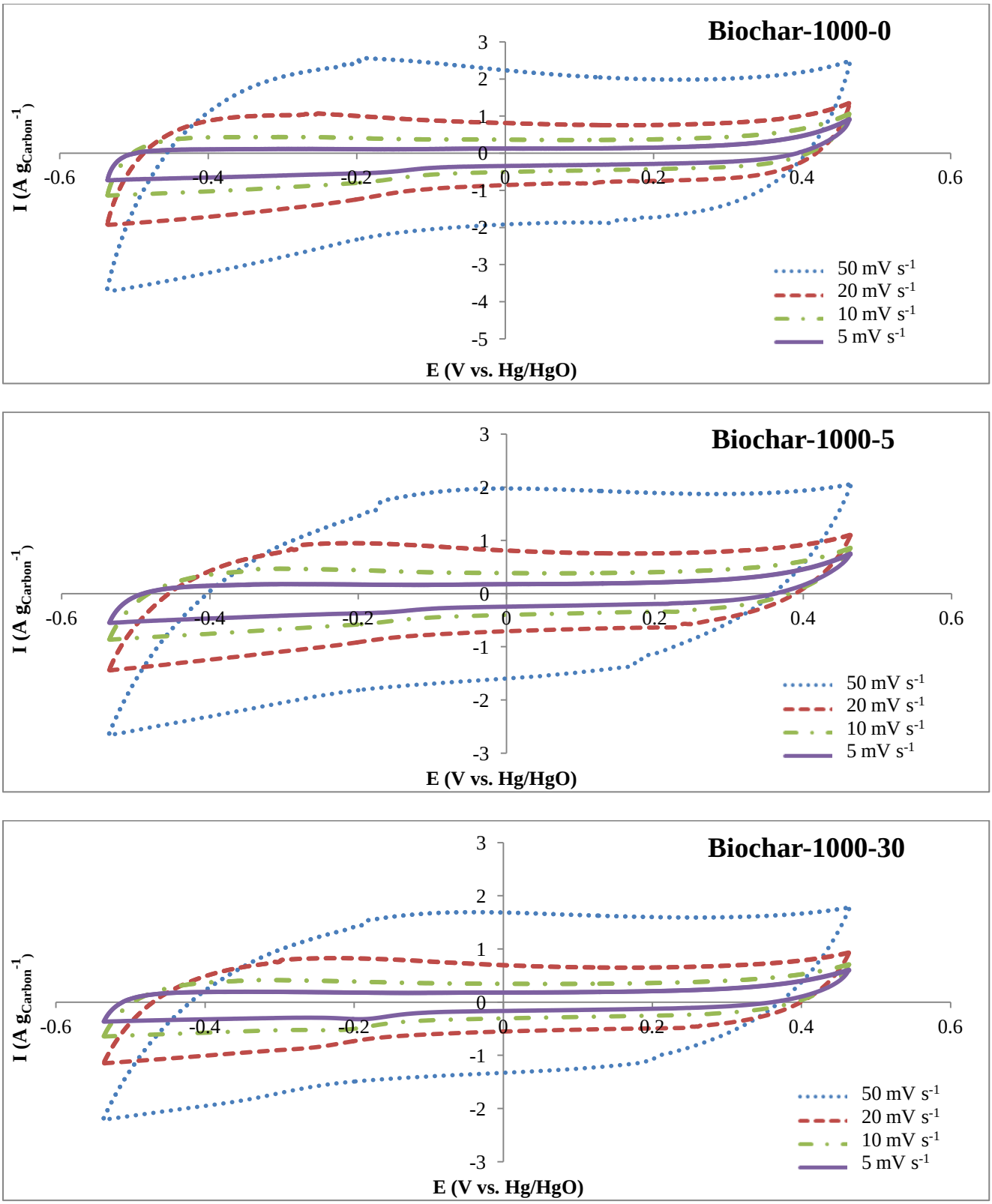

Figure 4.7 CV diagrams of Biochar-1000 electrodes at different sweep rates with 0, 5, and 30 wt.% Nafion content using 0.1 mol L^{-1} NaCl in 0.1 mol L^{-1} NaOH electrolyte.

As depicted in Figure 4.8, increasing the Nafion® content in Biochar-675 electrodes from 0 to 30 wt.% (i.e., from Biochar-675-0 to Biochar-675-30) resulted in a decrease of the total capacitance from 167 to 122 F g^{-1}. The Biochar-1000 electrodes showed a similar trend of decreased total capacitance with increasing Nafion® content, albeit the Biochar-1000 electrodes have a lower total capacity than Biochar-675. The Vulcan electrodes revealed significantly smaller total capacitance (between 3.2 and 16.7 F g^{-1}) than any of the activated biochar samples. These results support the hypothesis of using biochar-based electrodes in EDL-based applications.

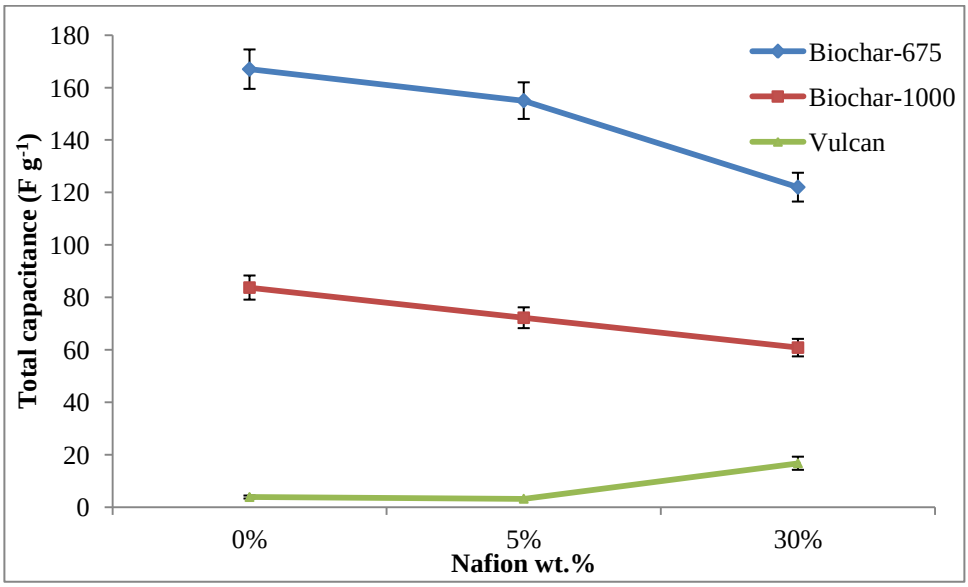

Figure 4.8 Total capacitance per unit mass of carbon versus Nafion® content for carbon electrodes obtained from Figure C1, Appendix C. Electrolyte: 0.1 mol L^{-1} NaCl in 0.1 mol L^{-1} NaOH[1].

In order to further investigate the role of micropores and mesopores on the capacitive behaviour of biochar-based electrodes, the total capacitance of the electrodes presented in Figure 4.8 were normalized by the respective total mesopore volumes given in Table 4.1. The results are shown in Table 4.5.

[1] Error bars are indicative of the standard deviation of triplicate experiments using each electrode.

Table 4.5 Total mesopore volume and normalized capacitance per mesopore volume of biochar electrodes

Electrode	Total capacitance per mesopore volume ($F\ cm^{-3}$)
Biochar-675-0	282
Biochar-675-5	261
Biochar-675-30	207
Biochar-1000-0	133
Biochar-1000-5	114
Biochar-1000-30	95.9

The mesopore volumes of Biochar-675 and 1000 electrodes are very similar: 0.59 and 0.63 $cm^3\ g^{-1}$, respectively (Table 4.1). However, Table 4.5 shows the total capacitance per mesopore volume of the Biochar-675 electrode is more than two times higher than the total capacitance of the Biochar-1000 electrode, potential reasons being: i) the higher micropore content of Biochar-675 (Table 4.1) could provide additional useful surface area for EDL formation in spite of the possibility of EDL-overlap; and ii) the higher content of oxygen-containing functional groups in Biochar-675 (as shown in Elemental Analysis, Table 4.2, and FT-IR results, Figure 4.3) could also contribute to the total capacitance in the form of pseudo-capacitance and increased wettability [171]. The role of the micropores in the generation of the Biochar-675 total capacitance is qualitatively illustrated by the potential sweep rate induced distortion of the cyclic voltammograms at 20 and 50 $mV\ s^{-1}$ (comparing Figures 4.6 and 4.7).

4.2.1.7 Galvanostatic charge/discharge analysis

In EDL-based processes, both the adsorption and desorption of ions from the electrode surface are essential. Desorption affects the regeneration of the electrodes in capacitive deionization applications, whereas in supercapacitor applications, it determines the discharge

capacitance. The adsorption and desorption capability of an EDL electrode is commonly investigated by galvanostatic charge/discharge analysis. Electrodes are charged at a constant current for a specific time, followed by discharging at the reversed charging current (i.e., discharge current) for the same amount of time. The electrode potential is monitored versus time. Further details are given in Chapter 3. Figures 4.9 and 4.10 present the galvanostatic charge/discharge profiles of the activated biochars as a function of the Nafion content, while Figure 4.11 presents the galvanostatic charge/discharge profile of the reference Vulcan XC-72 electrode.

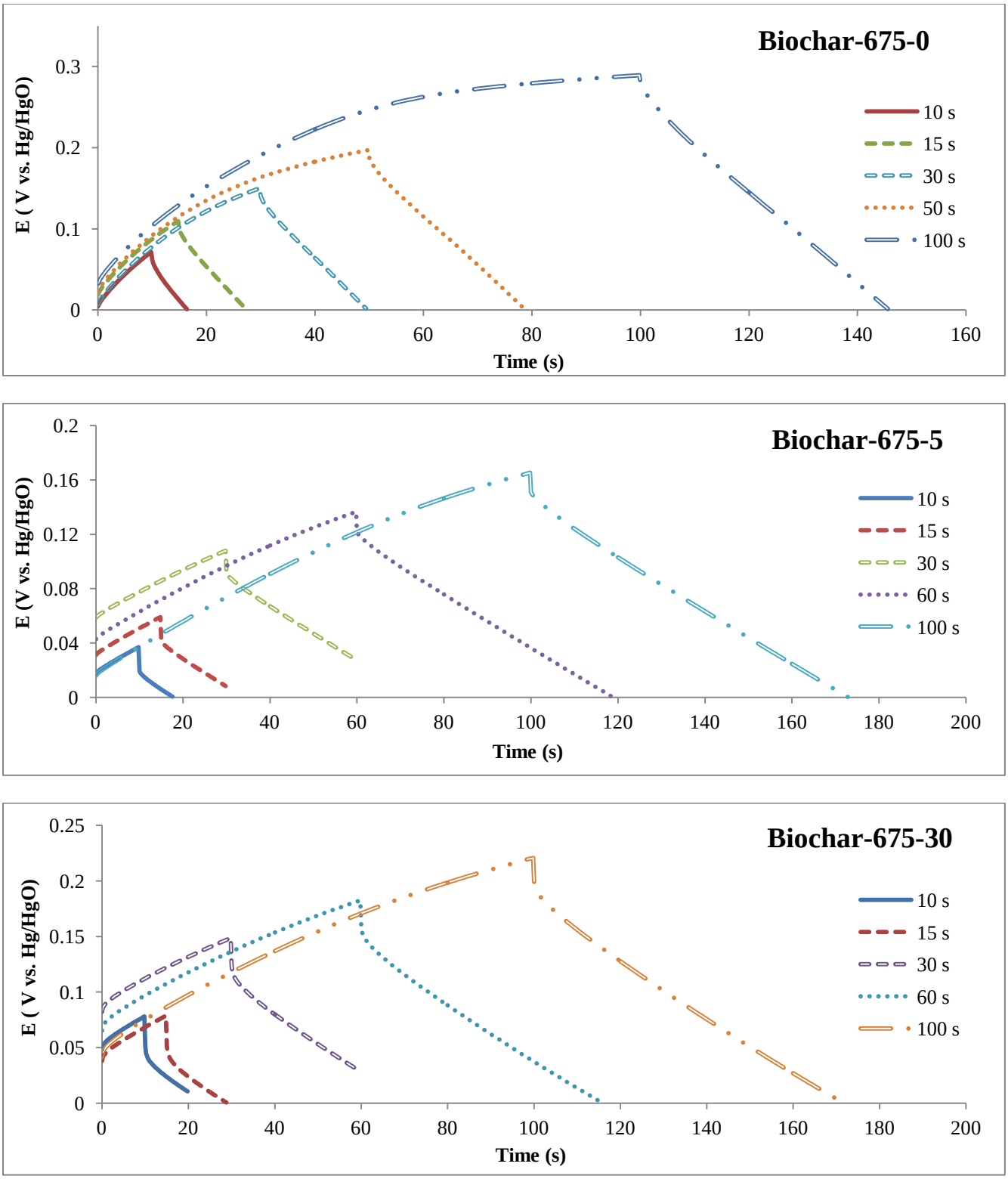

Figure 4.9 Galvanostatic charge/discharge of Biochar-675 electrodes using +2 mA and –2 mA charge and discharge currents, respectively. Electrolyte: 0.1 mol L^{-1} NaCl in 0.1 mol L^{-1} NaOH.

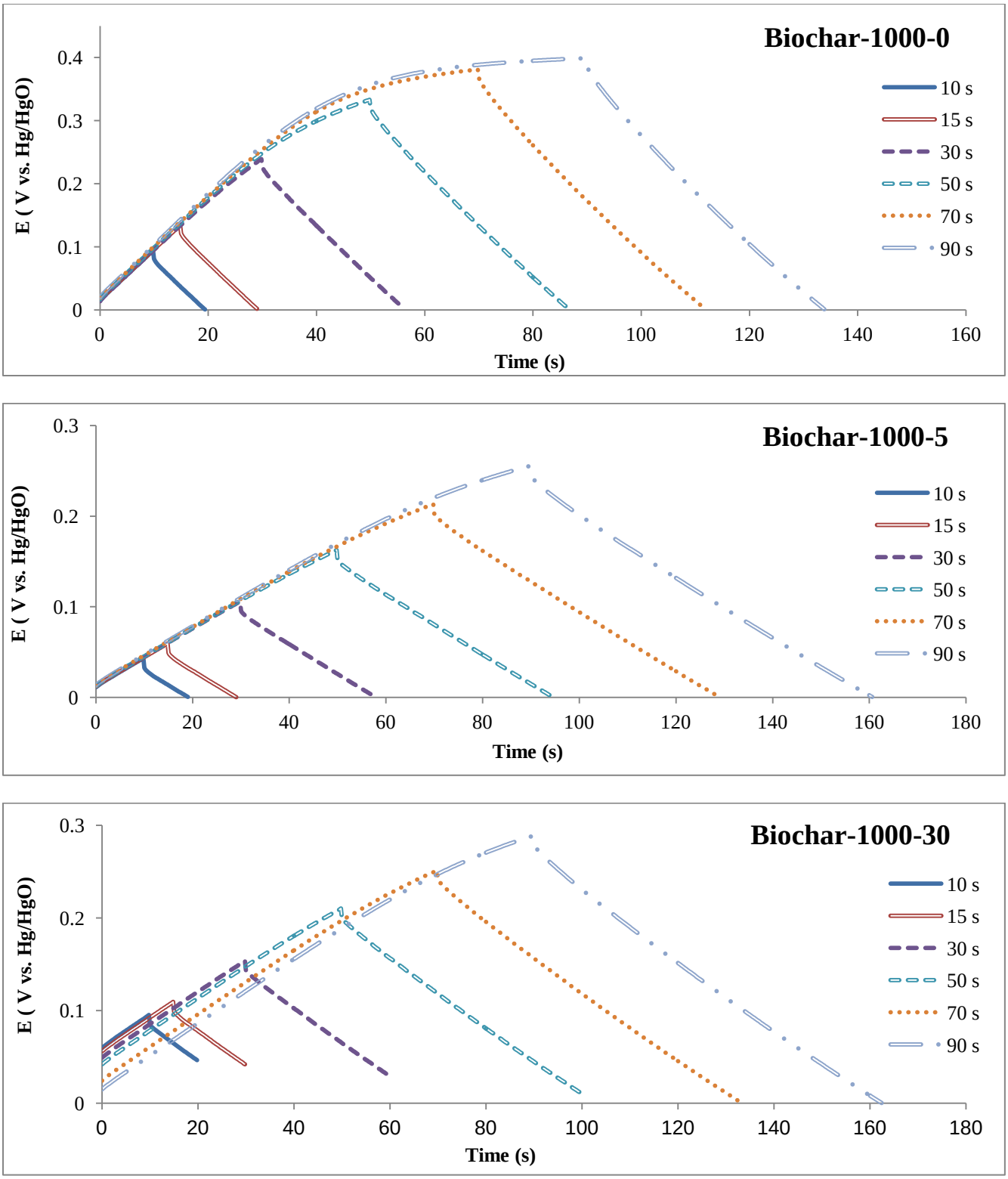

Figure 4.10 Galvanostatic charge/discharge of Biochar-1000 electrodes using +2 mA and –2 mA charge and discharge currents, respectively. Electrolyte: 0.1 mol L^{-1} NaCl in 0.1 mol L^{-1} NaOH.

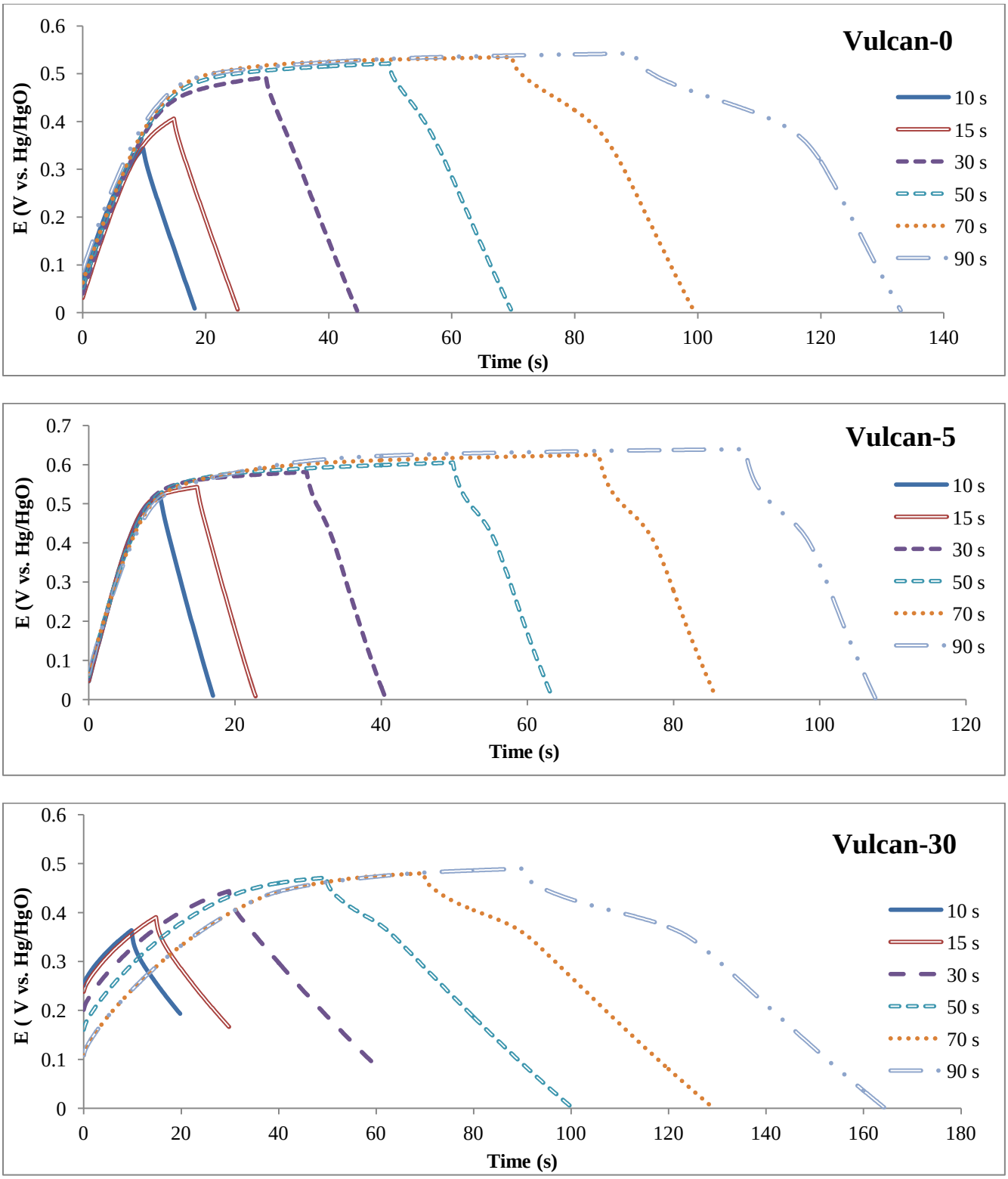

Figure 4.11 Galvanostatic charge/discharge of Vulcan electrodes using +2 mA and –2 mA charge and discharge currents, respectively. Electrolyte: 0.1 mol L^{-1} NaCl in 0.1 mol L^{-1} NaOH.

The sudden potential drop while switching the charging current to discharge current is the Ohmic potential drop (or IR-Drop). The Ohmic potential drop of each electrode was measured from the potential difference between the last point on the charging curve and the first point on the discharge curve. This is essentially an application of the current interrupt method for Ohmic drop measurement [165], [184].

Table 4.6 presents the Ohmic potential drops associated with each of the investigated electrodes. The IR-Drop of the Biochar-675 electrodes decreased from 1.23 to 0.89 V g^{-1} with 5 wt.% increase of the Nafion® content. This could be attributed to the improved accessibility of ions within the micropores of Biochar-675 as a result of 5 wt.% Nafion® addition. However, at the highest Nafion loading, the polymer electrolyte film formed in the highly microporous Biochar-675 sample imposes a high ohmic drop (1.12 V g^{-1}). For the Biochar-1000 electrodes, characterized by very low micropore content (Table 4.1), the Ohmic potential drop showed comparable trend to Biochar-675 electrodes when increasing the Nafion® content from 0 to 5 wt.%; while, for Biochar-1000-5 and Biochar-1000-30 electrodes the Ohmic drop was virtually independent of the Nafion content. Moreover, the Ohmic potential drop for all the Biochar-1000 electrodes is very similar to that of Vulcan electrodes.

Table 4.6 The Ohmic potential drop and discharge capacitance of the carbon electrodes calculated from the galvanostatic charge/discharge profiles

Electrode	Ohmic potential drop ($V\ g^{-1}$)	Discharge capacitance ($F\ g^{-1}$)
Biochar-675-0	1.23	42.1
Biochar-675-5	0.89	55.4
Biochar-675-30	1.12	33.2
Biochar-1000-0	0.58	31.5
Biochar-1000-5	0.50	30.6
Biochar-1000-30	0.46	24.6
Vulcan-0	0.42	1.8
Vulcan-5	0.79	1.4
Vulcan-30	0.53	8.3

The discharge capacitance of each electrode has been calculated by multiplying the $\Delta t/\Delta E$ term obtained from the linear section of the discharge portion of the galvanostatic charge/discharge diagrams (Figures 4.9–4.11) with the discharge current of –2 mA. The resultant values were then normalized per mass of carbon-based material used to fabricate the electrode. As shown in Table 4.6, the discharge capacitances of all the prepared electrodes follow the same trend as the total capacitance obtained from cyclic voltammetry (Table 4.5). The discharge capacitances at –2 mA for Biochar-675 and Biochar-1000 electrodes were significantly higher (up to thirty times higher) than those of Vulcan-based electrodes (Table 4.6). A direct comparison with other carbon-based electrodes reported in the literature is difficult due to the different electrode preparation and test conditions utilized (e.g., electrolyte type and concentration). Nevertheless, the obtained total capacitance values of activated biochar

electrodes are competitive to the reported carbon-based material in the literature with much more complicated preparation steps (Table 4.7). Moreover, the reported typical ranges of discharge capacitances for other carbon-based electrodes are: 23 F g^{-1} for carbon aerogel, 19 F g^{-1} for activated carbon, and 10 F g^{-1} for carbon-black electrodes [185]. Hence, based on Table 4.6 the activated Biochar electrodes with discharge capacitances between 24.6 and 42.1 F g^{-1} are advantageous compared to other carbon electrodes reported in the literature (as shown in Table 4.7).

Table 4.7 Summary and comparison of the electric double layer total capacitances of the activated biochar electrodes and other relevant carbon-based electrodes

Electrode type	Total capacitance (F g^{-1})	Electrolyte	Reference
Biochar-675	122–167	0.1 M NaCl in 0.1 M NaOH	—
Biochar-1000	61–84	*idem*	
Vulcan XC-72	4–17		
Single-wall Carbon Nanotube on Carbon Cloth (CNTs/CC)	190–210	0.5 M Na_2SO_4	[183]
Graphene- PEDOT[1]	116–304	2 M HCl	[54]
Activated carbon cloth	41.5	Not specified	[37]
Multi Walled Carbon Nano Tube	10–15	1.96 M $TEMABF_4$	[186]
Carbon aerogel	95	1 M H_2SO_4	[187]
Modified carbon aerogel with Ru	206	*idem*	
Activated carbon from fibers of oil palm fruit bunches	150	1 M H_2SO_4	[61]

[1] Polyethylenedioxythiophene

4.2.2 Effect of surface chemical group modification on EDL performance

In addition to the surface area and porous structure, surface functional groups of carbon-based material affect the ionic adsorption performance in EDL applications [102], [176], [177], [188], [189]. The main surface chemical groups of carbon electrodes are oxygen containing groups, e.g., carboxylic, phenolic, lactonic, and quinone. By modifying these functional groups, the electrosorption of ions can be improved through increased wettability (and transport of ions within the small pores in aqueous electrolytes) and possible charge transfer reactions on the surface (i.e., so-called pseudo-capacitance). Different methods reported in the literature for oxidation of the carbon surface using HNO_3, KOH, H_2O_2, and oxidizing gases [177].

Oh et al. studied the oxidation of activated carbon cloth (ACC) electrodes by KOH or HNO_3 treatment reduced the specific surface area by 16 and 5%, respectively [188]; while, the average pore size remained unchanged. Higher electrosorption capacity observed attributed to the opening of the closed pores (due to activation of carbon) [188]. Nian and Teng treated activated carbon fabric (ACF) with 2 mol L^{-1} HNO_3 at 90°C followed by calcination at different temperatures (150–750°C). The electrochemical capacitance of the treated ACF electrodes was enhanced due to the increased charge transfer of the functional groups as well as increased wettability of the carbon material. The 450°C calcination temperature reported as the optimum condition resulting the highest capacitance (i.e., 40% increase) and lowest electrode resistance due to increased charge transfer from oxygen-containing groups and improved wettability, respectively [176].

To study the effect of surface oxidation on the EDL performance (including potentially improved ionic transport and increased capacitance), selected activated biochar was prepared at 675°C carbonization temperature with 12 h pre-carbonization drying time under air, i.e.,

Biochar-675-SD[1]. The activated biochar sample was then oxidized by 1 mol L^{-1} HNO_3 followed by calcination at 150 and 450°C based on the method reported by Nian and Teng [176]. Oxygen containing groups (e.g., carboxylic, phenolic, and quinone) are expected to be incorporated on biochar matrix based on the reported method. About 0.9 g of activated biochar was mixed with 100 mL of 1 mol L^{-1} HNO_3 at 80°C and stirred for 75 min. The oxidized sample was then washed with deionized water several times until the wash water became neutral. To further modify the surface groups, the oxidized sample were calcined under N_2 (at 258 mL min^{-1}) at two different temperatures of 150 and 450°C for 1 h according to the reported method [176]. The calcined samples were then washed with distilled water and dried in oven at 110°C overnight.

For simplicity in referring to the prepared samples, the activated biochar sample treated with HNO_3 is referred to as B675-SD-HNO3. Moreover, the HNO3-150C and HNO3-450C notations refer to the acid treatment followed by the calcination at corresponding temperatures of 150 or 450°C, respectively.

4.2.2.1 Surface area and porosity

Surface area, micro-, and mesopore volume of the Biochar-675-SD as well as HNO_3-treated samples are shown in Table 4.8. Biochar-675-SD showed higher surface area and larger micropore volume compared to the Biochar-675 sample (compare values in Tables 4.8 and 4.1[1]). The HNO_3 treatment of the biochar sample resulted in slight decrease of the surface area by 15–20%. All HNO_3 treated samples showed comparable surface area and porosity results as shown in Table 4.8.

Table 4.8 Surface area and porosity of HNO_3-treated activated biochar samples

[1] Further discussions related to the cause-effect relation between pre-carbonization drying conditions and the porous structure development is provided in Chapter 5.

Sample	BET surface area ($m^2 g^{-1}$)	Average pore size (nm)	t-plot micropore volume ($cm^3 g^{-1}$)	BJH mesopore volume ($cm^3 g^{-1}$)	Total pore volume ($cm^3 g^{-1}$)
Biochar-675-SD	1294	1.97	0.53	0.09	0.62
B675-SD-HNO3	1049	1.98	0.43	0.08	0.51
B675-SD-HNO3-150C	1068	1.91	0.45	0.05	0.50
B675-SD-HNO3-450C	980	1.89	0.44	0.05	0.49

4.2.2.2 Surface functional groups

To investigate the surface functional groups, FT-IR analysis was conducted on the HNO_3-treated samples (Figure 4.12). All samples showed peaks at 1530, 2850, and 2900 cm^{-1} attributed to the aromatic C=C, i.e., peak (2), and CH aromatic bonds, i.e., peaks (5) and (6). A small peak at 1440 cm^{-1} can also be observed for all samples attributed to C=C bonds [53].

The B675-SD-HNO3 and B675-SD-HNO3-150C samples showed distinctive peaks at 1170, 1600, and 1710 cm^{-1}, i.e., peaks (1), (3), and (4). Peak (1) is typically attributed to the vibration modes of either phenolic groups (-OH bonds) or carboxylic groups [53], [177], [190]; while, peak (3) is attributed to quinone groups. Additional peak at 1710 cm^{-1} observed for B675-SD-HNO3 and B675-SD-HNO3-150C samples is assigned to C=O bond in carboxylic groups further confirming the presence of this acidic group on the surface [53], [177], [191].

Peaks (1), (3), and (4) are clearly absent in the FT-IR spectrum of B675-SD-Plain confirming the incorporation of oxygen-containing groups to B675-SD-Plain upon HNO_3 treatment. However, the spectrum of B675-SD-HNO3-450C also showed no traces of the mentioned peaks. This could be due to the removal of oxygen-containing groups at 450°C calcination [176]. Consequently, the FT-IR spectrum of B675-HNO3-450C and B675-SD-Plain were quite similar suggesting comparable surface functional groups. Similar observation can be

made comparing B675-SD-HNO3 and B675-SD-HNO3-150C samples suggesting comparable surface functional groups. These results can be confirmed by Elemental Analysis of the treated samples (Appendix E).

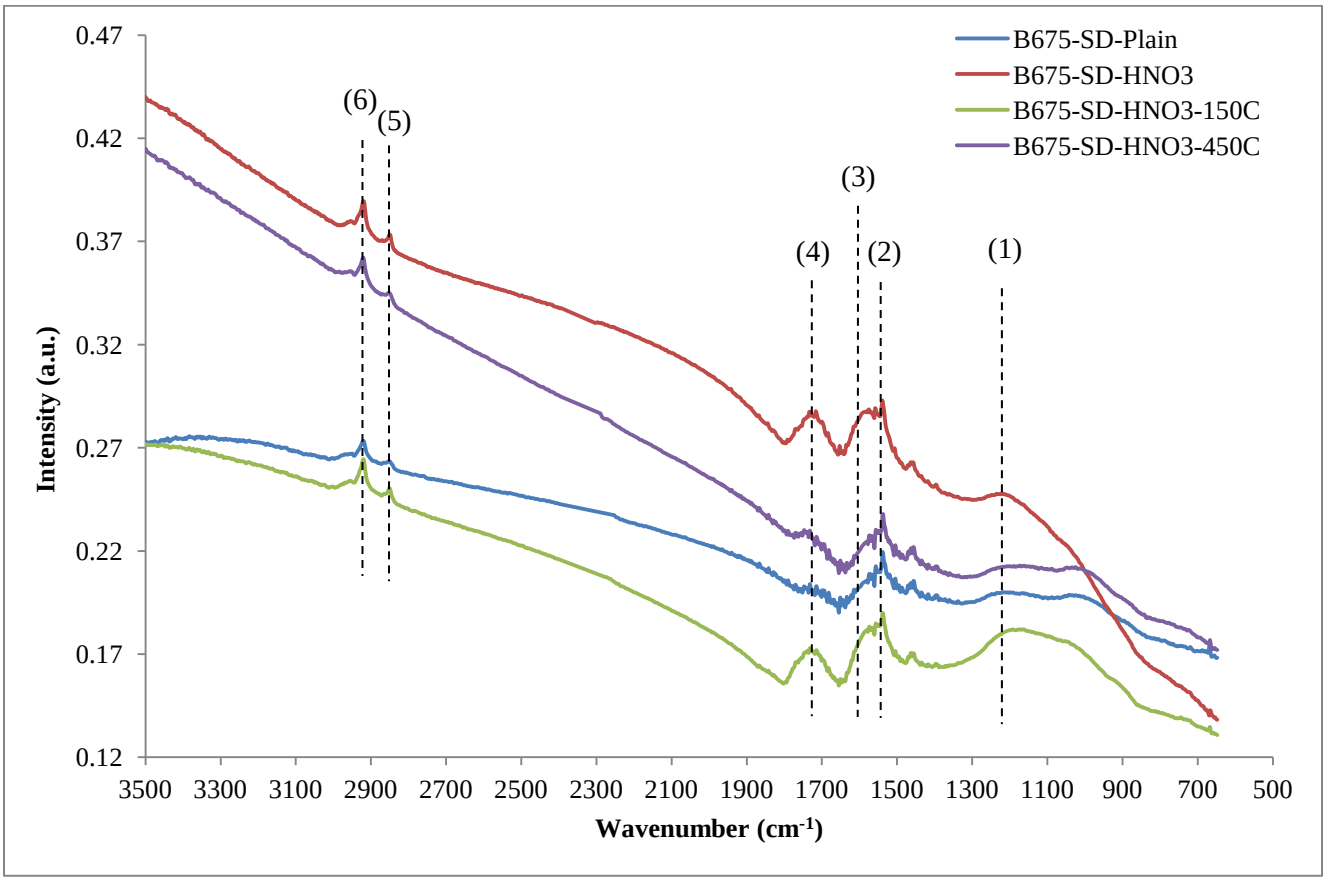

Figure 4.12 FT-IR spectra of HNO_3 treated activated biochar.

4.2.2.3 CV and GCD analyses of HNO_3 treated samples

Four electrodes were prepared from HNO_3-treated Biochar-675-SD sample on Ni mesh with 5 wt.% Nafion®: B675-SD-Plain, B675-SD-HNO3, B675-SD-HNO3-150C, and B675-SD-HNO3-450C. The first electrode (i.e., B675-SD-Plain) was made from untreated activated biochar without any HNO_3 treatment.

CV and GCD analyses conducted in a three electrode configuration system using prepared electrodes. The total capacitance of the electrodes calculated based on the current difference at

linear section of the CV voltammograms plotted against corresponding sweep rates, similar to the method explained in Section 4.2.1.6. Unlike Biochar-675 and Biochar-1000, the Biochar-675-SD electrodes (with 0, 5, and 30 wt.% Nafion®) showed poor linearity between current difference and sweep rate specifically at fast sweep rates, i.e., 10, 20, and 50 mV s^{-1} (Figure D2, Appendix D). This could be due to the limited transport of ions within the microporous structure as also reported in the literature [95], [107], [192]. Thus, to calculate the total capacitance, slower CV analysis at slower sweep rates (2–5 mV s^{-1}) were performed. The total capacitance of Biochar-675-SD electrodes was calculated based on the slope of linear section of current difference vs. sweep rates plot at slow scanning rates (i.e., 2, 3, and 5 mV s^{-1}).

Table 4.9 summarizes the total capacitance of electrodes made from Biochar-675-SD sample (5 wt% Nafion®) with or without HNO_3 treatment. The B675-SD-Plain electrode showed higher total capacitance compared to Biochar-675-5 electrode (195 vs. 154 F g^{-1}; values provided in Table 4.9 and Figure 4.8, respectively). This could be attributed to the larger micropore content of Biochar-675-SD compared to Biochar-675 [38], [193]. A considerable decrease in the total capacitance was observed upon treating the activated biochar with HNO_3 (B675-SD-Plain vs. B675-SD-HNO3) (Table 4.9). Further comparison between the HNO_3 treated samples suggested a slight increase in total capacitance upon calcination of HNO3-treated sample at 150°C (compare B675-HNO3 with B675-HNO3-150C). More interestingly, a significant increase was observed with further increasing the calcination temperature to 450°C. These results are in agreement with the Nian and Teng report [176]. Thus, the highest capacitance among the HNO3-treated samples obtained for B675-HNO3-450C. However, this total capacitance is just slightly larger than that of B675-SD-Plain sample.

Further comparison between the electrodes can be made through GCD analysis (Table 4.9). All HNO_3-treated samples showed significantly larger Ohmic potential drop (IR-Drop) compared to the untreated Biochar-675-SD sample. This is due to the incorporation of oxygen-containing group in the carbon network of biochar and increasing the heteroatom content. As a result, the electrical conductivity reduced and consequently IR-Drop increased. According to Nian and Teng, another possible factor contributing to the higher IR-Drop is the increased ion migration resistance in the micropores. Surface oxides contributed to the formation of water aggregates and thus, retarding the access of ions in the micropores [176]. Further comparing the HNO_3-treated samples suggested an increase of IR-Drop by calcination at 150°C. However, further increasing the calcination temperature to 450°C resulted in the lowest IR-Drop which could be due to the removal of some oxygen-containing groups as a result of calcination.

Table 4.9 Surface area and porosity of HNO_3-treated activated biochar samples

Electrode	Total capacitance (F g^{-1})	IR-Drop[1] (V g^{-1})
B675-SD-Plain	195	2.25
B675-SD-HNO3	109	12.9
B675-SD-HNO3-150	118	20.1
B675-SD-HNO3-450	218	12.5

These results suggested that HNO_3 treatment with or without calcination at 150°C has negatively affected the EDL performance by decreasing the total capacitance and increasing the Ohmic potential drop. However, increasing the calcination temperature to 450°C led to

[1] At 0.25 mA cm^{-2} current density

increasing the total capacitance to values comparable to the untreated activated biochar. Yet, the Ohmic potential drop is significantly higher than that of untreated biochar.

4.3 Conclusion

Activated biochar electrodes were prepared and their electric double layer (EDL) behaviour was investigated. The as-received biochar material (Biochar-AR) was chemically activated with 7 mol L^{-1} KOH and thermally treated at 675°C (Biochar-675) and 1000°C (Biochar-1000), respectively. As a result of the chemical and thermal treatment, the surface area of the biochar increased from 1.66 m^2 g^{-1} (as-received biochar) up to 990 m^2 g^{-1}, and the porosity increased as well from virtually negligible (for the as-received sample) up to 0.9 cm^3 g^{-1}. Furthermore, the chemical and thermal activation (Biochar-675 and Biochar-1000) caused the removal of heteroatoms and tarry materials evidenced by Elemental Analyses, FT-IR and XRD results. Additionally, XRD, TEM, and electrical conductivity analyses suggested more graphite-like structure and higher electrical conductivities for Biochar-1000 compared to Biochar-675. Electrodes were fabricated and investigated for electric double layer (EDL) application using the two types of activated biochar samples (Biochar-675 and Biochar-1000). The electrode fabrication method included spraying of the carbon-based inks on Ni mesh using Nafion® as binder. The Nafion content of the electrodes was between 0 and 30 wt.% and the corresponding effect on the EDL performance was also investigated. Cyclic voltammetry (CV) and galvanostatic charge/discharge experiments confirmed unequivocally the potential of these novel electrodes to be employed in electric double layer related applications. The total capacitance of the activated biochar electrodes measured by cyclic voltammetry analysis was up to fifty times higher than that of Vulcan electrodes prepared by the same technique (Table 4.7). Furthermore, the total capacitances of the Biochar electrodes are also competitive with much more expensive

systems such as CNTs and graphene-based electrodes (Table 4.7). The activated biochar electrodes showed also effective galvanostatic charge/discharge cycling behaviour and electrical conductivity.

Modification of the surface oxygen-containing groups of an activated biochar (with majorly microporous structure) and its effect on EDL performance was also investigated. The activated biochar sample mixed with 1 mol L^{-1} HNO_3 followed by calcination at 150 or 450°C. HNO_3 treatment showed an increase in oxygen-containing groups (i.e., carboxylic and phenolic) compared to the untreated activated biochar. Calcination of the HNO_3-treated sample at 150°C showed very similar surface functionality to the HNO_3-treated samples without calcination. However, further increasing the calcination temperature to 450°C resulted in removal of the most of oxygen-containing groups and consequently similar surface chemistry to the untreated activated biochar was obtained. The total capacitance of HNO_3-treated activated biochar showed significant reduction compared to the untreated activated biochar (109 vs. 195 F g^{-1}, respectively); while, showing larger Ohmic potential drop (12.9 vs. 2.25 V g^{-1}, respectively). Calcination at 150°C followed to the HNO_3-treatment showed similar reduction in total capacitance. However, further increasing the calcination temperature at 450°C led to an increase in total capacitance to the value comparable to that of untreated activated biochar. There results suggested that HNO_3-treatment of activated biochar is not advantageous in EDL performance.

Chapter 5: Phase II - Tailoring the porous structure of biochar and its effect on EDL performance[1]

5.1 Introduction

In Chapter 4, biochar was investigated as a promising electrode material for Electric Double Layer (EDL) processes. Surface area and porosity of activated biochar samples showed considerable effect on EDL performance. This chapter extends the investigations on the correlation between controlled porosity (via novel and modified KOH-activation method) and EDL performance of activated biochar electrodes. Development of tailored pore structure to yield promising electrodes for EDL-based application is emphasized in the literature [110], [194]. Tailored activated biochar could introduce a new generation of low-cost and renewable electrodes with improved performance for CDI.

Chemical activation is one of the well-known processes to produce activated carbon (AC) in which carbonaceous precursor is impregnated with chemical reagent and carbonized [13], [144]–[149]. A large number of studies in the literature focused on the correlation between porosity development and activation process parameters including: activating reagent type [147], [195]; mass ratio of activating reagent to substrate [13], [148], [196], [197]; carbonization temperature [13], [148], [149], [198]; flow rate of inert gas during carbonization [13], [196], [197], [199]; carbonization time [13], [200]; method of mixing [148], [196]; and washing step [197]. Even though the majority of reports have investigated different chemical activation parameters, the sample drying process prior to carbonization (i.e., a key step in all chemical activation processes) has not been investigated in detail.

[1] A version of this chapter has been published in the *Journal of Biomass & Bioenergy*.
Parts of Sections 5.2.1 and 5.2.3 were presented in the Annual World Conference on Carbon: "Innovation with carbon materials" in Dresden, Germany, July 2015.

Drying conditions prior to carbonization affected the porosity development due to the potential conversion of activating reagents (e.g., KOH and NaOH) to their corresponding carbonates (i.e., K_2CO_3 and Na_2CO_3) in the presence of CO_2 in the air-dried atmosphere [146], [196]. According to the literature, chemical activation using KOH produced high surface area ACs with mostly microporous structure [13], [147], [148], [199]; while, K_2CO_3 produced ACs with both micro- and mesoporosity depending on the carbonization temperature [155], [201], [202]. Thus, further investigation of the different drying conditions on the conversion of KOH to K_2CO_3, including the presence or absence of CO_2 in the drying atmosphere (i.e., drying under air vs. N_2), and its role in tailoring the porosity at specific temperatures are warranted. Modification of drying conditions could be potentially an easy and low-cost process for tailoring the AC porous structure comparing to other methods such as Chemical Vapor Deposition (CVD) and silica templates [203], [204].

The goal of this chapter is to investigate an easy-to-prepare method for tailoring the micro-/mesoporous structure of KOH-activated biochar by exploiting synergistic effects, overlooked thus far in the literature, between biochar drying conditions (air vs. N_2 and time), and carbonization temperature (475, 675, and 875°C with 2 h dwell time). The mechanism responsible for the observed effects is studied to provide insights into the pore forming processes. Furthermore, the EDL performance of the activated biochar samples with tailored porous structure is studied. The schematic presentation of the modified chemical activation method is presented in Figure 5.1.

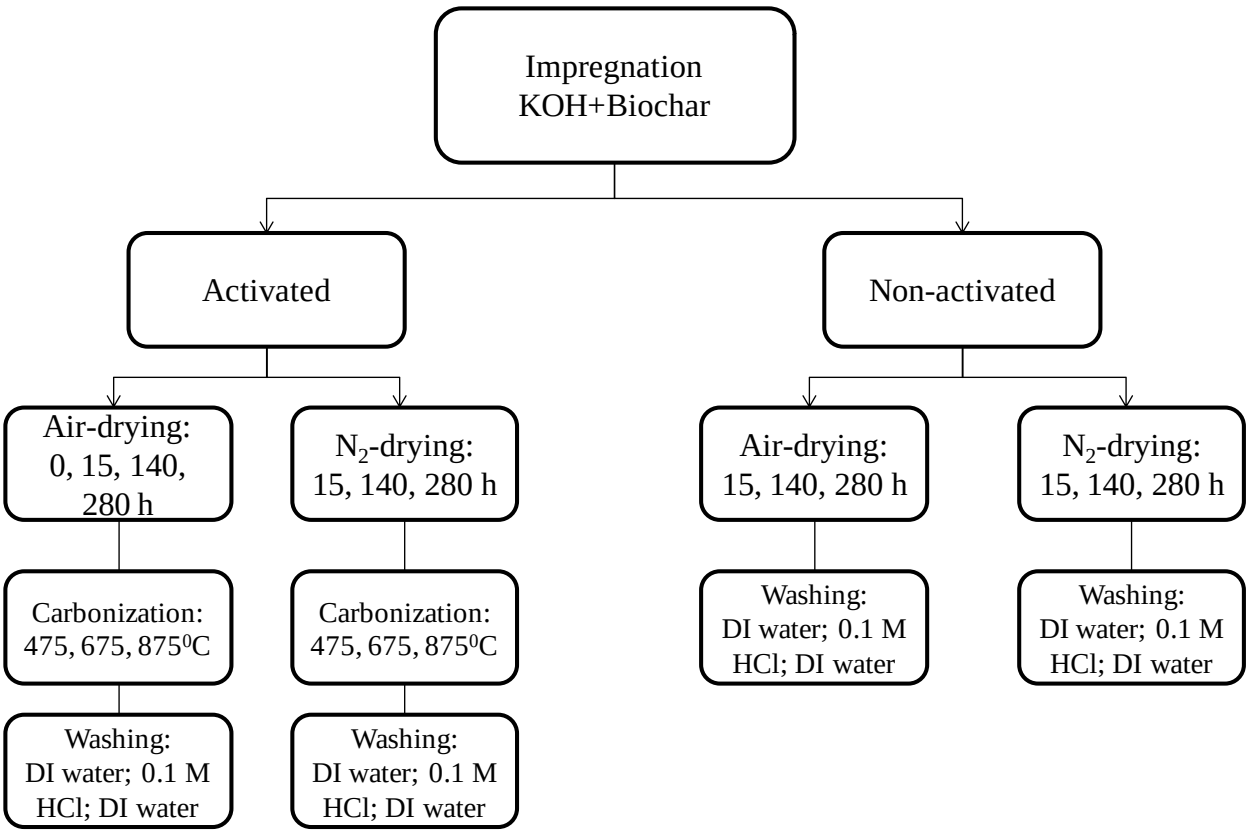

Figure 5.1 Schematic representation of activated biochar preparation.

For simplicity in referring to the prepared samples, the notations B475, B675, and B875 are assigned to the activated biochar samples carbonized at 475, 675, and 875°C, respectively; while, the notation B-KOH was used for the non-activated samples. Furthermore, ND, SD, LD and LLD abbreviations correspond to the drying duration of the samples: Not dried (ND), short dried (SD) for 15 h, long dried (LD) for 140 h and extra-long dried (LLD) for 280 h. Additionally, the drying gas (N_2 or air) followed the samples' name. For example: "B675-SD-15h-Air" refers to the activated biochar sample dried under air for 15 h (SD) and subsequently carbonized at 675°C. Further, the sample "B-KOH-LD-140h-N_2" refers to the sample dried under nitrogen for 140 h (LD) without carbonization.

5.2 Results and discussion

One of the working hypotheses is that the drying conditions prior to carbonization, such as drying gas (air vs. N_2), temperature and drying time can have a significant role on porous structure development through synergistic effects, an aspect largely neglected in the literature.

Regarding the drying gas, air drying of the KOH impregnated samples inherently exposes them to CO_2 and carbonate formation will occur, i.e., Equation (5.1).

$$4KOH+2CO_2 \Leftrightarrow 2K_2CO_3+2H_2O,\ \Delta G° = -141.07\ kJ\ mol^{-1}\ CO_2\ at\ 25°C \quad (5.1)$$

Longer air drying time is expected to yield higher amount of K_2CO_3; consequently, it is hypothesized that different porous structures will be generated during the carbonization step. The conversion of KOH to K_2CO_3 under different drying conditions and its synergetic effect on tailoring the porosity at different carbonization temperatures are investigated in the following sections.

5.2.1 Effect of drying conditions on conversion of KOH to K_2CO_3 prior to carbonization

5.2.1.1 Surface chemistry analysis of impregnated biochar

First, the surface chemistry of air- and N_2-dried samples for different lengths of time was analyzed using FT-IR. Figure 5.2 shows the FT-IR spectra of air-dried samples along with pure K_2CO_3. A broad peak around 3200 cm^{-1} in the B-KOH-ND and B-KOH-SD-15h-Air spectra is attributed to the presence of water which is absent in samples dried for 140 and 280 h. This broad peak at 3200 cm^{-1} might also overlapped the distinctive sharp peak around 3500 cm^{-1}, characteristic of the OH group in KOH [205] (see Figure 5.3; KOH spectrum). Additionally, both B-KOH-LD-140h-Air and B-KOH-LLD-280h-Air showed similar peaks to the pure K_2CO_3 spectrum (Figure 5.2), most probably due to the conversion of KOH to K_2CO_3. The spectra of air-dried samples compared with pure K_2CO_3 also reveal two additional peaks at 1580 and 760

cm^{-1} corresponding to the aromatic structure of biochar. The former peak is attributed to the aromatic C=C bonding within the ring; while, the latter stands for the out-of-plane bonding of C-H bonds of aromatic and heteroatomic species [6], [205].

To further investigate the effect of drying condition, samples were dried under N_2 (i.e., for 15, 140, and 280 h) and analyzed using FT-IR. As shown in Figure 5.3, a distinctive sharp peak at 3500 cm^{-1} along with broad peaks at 2700, 2450 and 1900 cm^{-1} can be observed for all N_2-dried samples similar to the pure KOH spectrum. However, comparing the spectra of air-dried samples suggested a trend of absence of peaks at 2700, 2450 and 1900 cm^{-1} as increasing the drying time (Figure 5.2). Hence, it is proposed that KOH is virtually absent in the air-dried samples. Additionally, comparing the FT-IR spectra of B-KOH-SD-15h-Air and B-KOH-SD-15h-N_2 (Figures 5.2 and 5.3) reveals the absence of the broad peak around 3200 cm^{-1} (i.e., representative of the water in the sample) in B-KOH-SD-15h-N_2 sample. Since both samples were dried at the same temperature and time, the origin of the water present in the air-dried sample could be from the conversion of KOH to K_2CO_3 based on Equation (5.1). Hence, comparing Figures 5.2 and 5.3 suggest the conversion of KOH to K_2CO_3 under air and the preservation of KOH under N_2.

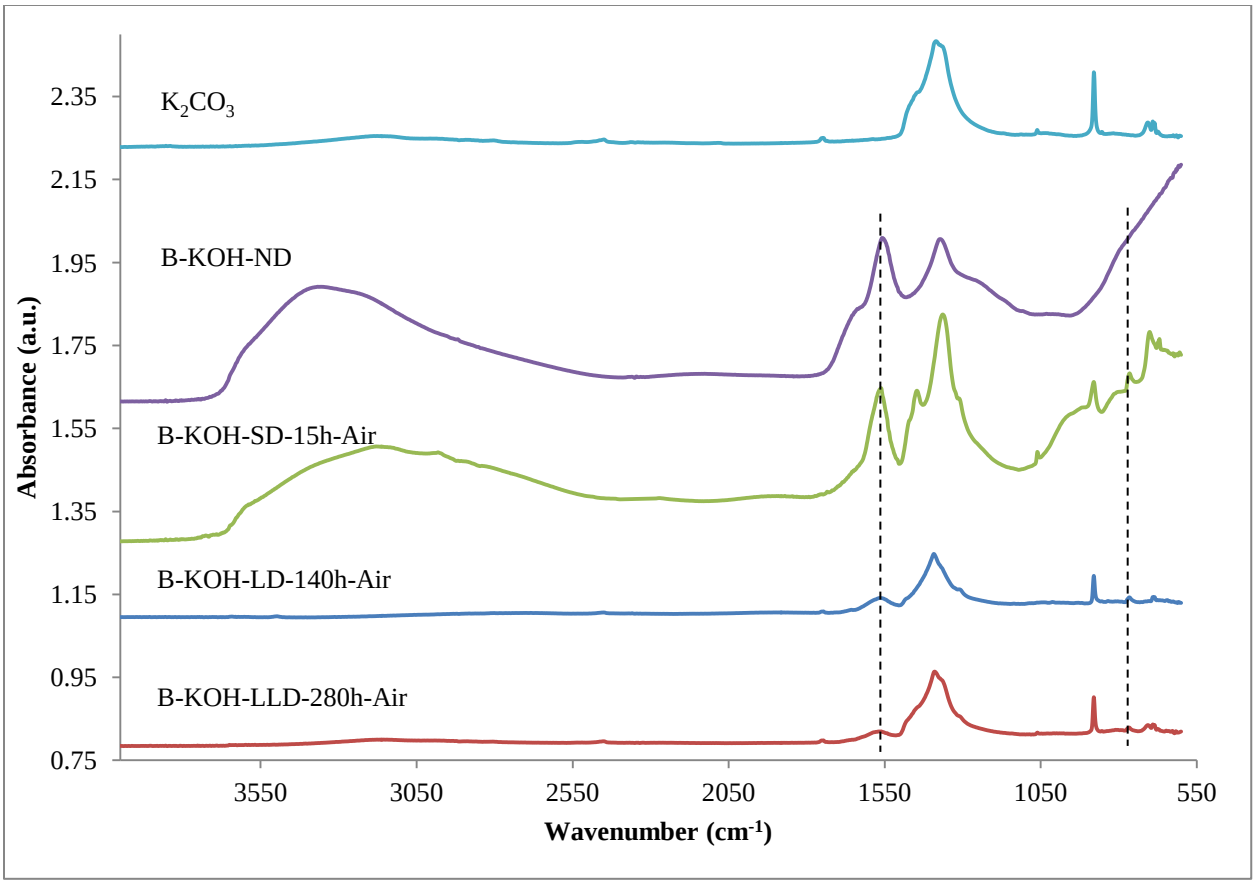

Figure 5.2 FT-IR spectra of Air-dried samples compared with K_2CO_3.

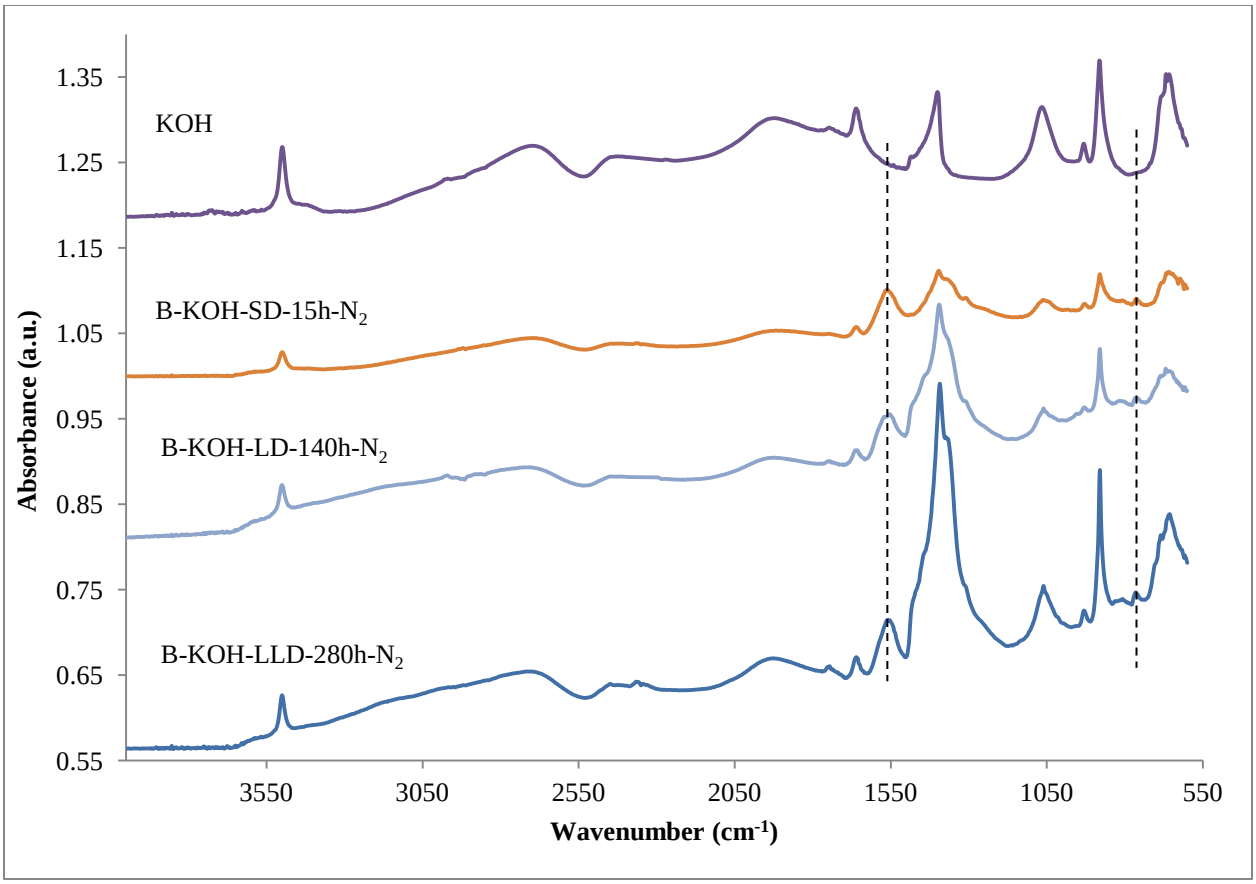

Figure 5.3 FT-IR spectra of N_2-dried samples compared with KOH.

To further confirm the conversion of KOH to K_2CO_3, the B-KOH-LLD-280h-Air and B-KOH-LLD-280h-N_2 samples were analyzed via XRD spectroscopy (Figure 5.4). The XRD pattern showed peaks corresponding to the K_2CO_3 crystalline structure namely at 2θ = 13, 26, 29, 38, 48 and 51° which were clearly absent for the B-KOH-LLD-280h-N_2 sample.

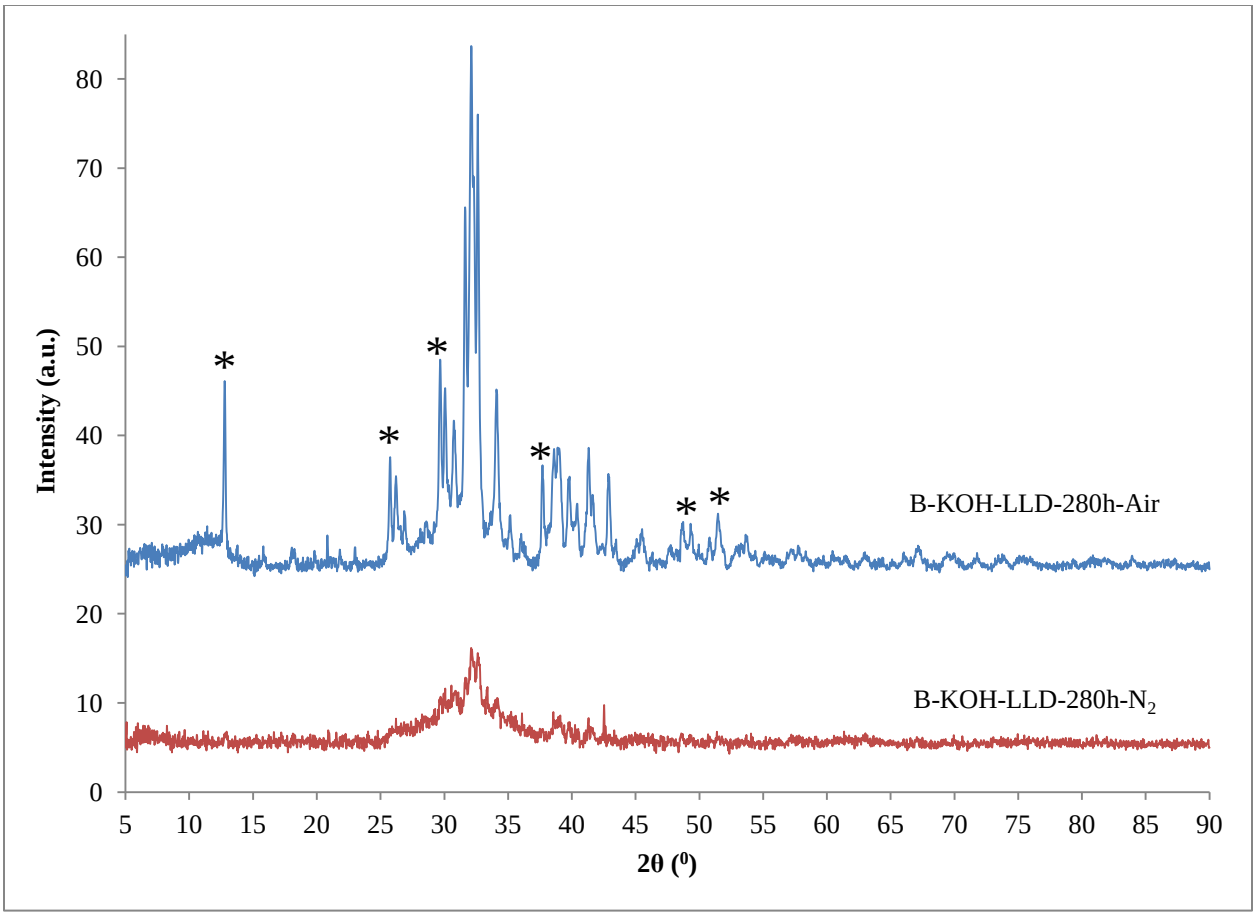

Figure 5.4 XRD pattern of B-KOH-LLD-280h-Air and B-KOH-LLD-N_2 (starred peaks are indicative of K_2CO_3 from KOH crystalline structure).

5.2.1.2 Physical characteristics of air- or N_2-dried samples

The effect of drying conditions on the impregnated samples is expressed as drying percentage, i.e., defined as the percentage of water removed from the sample by drying compared to the initial (non-dried) sample mass. Results suggested virtually constant drying percentage between 54% and 58% comparing air-dried and N_2-dried samples at different lengths. The air- or N_2- dried samples were washed with distilled water and HCl (Section 3.1.1) and further analyzed via N_2 adsorption isotherms (at –196°C). The BET surface area and porosity of the air- and N_2-dried samples (without carbonization) showed negligible increase compared to

the as-received biochar, i.e., <1 m^2 g^{-1} suggesting no structural development as a result of different drying conditions.

5.2.2 Tailoring the biochar porous structure: Synergy between drying conditions and different carbonization temperatures

The combined effects of drying conditions (i.e., under N_2 or air for 15, 140, and 280 h) and carbonization temperature (i.e., 450, 675, and 875°C) on tailoring the porous structure of activated biochar is investigated.

There are different interpretations in the literature regarding the chemical activation mechanism of carbons. In general, activation with alkali metal hydroxides includes oxidation of carbon and reduction of hydroxide. It is commonly reported in the literature that chemically activated carbon with KOH has mostly microporous structure (i.e., >85% of total pore volume) with high surface area (900–3000 $m^2 g^{-1}$) [13], [199], [206], [207]. Lillo-Rodenas et al. measured Gibbs energies of their proposed reactions for chemical activation using alkali metal hydroxides [146]. According to the calculated standard Gibbs energies, the reaction of carbon with alkali-metal hydroxide (e.g., KOH) producing carbonate and hydrogen is the beginning of chemical activation process, i.e., Equation (5.2). This reaction is thermodynamically possible at temperatures around 475–530°C [146], [207], [208]. The produced metallic K is mobile within biochar matrix further contributing to pore enlargement through intercalation between the carbon sheets at >600°C [174], [207], [209]. As a result, several atomic layers of carbon can be widened (i.e., expanded van der Waals gap between the carbon layers) forming pores. Further discussion regarding intercalation of alkali metals within the carbon structures is provided in [210].

$$6KOH + 2C \Leftrightarrow 2K + 2K_2CO_3 + 3H_2 \quad (5.2)$$

Chemical activation via K_2CO_3 has been also reported in the literature [155], [198], [201], [211]. Reaction (5.3) was proposed by McKee at temperatures around 700°C for gasification of graphite, where carbon is consumed by K_2CO_3 to produce K and CO [211]. The produced metallic K could further develop porosity by intercalation through carbon sheets to enlarge the pores. Hayashi et al. reported K_2CO_3 as an effective chemical activation reagent with different porosity development behaviour at temperatures below or above 600°C [198], [201]. At temperatures <600°C both micro- and mesoporosity were developed with the majority of the former structure due to the removal of tarry material within the pores. The surface area and mesopore volume increased considerably with activation temperature in the range of 700–900°C due to gasification of carbon generating additional porosity followed by intercalation of metallic K to enlarge the pores. Adinata et al. has made similar observation using K_2CO_3 at 600–1000°C [202]; noting, the highest mesopore volume and surface area were obtained at 800°C based on Equation (5.3).

$$K_2CO_3+2C \rightarrow 2K+3CO \quad (5.3)$$

Increasing the carbonization temperature >800°C would further change the mechanism of porosity development. Potassium carbonate is known to decompose >800°C resulting in potassium oxide and CO_2 as shown in Equation (5.4) [201], [208]. These products can further develop the porosity based on two phenomena: (a) potassium oxide reacts with carbon to produce metallic K and CO which further contributing to the pore enlargement and (b) CO_2 oxidizes carbon to generate porosity as an activating reagent similar to physical activation mechanism. Equations (5.4) and (5.5) show the major reactions occurring >800°C.

$$K_2CO_3 \rightarrow K_2O+CO_2 \quad (5.4)$$

$$K_2O+C \rightarrow 2K+CO \quad (5.5)$$

Based on Equations (5.2) – (5.5), it can be deduced that K_2CO_3 and KOH both have important effects on developing the surface area and porosity of carbon at different activation temperatures. The results presented in Section 5.2.1.1 suggested conversion of KOH to K_2CO_3 in air-dried samples specifically with long drying times (i.e., 140 and 280 h); while, KOH was preserved under N_2 at all drying times. Hence, it is speculated that the drying conditions can be used to tailor the structure of activated biochar at different temperatures as will be discussed in the following sections.

5.2.2.1 Effect of drying conditions at 475°C carbonization temperature

Table 5.1 shows the effect of drying conditions on the surface area and porosity of the activated biochar at 475°C. The BET surface area and the micropore volume of air-dried samples showed decreasing trends with increasing drying time from 814 to 488 $m^2\ g^{-1}$ and 0.32 to 0.17 $cm^3\ g^{-1}$, respectively. However, prolonging drying under N_2 did not result in significant change of either surface area or micro-/mesopore volumes (i.e., <2% drop in values). The surface area and porosity results of N_2-dried samples were also comparable to those of B475-ND (i.e., carbonization without drying). These results suggest that activated biochar samples with high micropore volume and surface area can be produced upon drying the samples under N_2 prior to carbonization at 475°C; while, drying samples under air prior to carbonization produced mixed micro- and mesopore structure with reduced micropore volume and surface area.

5.2.2.2 Effect of drying conditions at 675°C carbonization temperature

Increasing the carbonization temperature from 475 to 675°C has almost doubled both the surface area and micropore volume of the activated samples dried under either air or N_2, most probably due to the higher rates of Equations (5.2) and (5.3) (Table 5.1). Moreover, both air- and N_2-dried samples activated at 675°C showed similar trends of surface area and porosity change

to those of analogous samples activated at 475°C: A trend of decreasing surface area (i.e., by 33%) and micropore volume (i.e., by 39%) with increasing the air drying time and comparable surface area with majority of microporosity for N_2-dried samples (i.e., <5% difference) (Figure 5.5). These results could further confirm the preservation of KOH in N_2-dried samples leading in significantly higher surface area, micropore volume, and carbon burn-off (i.e., carbonization yield in Table 5.1) compared to air-dried samples.

It is interesting to note that all air-dried samples activated at either 475 or 675°C showed higher mesopore volume (almost twice) comparing to the analogous N_2-dried samples resulting in activated biochar with both meso- and micropore structure.

5.2.2.3 Effect of drying conditions at 875°C carbonization temperature

As shown in Table 5.1, increasing the carbonization temperature to 875°C generated considerably higher surface area (i.e., >2000 $m^2 g^{-1}$) and mesopore volume (i.e., >1.5 $cm^3 g^{-1}$). Typically, high surface areas of chemically activated samples with KOH is attributed to their microporous structure [13], [199], [206], [207]. However, the high surface area of air-dried and N_2-dried biochar samples activated at 875°C in the present study is mostly mesoporous, i.e., constituting >90% of the total pore volume (Figure 5.5).

The mesopore volume of the B875 samples dried under N_2 and air was comparable with <2% difference (Table 5.1 and Figure 5.5). This is in contrary to the mesopore volume change of air- and N_2-dried samples activated at lower temperatures of 475 and 675°C (Table 5.1 and Figure 5.5). This difference may be due to the decomposition of K_2CO_3 during carbonization at 875°C vs. 475 and 675°C as previously shown in Equation (5.4). Therefore, conversion of KOH to K_2CO_3 (i.e., as a result of pre-carbonization drying) did not result in different mesoporosity of air-dried and N_2-dried samples activated at 875°C.

Decomposition of K_2CO_3 at 875°C and its contribution to pore development of biochar samples via Equation (5.5) can be further confirmed through significantly smaller CY values of B875 samples compared to B475 and B675 (see Table 5.1).

For B875 samples with large mesopore volumes, the amount of micropore estimated via t-plot method might not be exact due to capillary condensation in the mesopores. Capillary condensation is the process in which pores are filled with condensed vapour of adsorbing gas occurring at pressures lower than saturation vapor pressure [212]. To further investigate the micropore content, the B875 samples were analyzed via Horvath Kawazoe (HK) method specifically used to measure the micropore content and distribution [213]–[215]. The HK micropore volume of B875 samples were ranged between 0.65 and 0.85 $cm^3\ g^{-1}$ (Table F1 in Appendix F). As a representative value, the HK micropore content of B875-SD-15h-Air sample was 0.65 $cm^3\ g^{-1}$ (with 0.79 nm median pore width) much higher than t-plot micropore presented in Table 5.1 (i.e., 0.10 $cm^3\ g^{-1}$); however, the majority of B875-SD-15h-Air structure has remained mesoporous (i.e., ~70%) upon recalculation of total pore volume based on the HK micropore.

Table 5.1 Surface area and porosity of activated biochar samples with different drying conditions and activation temperatures

Sample	BET surface area[1] ($m^2 g^{-1}$)	t-plot micropore volume ($cm^3 g^{-1}$)	BJH mesopore volume ($cm^3 g^{-1}$)	Average pore width[a] (nm)	CY[b] (%)	WY[c] (%)
B475-ND	814	0.32	0.05	1.94	40	17
B475-SD-15h-Air	643	0.24	0.10	2.21	85	15
B475-LD-140h-Air	639	0.19	0.36	3.11	93	15
B475-LLD-280h-Air	488	0.17	0.14	2.41	94	13
B475-SD-15h-N_2	894	0.35	0.06	1.95	75	15
B475-LD-140h-N_2	868	0.34	0.06	1.95	83	12
B475-LLD-280h-N_2	841	0.33	0.07	2.01	94	15
B675-ND[2]	1675	0.67	0.09	1.91	37	12
B675-SD-15h-Air	1317	0.54	0.22	2.20	87	12
B675-LD-140h-Air	876	0.33	0.20	2.31	91	13
B675-LLD-280h-Air	961	0.31	0.43	2.77	91	12
B675-SD-15h-N_2	1807	0.73	0.09	1.90	82	10
B675-LD-140h-N_2	1784	0.72	0.10	1.92	83	11
B675-LLD-280h-N_2	1695	0.69	0.12	1.95	80	11
B875-SD-15h-Air	2024	0.10[3]	1.36	2.82	49	7.1
B875-LD-140h-Air[4]	2079	0.18	1.70	3.43	62	7.5
B875-LLD-280h-Air	2046	0.22	1.33	2.90	49	9.5
B875-SD-15h-N_2	2247	0.08	1.41	2.76	37	5.5
B875-LD-140h-N_2	2673	0.04	1.64	2.70	40	9.3
B875-LLD-280h-N_2	2242	0.09	1.33	2.67	39	7

a Calculated based on BET method (4V/A)
b CY: Carbonization Yield = (mass of impregnated sample after carbonization) / (mass of impregnated sample before carbonization)
c WY: Washing Yield = (mass of carbonized sample after washing) / (mass of carbonized sample before washing)

[1] Standard deviation (from triplicate measurements of the same sample) is within ± 3% of the reported values.
[2] Standard deviation (from triplicate experiments) is within ± 5% of the reported values.
[3] t-plot values of B875 samples are underestimated due to capillary condensation. HK values are shown in Appendix F.
[4] Standard deviation (from triplicate experiments) is within ± 5% of the reported values.

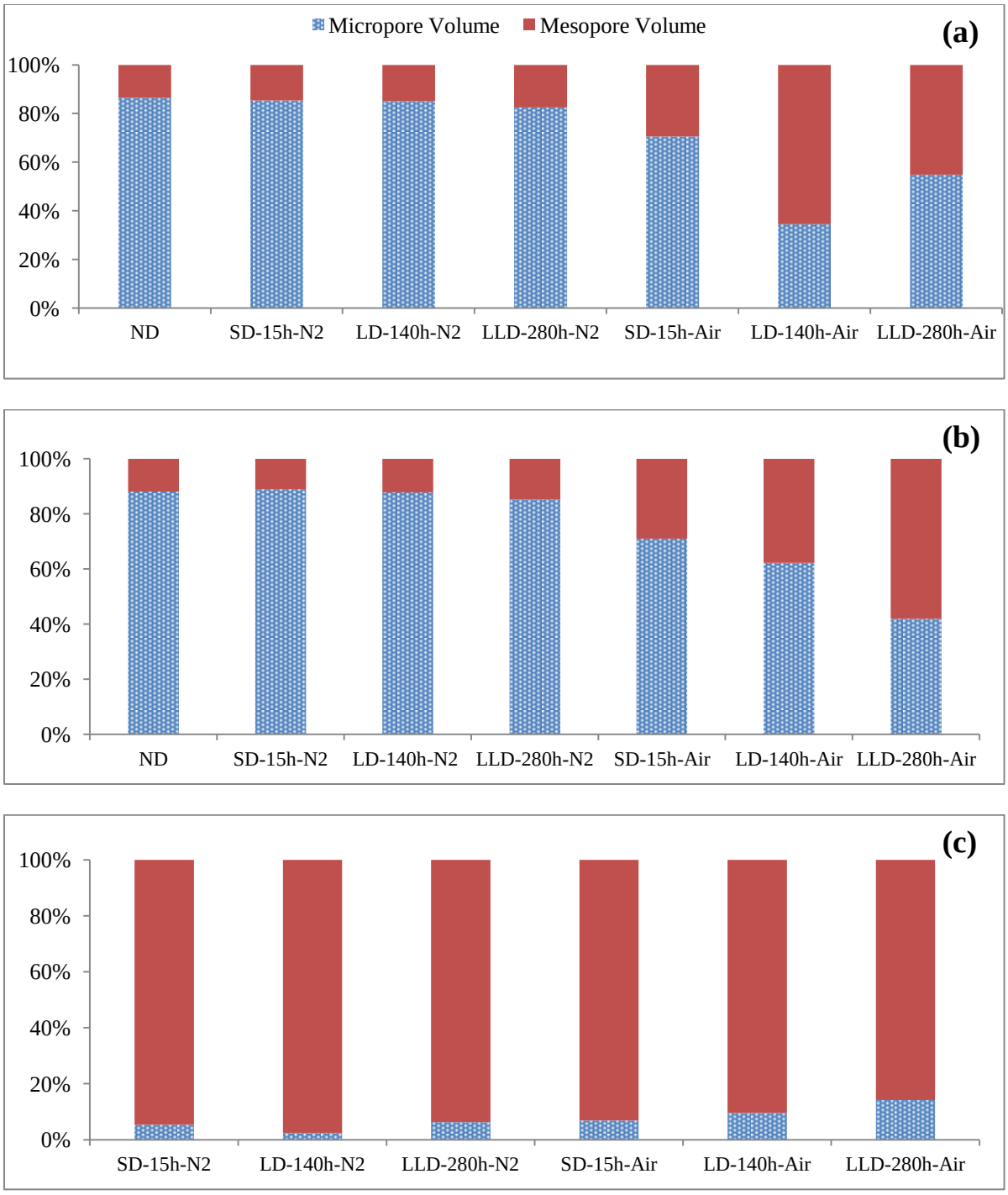

Figure 5.5 Micropore and mesopore distribution (i.e., based on total pore volume calculated as the sum of BJH mesopore volume and t-plot micropore volume) of activated biochar samples: (a) B475; (b) B675; and (c) B875 samples.

To further study the origin of mesoporous structure of B875 samples, transmission electron microscopy (TEM) images were obtained. The TEM images of B875 samples were compared with those of B475 and B675 dried under either N_2 or air (Figures 5.6 and 5.7). B475 and B675 samples showed amorphous structure; while, the B875 samples (both N_2 and air dried) showed tube-like structures most probably responsible for the large mesopore volumes of these samples. These tube-like structures could be attributed to the excessive intercalation of mobile metallic K at 875°C (Equation (5.4)) resulting in bending the carbon sheets. Further analysis of the tube-like structure of B875 samples will be discussed in Section 6.2.3.

a)

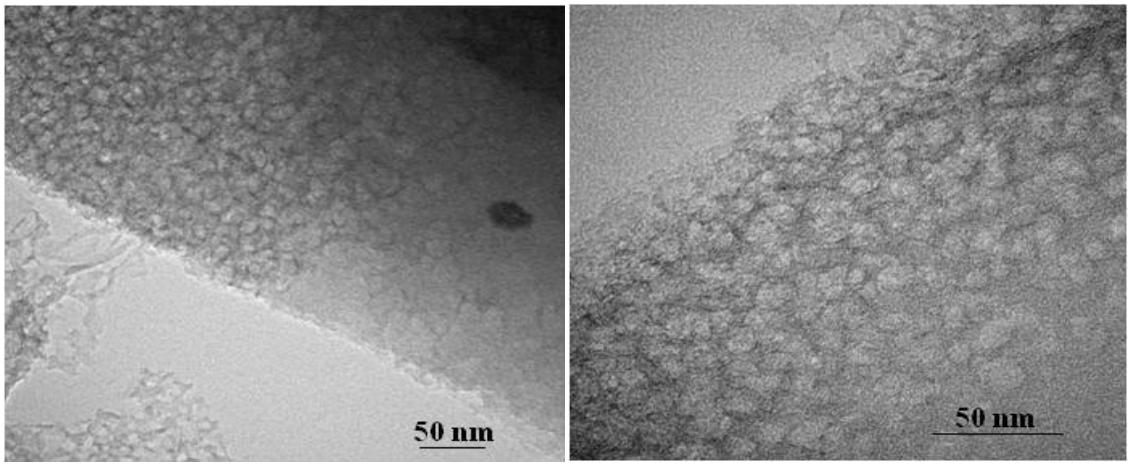

b)

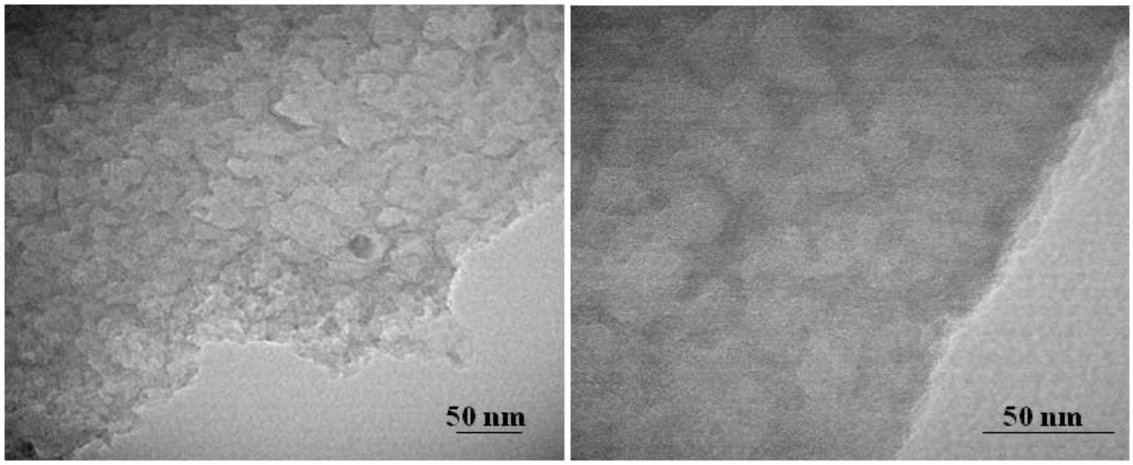

c)

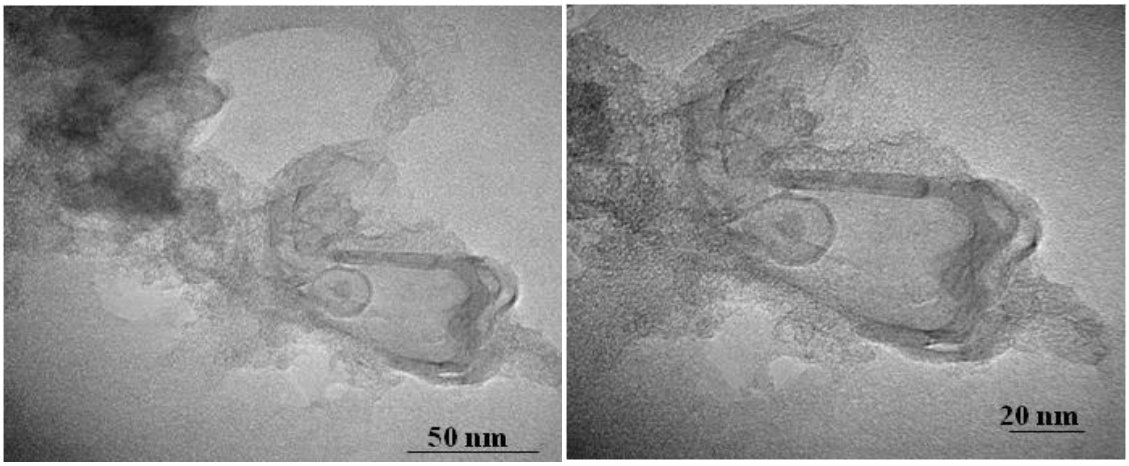

Figure 5.6 TEM images of: a) B475-LD-140h-Air; b) B675-LD-140h-Air; and c) B875-LD-140h-Air.

a)

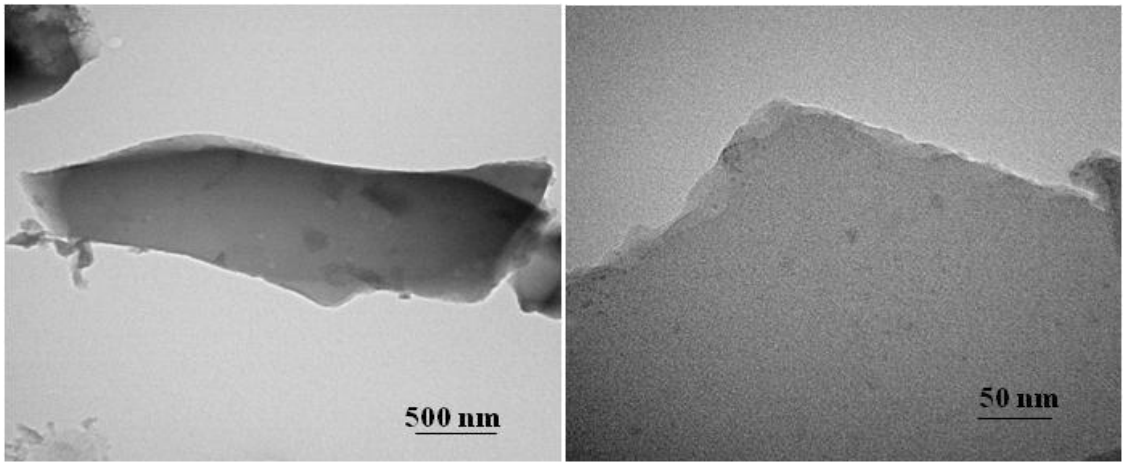

b)

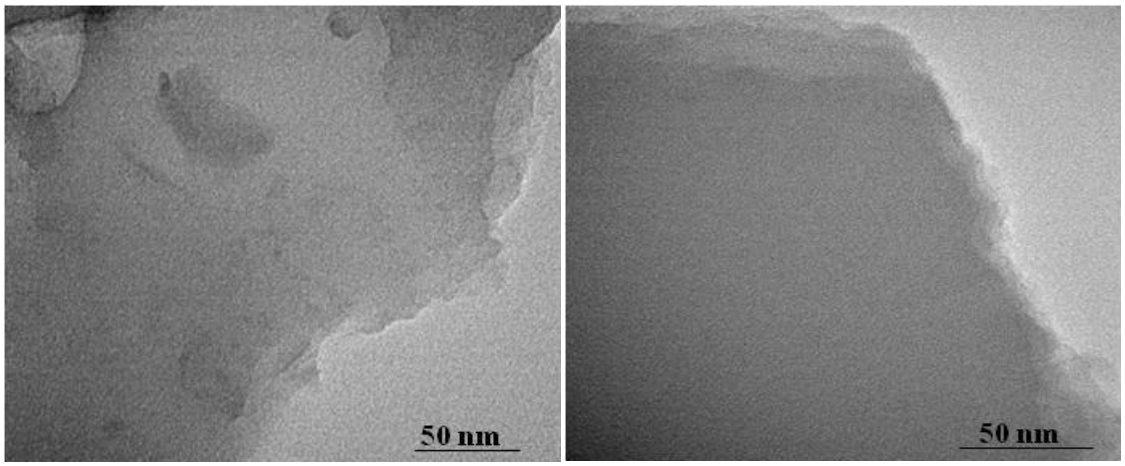

c)

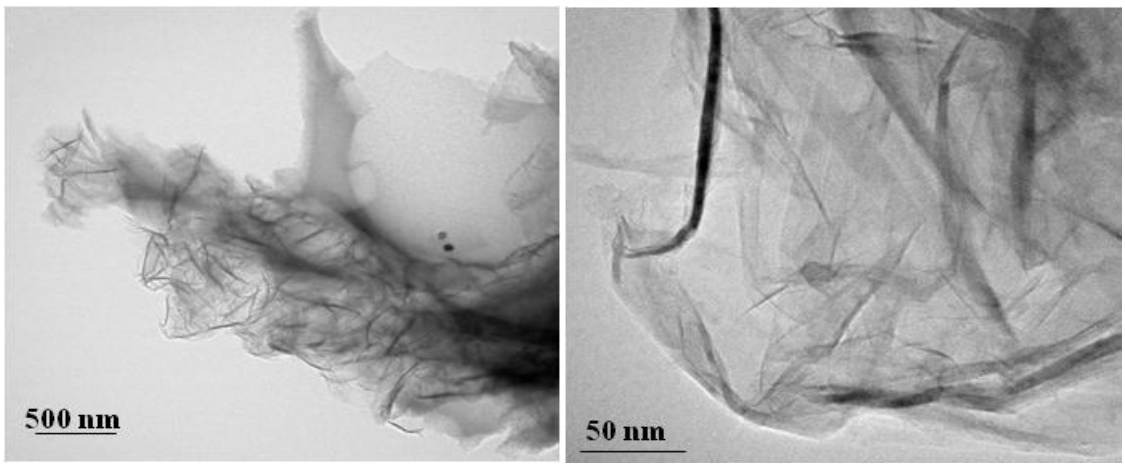

Figure 5.7 TEM images of: a) B475-LD-140h-N2; b) B675-LD-140h-N2; and, c) B875-LD-140h-N2.

5.2.3 Effect of tailored structure on EDL performance

The EDL performance of tailored activated biochar samples was investigated. Three groups of electrodes were fabricated from selected activated biochar samples with tailored porosity: group (a) majorly microporous (>85% of the total pore volume), i.e., B675-SD-15h-N2, B675-LD-140h-N2 and B675-LLD-280h-N2; group (b) mixed microporous and mesoporous, i.e., B675-LD-140h-Air and B675-LLD-280h-Air (40-50% of total pore volume); group (c) majorly mesoporous (>90% of the total pore volume), i.e., B875-LD-140h-Air, B875-LLD-280h-Air, B875-LD-140h-N2, and B875-LLD-280h-N2. Electrodes were fabricated by spraying the mixture of activated biochar powder (ground and sieved between 10 and 50 μm mesh size), isopropanol (99.9% assay Fisher Scientific), and Nafion® (5 wt.%, Sigma Aldrich) on Ni mesh (Monel® alloy, 150 × 150 mesh size, McMaster-Carr). The weight percentage of activated biochar to binder (i.e., Nafion®) was 95:5. Further electrode preparation details are described in Section 3.1.2. The geometric area of electrodes was 8.54 ± 0.90 cm^2.

The CV analysis of the selected electrodes is shown in Figures 5.8 and 5.9. According to the literature, an ideal EDL material has a rectangular-shaped voltammogram [103]. At the fastest sweep rate (i.e., 50 mV s^{-1}) the samples with the majorly microporous structure, i.e., group (a) electrodes, showed the highest deformation from rectangular shape (Figure 5.8). This can be attributed to the limited accessibility of ions to the micropores of activated biochar. Increasing the mesopore content, i.e., groups (b) and (c) electrodes, resulted in improved voltammograms in terms of decreased deformation and consequently more rectangular shape at fast scanning rates. Nonetheless, as sweep rate reduced to 0.5–5 mV s^{-1}, all voltammograms showed minimal distortion from rectangular shape (Figure 5.9) most probably due to the longer time available for the ions to access the micropore content of the electrodes [95].

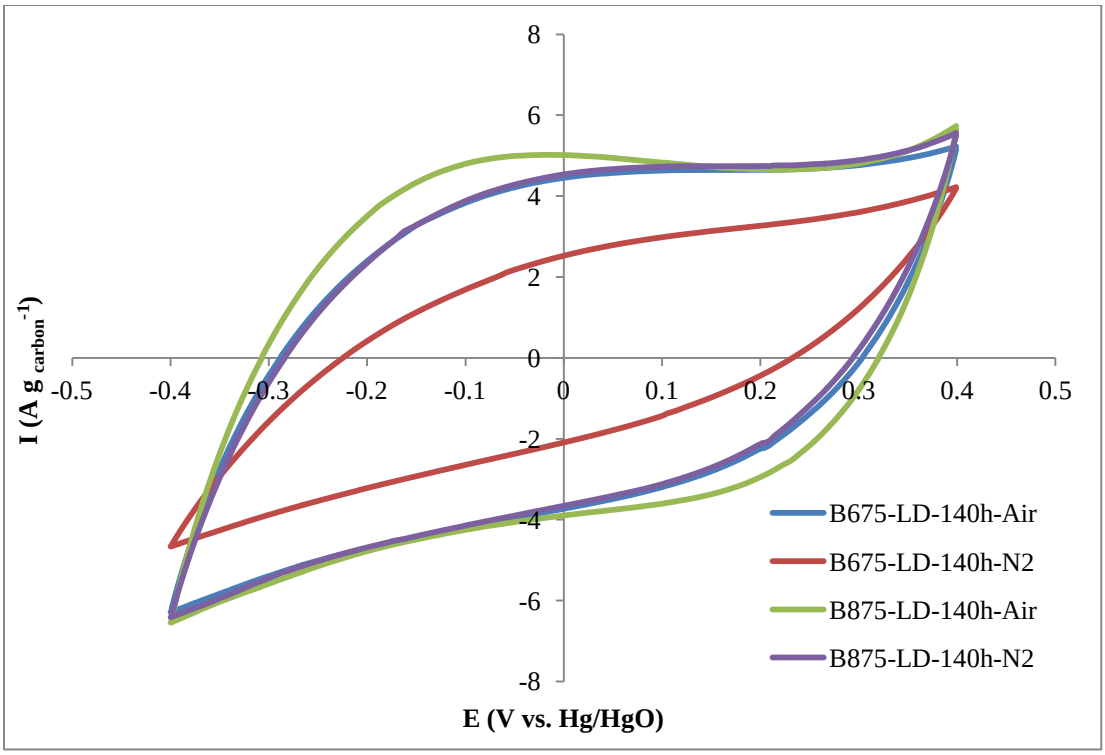

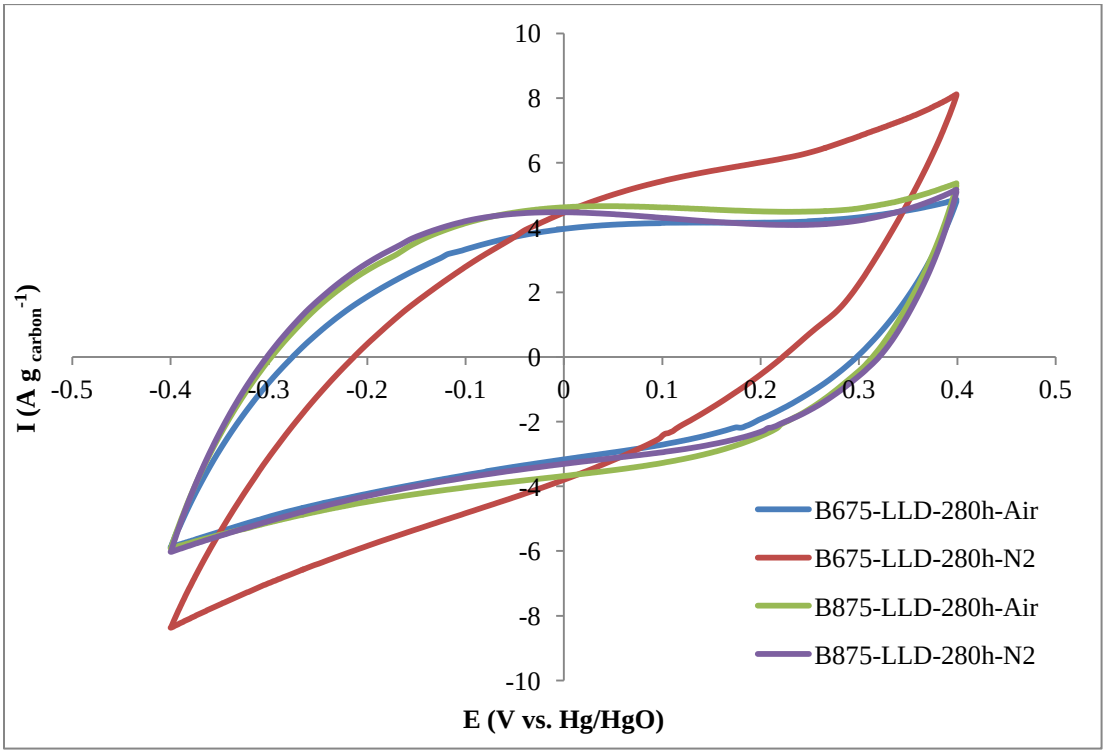

Figure 5.8 CV diagrams of tailored activated biochar electrodes at 50 mV s^{-1} in 0.1 mol L^{-1} NaCl/0.1 mol L^{-1} NaOH electrolyte.

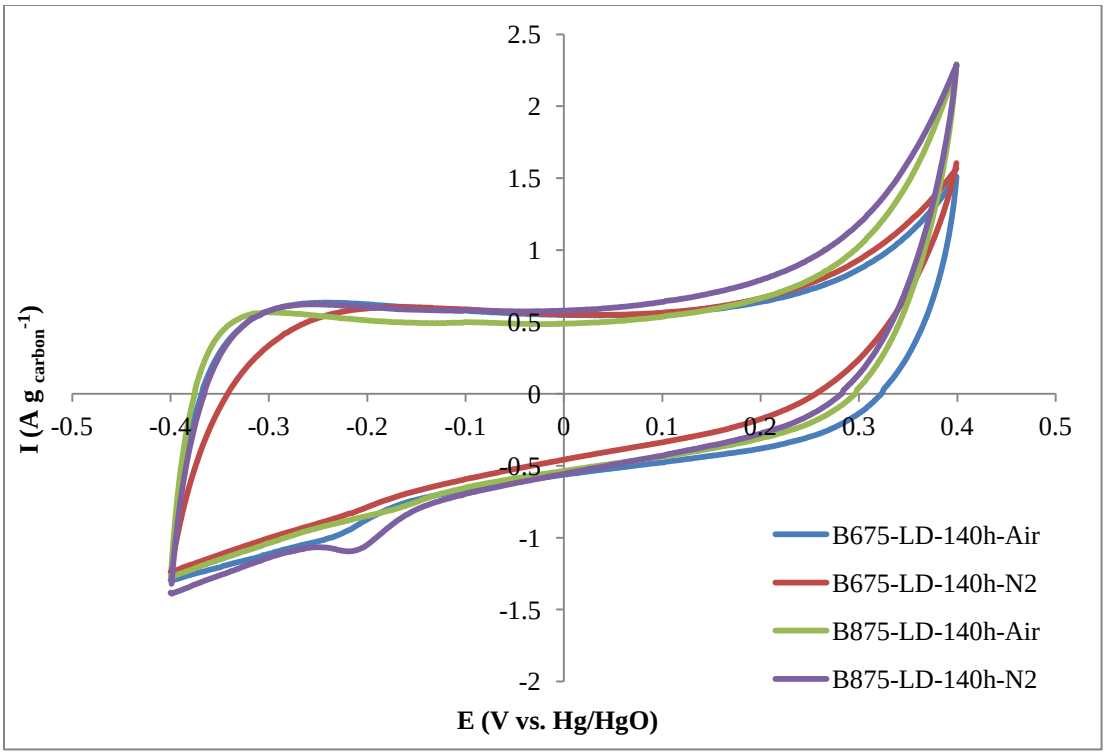

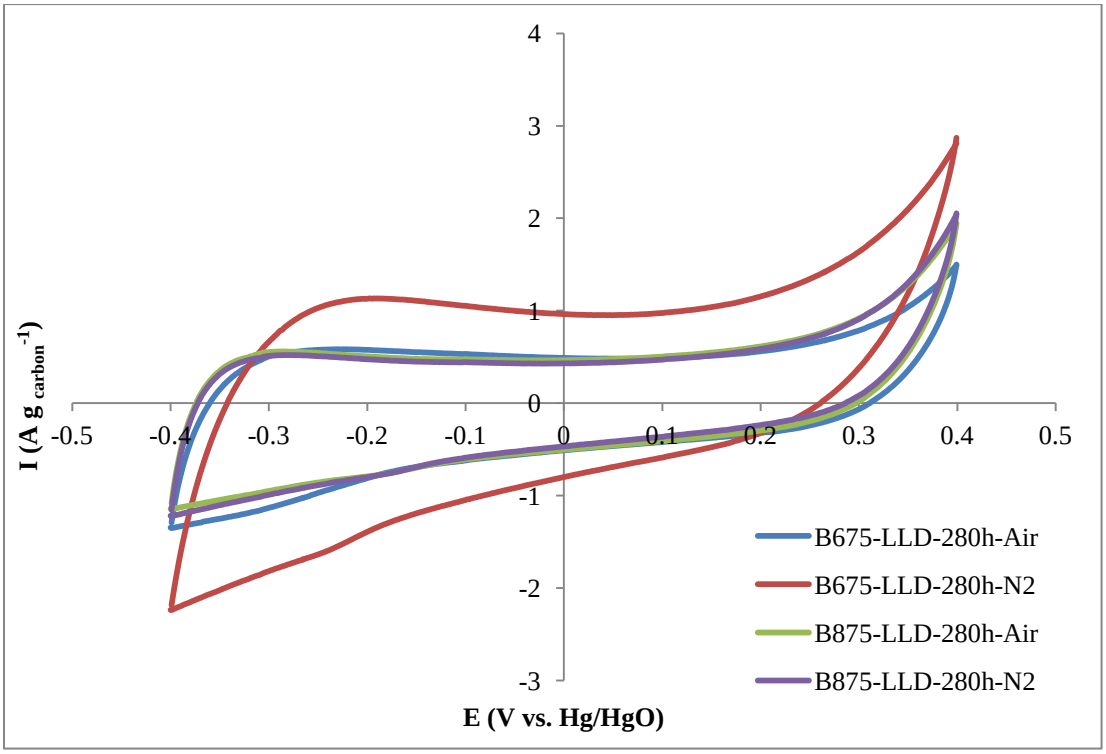

Figure 5.9 CV diagrams of tailored activated biochar electrodes at 5 mV s^{-1} in 0.1 mol L^{-1} NaCl/0.1 mol L^{-1} NaOH electrolyte.

To measure the total capacitance of the electrodes, the anodic and cathodic current difference ($\Delta I = I_a - I_c$) at the EDL plateau region of the CV voltammograms was plotted against corresponding sweep rate (i.e., 0.5–3 mV s^{-1}), similar to the method used in Chapter 4. The slope of the plot was then quantified and normalized per mass of each electrode to calculate the total capacitance in F g^{-1} (Table 5.2). Group (a) electrodes with microporous structure (i.e., N2-dried B675 samples) showed 10%–20% higher total capacitance values comparing to group (b) electrodes with mixed micro-/mesoporous structure (i.e., B675-LD-140h-Air and B675-LLD-280h-Air). This could be attributed to the higher content of micropore volume in N_2-dried B675 samples vs. air-dried B675. According to the literature, micropores between 0.5 and 2 nm contribute to the electro-adsorption of simple hydrated ions (e.g., Na^+, OH^-, and K^+), hence, increasing the total capacitance [193]. B875-LD-140h-Air and B875-LLD-280h-Air electrodes of group (c) (i.e., majorly mesoporous structure) showed total capacitance values comparable to B675-LD-140h-Air and B675-LLD-280h-Air electrodes with mixed micro-/mesoporous structure (Table 5.2). The highest total capacitance was obtained for B875-LD-140h-N2 (i.e., 95% mesoporous structure) and B675-SD-15h-N2 (i.e., 88% microporous structure) electrodes, i.e., 240 and 245 F g^{-1}, respectively. Despite of similar total capacitance of these two electrodes, the B875-LD-140h-N2 electrode showed more rectangular shape voltammogram indicative of its mesoporous structure and improved ion accessibility into the pores (Figure 5.8). The total capacitances of activated biochar electrodes with tailored porosity are competitive with other carbon-based electrodes in the literature, albeit with high-cost and complicated preparation methods, e.g., modified carbon aerogel with Ru (206 F g^{-1}) [187], graphene-PEDOT[1] (125–261 F g^{-1}) [54], Single wall carbon nanotubes on carbon cloth (190–210 F g^{-1}) [183], and AC from fibers of oil palm (150 F g^{-1}) [61].

[1] Polyethylenedioxythiophene

Table 5.2 EDL capacitive properties of selected tailored activated biochar

Electrodes	Total capacitance ($F\ g^{-1}$)	Discharge capacitance ($F\ g^{-1}$)	Ohmic drop ($V\ g^{-1}$)	R_{ct} ($\Omega\ cm^{-2}$)	R_s ($\Omega\ cm^{-2}$)
Group (a)					
B675-SD-15h-N2	245	55	0.71	0.203	0.108
B675-LD-140h-N2	224	65	1.14	0.246	0.064
B675-LLD-280h-N2	222	72	1.24	0.266	0.041
Group (b)					
B675-LD-140h-Air	212	62	0.62	0.154	0.052
B675-LLD-280h-Air	204	63	1.07	0.222	0.047
Group (c)					
B875-LD-140h-Air	218	58	0.33	0.114	0.026
B875-LLD-280h-Air	201	63	0.23	0.124	0.035
B875-LD-140h-N2	240	82	0.22	0.063	0.032
B875-LLD-280h-N2	182	55	0.29	0.092	0.026

The Galvanostatic Charge Discharge (GCD) tests were performed to further analyze the adsorption and desorption behaviour of ions from surface of electrodes. Figure 5.10 demonstrates the charge discharge profiles (at 0.25 and –0.25 mA cm^{-2}) of selected activated biochar electrodes with tailored porosity. All GCD profiles showed typical triangle shape confirming the promising EDL behaviour of activated biochar. The sudden potential drop at the beginning of the discharge curve is known as Ohmic drop (i.e., IR-Drop) resulting from the total resistance of electrode majorly associated with electrical connection, bulk solution, and ion migration into pores [103], [194]. The major difference in Ohmic drop of tailored electrodes is attributed to ion migration resistance into pores and the electrical conductivity (EC) of the activated biochar samples. Group (c) electrodes with >90% mesoporosity showed the lowest Ohmic drop values; while, group (b) electrodes with the majority of microporous structure (i.e., N_2-dried B675 samples) showed the highest Ohmic drop (Table 5.2). These results suggest reduced electrode

resistance due to increased mesoporosity and consequently improved ion accessibility. The discharge capacitance was calculated by multiplying the slope of the linear portion of discharge diagram ($\Delta t/\Delta E$) with the amount of applied current density (–0.25 mA cm^{-2}) (Table 5.2). The highest discharge capacitance (i.e., 82 F g^{-1}) was obtained for B875-LD-N2 electrode with the highest mesoporosity content (95%); where, the discharge capacitance of group (a) electrodes (with >88% microporosity) ranged between 56 and 72 F g^{-1}. The discharge capacitance values obtained using tailored activated biochar are significantly larger than other carbon-based electrodes in the literature, e.g., commercial carbon aerogel (23 F g^{-1}), carbon black (10 F g^{-1}) and activated carbon (19 F g^{-1}) [185].

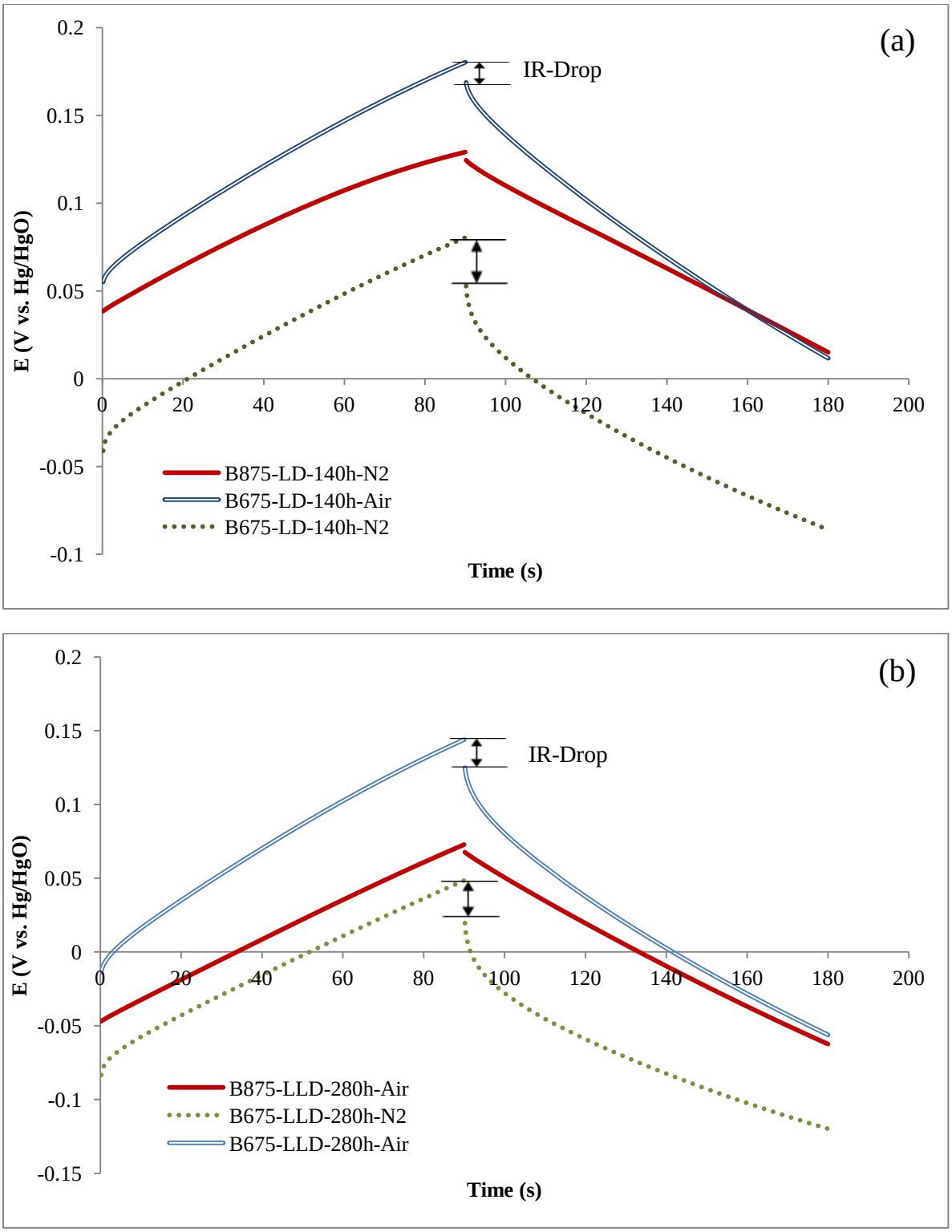

Figure 5.10 GCD plots of activated biochar electrodes with tailored porous structure prepared at: a) 140 h and b) 280 h of drying (in 0.1 mol L^{-1} NaCl/0.1 mol L^{-1} NaOH electrolyte).

The tailored biochar electrodes were also characterized through electrochemical impedance spectroscopy (EIS), with the Nyquist plots (i.e., complex impedance plots) shown in Figure 5.11. The typical Nyquist plot of an EDL capacitor includes a semi-circle at high frequencies, a mass transfer limited region shown by a linear line (Warburg region with ~45° phase angle), and a nearly vertical line at low frequencies (i.e., representative of ideal capacitive behaviour) [194], [216], [217]. The Nyquist plot of group (a) electrodes showed a depressed semi-circle at high frequencies followed by a linear region at low frequencies (i.e., diffusion-limited) mainly due to the high content of microporosity (Figure 5.11). Group (b) electrodes showed similar trend except for the steeper slope in the diffusion-limited region indicative of improved diffusion and better capacitive behaviour [194]. The activated biochar electrodes with majorly mesoporous structure showed perfect semi-circle (inset of Figure 5.11) indicative of double layer performance followed by nearly vertical line confirming the ideal capacitive behaviour and minimal mass transfer limitations.

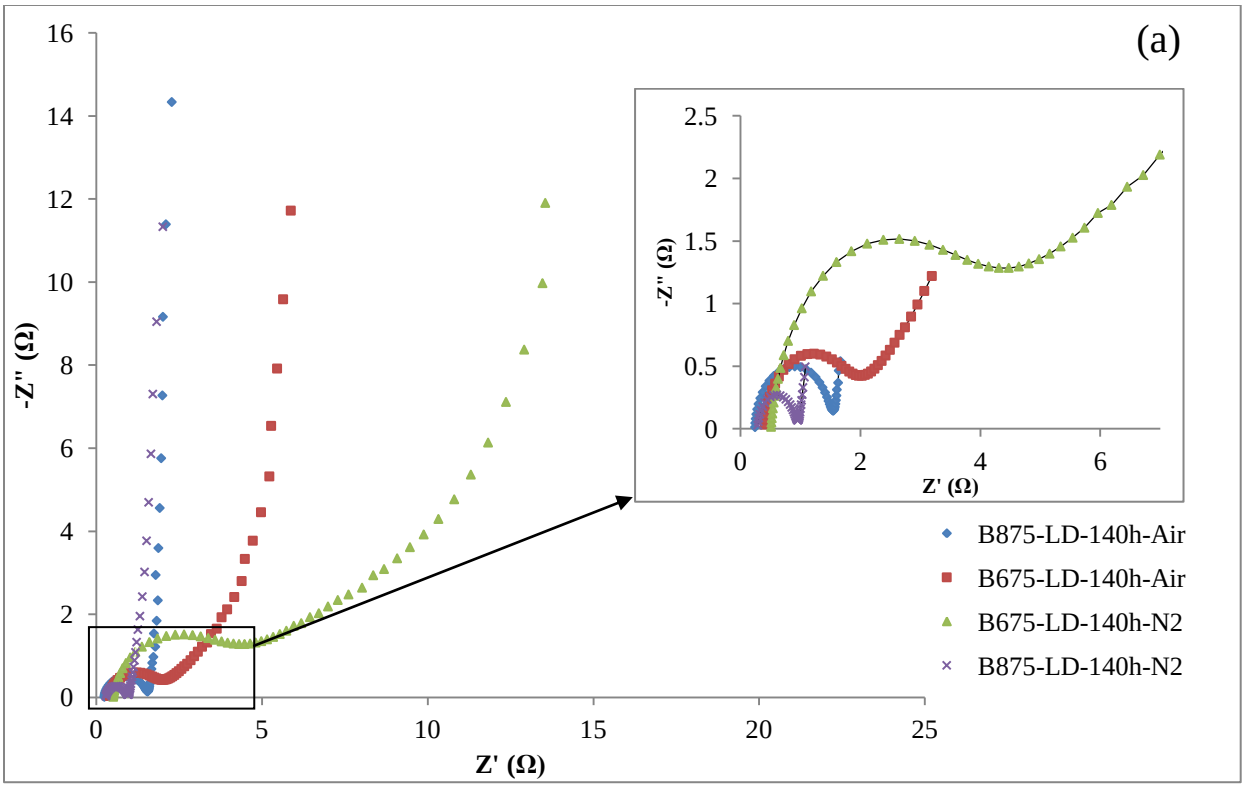

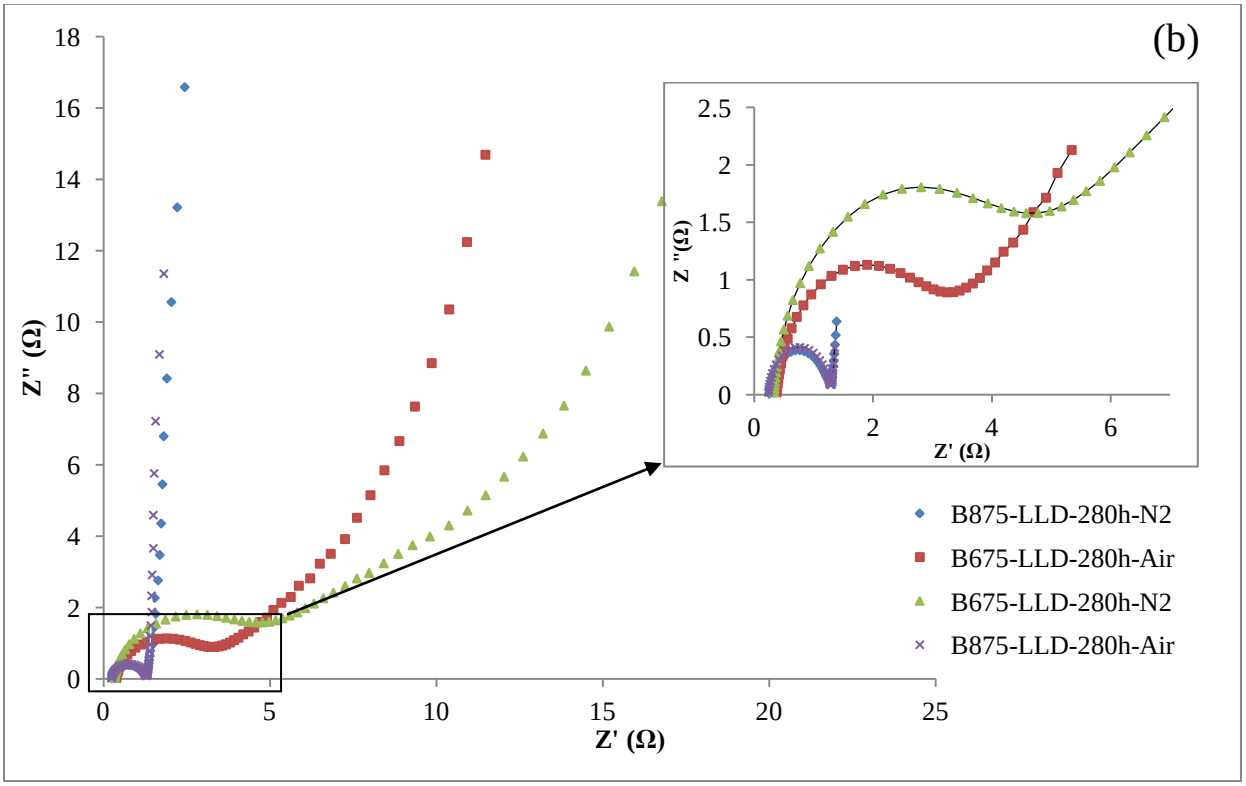

Figure 5.11 Nyquist plots of activated biochar electrodes with tailored porous structure prepared at: (a) 140 h and (b) 280 h of drying (0.1 mol L^{-1} NaCl/0.1 mol L^{-1} NaOH electrolyte).

The intercept of semi-circle curve on the real part axis of impedance (Z') stands for the bulk solution resistance (Rs); while, the radius of the semi-circle represents the internal electrode resistance (Rct, charge-transfer resistance). Rs is mainly dependent on the resistance associated with the solution and connectivity of particles to the current collector; where, Rct is related to the ionic transfer resistance into the pores of electrode [194], [218]. The Randles equivalent circuit (consists of a bulk solution resistance, Rs, in series with a parallel combination of double layer capacitance, Cdl, and Rct) was used to simulate the EIS data and quantify the values of Rs and Rct (Table 5.2). As expected, the mesoporous electrodes of group (c) showed the lowest Rct; followed by group (b) electrodes with mixed micro-mesoporous structure; and group (a) with microporous structure.

The Electrical Conductivity (EC) of powder activated biochar was also measured via dry-cell polarization experiment (Table 5.3). EC is one of the major characteristics of a double layer material affecting electrical connectivity and charge transfer within the electrode. The B475 samples (either N_2 or air dried) showed negligible EC (i.e., $>10^{-7}$ S cm^{-1}) which could be the main reason responsible for the poor EDL performance of the prepared electrodes despite of having large surface area and porosity (data not shown). Increasing the activation temperature to 675°C resulted in significantly improved EC (Table 5.3). Interestingly, further increase of EC was obtained for B875 samples with the mesoporous structure; while, EC is expected to be reduced by increasing porosity. The increased EC of the B675 and specifically B875 samples could be attributed to the removal of heteroatom from the carbon matrix and increased electrons associated with π-bond as charge carriers [110], [219].

Table 5.3 Electrical Conductivity of activated biochar powders

Sample	Electrical Conductivity (S cm^{-1} g^{-1})
B475-LD-Air	Negligible
B475-SD-N2	Negligible
B675-SD-N2	0.21
B675-LD-N2	0.04
B675-LLD-N2	0.04
B675-LD-Air	0.32
B675-LLD-Air	0.15
B875-LD-Air	2.10
B875-LLD-Air	1.03
B875-LD-N2	0.54
B875-LLD-N2	1.30

The EDL performance results of tailored biochar electrodes suggest different range of applications from desalination of water with small hydrated ions (e.g., Na^{+}, Cl^{-}, Cu^{2+}, K^{+}, Mg^{2+}) using microporous electrodes to electrosorption of larger ions in industrial wastewater (e.g., Zn^{2+}, Cd^{3+}, Cr^{3+}) using mesoporous electrodes. Furthermore, microporous electrodes with high total capacitance can be employed in supercapacitors using aqueous electrolytes (NaOH, KOH, H_2SO_4); while, mesoporous electrodes can be used in electrolytes with larger ionic radius (e.g., ionic liquids and aprotic electrolytes) to increase the energy density of the supercapacitor. These results confirm the importance and practicality of activated biochar with tailored structure to improve the performance in an adsorption-specific process.

5.3 Conclusion

It was demonstrated for the first time that by modifying the drying conditions (drying gas and time) prior to carbonization at 475, 675, or 875°C, activated biochar samples with tailored porosity (microporous, mesoporous, or a combination of both) can be prepared. The KOH impregnated biochar was dried under air and N_2 for 0, 15, 140, and 280 h.

The surface chemistry of air-dried and N_2-dried samples was analyzed via FT-IR suggesting conversion of KOH to K_2CO_3 under air-drying particularly during prolonged drying; while, N_2-drying resulted in preservation of KOH independent of drying time. The effect of KOH to K_2CO_3 conversion as a result of drying conditions was found to have a significant effect on porosity development during carbonization at 475, 675 and 875°C. Air-dried samples carbonized at 475 and 675°C resulted in mixed micro- and mesoporous structures with a decreasing trend of surface area and micropore volume with increasing drying time. However, N_2-dried samples showed majorly microporous structure with comparable surface areas (i.e., <5% difference) at 475 and 675°C independent of drying time. These results are attributed to the conversion of KOH to K_2CO_3 in the air-dried samples and preservation of KOH under N_2 drying condition. Increasing the carbonization temperature to 875°C using either air- or N_2-dried samples resulted in significantly high surface areas 2000–2672 $m^2\ g^{-1}$ with >90% mesoporous structure. The implication of this finding is extremely important in adsorption, catalysis, electro-catalysis and electric double layer based applications requiring both high surface area and excellent mass transfer in the porous structure.

Application of activated biochar with tailored porosity was investigated for EDL applications. Biochar electrodes with majorly microporous structure showed very high total capacitance (222–245 $F\ g^{-1}$) mainly due to their high content of micropores. However, the

increased capacitance was associated with hindered accessibility of ions to the pores resulting in larger electrode resistance as supported by Ohmic drop results. Increasing the mesopore content (to 40–50% of the total pore volume) resulted in slightly reduced total capacitance (by 5%) while decreasing the total resistance of electrodes compared to the microporous electrodes. Further increasing the mesopore content of the activated biochar (>90% of the total pore volume) resulted in almost ideal capacitive behaviour with the smallest mass transfer limitation and electrode resistance as evidenced by impedance spectroscopy and galvanostatic charge/discharge studies. Total capacitance of mesoporous electrodes was in the range of 187–240 F g^{-1} depending on the drying conditions. These results confirm the effect of controlled surface area and porous structure on improvement of activated biochar as a value-added renewable material in EDL applications.

Chapter 6: Phase III - Activated biochar for capacitive deionization (CDI)[1]

6.1 Introduction

In Chapter 5, a modified KOH activation method was investigated to tailor the porous structure of activated biochar. The effect of controlled porous structure on EDL performance was further studied suggesting increased total capacitance with increasing micropore content. Moreover, the mesopore content resulted in improving the ion transport within the pores and reducing the electrode resistance. Further research toward utilizing biochar for CDI specifically focusing on the effects of controlled porosity on electrosorption performance (in a 200 mL batch-mode setup) is covered in the present chapter.

Numerous reports in the literature investigated different mesoporous carbon for NaCl CDI including modified carbon aerogels, ordered mesoporous carbon (OMCs) with polymeric substrate, carbon nano-tubes, modified activated carbon prepared from pyrolyzed polymers, and carbon nano-fiber fabricated via electro-spinning [44], [47]–[49], [220]. Despite the reported advantages for the mesoporous material, studies also suggest that some microporous material such as Carbide-derived Carbon (CDC) could outperform the mesoporous carbon [38]. An increasing trend of capacitance was reported with decreasing the pore size to values comparable to the hydrated ion size of adsorbate species due to distortion of hydrated shell of ions while entering the sub-nanometre pores [38], [45], [46], [92], [109]. These reports confirm the advantages of both micro- and mesoporous structures in removal of NaCl. However, further comparison and investigation of the combined effects of micro- and mesoporous structures in electrosorption of ions with different size is yet to progress. Studying electrode material with

[1] A version of this chapter has been published in the *Journal of Microporous and Mesoporous Materials*.

tailored porous structure in electrosorption of ions with different size could further contribute to the CDI electrode development.

In the present chapter the selected activated biochar with tailored porous structures were investigated for capacitive deionization of Na^+ and Zn^{2+} from NaCl and $ZnCl_2$ solutions. These results can directly relate to desalination as well as wastewater treatment of industrial effluents such as mining tailings. The effect of pore size on ionic accessibility of Na^+ and Zn^{2+} (with different size) leads to a better understanding of the synergic effects of micropores and mesopores on CDI performance. Moreover, these investigations could contribute to the development of activated biochar with tailored structure as a renewable carbon-based electrode for capacitive deionization.

To prepare three activated biochar samples with tailored porous structure, the method explained in Chapter 5 was employed using prolonged pre-carbonization drying time (0, 65, and 140 h) combined with carbonization temperatures (675 or 875°C). The prepared samples are referred to as: B675-ND, B675-MD-Air, and B875-LD-Air. The B675 and B875 notations are assigned to samples carbonized at 675 or 875°C, respectively; while, the ND, MD, and LD corresponds to the 0, 65, and 140 h of drying under air prior to carbonization, respectively.

6.2 Results and discussion

6.2.1 Elemental analysis and ash content

The C, H, O, and N content of activated biochar samples are presented in Table 6.1. Comparing to the as-received biochar, chemical activation resulted in increasing the carbon content and decreasing the H/C and O/C ratios due to the removal of heteroatoms from biochar matrix. Further comparison between the tailored activated biochar suggested decreasing H/C and O/C ratios with increasing activation temperature (i.e., B875-LD-Air) indicative of increased

heteroatom evaporation and consequently increased carbonization within the samples. Additionally, B675-MD-Air showed higher O/C ratio than B675-ND most probably due to oxidation of carbon as a result of prolonged exposure to KOH during drying step prior to carbonization at 675°C. Decrease in H/C ratio is a commonly used measure of the increased unsaturation degree (i.e., number of C=C bonds) of organic material [1], suggesting that B875-LD-Air sample has the highest number of C=C bonds. This observation can be confirmed by the reported graphite-like structural development of biochar as carbonization temperature is increased (see Section 2.6.2).

The ash content of the tailored biochar samples was measured separately by Exova Labs in Surrey, BC, Canada. All tailored biochar samples showed smaller ash content compared to the as received biochar.

Table 6.1 Elemental analysis (as wt.%) and ash content of activated biochar samples

Sample	C	H	N	O[1]	H/C	O/C	Ash content (%)
Biochar (as-received)	64.65	2.23	<0.3	23.03	0.034	0.36	13.6
B675-ND	84.44	0.71	<0.3	10.01	0.008	0.12	4.5
B675-MD-Air	71.33	1.84	<0.3	20.23	0.025	0.28	11.1
B875-LD-Air	89.89	0.36	<0.3	3.95	0.004	0.044	4.4

6.2.2 Surface area and porosity

As shown in Table 6.2, the porous structures of activated biochar were successfully tailored: two significantly different porous structures were obtained for B675-ND and B875-LD-Air samples, while having similar BET surface area values (<5% difference). The former sample has majorly microporous structure (i.e., 87% of total pore volume); while, the latter is predominantly

[1] Organic content

mesoporous with 72% of the total pore volume being mesopores. In order to produce combined micro- and mesoporous structures, a median-drying time under air (65 h) was employed followed by carbonization at 675°C resulting in 58 and 42% of the total pore volume being micro- and mesoporous, respectively (i.e., B675-MD-Air, Table 6.2). Pore size distribution (PSD) of the samples in the micropore region (<2 nm) was analyzed through Horvath Kawazoe (HK) method (Figure 6.1 a); while, the PSD in the mesoporous region (2-50 nm) obtained through BJH Desorption isotherms (Figure 6.1 b). Table 6.3 further details the sub-nanometre micropore distribution based on the Horvath-Kawazoe (HK) method. Figure 6.1 and 6.2 presents the N_2 adsorption isotherms at two separate ranges of relative pressures between 0.01 and 0.99 and 4×10^{-7} and 0.06, respectively. Based on the obtained isotherms, the Barret-Joyner-Halenda (BJH) and HK methods were used to characterize the meso- and micropore distributions, respectively (Tables 6.2 and 6.3). The B675-ND sample showed a Type I isotherm according to IUPAC classification, confirming its microporous structure (Figure 6.1 a). The isotherms for B675-MD-Air and B875-LD-Air exhibited a hysteresis effect (Type H4) indicative of the presence of both meso- and microporosity [213]. The desorption part of N_2 isotherms (Figure 6.2 a) has been used for BJH mesopore distribution analysis similar to the other studies presented in the literature for comparable materials [107], [221]–[225]. The BJH method is based on the modified Kelvin equation and is one of the commonly used methods to analyze the pore size distribution (PSD) specifically in the mesopore region [213], [214], [226], [227]. Additionally, N_2 adsorption data were obtained at low relative pressure (4×10^{-7} to 0.05) and analyzed by the HK method, i.e., an accurate method specifically analyzing the micropore distribution [214], [215], [228], [229] (Figure 6.2 a).

Table 6.2 Surface area and porosity of activated biochar samples with tailored structure

Sample	BET surface area ($m^2 g^{-1}$)	BJH mesopore volume ($cm^3 g^{-1}$)	HK total micropore volume ($cm^3 g^{-1}$)	Total pore volume[1] ($cm^3 g^{-1}$)	Average pore width (nm)
B675-ND	1600	0.09	0.64	0.73	1.91
B675-MD-Air	971	0.28	0.42	0.70	2.60
B875-LD-Air	1674	0.94	0.63	1.57	2.97

[1] Total pore volume calculated as the sum of BJH mesopore volume and HK micropore volume.

Table 6.3 Cumulative pore volume at sub-nanometre pore widths measured by the Horvath-Kawazoe (HK) method

Electrodes	Pore volume between 0.2 and 0.72 nm ($cm^3 g^{-1}$)	Pore volume between 0.72 and 0.86 nm ($cm^3 g^{-1}$)
B675-ND	0.34	0.12
B675-MD-Air	0.28	0.06
B875-LD-Air	0.33	0.14

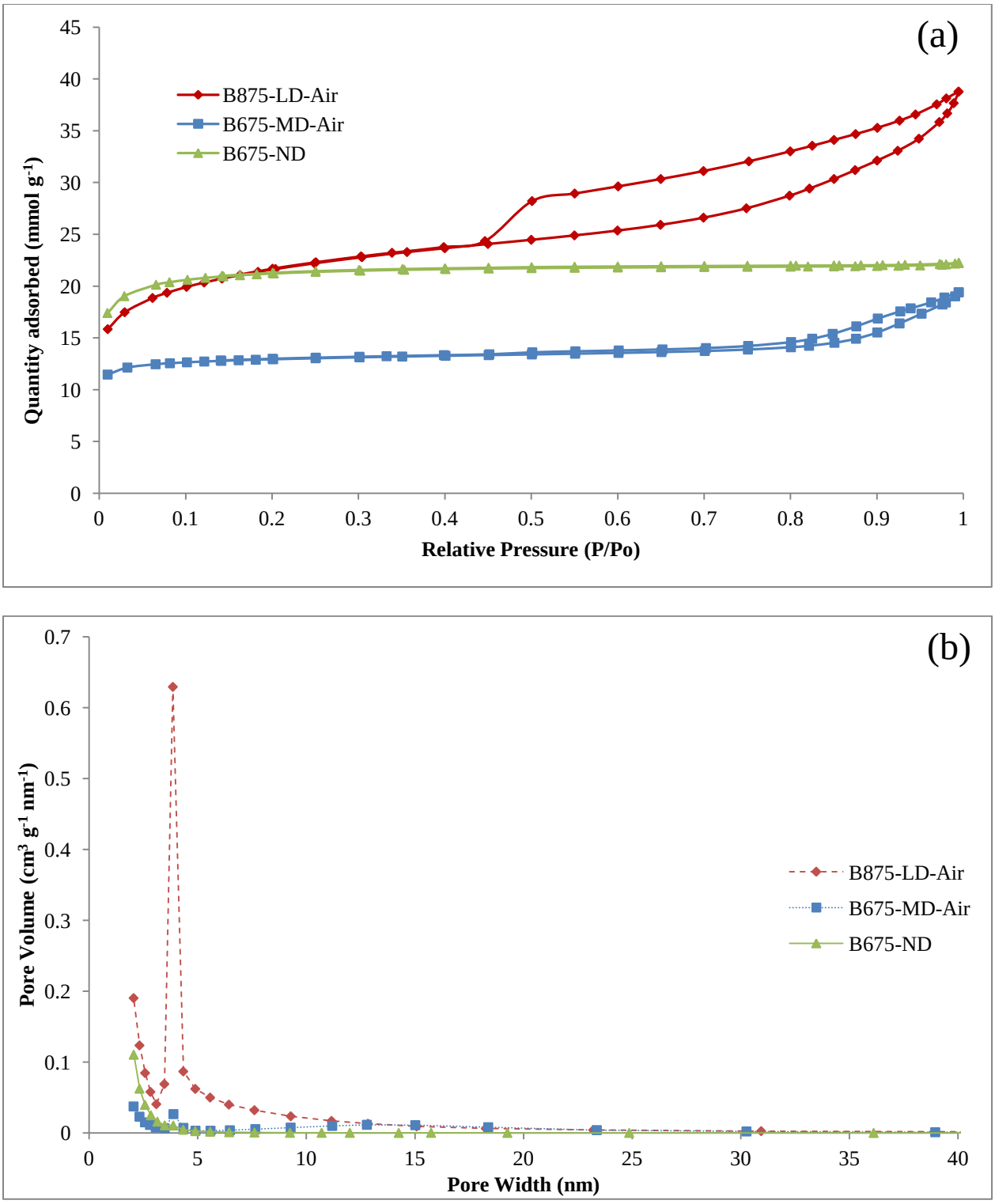

Figure 6.1 N_2 isotherms and pore size distribution: (a) adsorption/desorption isotherms at relative pressure between 0.01 and 0.99; and, (b) mesopore distribution calculated by BJH method.

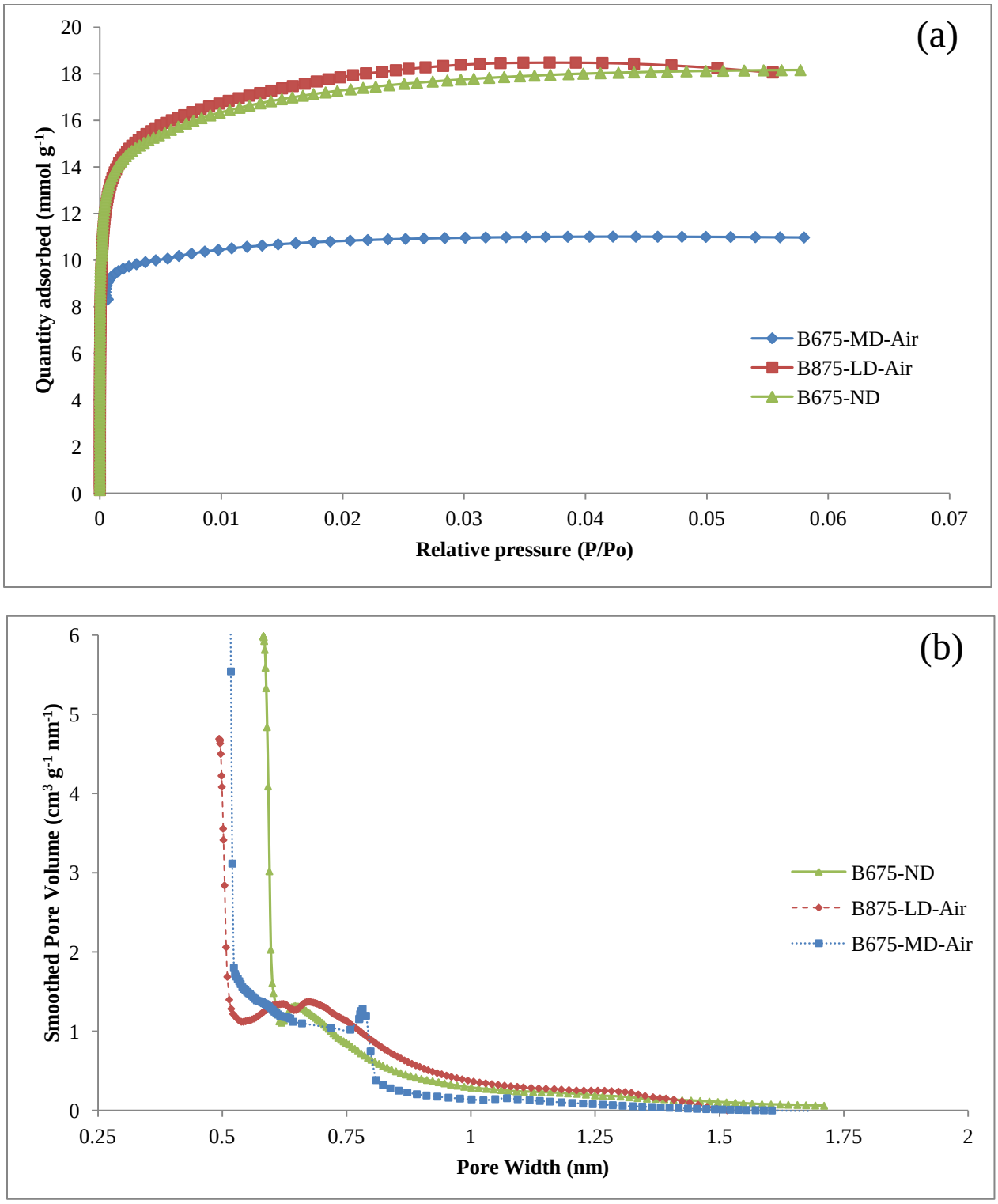

Figure 6.2 (a) N_2 adsorption isotherms at relative pressure between 4×10^{-7} and 0.06; (b) micropore distribution calculated by HK method.

Figure 6.3 shows the schematic representation of the micro- and mesopore volume as a percentage of total pore volume of the tailored activated biochar. The average micropore width of all samples was between 0.62 and 0.78 nm as measured by HK method (Figure 6.2 b). The microporous B675-ND sample showed a narrow PSD with a single peak at 0.65 nm (Figure 6.2 b); while, the B675-MD-Air sample showed two peaks at 0.78 and 3.8 nm in both micro- and mesopore regions as shown in Figures 6.2 b and 6.1 b, respectively. An interesting PSD was obtained for B875-LD-Air sample with majorly mesoporous structure, where two peaks around 0.62 and 0.67 nm in the sub-nanometre region were observed (Figure 6.2 b) as well as a distinctive sharp peak at 3.8 nm in the mesopore region (Figure 6.1 b). These results suggest bi-modal porous structure for B675-MD-Air and B875-LD-Air, whereas the B675-ND sample showed a uni-modal microporous structure.

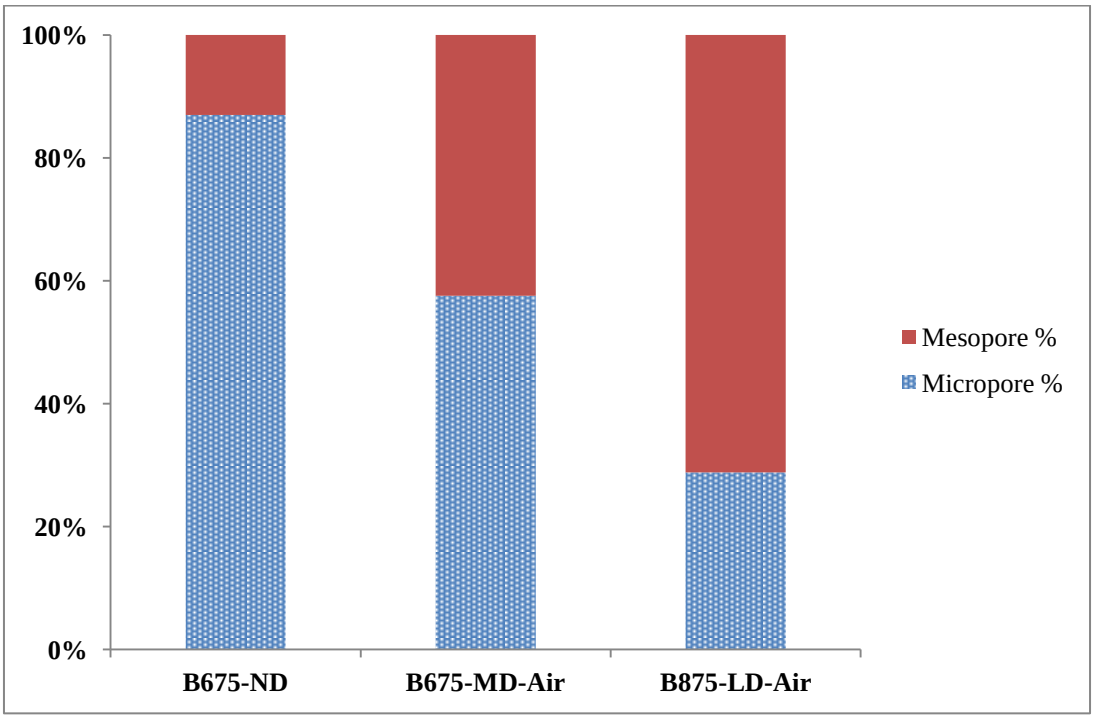

Figure 6.3 Schematic representation of the micro- and mesopore volume as a percentage of total pore volume.

6.2.3 Morphology and structural analysis

The morphology and structure of the tailored biochar samples were studied by field emission scanning electron microscopy (FESEM) and transmission electron microscopy (TEM). The B675-ND sample showed layered-structure with smooth surface where small layers agglomerated on larger layers (Figure 6.4 a). Similarly, FESEM images of B675-MD-Air demonstrated layered morphology; however, the layers showed roughness on some parts unlike B675-ND sample (Figures 6.4 a and b). The B875-LD-Air sample showed significantly porous layers probably due to the partial gasification of carbon layers in the presence of CO_2 from decomposition of K_2CO_3 during chemical activation at 875°C, as reported by Hayashi et al. [198], and also in Section 5.2.2. The FESEM images of B675-MD-Air confirmed a transitional morphology between the smooth layered B675-ND and the porous structure of B875-LD-Air (Figure 6.4 c).

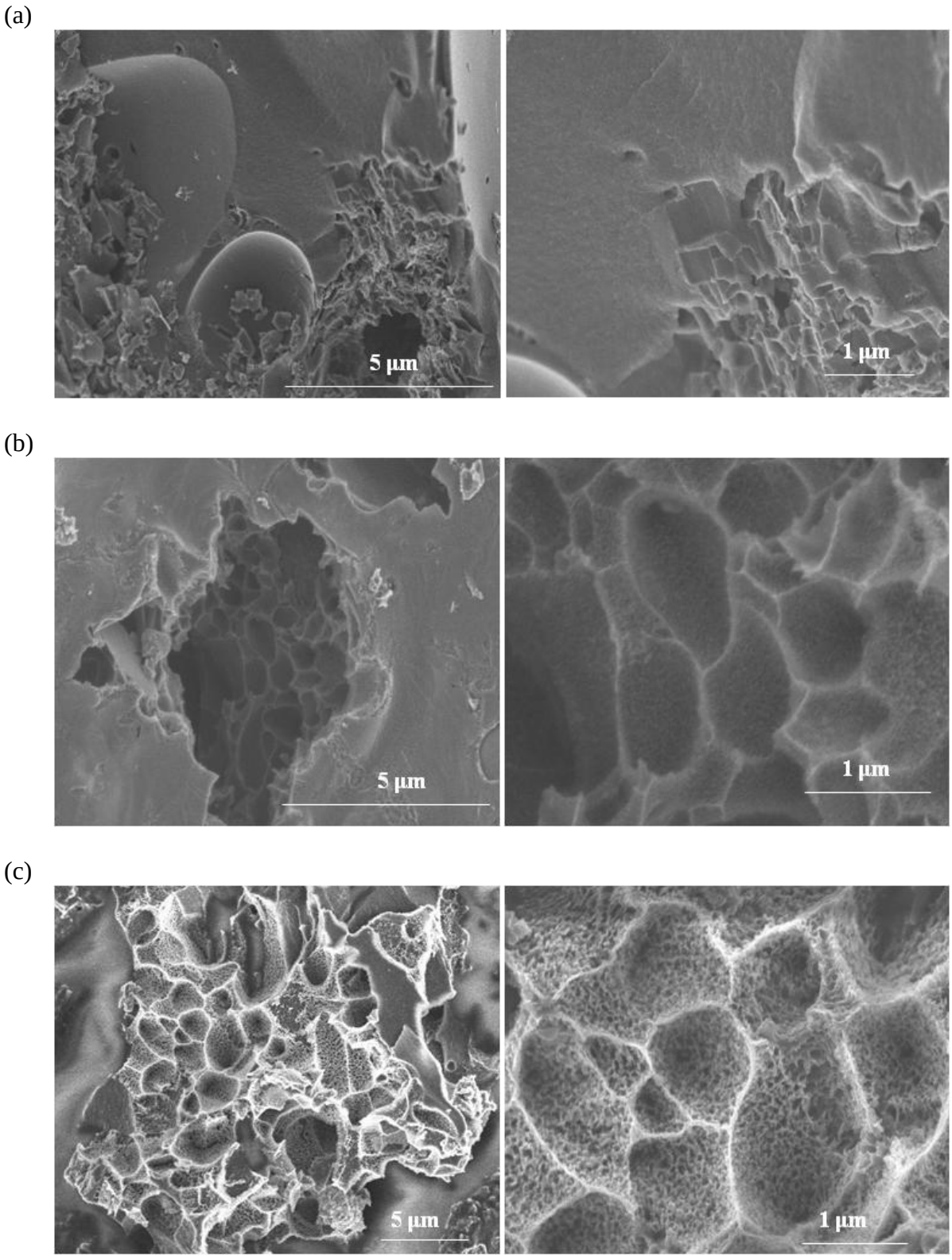

Figure 6.4 FESEM images of: (a) B675-ND; (b) B675-MD-Air; (c) B875-LD-Air.

To investigate the structure of the prepared samples, TEM analysis was performed (Figure 6.5). B675-ND sample showed typical amorphous carbon structure with smooth layers; while, the B675-MD-Air sample showed similar smooth planar structure to B675-ND in addition to the disordered structure consisting of small flakes at some regions (Figure 6.5). The TEM images of B875-LD-Air demonstrated two different features comparrd with B675-ND and B675-MD-Air: thin layers and tube-like structure at the edges of the layers. The tubular structure of B875-LD-Air might be due to the folding of thin layers as a result of potassium intercalation at 875°C [202], [210], [230]. This type of structure could be responsible for the significantly large mesopore volume of B875-LD-Air. Quite similar TEM results were reported for folded graphene samples [231]: the wrinkles at the edges of carbon layers (similar to Figure 6.5) as well as tubular structure.

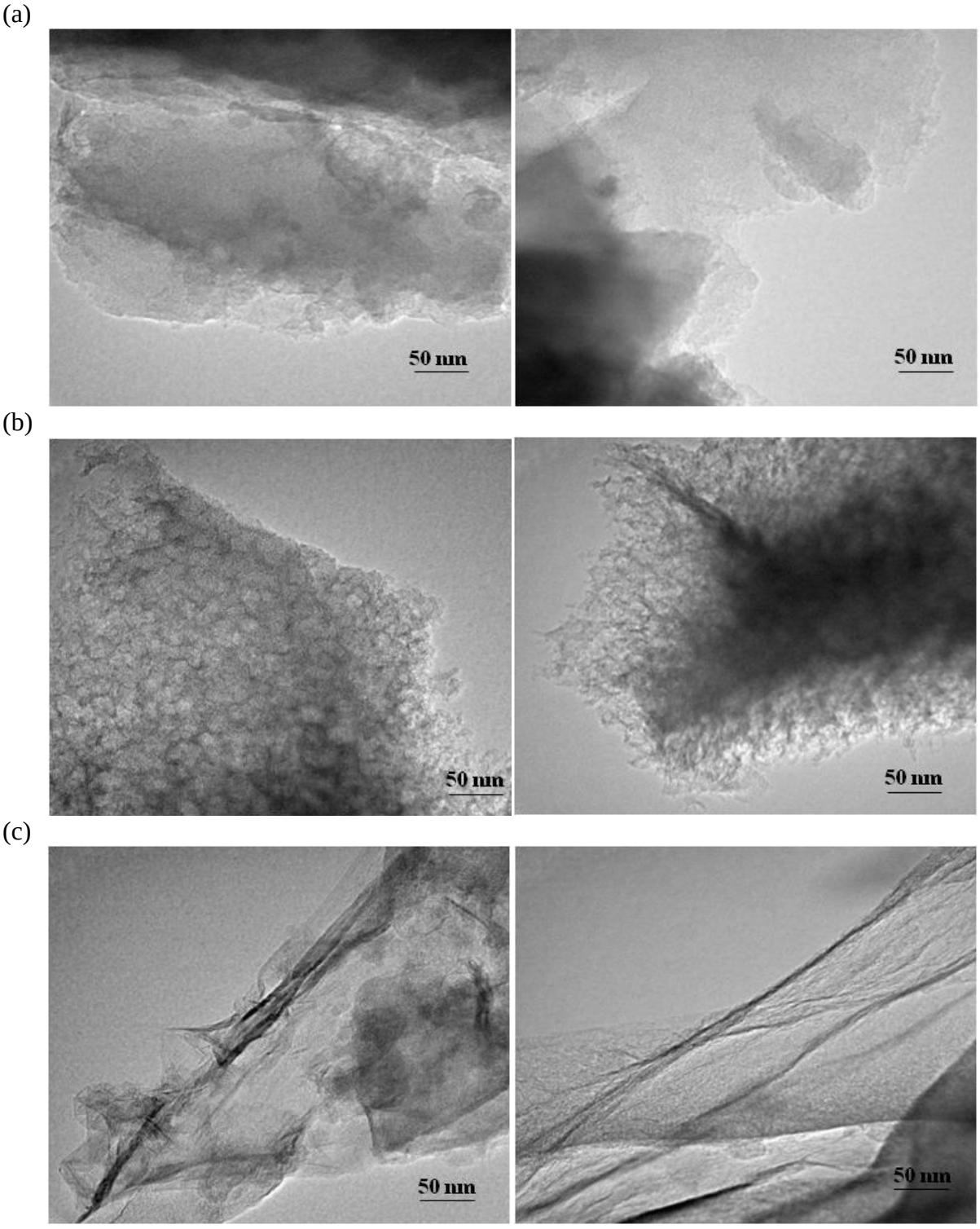

Figure 6.5 TEM images of: (a) B675-ND; (b) B675-MD-Air; (c) B875-LD-Air.

To further study the structure of tailored biochar samples, Raman spectroscopy was conducted. Raman spectroscopy is one of the major characterization methods in studying the

development of structural order in carbon material. From Figure 6.6, the most important features in Raman spectra of carbon material are G and D bands at around the 1580 and 1360 cm^{-1} region. The graphitic G peak (assigned to E_{2g} vibrational modes) is attributed to the bond stretching of all sp^2 atoms in chains and rings; while, the D peak corresponded to the breathing mode of sp^2 atoms in rings characteristic of disorder and defect within the carbon matrix [232], [233]. The presence of D peak in Raman spectra could also be indicative of nano-crystalline graphite structure as opposed to a perfect graphitic structure [232]. The ratio of D/G peak intensity has been extensively used in studying the structural development from amorphous to ordered graphite-like in carbon material [234]. Decreasing the D/G ratio is characteristic of developing more graphite-like order in carbon structure (increased sp^2 domain). The D/G peak intensity ratio of B675-ND, B675-MD-Air and B875-LD-Air was 1.28, 1.20 and 1.00, respectively. The B675-ND and B675-MD-Air samples showed comparable D/G peak ratio; however, the B875-LD-Air sample carbonized at 875°C showed the lowest D/G ratio (i.e., highest ordered structure). This could be attributed to the removal of heteroatoms from biochar matrix and attachment of small carbon sheets to form larger ones (i.e., more graphite-like structure within nano-crystalline matrix) at >800°C as reported in the literature [1], [174], [175]. This further ordering between the carbon sheets is also confirmed by the presence of a distinctive peak at around 2639 cm^{-1} (i.e., second order 2D peak) in B875-LD-Air Raman spectra. According to Ferrari et al., the presence of 2D peak is a characteristic of structural transformation from amorphous to graphitic [232]. Additionally, the position and sharpness of the 2D peak indicates a number of graphitic layers: sharper peaks with downshift from 2700 to 2630 cm^{-1} are attributed to large carbon sheets with similar structure to graphene. The B875-LD-Air Raman spectrum also showed strong features around G peak resulting in shoulders at 1583

and 1596 cm^{-1} assigned to the curvature of thin carbon layers and fingerprint of carbon nanotubes structure [235], [236]. The Raman features of B875-LD-Air sample including shoulder peaks at 1583 and 1596 cm^{-1} in addition to the sharp 2D peak at 2639 cm^{-1} suggest ordered large carbon sheets with curvature at some edge area (similar to the tubular structure of nanotubes) most probably contributing to the large mesopore volume of the sample. These results further confirm the TEM images of B875-LD-Air sample showing large thin layers of carbon with curvature at some edges imitating the tubular structure (Figure 6.5).

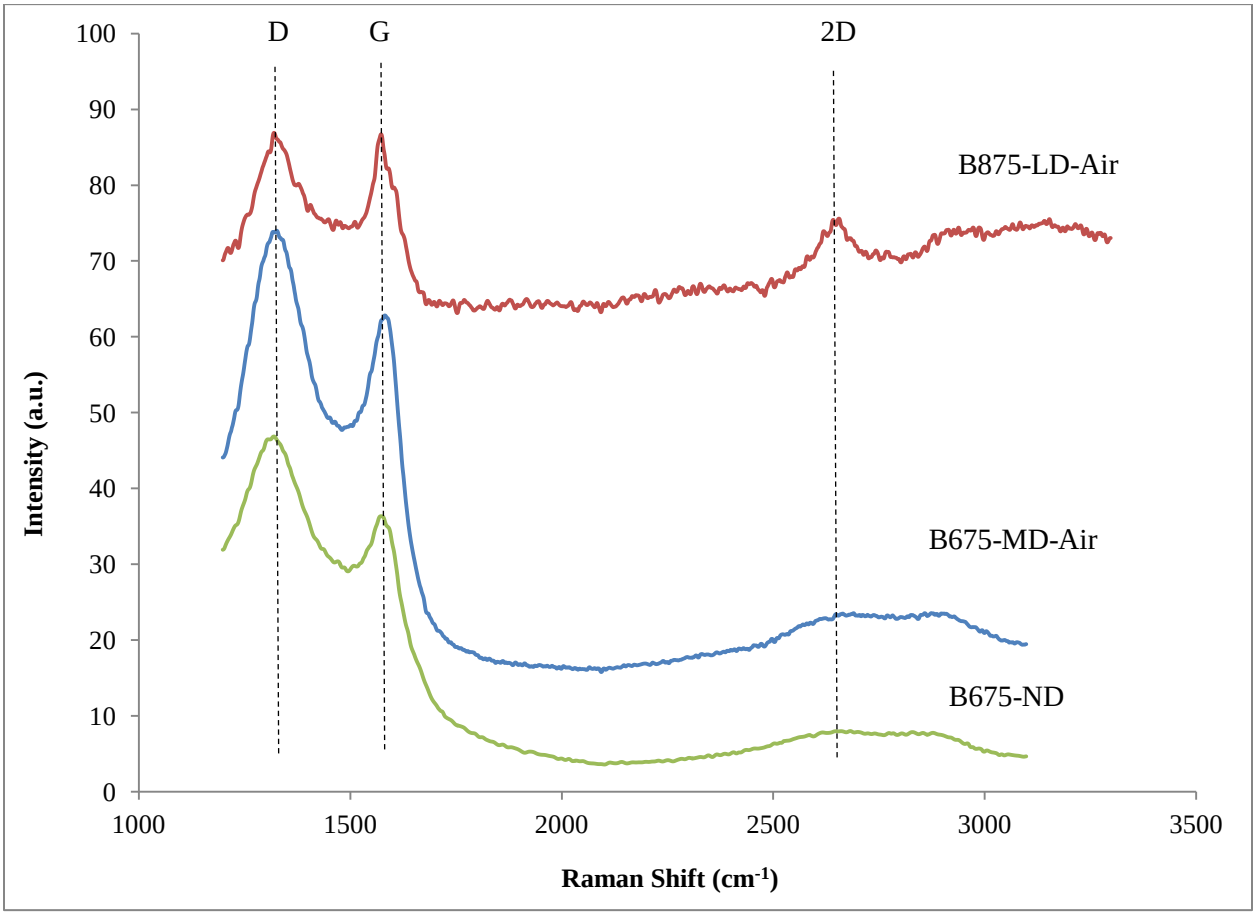

Figure 6.6 Raman spectra of tailored biochar samples.

6.2.4 FT-IR analysis[1]

The surface chemical groups of tailored biochar samples were studied by FT-IR spectroscopy (Figure 6.7). An IR band around 900 cm^{-1} (i.e., peak 2) corresponded to the out-of-plane bending of ring C-H bonds of aromatic and heteroatomic compounds observed clearly in B675-ND and broadly in B675-MD-Air spectra. The B675-ND demonstrated a distinctive peak at 1050 cm^{-1} assigned to C-O stretch in either carboxylic acid or ethers (i.e., peak 3) [53], [177], [190]. Moreover, B675-ND and B675-MD-Air samples showed peaks at 1600 cm^{-1} characteristic of quinone groups (i.e., peak 4) [177]. These results suggested the presence of oxygen-containing groups in B675-ND and B675-MD-Air as also evidenced by Elemental Analysis (see Table 6.1). By contrast, peaks corresponding to the oxygen-containing functional groups (i.e., quinone and ethers: peaks 4 and 3, respectively) were clearly absent in the B875-LD-Air spectrum. This could be due to the higher heteroatom removal at 875°C as also evidenced by the Elemental Analysis summarized in Table 6.1. However, B875-LD-Air showed a broad peak around 840 cm^{-1} (i.e., peak 1) assigned to the cyclic compounds with conjugated C=C which is expected for the ordered graphite-like structure of B875-LD-Air confirmed by Raman and Elemental analyses [191]. Weak peaks at around 2950 cm^{-1} in B675-ND and B675-MD-Air (i.e., peak 5) could be attributed to the aliphatic C-H stretching which is clearly absent in B875-LD-Air.

[1] Surface functional group analysis of the tailored samples was investigated by FT-IR spectroscopy using a Nicolet 4700 spectrometer. An aperture setting of 4 cm^{-1} with a wave number range of 3500-650 cm^{-1} and scan speed of 2.5 kHz was employed for spectra collection with 64 scans collected for each sample to improve the signal-to-noise ratio. Samples were diluted in dried KBr for FTIR spectroscopy.

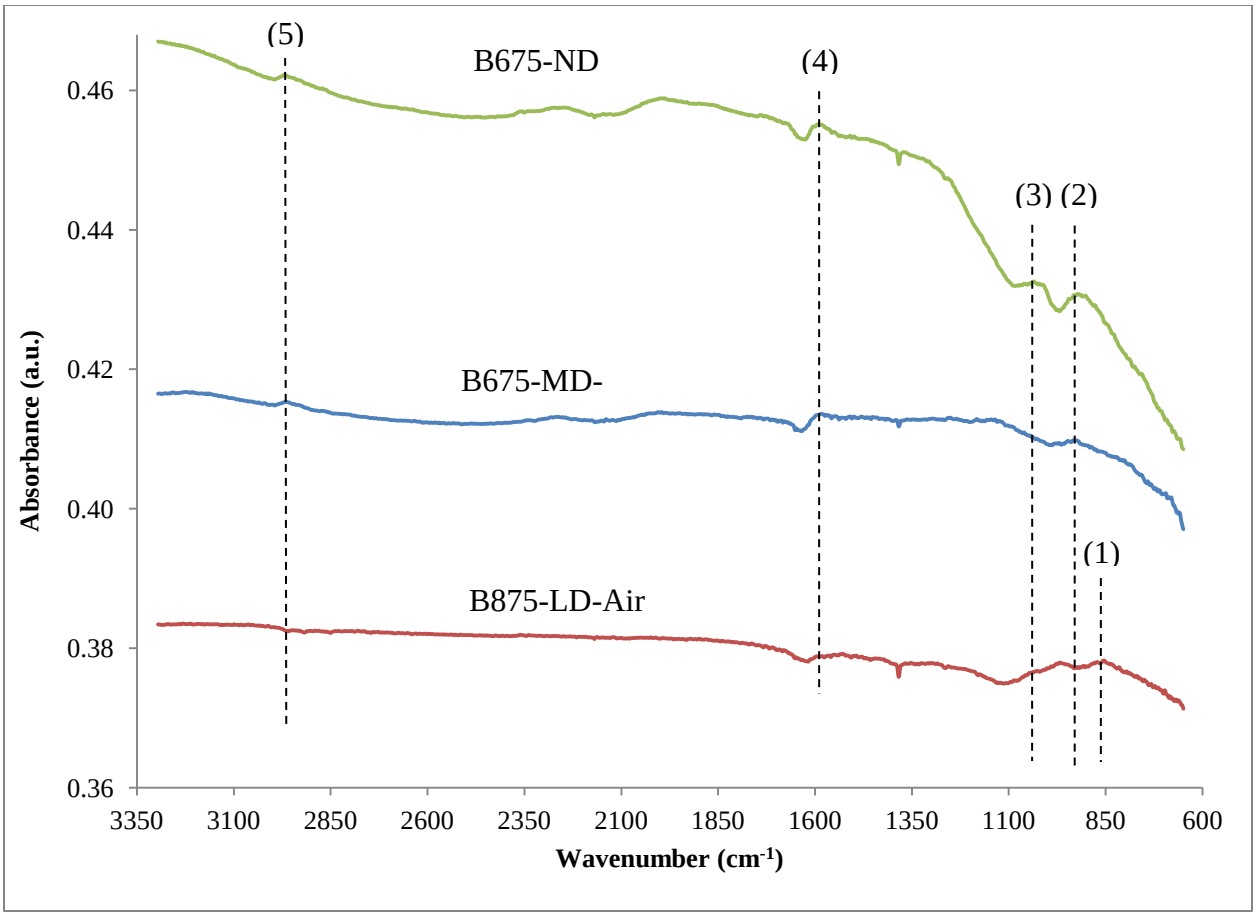

Figure 6.7 FT-IR spectra of tailored activated biochar samples.

6.2.5 Electric double layer (EDL) behaviour of tailored activated biochar electrodes

The EDL performance of tailored activated biochar samples was investigated by cyclic voltammetry (CV) and galvanostatic charge/discharge (GCD) tests in 0.1 mol L^{-1} NaCl – 0.1 mol L^{-1} NaOH electrolyte. Electrodes were made from activated biochar samples with tailored porous structure (10–50 µm mesh size) manually sprayed on carbon cloth as current collector (30 mm × 30 mm) with 10 wt.% of Nafion® as binder. Two sets of electrodes were made from each tailored activated biochar sample to be employed in preliminary electric double layer analysis (e.g., cyclic voltammetry and galvanostatic charge/discharge analyses) and capacitive deionization investigations (Section 6.2.6).

It is commonly known that an ideal EDL material shows a rectangular shaped CV voltammogram. Figures 6.8 and 6.9 represent the CV voltammograms of activated biochar samples at different scanning rates. At the fastest scanning rate (i.e., 50 mV s^{-1}) all three samples showed significantly deformed voltammograms compared to the rectangular shape, similar to the results obtained in Section 5.2.3, Figures 5.8 and 5.9[1]. This can be attributed to the hampered ionic accessibility into the micropores during the shortest time of analysis [107], [192]. Decreasing the scanning rate to 20 and 5 mV s^{-1} resulted in shape change of voltammograms with the highest transformation observed for the majorly mesoporous sample (i.e., B875-LD-Air) showing more rectangular-shaped voltammogram compared to the other samples. This is expected as larger pores facilitate the ion transport into the porous structure of electrode material. However, the sample with the highest micropore percentage [2] (i.e., B675-ND) showed considerable distortion from rectangular shape even at slow scanning rate of 5 mV s^{-1} further confirming the negative effect of micropore structure on EDL behaviour at fast scanning rates due to ionic accessibility limitation. Nonetheless, at slow scanning rates (i.e., 0.5–2 mV s^{-1}), all samples showed almost perfect rectangular shaped voltammogram with comparable produced current per mass of active material (Figure 6.9).

Beyond the typical EDL domain, voltammograms of the activated biochar samples showed also features associated with faradaic reactions such as dissolved oxygen reduction (e.g., catalyzed by the quinone-type surface functional groups) generating the small peaks around –0.25 and –0.3 V at 1 mV s^{-1}, hydrogen and oxygen evolution reactions at negative and positive potentials, respectively (Figure 6.9). Generally, the highest faradaic currents are obtained with the samples that contain a significant fraction of mesopores (B875-Air, B675-MD) due to better

[1] The voltammograms are not IR-Corrected.
[2] Percentage of micropore volume out of total pore volume.

electrolyte accessibility. This is yet another indication of porous structural differences among the samples.

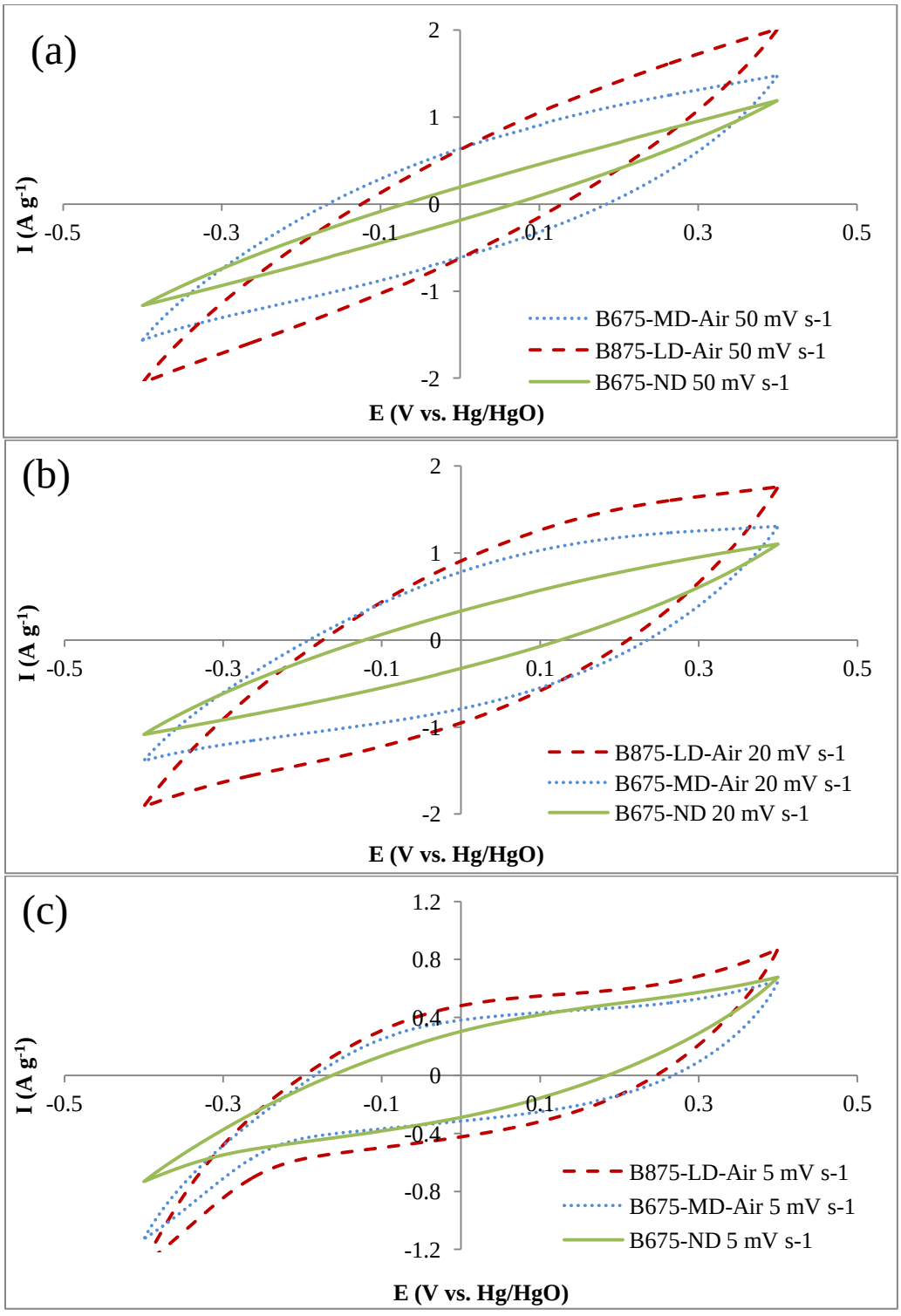

Figure 6.8 CV diagrams of tailored biochar electrodes at fast scanning rates: (a) 50 mV s^{-1}; (b) 20 mV s^{-1}; and (c) 5 mV s^{-1} in 0.1 mol L^{-1} NaCl/0.1 mol L^{-1} NaOH.

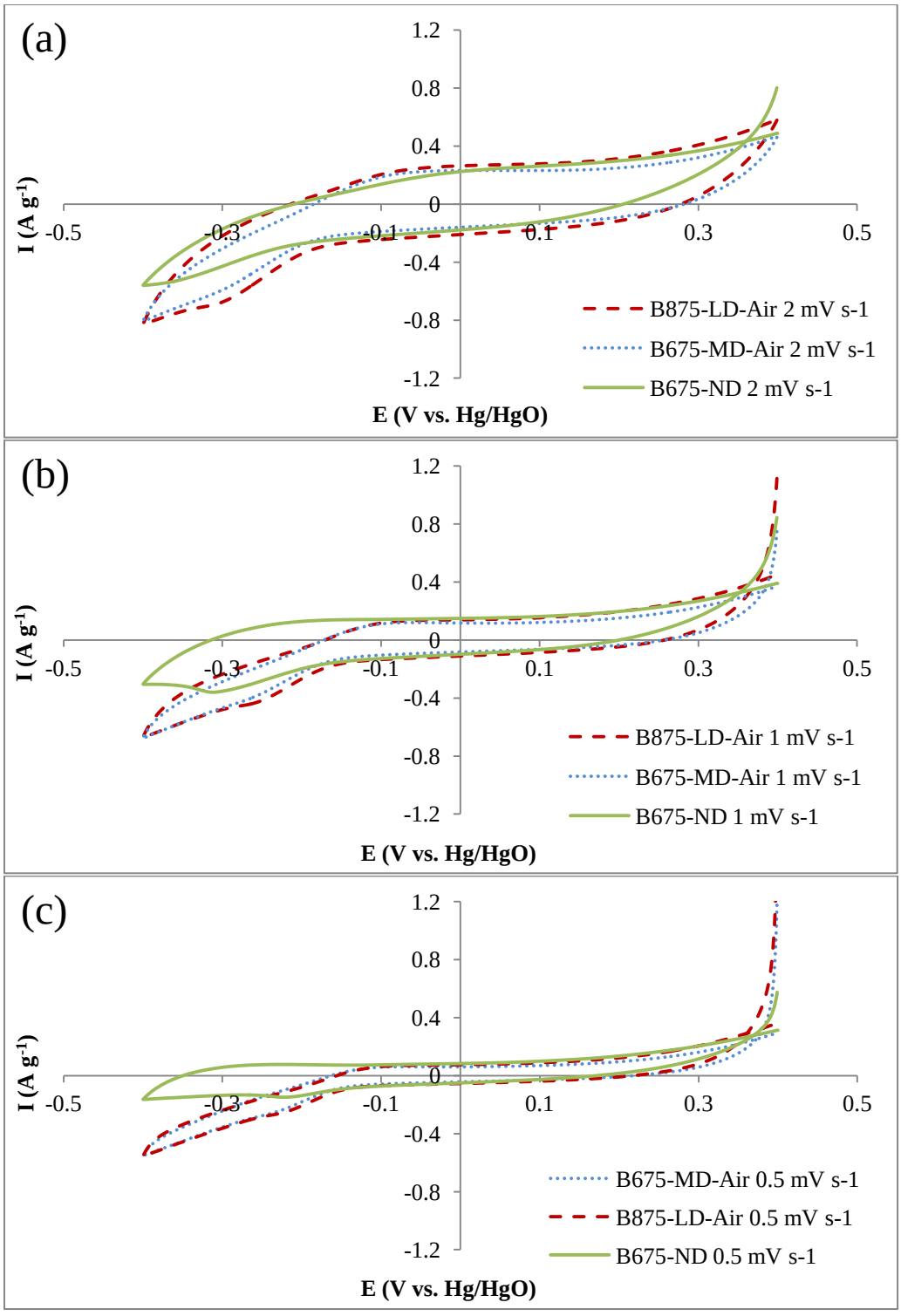

Figure 6.9 CV diagrams of tailored biochar electrodes at slow scanning rates: (a) 2 mV s^{-1}; (b) 1 mV s^{-1}; and (c) 0.5 mV s^{-1} in 0.1 mol L^{-1} NaCl/0.1 mol L^{-1} NaOH.

The total capacitance of the electrodes was quantified from anodic and cathodic current differences at 0.5, 1 and 2 mV s^{-1} sweep rates (Table 6.4). B675-ND showed slightly higher total capacitance than B675-MD-Air possibly due to the larger micropore volume with narrow distribution around 0.62 nm, which is reported to be favourable for electrosorption of hydrated ions such as Na^+ and Cl^- [38], [193]. Moreover, B875-LD-Air electrode showed the highest total capacitance despite of having almost similar surface area (<5% difference) suggesting the significance of mesoporous structure on EDL behaviour and capacitance.

Galvanostatic charge discharge (GCD) analysis was also conducted to further investigate the EDL performance of activated biochar samples with tailored porous structure (Figure 6.10). All tailored biochar samples showed triangular-shaped GCD diagrams, i.e., indicative of ideal EDL behaviour. The total electrode resistances (i.e., IR-Drop) as well as the ex situ electrical conductivity of powder samples are shown in Table 6.4. The B875-LD-Air sample showed significantly lower electrode resistance compared to B675-MD-Air and B675-ND. This could be due to two important features of B875-LD-Air electrode: (a) the highest electrical conductivity as a result of higher degree of graphitization (evidenced by Raman, FT-IR, and Elemental Analysis) and (b) the large content of mesopores and consequently improved ionic accessibility into the pores. The B675-MD-Air electrode showed the second lowest resistance most probably because of its considerably larger mesopore content than B675-ND despite of the slightly lower electrical conductivity (see Table 6.4). To further compare the powder electrical conductivities of tailored biochar samples, the electrical conductivity of Vulcan XC-72 was also measured and shown in Table 6.4. The B875-LD-Air sample had the same order of magnitude electrical conductivity as Vulcan XC-72 (i.e., 2.1 vs. 5.8 S cm^{-1} g^{-1}); whereas the B675-ND and B675-MD-Air, had an order of magnitude lower conductivities.

Table 6.4 Total capacitance (calculated from Figure 6.5 CVs), Ohmic (or IR) potential drop (calculated from Figure 6.6 GCD results) and powder electrical conductivity of tailored biochar electrodes.

Electrode	Total Capacitance ($F\ g^{-1}$)	IR-Drop ($V\ g^{-1}$)	Electrical Conductivity ($S\ cm^{-1}\ g^{-1}$)
B675-ND	213	1.65	0.43
B675-MD-Air	197	0.61	0.32
B875-LD-Air	240	0.35	2.1
Vulcan XC-72	—	—	5.8

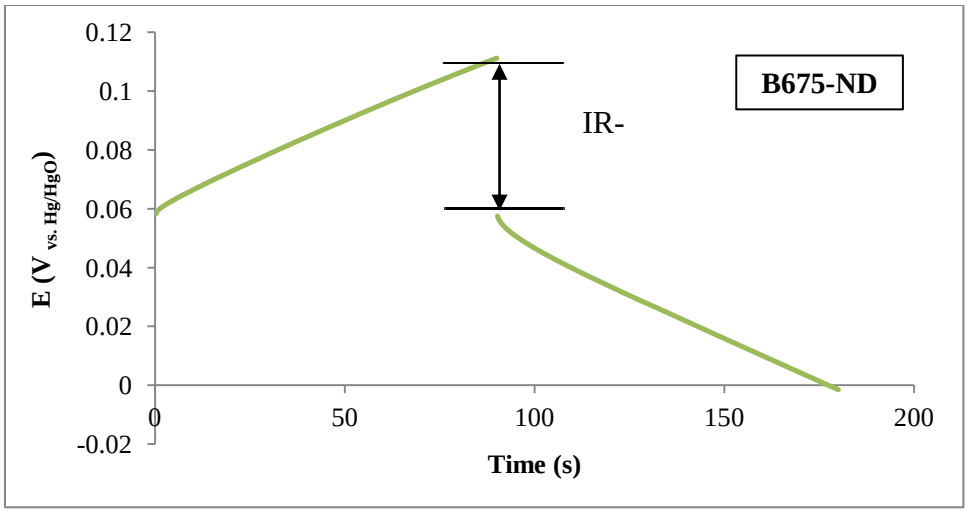

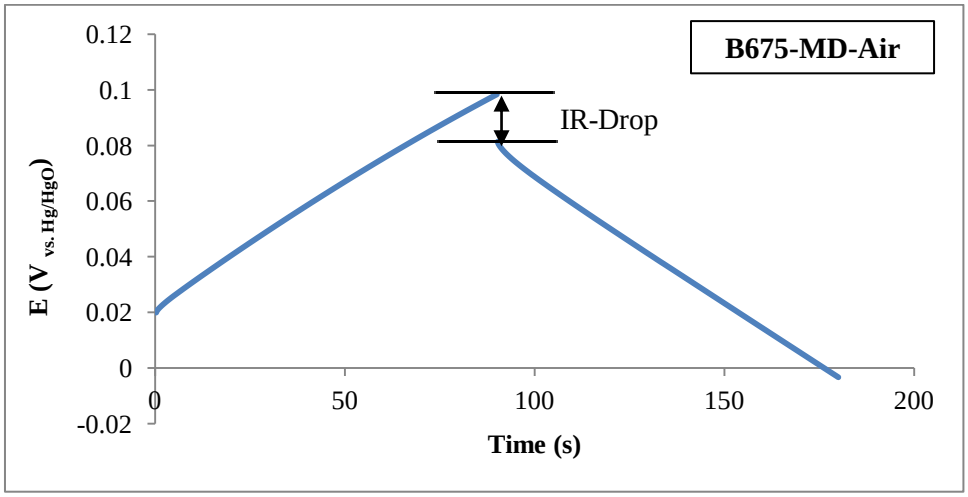

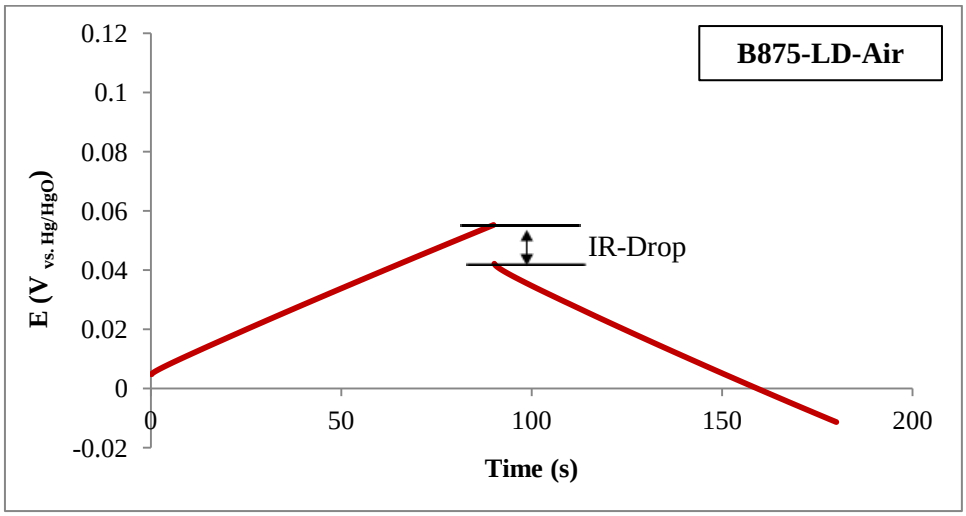

Figure 6.10 GCD plots of tailored biochar electrodes in 0.1 mol L^{-1} NaCl/0.1 mol L^{-1} NaOH.

6.2.6 Capacitive deionization

One of the primary general characteristics of an electrode material for capacitive deionization (CDI) is high surface area and pore volume. However, having a high surface area does not necessarily translate linearly in large removal capacitance due to EDL-overlap in micropores; hence, only a lower percentage of the total surface area is available for electrosorption [27], [34]. Nonetheless, studies also reported anomalous increase of electrosorption capacitance when pore width becomes comparable to the hydrated ion size of adsorbate species (i.e., <1 nm) [45], [46], [109], [237]. This unexpected behaviour was explained by the distortion of the hydrated shell of ions while entering into sub-nanometre pores as a result of applied potential [46], [237]. According to Porada et al., there is no direct correlation between either surface area or total pore volume of electrode material with electrosorption capacitance of NaCl; however, desalination is positively correlated with the volume of sub-nanometre pores [238]. Their report is in contrast to the commonly held view about the effect of micropores on EDL-overlap and electrosorption capacitance.

To further study the effect of tailored porous structure on electrosorption of ions with different size and charge (i.e., resulting in different hydration of ions), the activated biochar samples with controlled porous structure were investigated for electrosorption of Na^+ and Zn^{2+} from corresponding NaCl and $ZnCl_2$ solutions, respectively. Additionally, electrosorption of Zn^{2+} ions could be of interest to industries with wastewater effluents consisting of heavy and transitional metal ions (e.g., mining); while, deionization of NaCl could be related to desalination of brackish water.

Another important factor to consider in CDI of Na^+ and Zn^{2+} is the motion of ions in the solution which can be described as ionic mobility. The mobility of an ion under an electric field can be defined as the velocity per unit electric field, Equation (6.1):

$$u_i = {|v_i|}/{|E|} \tag{6.1}$$

where, u_i, v_i, and E are ionic mobility, ion velocity and electric field, respectively. Ionic mobility can be related to molar conductivity (i.e., conductivity of an electrolyte divided by its molar concentration) by Equation (6.2):

$$u_i = \frac{\Lambda_i}{F.|Z_i|} \tag{6.2}$$

At infinite dilution, the molar conductivities (Λ_i^o) of different ions are reported [65]. Thus, the ionic mobility for Na^+ and Zn^{2+} can be calculated using Equation (6.2) at infinite dilution (u_i^o). The measured ionic mobilities suggested comparable values (5.47×10^{-4} vs. 5.19×10^{-4} m^2 V^{-1} s^{-1}) for both ions despite different charge and size.

6.2.6.1 Capacitive deionization of NaCl

The tailored activated biochar electrodes were first investigated for capacitive deionization (CDI) of 10 mmol L^{-1} NaCl[1]. According to the literature, concentration of the testing solution can affect the electrosorption capacity in the batch-mode CDI experiments [38]. Solutions with lower starting salinity (i.e., below 5 mmol L^{-1}) showed smaller electrosorption capacities most probably due to further decrease of ion concentration during adsorption process and consequently higher solution resistance (i.e., lower ionic conductivity). Porada et al. reported a dependence of adsorbed amount of salt as a function of electrolyte concentration [38].

[1] Prior to the CDI experiments, the electrodes were studied at no applied current condition to ensure that there was no NaCl removal in the absence of induced electrical charge.

Biochar electrodes were charged at constant current condition (i.e., 0.22 mA cm^{-2}) followed by two step regeneration in 1 mmol L^{-1} NaCl (6800 s) and deionized water (17 h), both at zero applied current (charge – discharge diagrams are shown in Appendix G). All activated biochar electrodes with tailored porosity showed promising Na^+ removal capacities and durability after four cycles as shown in Figure 6.11. The electrodes with higher mesoporous content (i.e., B675-MD-Air and B875-LD-Air) showed a slight decrease in removal capacity after the first cycle followed by nearly constant values in cycles nr. 2 to 4. The B675-ND with predominantly microporous structure showed slightly smaller removal capacity than B675-MD-Air and B875-LD-Air in cycle 1; however, in cycles 2 to 4 all electrodes demonstrated comparable capacities. Our results suggest no specific correlation between the surface area or pore volume distribution (micro or meso) and Na^+ removal capacity.

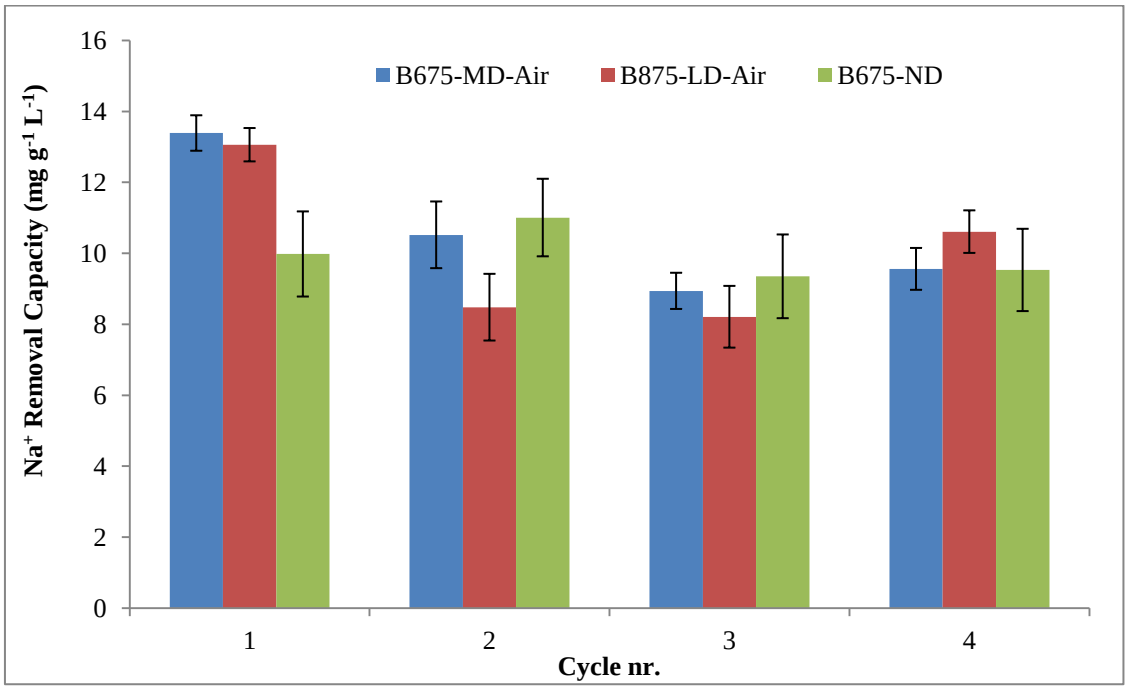

Figure 6.11 Capacitive deionization of Na^+ using activated biochar electrodes with tailored porous structure.

To evaluate the impact of sub-nanometre pore distribution (Table 6.3) we considered the proposal by Chmiola et al. reporting increased electrosorption capacity with decreasing the size

of pores from those that are comparable to the hydrated ion down to crystallographic ionic size [46]. The hydrated, Stokes and crystallographic diameter of Na^+ are: 0.66 – 0.72 nm, 0.37 nm and 0.19 nm, respectively [239]. Table 6.3 shows that the sub-nanometre pore volumes in the 0.2 to 0.72 nm range (i.e., in the range relevant to Na^+) are fairly similar for all the samples (about 0.3 $cm^3\ g^{-1}$), which could explain the comparable deionization results reported in Figure 6.11.

These results could be indicative of the sub-nanometre pore volume contribution of activated biochar (at pore width comparable to the hydrated size of Na^+ ion) to deionization capacity, similar to the behaviour reported recently in the literature [45], [46], [237].

6.2.6.2 Electrosorption of Zn^{2+}

To further investigate the effect of tailored porous structure on electrosorption of activated biochar electrodes, removal of Zn^{2+} ions with larger hydrated and Stokes diameters than Na^+ (0.86 and 0.70 nm, respectively) was also studied. Removal of zinc from wastewater streams is crucial due to its high degree of toxicity and carcinogenicity. Zinc is listed as one of the priority toxic pollutants by the National Recommended Water Quality Criteria and is also on the Priority List of Hazardous Substances of Comprehensive Environmental Response, Compensation, and Liability Act [166], [167]. The electrosorption of Zn^{2+} was conducted under identical constant current condition to Na^+ removal as presented in Section 3.3.6. Electrosorption has been performed for four consecutive cycles with electrodes being regenerated between the cycles. Zinc removal capacities are presented in Figure 6.12.

The tailored biochar electrodes showed significantly different behaviour for Zn^{2+} removal (Figure 6.12), unlike in the case of Na^+ removal. The most significant difference was the reduction of B675-ND electrosorption capacity from cycle nr. 1 to 4, leading to a ~75% capacity drop. The electrode with mostly mesoporous structure (i.e., B875-LD-Air, Table 6.2) showed the

best Zn^{2+} electrosorption performance in terms of capacity in conjunction with durability (Figure 6.12).

The difference between the electrosorption capacity of B875-LD-Air and B675-MD-Air could be explained by the more than two times higher cumulative pore volume between 0.72 and 0.86 nm of the former (Table 6.3). The B675-ND electrode also showed higher pore volume between 0.72 and 0.86 nm than B675-MD-Air that might be responsible for the significantly higher removal capacity in the first cycle. However, the removal capacity of B675-ND electrode dropped significantly during cycles nr. 2 to 4. Thus, the B675-ND electrode exhibited a regeneration problem in case of Zn^{2+} removal (Figure 6.12). The high microporous and sub-nanometre pore volume of B675-ND has a major beneficial impact only on the first or maximum two adsorption cycles. These results are not consistent with the Na^{+} deionization results (Figure 6.11), where the mostly microporous samples demonstrated more significant contribution to the electrosorption capacity throughout the four cycles.

This contrary behaviour could be explained by considering the effect of mesoporous network for facilitating the Zn^{2+} transport in and out of the pores. The electrode with the majorly mesoporous network (i.e., B875-LD-Air) showed the best Zn^{2+} electrosorption performance in terms of capacity in conjunction with durability. For ions with large hydrated radius (e.g., Zn^{2+}) mesopores provide more favourable pathways for ion access during charging and regeneration.

The Zn^{2+} electrosorption behaviour of B675-ND electrode could further confirm this hypothesis: considerable removal capacity in the first cycle (i.e., due to high sub-nanometre pore volume) followed by continuous decrease in the following cycles most probably due to the lack of larger pores providing better accessibility of ions into and out of the pores during electrosorption and regeneration, respectively.

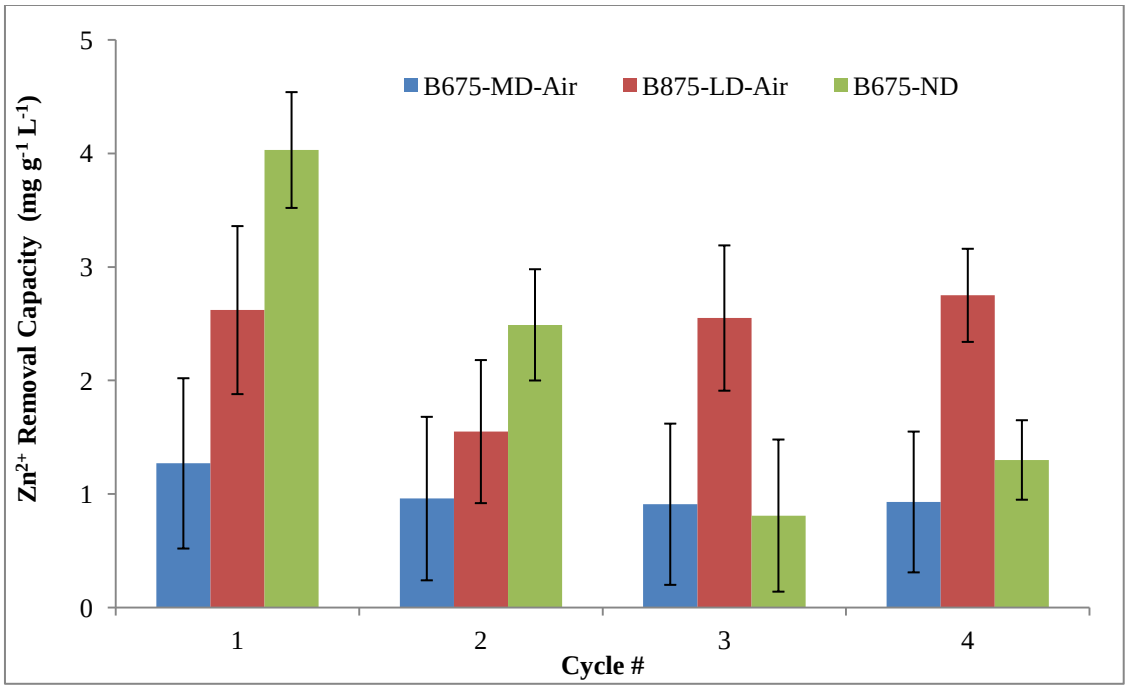

Figure 6.12 Electrosorption of Zn^{2+} using activated biochar electrodes with tailored porous structure.

6.2.7 Effect of pH on the surface charge characteristics of tailored biochar samples

To study the effect of pH on the surface electrical characteristics, the Zeta potentials (defined as the electrical potential at the slipping plane, which is in close proximity of the outer Helmholtz plane) were measured at pH values between 2.1 and 11 (Figure 6.13). The pH at which the Zeta potential is virtually equal to zero is referred to as the iso-electric point (IEP) [240]–[242]. The correlation between pH and Zeta potential can be used to compare the CDI performance of tailored biochar electrodes for both adsorption and desorption (during regeneration) of Na^+ and Zn^{2+} ions. The IEPs of B875-LD-Air, B675-MD-Air, and B675-ND samples were as follows: 4.5, 2.9, and <2.0, respectively (Figure 6.13). According to the literature, addition of oxygen containing groups to the carbon matrix shifts the IEP to smaller values [15], [240], [242]. The B875-LD-Air sample showed the highest IEP, most probably due to the lowest amount of oxygen-containing functional groups on the surface as also evidenced by elemental analysis. Moreover, the IEP of B675-ND was not reached in the experimental pH

window suggesting values <2.0. This could be attributed to the highest content of oxygen containing surface functional groups for the B675-ND sample compared to B675-MD-Air and B875-LD-Air.

As shown in Figure 6.13, all biochar samples showed negative Zeta potentials at pH 5.7 corresponding to the NaCl and $ZnCl_2$ electrolytes employed (dashed line in Figure 6.13). At the latter pH, the most negative Zeta potential was obtained for B675-ND followed by B675-MD-Air and lastly B875-LD-Air. Thus, all three samples have an intrinsic surface property for electrosorption of positive ions. The difference in Zeta potential at specific pH of the testing solutions can also affect the regeneration. Thus, more efficient regeneration is expected for the sample with the highest Zeta potential at the pH of the testing electrolyte (i.e., B875-LD-Air). This could be another possible reason for more effective regeneration of B875-LD-Air electrodes as opposed to B675-MD-Air and B675-ND in case of Zn^{2+} removal.

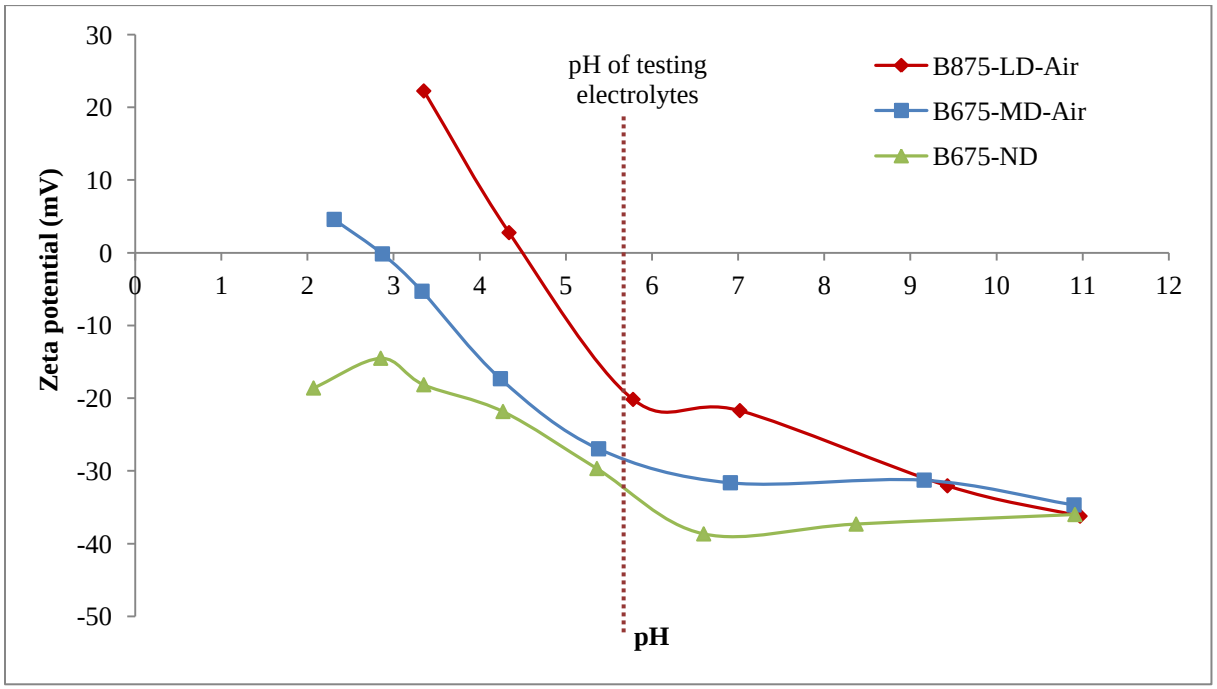

Figure 6.13 Effect of pH on surface charge characteristics (i.e., Zeta potential) of tailored biochar samples.

6.2.8 Significance of biochar electrodes with tailored structure as novel promising material for CDI

The electrosorption capacity of activated biochar electrodes for NaCl desalination was compared to other promising carbon-based materials reported in the literature (Table 6.5). Results suggested comparable (and in many cases higher) capacity for NaCl removal for the biochar in the present work, compared to other materials: carbon nanotubes (single or multi wall), graphene, and ordered mesoporous carbon (OMC). The tailored biochar electrodes also showed promising durability (<7% drop in capacity after four cycles) in NaCl capacitive deionization, whereas many literature studies present only one cycle results. Moreover, tuning the mesoporous structure of activated biochar resulted in promising capacity and durability for electrosorption of Zn^{2+} and potentially similar heavy and transitional metal ions with comparable hydrated ion size (e.g., Zn^{2+}, Fe^{3+}, Cd^{3+}, and Cr^{3+}). The combination of the high surface area, majorly mesoporous structure (i.e., nano-crystalline graphite with tubular structure as confirmed by TEM and Raman), and high sub-nanometre pore volume available for electrosorption of ions with different sizes could make the B875-LD-Air sample a promising electrode material for the CDI technology. Based on the obtained results, the required specifications of the electrodes (e.g., amount of active material and geometric area) can be projected for specific salt removal concentrations (Appendix H).

Table 6.5 NaCl CDI removal comparison between biochar electrodes with tailored porous structure and promising carbon-based electrodes in the literature.

Electrode material	Surface Area ($m^2 g^{-1}$)	Mesopore volume ($cm^3 g^{-1}$)	Micropore volume ($cm^3 g^{-1}$)	NaCl removal capacity ($mg g_c^{-1}$)	Reference
Ordered mesoporous carbon	950-1491	0.9-1.3	0.2-0.3	0.52-0.93	[50]
Activated carbon nanofiber web	335-712	0.05-0.09	0.15-0.27	2.74-4.64	[94]
Activated carbon	917-2030	0.09-0.44	0.41-0.64	2.8-4.6	[47]
Microporous carbon aerogel monoliths	500	-	70% of total pore volume	9.6	[51]
N-doped monolithic carbon aerogel	601-725	0.03-0.56	0.2	0.75-8.5	[243]
Mesoporous carbon black-aerogel composites	854-954	0.92-2.21	0.22	2-10.3	[244]
Ordered mesoporous carbide-derived carbon	2720	-	-	12.8	[238]
Microporous biochar	1600	0.09	0.60	5.07	This work
Micro/meso-porous biochar	971	0.28	0.38	5.39	This work
Mesoporous biochar	1674	0.94	0.38	5.13	This work
Carbon aerogel	400-1100	-	-	3.33	[245]

6.3 Conclusion

The porous structure of activated biochar was tailored to prepare three type of electrodes: a) primarily microporous (i.e., B675-ND with 87 % micropores[1]); b) mesoporous (i.e., B875-LD-Air with 72% mesopores); and c) a combination of both structures (i.e., B675-MD-Air with 58 % micro and 42% mesopores). All samples showed narrow pore size distribution in both micropore and mesopore regions as investigated by N_2 adsorption isotherms through Horvath Kawazoe (HK) and Barrett-Joyner-Halenda (BJH) methods, respectively. The functional groups and structural changes of the prepared samples were studied through TEM, Raman, and FT-IR analyses. The development of nano-crystalline graphitic structure was observed in the sample prepared at 875°C including thin carbon layers with tubular structures at the edges. The samples with majorly micropores or combined micro- and mesopores showed typical amorphous carbon structure.

The electric double layer characteristics of all the tailored activated biochar samples were studied using cyclic voltammetry and galvanostatic charge/discharge. The majorly mesoporous electrode (B875-LD-Air) showed the lowest total electrode resistance (i.e., IR-potential drop of 0.35 V g^{-1}) followed by the B675-MD-Air and B675-ND (i.e., 0.61 and 1.65 V g^{-1}, respectively). The main source of electrode resistance is attributed to the electrical conductivity of the biochar powder samples (due to the heteroatomic elemental content) and the ion migration (i.e., ionic conductivity) in the pores.

Electrosorption of Na^+ and Zn^{2+} ions were investigated in a batch-mode CDI experiment under constant current charging condition. The tailored biochar electrodes were charged in four consecutive cycles while being regenerated by washing at zero current between the cycles. All

[1] Out of total pore volume

electrodes showed comparable and promising NaCl removal capacity with <7% capacity drop from cycle nr. 1 to 4. The removal capacity was correlated with the sub-nanometre pore volume of the samples at pore sizes comparable to the hydrated ion size of Na^+. The electrosorption of zinc ions showed different results, where the electrode B875-LD-Air with mostly mesoporous content (72% of total pore volume) had the best performance in terms of removal capacity in conjunction with durability.

These results demonstrate the competitiveness of tailored biochar samples with other carbon-based materials with more complex and costly preparation methods for capacitive deionization of NaCl and $ZnCl_2$ solutions. Developing biochar electrodes as a low-cost and promising carbon-based material for CDI technology can contribute to reducing the overall cost of electrode preparation. Furthermore, the present study also contributes to the better understanding of sometimes controversial effects of porous structure on electrosorption performance.

Chapter 7: Conclusions and recommendations for future work

7.1 Conclusions

The main contribution of the present work is the development of a novel generation of renewable electrodes prepared from a cost-efficient carbon precursor, i.e., biochar, for capacitive deionization (CDI). In order for CDI technology to grow successfully as a commercial water treatment method, an electrode material with effective electrosorption performance must be developed cost effectively and with minimal environmental impacts. Surface area and porosity, chemical group functionality, and structure of biochar were developed by a thermo-chemical process to optimize its electrosorption performance.

In the first phase of the research (Chapter 4), experiments were conducted investigating the biochar material with different surface areas, structure, and chemical functionality for the basic concept of CDI, i.e., electric double layer phenomenon. In the second phase (Chapter 5), a novel method to control the surface area and porous structure of biochar was presented and studied. Biochar samples with differently tailored structures (micro- or mesoporous or a combination of both) were produced, and the effect of porous structure on EDL performance was studied. In the last phase of the studies (Chapter 6), three biochar samples with tailored porous structure were utilized as electrodes in a batch-mode (200 mL) CDI unit. Electrosorption of Na^+ and Zn^{2+} ions with different ionic sizes was studied with respect to the controlled porous structure of biochar electrodes.

Key findings of the research are summarized as follows:

Phase I: Proof of concept

- The surface area and porosity of the biochar material has a significant role in electric double layer (EDL) behaviour. The as-received biochar with <1 m^2 g^{-1} surface area

showed negligible double layer behaviour, whereas increasing the surface area to >600 m g^{-1} resulted in significantly improved EDL performance.

- A thermo-chemical process (i.e., chemical activation with KOH) at different carbonization temperatures and dwell times (675°C for 2 h or 1000°C for 5 h) was employed to develop the surface area and structure of biochar to provide promising electrostatic capacitive performance. Carbonization at 1000°C resulted in a smaller surface area of activated biochar (and consequently smaller total capacitance of the corresponding electrode) compared with the sample carbonized at 675°C. However, the more graphitic structure developed in the first sample resulted in higher electrical conductivity and smaller electrode resistance.
- The activated biochar electrodes showed higher capacitance (~10 times) compared with carbon black electrodes (as reference) investigated in a similar setup.
- During examination of the effect of the surface hydrophobicity, oxygen-containing functionalities were implemented on biochar samples by oxidation with HNO_3. To modify the oxygen-containing groups, the HNO_3-treated samples were calcined under N_2 at two different temperatures (150°C and 450°C). Calcination showed a positive effect on the total capacitance and electrode resistance of HNO_3-treated samples. However, comparable total capacitance and higher electrode resistance obtained for all HNO_3-treated samples as opposed to the untreated biochar sample confirmed the ineffectiveness of surface group oxidation on EDL performance.

Phase II: Tailoring the porous structure and its effect on EDL performance

- Modifying the pre-carbonization drying conditions (atmosphere and time) resulted in conversion of the chemical activation reagent as investigated by FT-IR analysis.

Prolonged exposure to air (>65 h) resulted in KOH to K_2CO_3 conversion, whereas drying under N_2 (independent of the length) resulted in preserving KOH as an activation reagent.

- KOH and K_2CO_3 showed different mechanisms of activation at various carbonization temperatures (475°C–875°C) resulting in different porous structures.
- Activated biochar with predominantly micro-, mesoporous, or a combination of both structures were prepared. The surface area and micropore and mesopore volumes were tailored between 488 and 2670 $m^2\ g^{-1}$, 0.04 and 0.72 $cm^3\ g^{-1}$, and 0.05 and 1.70 $cm^3\ g^{-1}$, respectively. All samples showed narrow pore size distribution between 0.5 and 0.7 nm. The activated biochar with majorly mesoporous structure (>70 % of total pore volume) showed the highest surface area (>2000 $m^2\ g^{-1}$).
- The high content of mesoporosity could be attributed to the tubular structure of carbon sheets of biochar at high temperatures, as evidenced by morphological and structural analyses.
- The tailored activated biochar samples were used to prepare electrodes for EDL applications. The microporous biochar samples showed higher total capacitance compared with the sample with combined micro- and mesoporous structure. The mesoporous biochar showed comparable total capacitance with that of microporous samples with significantly smaller Ohmic drop, i.e., an indication of improved ion accessibility within the pores.

Phase III: Application of activated biochar samples with controlled porous structure in CDI of NaCl and $ZnCl_2$

- Based on the method developed in Phase II, high surface area biochar samples (i.e., 971 to 1675 $m^2\ g^{-1}$) were prepared with three types of tailored porous structure:

(a) predominately microporous (87% of total pore volume), (b) mesoporous (72% of total pore volume), and (c) a combination of both structures (58% and 42% micro- and mesopore, respectively).

- The prepared samples were used to fabricate electrodes (sprayed on carbon cloth as the current collector) for NaCl and $ZnCl_2$ removal. The effect of the different porous structures on electrosorption was studied by electrochemical techniques (i.e., cyclic voltammetry, galvanostatic charge/discharge, and batch-mode CDI) complemented by morphological, surface structural, and compositional analyses.
- For NaCl removal, all samples showed promising capacity (i.e., up to 5.13 mg NaCl g^{-1}) and durability through four consecutive cycles. In the case of $ZnCl_2$, on the other hand, the microporous sample showed considerable drop in removal capacity (>75% drop) from cycle 1 to 4, while the combined micro- and mesoporous sample showed relatively small electrosorption capacity. Interestingly, the sample with a mostly mesoporous structure showed the highest removal capacity (i.e., 1.15 mg $ZnCl_2$ g^{-1}) and durability for Zn^{2+} removal.
- The CDI removal efficiencies of biochar electrodes are comparable to, and in most cases higher than, those of carbon-based materials described in the literature that have considerably more complicated and costly preparations along with potential environmental issues.
- Moreover, these results emphasize the importance of tailoring the porous structure of the biochar electrode material as a function of the specific size of adsorbate ions to improve the CDI performance.

7.2 Contributions to knowledge

The key contributions from this research can be summarized as follows:

- Biochar as a renewable and low-cost carbon precursor was successfully developed for EDL applications. A novel generation of renewable material is introduced to be used in desalination and wastewater treatment (CDI) as well as energy storage applications.
- A novel variant of a chemical activation method was developed to tailor and tune the porous structure of activated biochar. The prepared samples could be potentially used in adsorption-specific applications ranging from pollution abatement to energy storage. Modification of drying conditions could be an easy and low-cost process for tailoring the activated carbon porous structure compared with other methods such as chemical vapor deposition (CVD) and silica templates.
- The significantly large mesoporous surface area of B875 samples, reported for the first time in this study, could be very advantageous for the employment of the activated biochar samples in applications requiring specific mesoporous structures, such as catalyst supports in fuel cells and in electric double layer capacitors.
- Biochar with a tailored structure was investigated for the removal of different ions with varying sizes in a small-scale CDI unit, and the synergic effects of micro- and mesopores on the electrosorption performance were reflected on. The results could be related to both desalination of NaCl and wastewater treatment of industrial effluents (e.g., mining tailings containing heavy and transitional ions).
- The research presented broadens the applications of biochar as a renewable carbon-based candidate for different processes. This could further increase the potential market of biochar as a value-added material enhancing the economic feasibility of pyrolysis processes.

7.3 Recommendations for future work

Based on the findings of the present study, future research could be conducted in two groups: EDL-based experiments for potential manufacturing of supercapacitors and CDI studies for potential large-scale applications. The former group includes experiments to further test activated biochar electrodes and testing conditions (e.g., type of current collector, working electrolyte, and potential window) for supercapacitor fabrication, while the latter group could focus on optimizing the CDI process conditions and studying the larger-scale CDI unit using biochar electrodes (with the batch mode setup studied in this work). Further research should also be conducted to investigate continuous flow CDI systems that have been widely reported in the literature for large-scale applications [28], [30], [38]. The specific recommendations are as follows:

EDL-based experiments for potential supercapacitor fabrication:

- To study different solutions (e.g., highly concentrated acidic and basic solutions such as H_2SO_4 and KOH) as electrolytes in electrochemical analyses with the correct choice of current collector;
- To study the effect of a potential window in CV analysis on double layer behaviour; and,
- To prepare supercapacitor testing units using biochar as an active working and counter electrode material.

To optimize the process conditions in the batch-mode setup:

- Study the effect of increasing charging current density on electrosorption capacity.
- Study the optimum charging and discharging times.

- Study the durability of electrodes through an increased number of cycles (>100 cycles) as a necessary characteristic for large-scale purposes.
- Investigate the effect of ion charge and radius on removal efficiency.

Large-scale application (based on the optimized conditions):

- To design electrodes with larger geometric areas and investigate the effect of electrode properties (e.g., active material loading per geometric area and binder type) on electrosorption performance.
- Different electrode shapes (e.g., rolled) can be designed to optimize the electrosorption capacitance. The form of electrodes studied in this work (sprayed on current collectors) proposes flexibility regarding different potential electrode setups in electrosorption units.
- Addition of ion exchange membranes on electrodes, i.e., membrane-assisted capacitive deionization (MCDI). This method has recently showed promising results in both adsorption and regeneration of electrodes [38]. Ion exchange membranes allow access of a specific ion while blocking the counter-ion.
- Design and study a continuous-flow system and study the effects of process conditions (e.g., flow rate and charging time). Moreover, the effect of recycling the flow through electrodes to optimize the electrosorption capacity could be investigated.

Further studies are recommended to investigate the potential of various biochar samples produced by pyrolysis or gasification processes from different feedstock (e.g., biomass waste or municipal solid waste) for CDI. These could further examine the specific properties of various biochars (e.g., ash content, initial surface area, and reaction yield) and their effect on EDL-based applications. Also, studies to investigate the potential of large-scale activated biochar production via KOH chemical activation could be conducted. Optimizing the mass

ratio of KOH to biochar, reusing the KOH solution for consecutive processes, and improving the yield of activated biochar production could be essential for large-scale production prospects.

“Science is a way of thinking much more than it is a body of knowledge.”

Carl Sagan

Bibliography

[1] J. Lehmann and S. Joseph, *Biochar for Environmental Management: Science and Technology*. Earthscan Publications Ltd., 2009.

[2] D. Mohan, Pittman, and P. H. Steele, "Pyrolysis of wood/biomass for bio-oil: a critical review," *Energy Fuels*, vol. 20, no. 3, pp. 848–889, May 2006.

[3] A. V. Bridgwater, D. Meier, and D. Radlein, "An overview of fast pyrolysis of biomass," *Org. Geochem.*, vol. 30, no. 12, pp. 1479–1493, Dec. 1999.

[4] P. Rutkowski, "Pyrolysis of cellulose, xylan and lignin with the K2CO3 and ZnCl2 addition for bio-oil production," *Fuel Process. Technol.*, vol. 92, no. 3, pp. 517–522, Mar. 2011.

[5] O. Ioannidou and A. Zabaniotou, "Agricultural residues as precursors for activated carbon production--A review," *Renew. Sustain. Energy Rev.*, vol. 11, no. 9, pp. 1966–2005, Dec. 2007.

[6] C. E. Brewer, K. Schmidt-Rohr, J. A. Satrio, and R. C. Brown, "Characterization of biochar from fast pyrolysis and gasification systems," *Environ. Prog. Sustain. Energy*, vol. 28, no. 3, pp. 386–396, Oct. 2009.

[7] J. Lehmann, M. C. Rillig, J. Thies, C. A. Masiello, W. C. Hockaday, and D. Crowley, "Biochar effects on soil biota – A review," *Soil Biol. Biochem.*, vol. 43, no. 9, pp. 1812–1836, Sep. 2011.

[8] D. Woolf, J. E. Amonette, F. A. Street-Perrott, J. Lehmann, and S. Joseph, "Sustainable biochar to mitigate global climate change," *Nat. Commun.*, vol. 1, p. 56, Aug. 2010.

[9] M. Ahmad, A. U. Rajapaksha, J. E. Lim, M. Zhang, N. Bolan, D. Mohan, M. Vithanage, S. S. Lee, and Y. S. Ok, "Biochar as a sorbent for contaminant management in soil and water: A review," *Chemosphere*, vol. 99, pp. 19–33, Mar. 2014.

[10] D. Mohan, A. Sarswat, Y. S. Ok, and C. U. Pittman Jr., "Organic and inorganic contaminants removal from water with biochar, a renewable, low cost and sustainable adsorbent – A critical review," *Bioresour. Technol.*

[11] A. M. Dehkhoda, A. H. West, and N. Ellis, "Biochar based solid acid catalyst for biodiesel production," *Appl. Catal. Gen.*, vol. 382, no. 2, pp. 197–204, Jul. 2010.

[12] W.-J. Liu, F.-X. Zeng, H. Jiang, and X.-S. Zhang, "Preparation of high adsorption capacity bio-chars from waste biomass," *Bioresour. Technol.*, vol. 102, no. 17, pp. 8247–8252, Sep. 2011.

[13] R. Azargohar and A. K. Dalai, "Steam and KOH activation of biochar: Experimental and modeling studies," *Microporous Mesoporous Mater.*, vol. 110, no. 2–3, pp. 413–421, Apr. 2008.

[14] R. Azargohar and A. Dalai, “Biochar as a precursor of activated carbon,” *Appl. Biochem. Biotechnol.*, vol. 131, no. 1, pp. 762–773, Mar. 2006.

[15] R. Chand Bansal and M. Goyal, *Activated Carbon Adsorption*. CRC Press, 2005.

[16] K.-L. Yang, T.-Y. Ying, S. Yiacoumi, C. Tsouris, and E. S. Vittoratos, “Electrosorption of Ions from Aqueous Solutions by Carbon Aerogel: An Electrical Double-Layer Model,” *Langmuir*, vol. 17, no. 6, pp. 1961–1969, Mar. 2001.

[17] K. Y. Foo and B. H. Hameed, “A short review of activated carbon assisted electrosorption process: An overview, current stage and future prospects,” *J. Hazard. Mater.*, vol. 170, no. 2–3, pp. 552–559, Oct. 2009.

[18] “UN-Water, FAO, Coping with water scarcity: challenge of the twenty-first century, (2007).”

[19] M. A. Montgomery and M. Elimelech, “Water and sanitation in developing countries: including health in the equation,” *Environ. Sci. Technol.*, vol. 41, no. 1, pp. 17–24, 2007.

[20] M. A. Shannon, P. W. Bohn, M. Elimelech, J. G. Georgiadis, B. J. Mariñas, and A. M. Mayes, “Science and technology for water purification in the coming decades,” *Nature*, vol. 452, no. 7185, pp. 301–310, Mar. 2008.

[21] M. Black, *The No-nonsense Guide to Water*. Verso, 2004.

[22] “Human Activity and the Environment: Section 4: Wastewater discharges.”. Available: http://www.statcan.gc.ca/pub/16-201-x/2012000/part-partie4-eng.htm. [Accessed: 03-Sep-2015].

[23] R. C. Marques and P. T. F. Simões, *Regulation of water and wastewater services: An international comparison*. IWA Publishing, 2010.

[24] R. Borsani and S. Rebagliati, “Fundamentals and costing of MSF desalination plants and comparison with other technologies,” *Desalination*, vol. 182, no. 1–3, pp. 29–37, Nov. 2005.

[25] I. C. Karagiannis and P. G. Soldatos, “Water desalination cost literature: review and assessment,” *Desalination*, vol. 223, no. 1–3, pp. 448–456, Mar. 2008.

[26] C. Fritzmann, J. Löwenberg, T. Wintgens, and T. Melin, “State-of-the-art of reverse osmosis desalination,” *Desalination*, vol. 216, no. 1–3, pp. 1–76, Oct. 2007.

[27] Y. Oren, “Capacitive deionization (CDI) for desalination and water treatment -- past, present and future (a review),” *Desalination*, vol. 228, no. 1–3, pp. 10–29, Aug. 2008.

[28] M. A. Anderson, A. L. Cudero, and J. Palma, “Capacitive deionization as an electrochemical means of saving energy and delivering clean water. Comparison to present desalination practices: Will it compete?,” *Electrochimica Acta*, vol. 55, no. 12, pp. 3845–3856, Apr. 2010.

[29] A. Subramani and J. G. Jacangelo, “Emerging desalination technologies for water treatment: a critical review,” *Water Res.*, vol. 75, pp. 164–187, May 2015.

[30] M. Suss, S. Porada, X. Sun, M. Biesheuvel, J. Yoon, and V. Presser, “Water desalination via capacitive deionization: what is it and what can we expect from it?,” *Energy Env. Sci*, 2015.

[31] J. Farmer, “Method and apparatus for capacitive deionization, electrochemical purification, and regeneration of electrodes,” US5425858 A, 20-Jun-1995.

[32] G. W. Murphy and D. D. Caudle, “Mathematical theory of electrochemical demineralization in flowing systems,” *Electrochimica Acta*, vol. 12, no. 12, pp. 1655–1664, Dec. 1967.

[33] A. M. Johnson and J. Newman, “Desalting by means of porous carbon electrodes,” *J. Electrochem. Soc.*, vol. 118, no. 3, pp. 510–517, Mar. 1971.

[34] C. J. Gabelich, T. D. Tran, and I. H. “Mel” Suffet, “Electrosorption of inorganic salts from aqueous solution using carbon aerogels,” *Environ. Sci. Technol.*, vol. 36, no. 13, pp. 3010–3019, Jul. 2002.

[35] S. Jeon, H. Park, J. Yeo, S. Yang, C. H. Cho, M. H. Han, and D. K. Kim, “Desalination via a new membrane capacitive deionization process utilizing flow-electrodes,” *Energy Environ. Sci.*, vol. 6, no. 5, pp. 1471–1475, Apr. 2013.

[36] J.-B. Lee, K.-K. Park, H.-M. Eum, and C.-W. Lee, “Desalination of a thermal power plant wastewater by membrane capacitive deionization,” *Desalination*, vol. 196, no. 1–3, pp. 125–134, Sep. 2006.

[37] S.-J. Seo, H. Jeon, J. K. Lee, G.-Y. Kim, D. Park, H. Nojima, J. Lee, and S.-H. Moon, “Investigation on removal of hardness ions by capacitive deionization (CDI) for water softening applications,” *Water Res.*, vol. 44, no. 7, pp. 2267–2275, Apr. 2010.

[38] S. Porada, R. Zhao, A. van der Wal, V. Presser, and P. M. Biesheuvel, “Review on the science and technology of water desalination by capacitive deionization,” *Prog. Mater. Sci.*, vol. 58, no. 8, pp. 1388–1442, Oct. 2013.

[39] J. C. Farmer, G. V. Mack, and D. V. Fix, “The use of carbon aerogel electrodes for deionizing water and treating aqueous process wastes,” 1996.

[40] L. Zou, G. Morris, and D. Qi, “Using activated carbon electrode in electrosorptive deionisation of brackish water,” *Desalination*, vol. 225, no. 1–3, pp. 329–340, May 2008.

[41] J. C. Farmer, S. M. Bahowick, J. E. Harrar, D. V. Fix, R. E. Martinelli, A. K. Vu, and K. L. Carroll, “Electrosorption of chromium ions on carbon aerogel electrodes as a means of remediating ground water,” *Energy Fuels*, vol. 11, no. 2, pp. 337–347, Mar. 1997.

[42] B. Corry, “Designing carbon nanotube membranes for efficient water desalination,” *J. Phys. Chem. B*, vol. 112, no. 5, pp. 1427–1434, Feb. 2008.

[43] K. Dai, L. Shi, J. Fang, D. Zhang, and B. Yu, “NaCl adsorption in multi-walled carbon nanotubes,” *Mater. Lett.*, vol. 59, no. 16, pp. 1989–1992, Jul. 2005.

[44] Y. Gao, L. Pan, H. Li, Y. Zhang, Z. Zhang, Y. Chen, and Z. Sun, “Electrosorption behavior of cations with carbon nanotubes and carbon nanofibres composite film electrodes,” *Thin Solid Films*, vol. 517, no. 5, pp. 1616–1619, Jan. 2009.

[45] S. Porada, L. Weinstein, R. Dash, A. van der Wal, M. Bryjak, Y. Gogotsi, and P. M. Biesheuvel, “Water desalination using capacitive deionization with microporous carbon electrodes,” *ACS Appl. Mater. Interfaces*, vol. 4, no. 3, pp. 1194–1199, Mar. 2012.

[46] J. Chmiola, G. Yushin, Y. Gogotsi, C. Portet, P. Simon, and P. L. Taberna, “Anomalous increase in carbon capacitance at pore sizes less than 1 nanometer,” *Science*, vol. 313, no. 5794, pp. 1760–1763, Sep. 2006.

[47] G. Wang, B. Qian, Q. Dong, J. Yang, Z. Zhao, and J. Qiu, “Highly mesoporous activated carbon electrode for capacitive deionization,” *Sep. Purif. Technol.*, vol. 103, pp. 216–221, Jan. 2013.

[48] C. Tsouris, R. Mayes, J. Kiggans, K. Sharma, S. Yiacoumi, D. DePaoli, and S. Dai, “Mesoporous carbon for capacitive deionization of saline water,” *Environ. Sci. Technol.*, vol. 45, no. 23, pp. 10243–10249, Dec. 2011.

[49] X. Wang, J. S. Lee, C. Tsouris, D. W. DePaoli, and S. Dai, “Preparation of activated mesoporous carbons for electrosorption of ions from aqueous solutions,” *J. Mater. Chem.*, vol. 20, no. 22, p. 4602, 2010.

[50] L. Li, L. Zou, H. Song, and G. Morris, “Ordered mesoporous carbons synthesized by a modified sol–gel process for electrosorptive removal of sodium chloride,” *Carbon*, vol. 47, no. 3, pp. 775–781, Mar. 2009.

[51] M. E. Suss, T. F. Baumann, W. L. Bourcier, C. M. Spadaccini, K. A. Rose, J. G. Santiago, and M. Stadermann, “Capacitive desalination with flow-through electrodes,” *Energy Environ. Sci.*, vol. 5, no. 11, pp. 9511–9519, Oct. 2012.

[52] M. E. Suss, P. M. Biesheuvel, T. F. Baumann, M. Stadermann, and J. G. Santiago, “In situ spatially and temporally resolved measurements of salt concentration between charging porous electrodes for desalination by capacitive deionization,” *Environ. Sci. Technol.*, vol. 48, no. 3, pp. 2008–2015, Feb. 2014.

[53] H. Li, T. Lu, L. Pan, Y. Zhang, and Z. Sun, “Electrosorption behavior of graphene in NaCl solutions,” *J. Mater. Chem.*, vol. 19, no. 37, pp. 6773–6779, Sep. 2009.

[54] F. Alvi, M. K. Ram, P. A. Basnayaka, E. Stefanakos, Y. Goswami, and A. Kumar, “Graphene–polyethylenedioxythiophene conducting polymer nanocomposite based supercapacitor,” *Electrochimica Acta*, vol. 56, no. 25, pp. 9406–9412, Oct. 2011.

[55] H. Li, L. Zou, L. Pan, and Z. Sun, “Novel graphene-like electrodes for capacitive deionization,” *Environ. Sci. Technol.*, vol. 44, no. 22, pp. 8692–8697, Nov. 2010.

[56] C. C. Nesbitt and X. Sun, "Consolidated amorphous carbon materials, their manufacture and use," US6350520 B1, 26-Feb-2002.

[57] C.-M. Yang, W.-H. Choi, B.-K. Na, B. W. Cho, and W. I. Cho, "Capacitive deionization of NaCl solution with carbon aerogel-silicagel composite electrodes," *Desalination*, vol. 174, no. 2, pp. 125–133, Apr. 2005.

[58] Y. Liu, C. Nie, X. Liu, X. Xu, Z. Sun, and L. Pan, "Review on carbon-based composite materials for capacitive deionization," *RSC Adv.*, vol. 5, no. 20, pp. 15205–15225, Jan. 2015.

[59] A. Burke, "R&D considerations for the performance and application of electrochemical capacitors," *Electrochimica Acta*, vol. 53, no. 3, pp. 1083–1091, Dec. 2007.

[60] P. Xu, J. E. Drewes, D. Heil, and G. Wang, "Treatment of brackish produced water using carbon aerogel-based capacitive deionization technology," *Water Res.*, vol. 42, no. 10–11, pp. 2605–2617, May 2008.

[61] R. Farma, M. Deraman, A. Awitdrus, I. A. Talib, E. Taer, N. H. Basri, J. G. Manjunatha, M. M. Ishak, B. N. M. Dollah, and S. A. Hashmi, "Preparation of highly porous binderless activated carbon electrodes from fibres of oil palm empty fruit bunches for application in supercapacitors," *Bioresour. Technol.*, vol. 132, pp. 254–261, Mar. 2013.

[62] M. Al-Shammiri and M. Safar, "Multi-effect distillation plants: state of the art," *Desalination*, vol. 126, no. 1–3, pp. 45–59, Nov. 1999.

[63] R. Semiat, "Present and Future," *Water Int.*, vol. 25, no. 1, pp. 54–65, Mar. 2000.

[64] A. D. Patwardhan, *Industrial wastewater treatment*. PHI Learning Pvt. Ltd., 2008.

[65] P. H. Rieger, *Electrochemistry*. Springer, 1994.

[66] J. Lyklema, *Fundamentals of Interface and Colloid Science: Soft Colloids*, 1st ed. Academic Press, 2005.

[67] M. V. Fedorov and A. A. Kornyshev, "Towards understanding the structure and capacitance of electrical double layer in ionic liquids," *Electrochimica Acta*, vol. 53, no. 23, pp. 6835–6840, Oct. 2008.

[68] A. A. Kornyshev, "Double-Layer in Ionic Liquids: Paradigm Change?," *J. Phys. Chem. B*, vol. 111, no. 20, pp. 5545–5557, May 2007.

[69] P. M. Biesheuvel, "Thermodynamic cycle analysis for capacitive deionization," *J. Colloid Interface Sci.*, vol. 332, no. 1, pp. 258–264, Apr. 2009.

[70] R. Zhao, P. M. Biesheuvel, H. Miedema, H. Bruning, and A. van der Wal, "Charge efficiency: A functional tool to probe the double-layer structure inside of porous electrodes and application in the modeling of capacitive deionization," *J. Phys. Chem. Lett.*, vol. 1, no. 1, pp. 205–210, Jan. 2010.

[71] M. Z. Bazant, K. Thornton, and A. Ajdari, “Diffuse-charge dynamics in electrochemical systems,” *Phys. Rev. E*, vol. 70, no. 2, p. 21506, Aug. 2004.

[72] R. Zhao, P. M. Biesheuvel, and A. van der Wal, “Energy consumption and constant current operation in membrane capacitive deionization,” *Energy Environ. Sci.*, vol. 5, no. 11, pp. 9520–9527, Oct. 2012.

[73] P. M. Biesheuvel, Y. Fu, and M. Z. Bazant, “Electrochemistry and capacitive charging of porous electrodes in asymmetric multicomponent electrolytes,” *Russ. J. Electrochem.*, vol. 48, no. 6, pp. 580–592, Jun. 2012.

[74] R. Zhao, M. van Soestbergen, H. H. M. Rijnaarts, A. van der Wal, M. Z. Bazant, and P. M. Biesheuvel, “Time-dependent ion selectivity in capacitive charging of porous electrodes,” *J. Colloid Interface Sci.*, vol. 384, no. 1, pp. 38–44, Oct. 2012.

[75] S. Porada, M. Bryjak, A. van der Wal, and P. M. Biesheuvel, “Effect of electrode thickness variation on operation of capacitive deionization,” *Electrochimica Acta*, vol. 75, pp. 148–156, Jul. 2012.

[76] K. Kamran, M. van Soestbergen, and L. Pel, “Electrokinetic salt removal from porous building materials using ion exchange membranes,” *Transp. Porous Media*, vol. 96, no. 2, pp. 221–235, Nov. 2012.

[77] B. Kastening and M. Heins, “Properties of electrolytes in the micropores of activated carbon,” *Electrochimica Acta*, vol. 50, no. 12, pp. 2487–2498, Apr. 2005.

[78] G. Feng, R. Qiao, J. Huang, B. G. Sumpter, and V. Meunier, “Ion distribution in electrified micropores and its role in the anomalous enhancement of capacitance,” *ACS Nano*, vol. 4, no. 4, pp. 2382–2390, Apr. 2010.

[79] H. A. Arafat, M. Franz, and N. G. Pinto, “Effect of salt on the mechanism of adsorption of aromatics on activated carbon,” *Langmuir*, vol. 15, no. 18, pp. 5997–6003, Aug. 1999.

[80] John W. Blair and George W. Murphy, “Electrochemical demineralization of water with porous electrodes of large surface area,” in *Saline Water Conversion*, vol. 27, 0 vols., American Chemical Society, 1960, pp. 206–223.

[81] B. B. Arnold and G. W. Murphy, “Studies on the electrochemistry of carbon and chemically-modified carbon surfaces” *J. Phys. Chem.*, vol. 65, no. 1, pp. 135–138, Jan. 1961.

[82] S. Evans and W. S. Hamilton, “The mechanism of demineralization at carbon electrodes,” *J. Electrochem. Soc.*, vol. 113, no. 12, pp. 1314–1319, Dec. 1966.

[83] G. W. Reid and U. S. O. of S. Water, *Field operation of a 20 gallons per day pilot plant unit for electrochemical desalination of brackish water*. U.S. Dept. of the Interior, 1968.

[84] J. Newman, R. G. Wilbourne, A. W. Venolia, A. M. Johnson, Marquardt Company., and United States., *The Electrosorb process for desalting water*. Washington, D.C.: U.S. Dept. of the Interior, 1970.

[85] Y. Oren and A. Soffer, “Electrochemical parametric pumping,” *J. Electrochem. Soc.*, vol. 125, no. 6, pp. 869–875, Jun. 1978.

[86] A. Soffer and M. Folman, “The electrical double layer of high surface porous carbon electrode,” *J. Electroanal. Chem. Interfacial Electrochem.*, vol. 38, no. 1, pp. 25–43, 1972.

[87] J. Chmiola, C. Largeot, P.-L. Taberna, P. Simon, and Y. Gogotsi, “Monolithic carbide-derived carbon films for micro-supercapacitors,” *Science*, vol. 328, no. 5977, pp. 480–483, Apr. 2010.

[88] K. Jost, C. R. Perez, J. K. McDonough, V. Presser, M. Heon, G. Dion, and Y. Gogotsi, “Carbon coated textiles for flexible energy storage,” *Energy Environ. Sci.*, vol. 4, no. 12, pp. 5060–5067, Nov. 2011.

[89] V. Presser, L. Zhang, J. J. Niu, J. McDonough, C. Perez, H. Fong, and Y. Gogotsi, “Flexible nano-felts of carbide-derived carbon with ultra-high power handling capability,” *Adv. Energy Mater.*, vol. 1, no. 3, pp. 423–430, May 2011.

[90] K. Hung, C. Masarapu, T. Ko, and B. Wei, “Wide-temperature range operation supercapacitors from nanostructured activated carbon fabric,” *J. Power Sources*, vol. 193, no. 2, pp. 944–949, Sep. 2009.

[91] T. J. Alencherry, S. Ghosh, and V. Rajanarayana, “Impregnated electrode for capacitive deionisation, process for preparing it and apparatus employing the electrodes,” WO2014090508 A1, 19-Jun-2014.

[92] H. Oh, J. Lee, H. Ahn, Y. Jeong, Y. Kim, and C. Chi, “Nanoporous activated carbon cloth for capacitive deionization of aqueous solution,” *Thin Solid Films*, vol. 515, no. 1, pp. 220–225, Sep. 2006.

[93] M.-W. Ryoo, J.-H. Kim, and G. Seo, “Role of titania incorporated on activated carbon cloth for capacitive deionization of NaCl solution,” *J. Colloid Interface Sci.*, vol. 264, no. 2, pp. 414–419, Aug. 2003.

[94] G. Wang, C. Pan, L. Wang, Q. Dong, C. Yu, Z. Zhao, and J. Qiu, “Activated carbon nanofiber webs made by electrospinning for capacitive deionization,” *Electrochimica Acta*, vol. 69, pp. 65–70, May 2012.

[95] V. V. Panić, R. M. Stevanović, V. M. Jovanović, and A. B. Dekanski, “Electrochemical and capacitive properties of thin-layer carbon black electrodes,” *J. Power Sources*, vol. 181, no. 1, pp. 186–192, Jun. 2008.

[96] H. Marsh and F. Rodríguez-Reinoso, “Chapter 2 - Activated carbon (origins),” in *Activated Carbon*, H. M. Rodríguez-Reinoso, Ed. Oxford: Elsevier Science Ltd, 2006, pp. 13–86.

[97] A. Ban, A. Schafer, and H. Wendt, “Fundamentals of electrosorption on activated carbon for wastewater treatment of industrial effluents.” *J. Appl. Electrochem*, vol. 28, pp. 227-236, Jan. 1998.

[98] C.-H. Jung, H.-Y. Lee, J.-K. Moon, H.-J. Won, and Y.-G. Shul, "Electrosorption of uranium ions on activated carbon fibers," *J. Radioanal. Nucl. Chem.*, vol. 287, no. 3, pp. 833–839, Oct. 2010.

[99] H.-J. Ahn, J.-H. Lee, Y. Jeong, J.-H. Lee, C.-S. Chi, and H.-J. Oh, "Nanostructured carbon cloth electrode for desalination from aqueous solutions," *Mater. Sci. Eng. A*, vol. 449–451, pp. 841–845, Mar. 2007.

[100] M. T. Z. Myint and J. Dutta, "Fabrication of zinc oxide nanorods modified activated carbon cloth electrode for desalination of brackish water using capacitive deionization approach," *Desalination*, vol. 305, pp. 24–30, Nov. 2012.

[101] L. Han, K. G. Karthikeyan, M. A. Anderson, J. J. Wouters, and K. B. Gregory, "Mechanistic insights into the use of oxide nanoparticles coated asymmetric electrodes for capacitive deionization," *Electrochimica Acta*, vol. 90, pp. 573–581, Feb. 2013.

[102] I. Cohen, E. Avraham, M. Noked, A. Soffer, and D. Aurbach, "Enhanced charge efficiency in capacitive deionization achieved by surface-treated electrodes and by means of a third electrode," *J. Phys. Chem. C*, vol. 115, no. 40, pp. 19856–19863, Oct. 2011.

[103] E. Frackowiak and F. Béguin, "Carbon materials for the electrochemical storage of energy in capacitors," *Carbon*, vol. 39, no. 6, pp. 937–950, May 2001.

[104] R. W. Pekala, J. C. Farmer, C. T. Alviso, T. D. Tran, S. T. Mayer, J. M. Miller, and B. Dunn, "Carbon aerogels for electrochemical applications," *J. Non-Cryst. Solids*, vol. 225, pp. 74–80, Apr. 1998.

[105] Y. Zhai, Y. Dou, D. Zhao, P. F. Fulvio, R. T. Mayes, and S. Dai, "Carbon materials for chemical capacitive energy storage," *Adv. Mater.*, vol. 23, no. 42, pp. 4828–4850, Nov. 2011.

[106] Takashi Kyotani, John Chmiola, and Yury Gogotsi, "Carbide-derived carbons and templated carbons," in *Carbons for Electrochemical Energy Storage and Conversion Systems*, 0 vols., CRC Press, 2009, pp. 77–113.

[107] L. Zou, L. Li, H. Song, and G. Morris, "Using mesoporous carbon electrodes for brackish water desalination," *Water Res.*, vol. 42, no. 8–9, pp. 2340–2348, Apr. 2008.

[108] V. Presser, M. Heon, and Y. Gogotsi, "Carbide-derived carbons – from porous networks to nanotubes and graphene," *Adv. Funct. Mater.*, vol. 21, no. 5, pp. 810–833, Mar. 2011.

[109] J. Dzubiella and J.-P. Hansen, "Electric-field-controlled water and ion permeation of a hydrophobic nanopore," *J. Chem. Phys.*, vol. 122, no. 23, p. 234706, Jun. 2005.

[110] A. G. Pandolfo and A. F. Hollenkamp, "Carbon properties and their role in supercapacitors," *J. Power Sources*, vol. 157, no. 1, pp. 11–27, Jun. 2006.

[111] E. Frackowiak, S. Delpeux, K. Jurewicz, K. Szostak, D. Cazorla-Amoros, and F. Béguin, "Enhanced capacitance of carbon nanotubes through chemical activation," *Chem. Phys. Lett.*, vol. 361, no. 1–2, pp. 35–41, Jul. 2002.

[112] Q. Jiang, M. Z. Qu, G. M. Zhou, B. L. Zhang, and Z. L. Yu, “A study of activated carbon nanotubes as electrochemical super capacitors electrode materials,” *Mater. Lett.*, vol. 57, no. 4, pp. 988–991, Dec. 2002.

[113] D. Zhang, L. Shi, J. Fang, K. Dai, and X. Li, “Preparation and desalination performance of multiwall carbon nanotubes,” *Mater. Chem. Phys.*, vol. 97, no. 2–3, pp. 415–419, Jun. 2006.

[114] X. Z. Wang, M. G. Li, Y. W. Chen, R. M. Cheng, S. M. Huang, L. K. Pan, and Z. Sun, “Electrosorption of ions from aqueous solutions with carbon nanotubes and nanofibers composite film electrodes,” *Appl. Phys. Lett.*, vol. 89, no. 5, p. 53127, Jul. 2006.

[115] K. Dai, L. Shi, D. Zhang, and J. Fang, “NaCl adsorption in multi-walled carbon nanotube/active carbon combination electrode,” *Chem. Eng. Sci.*, vol. 61, no. 2, pp. 428–433, Jan. 2006.

[116] D. Zhang, X. Wen, L. Shi, T. Yan, and J. Zhang, “Enhanced capacitive deionization of graphene/mesoporous carbon composites,” *Nanoscale*, vol. 4, no. 17, p. 5440, 2012.

[117] H. Wang, D. Zhang, T. Yan, X. Wen, L. Shi, and J. Zhang, “Graphene prepared via a novel pyridine–thermal strategy for capacitive deionization,” *J. Mater. Chem.*, vol. 22, no. 45, pp. 23745–23748, Oct. 2012.

[118] J.-B. Donnet, *Carbon Black: Science and Technology*, *Second Edition*. CRC Press, 1993.

[119] K. Kinoshita, “Carbon: electrochemical and physicochemical properties,” Jan. 1988.

[120] F. Beck, M. Dolata, E. Grivei, and N. Probst, “Electrochemical supercapacitors based on industrial carbon blacks in aqueous H2SO4,” *J. Appl. Electrochem.*, vol. 31, no. 8, pp. 845–853, Aug. 2001.

[121] P. M. Biesheuvel and A. van der Wal, “Membrane capacitive deionization,” *J. Membr. Sci.*, vol. 346, no. 2, pp. 256–262, Jan. 2010.

[122] P. M. Biesheuvel, R. Zhao, S. Porada, and A. van der Wal, “Theory of membrane capacitive deionization including the effect of the electrode pore space,” *J. Colloid Interface Sci.*, vol. 360, no. 1, pp. 239–248, Aug. 2011.

[123] Y. Bouhadana, M. Ben-Tzion, A. Soffer, and D. Aurbach, “A control system for operating and investigating reactors: The demonstration of parasitic reactions in the water desalination by capacitive de-ionization,” *Desalination*, vol. 268, no. 1–3, pp. 253–261, Mar. 2011.

[124] O. N. Demirer, R. M. Naylor, C. A. Rios Perez, E. Wilkes, and C. Hidrovo, “Energetic performance optimization of a capacitive deionization system operating with transient cycles and brackish water,” *Desalination*, vol. 314, pp. 130–138, Apr. 2013.

[125] P. Długołęcki and A. van der Wal, “Energy recovery in membrane capacitive deionization,” *Environ. Sci. Technol.*, vol. 47, no. 9, pp. 4904–4910, May 2013.

[126] E. Avraham, M. Noked, Y. Bouhadana, A. Soffer, and D. Aurbach, “Limitations of charge efficiency in capacitive deionization,” *J. Electrochem. Soc.*, vol. 156, no. 10, p. P157, 2009.

[127] Y.-J. Kim and J.-H. Choi, “Enhanced desalination efficiency in capacitive deionization with an ion-selective membrane,” *Sep. Purif. Technol.*, vol. 71, no. 1, pp. 70–75, Jan. 2010.

[128] Y.-J. Kim and J.-H. Choi, “Selective removal of nitrate ion using a novel composite carbon electrode in capacitive deionization,” *Water Res.*, vol. 46, no. 18, pp. 6033–6039, Nov. 2012.

[129] J.-H. Yeo and J.-H. Choi, “Enhancement of nitrate removal from a solution of mixed nitrate, chloride and sulfate ions using a nitrate-selective carbon electrode,” *Desalination*, vol. 320, pp. 10–16, Jul. 2013.

[130] V. Presser, C. R. Dennison, J. Campos, K. W. Knehr, E. C. Kumbur, and Y. Gogotsi, “The electrochemical flow capacitor: A new concept for rapid energy storage and recovery,” *Adv. Energy Mater.*, vol. 2, no. 7, pp. 895–902, 2012.

[131] K. B. Hatzell, E. Iwama, A. Ferris, B. Daffos, K. Urita, T. Tzedakis, F. Chauvet, P.-L. Taberna, Y. Gogotsi, and P. Simon, “Capacitive deionization concept based on suspension electrodes without ion exchange membranes,” *Electrochem. Commun.*, vol. 43, pp. 18–21, Jun. 2014.

[132] J. Lee, S. Kim, C. Kim, and J. Yoon, “Hybrid capacitive deionization to enhance the desalination performance of capacitive techniques,” *Energy Env. Sci*, vol. 7, no. 11, pp. 3683–3689, Aug. 2014.

[133] D. A. Laird, R. C. Brown, J. E. Amonette, and J. Lehmann, “Review of the pyrolysis platform for coproducing bio-oil and biochar,” *Biofuels Bioprod. Biorefining*, vol. 3, no. 5, pp. 547–562, Sep. 2009.

[134] L. Pulido-Novicio, T. Hata, Y. Kurimoto, S. Doi, S. Ishihara, and Y. Imamura, “Adsorption capacities and related characteristics of wood charcoals carbonized using a one-step or two-step process,” *J. Wood Sci.*, vol. 47, no. 1, pp. 48–57, Feb. 2001.

[135] F. G. Emmerich, J. C. de Sousa, I. L. Torriani, and C. A. Luengo, “Applications of a granular model and percolation theory to the electrical resistivity of heat treated endocarp of babassu nut,” *Carbon*, vol. 25, no. 3, pp. 417–424, 1987.

[136] S. Shackley, J. Hammond, J. Gaunt, and R. Ibarrola, “The feasibility and costs of biochar deployment in the UK,” *Carbon Manag.*, vol. 2, no. 3, pp. 335–356, Jun. 2011.

[137] C. Briens, J. Piskorz, and F. Berruti, “Biomass valorization for fuel and chemicals production -- A review,” *Int. J. Chem. React. Eng.*, vol. 6, no. 1, May 2008.

[138] F. Berruti, C. Briens, and R. Golden, “Apparatus and process for the pyrolysis of agricultural biomass,” US7943014 B2, 17-May-2011.

[139] J. L. Manganaro and A. Lawal, “Economics of thermochemical conversion of crop residue to liquid transportation fuel,” *Energy Fuels*, vol. 26, no. 4, pp. 2442–2453, Apr. 2012.

[140] T. R. Brown, M. M. Wright, and R. C. Brown, “Estimating profitability of two biochar production scenarios: slow pyrolysis vs fast pyrolysis,” *Biofuels Bioprod. Biorefining*, vol. 5, no. 1, pp. 54–68, Jan. 2011.

[141] “Activated Carbon — Roskill.” Available: http://www.roskill.com/reports/industrial-minerals/activated-carbon. [Accessed: 30-Apr-2014].

[142] R. Baccar, J. Bouzid, M. Feki, and A. Montiel, “Preparation of activated carbon from Tunisian olive-waste cakes and its application for adsorption of heavy metal ions,” *J. Hazard. Mater.*, vol. 162, no. 2–3, pp. 1522–1529, Mar. 2009.

[143] O. S. Amuda, A. A. Giwa, and I. A. Bello, “Removal of heavy metal from industrial wastewater using modified activated coconut shell carbon,” *Biochem. Eng. J.*, vol. 36, no. 2, pp. 174–181, Sep. 2007.

[144] M. Song, B. Jin, R. Xiao, L. Yang, Y. Wu, Z. Zhong, and Y. Huang, “The comparison of two activation techniques to prepare activated carbon from corn cob,” *Biomass Bioenergy*, vol. 48, pp. 250–256, Jan. 2013.

[145] M.-M. Titirici, *Sustainable Carbon Materials from Hydrothermal Processes*. John Wiley & Sons, 2013.

[146] M. A. Lillo-Ródenas, D. Cazorla-Amorós, and A. Linares-Solano, “Understanding chemical reactions between carbons and NaOH and KOH: An insight into the chemical activation mechanism,” *Carbon*, vol. 41, no. 2, pp. 267–275, Feb. 2003.

[147] M. Molina-Sabio and F. Rodríguez-Reinoso, “Role of chemical activation in the development of carbon porosity,” *Colloids Surf. Physicochem. Eng. Asp.*, vol. 241, no. 1–3, pp. 15–25, Jul. 2004.

[148] A. Ahmadpour and D. D. Do, “The preparation of activated carbon from macadamia nutshell by chemical activation,” *Carbon*, vol. 35, no. 12, pp. 1723–1732, 1997.

[149] J. Hayashi, A. Kazehaya, K. Muroyama, and A. P. Watkinson, “Preparation of activated carbon from lignin by chemical activation,” *Carbon*, vol. 38, no. 13, pp. 1873–1878, 2000.

[150] F. Rodriguez-Reinoso and M. Molina-Sabio, “Activated carbons from lignocellulosic materials by chemical and/or physical activation: an overview,” *Carbon*, vol. 30, no. 7, pp. 1111–1118, 1992.

[151] M. N. Alaya, B. S. Girgis, and W. E. Mourad, “Activated carbon from some sgricultural wastes under action of one-step steam pyrolysis,” *J. Porous Mater.*, vol. 7, no. 4, pp. 509–517, Jun. 2000.

[152] E. Raymundo-Piñero, P. Azaïs, T. Cacciaguerra, D. Cazorla-Amorós, A. Linares-Solano, and F. Béguin, “KOH and NaOH activation mechanisms of multiwalled carbon nanotubes with different structural organisation,” *Carbon*, vol. 43, no. 4, pp. 786–795, 2005.

[153] D. S. Argyropoulos, *Materials, Chemicals and Energy from Forest Biomass*, 1st ed. An American Chemical Society Publication, 2007.

[154] T. Zhang, W. P. Walawender, L. T. Fan, M. Fan, D. Daugaard, and R. C. Brown, "Preparation of activated carbon from forest and agricultural residues through CO2 activation," *Chem. Eng. J.*, vol. 105, no. 1–2, pp. 53–59, Dec. 2004.

[155] H. Deng, G. Li, H. Yang, J. Tang, and J. Tang, "Preparation of activated carbons from cotton stalk by microwave assisted KOH and K2CO3 activation," *Chem. Eng. J.*, vol. 163, no. 3, pp. 373–381, Oct. 2010.

[156] M. Ahmedna, W. E. Marshall, and R. M. Rao, "Surface properties of granular activated carbons from agricultural by-products and their effects on raw sugar decolorization," *Bioresour. Technol.*, vol. 71, no. 2, pp. 103–112, Jan. 2000.

[157] Z. Hu, M. P. Srinivasan, and Y. Ni, "Novel activation process for preparing highly microporous and mesoporous activated carbons," *Carbon*, vol. 39, no. 6, pp. 877–886, May 2001.

[158] Q. Hu, J. Pang, Z. Wu, and Y. Lu, "Tuning pore size of mesoporous carbon via confined activation process," *Carbon*, vol. 44, no. 7, pp. 1349–1352, Jun. 2006.

[159] T. Otowa, Y. Nojima, and T. Miyazaki, "Development of KOH activated high surface area carbon and its application to drinking water purification," *Carbon*, vol. 35, no. 9, pp. 1315–1319, 1997.

[160] I. M. Lima, A. A. Boateng, and K. T. Klasson, "Physicochemical and adsorptive properties of fast-pyrolysis bio-chars and their steam activated counterparts," *J. Chem. Technol. Biotechnol.*, vol. 85, no. 11, pp. 1515–1521, 2010.

[161] J. Park, I. Hung, Z. Gan, O. J. Rojas, K. H. Lim, and S. Park, "Activated carbon from biochar: Influence of its physicochemical properties on the sorption characteristics of phenanthrene," *Bioresour. Technol.*, vol. 149, pp. 383–389, Dec. 2013.

[162] R. Azargohar and A. K. Dalai, "Steam and KOH activation of biochar: Experimental and modeling studies," *Microporous Mesoporous Mater.*, vol. 110, no. 2–3, pp. 413–421, Apr. 2008.

[163] P. A. Webb and C. Orr, *Analytical Methods in Fine Particle Technology*, 1st ed. Micromeritics Instrument Corporation, 1997.

[164] L. Bao, J. Zang, and X. Li, "Flexible Zn2SnO4/MnO2 core/shell nanocable−carbon microfiber hybrid composites for high-performance supercapacitor electrodes," *Nano Lett.*, vol. 11, no. 3, pp. 1215–1220, Mar. 2011.

[165] S. Mitra and S. Sampath, "Electrochemical capacitors based on exfoliated graphite electrodes," *Electrochem. Solid-State Lett.*, vol. 7, no. 9, pp. A264–A268, 2004.

[166] "National Recommended Water Quality Criteria—Correction, 822-Z-99-001. Office of Water, Environmental Protection Agency, Washington, DC, (1999)." Available: http://www.atsdr.cdc.gov/spl/. [Accessed: 29-Jul-2015].

[167] "CERCLA Priority List Hazardous Substances. Agency for toxic substances and disease registry (ATSDR): Atlanta, GA, (2003)." .

[168] E. Ayranci and B. E. Conway, "Adsorption and electrosorption of ethyl xanthate and thiocyanate anions at high-area carbon-cloth electrodes studied by in situ UV spectroscopy: Development of procedures for wastewater purification," *Anal. Chem.*, vol. 73, no. 6, pp. 1181–1189, Mar. 2001.

[169] Y. Oren and A. Soffer, "Electrochemical parametric pumping," *J. Electrochem. Soc.*, vol. 125, no. 6, pp. 869–875, Jun. 1978.

[170] I. Ghodbane and O. Hamdaoui, "Removal of mercury(II) from aqueous media using eucalyptus bark: Kinetic and equilibrium studies," *J. Hazard. Mater.*, vol. 160, no. 2–3, pp. 301–309, Dec. 2008.

[171] E. Frackowiak and F. Béguin, "Carbon materials for the electrochemical storage of energy in capacitors," *Carbon*, vol. 39, no. 6, pp. 937–950, May 2001.

[172] J. Lehmann and S. Joseph, *Biochar for environmental management*. Earthscan, 2009.

[173] J. W. Patrick, *Porosity in Carbons: Characterization and Applications*. John Wiley & Sons Inc, 1995.

[174] R. E. Franklin, "Crystallite growth in graphitizing and non-graphitizing carbons," *Proc. R. Soc. Lond. Ser. Math. Phys. Sci.*, pp. 196–218, 1951.

[175] J. T. Yu, A. M. Dehkhoda, and N. Ellis, "Development of biochar-based catalyst for transesterification of canola oil," *Energy Fuels*, vol. 25, no. 1, pp. 337–344, Jan. 2011.

[176] Y.-R. Nian and H. Teng, "Nitric acid modification of activated carbon electrodes for improvement of electrochemical capacitance," *J. Electrochem. Soc.*, vol. 149, no. 8, pp. A1008–A1014, Aug. 2002.

[177] J. L. Figueiredo, M. F. R. Pereira, M. M. A. Freitas, and J. J. M. Órfão, "Modification of the surface chemistry of activated carbons," *Carbon*, vol. 37, no. 9, pp. 1379–1389, 1999.

[178] K. Sun, K. Ro, M. Guo, J. Novak, H. Mashayekhi, and B. Xing, "Sorption of bisphenol A, 17α-ethinyl estradiol and phenanthrene on thermally and hydrothermally produced biochars," *Bioresour. Technol.*, vol. 102, no. 10, pp. 5757–5763, May 2011.

[179] B. Singh, B. P. Singh, and A. L. Cowie, "Characterisation and evaluation of biochars for their application as a soil amendment," *Soil Res.*, vol. 48, no. 7, pp. 516–525, 2010.

[180] M. Keiluweit, P. S. Nico, M. G. Johnson, and M. Kleber, "Dynamic molecular structure of plant biomass-derived black carbon (biochar)," *Environ. Sci. Technol.*, vol. 44, no. 4, pp. 1247–1253, Feb. 2010.

[181] A. Celzard, J. Mareche, F. Payot, and G. Furdin, “Electrical conductivity of carbonaceous powders,” *Carbon*, vol. 40, no. 15, pp. 2801–2815, 2002.

[182] Z. D. Wei, C. Yan, Y. Tan, L. Li, C. X. Sun, Z. G. Shao, P. K. Shen, and H. W. Dong, “Spontaneous reduction of Pt(IV) onto the sidewalls of functionalized multiwalled carbon nanotubes as catalysts for oxygen reduction reaction in PEMFCs,” *J. Phys. Chem. C*, vol. 112, no. 7, pp. 2671–2677, Feb. 2008.

[183] Y.-K. Hsu, Y.-C. Chen, Y.-G. Lin, L.-C. Chen, and K.-H. Chen, “High-cell-voltage supercapacitor of carbon nanotube/carbon cloth operating in neutral aqueous solution,” *J. Mater. Chem.*, vol. 22, no. 8, p. 3383, 2012.

[184] G. Wang, Y. Ling, F. Qian, X. Yang, X.-X. Liu, and Y. Li, “Enhanced capacitance in partially exfoliated multi-walled carbon nanotubes,” *J. Power Sources*, vol. 196, no. 11, pp. 5209–5214, Jun. 2011.

[185] Y. Zhao, M. Zheng, J. Cao, X. Ke, J. Liu, Y. Chen, and J. Tao, “Easy synthesis of ordered meso/macroporous carbon monolith for use as electrode in electrochemical capacitors,” *Mater. Lett.*, vol. 62, no. 3, pp. 548–551, Feb. 2008.

[186] Y. Honda, T. Haramoto, M. Takeshige, H. Shiozaki, T. Kitamura, and M. Ishikawa, “Aligned MWCNT sheet electrodes prepared by transfer methodology providing high-power capacitor performance,” *Electrochem. Solid-State Lett.*, vol. 10, no. 4, pp. A106–A110, Apr. 2007.

[187] J. M. Miller, B. Dunn, T. D. Tran, and R. W. Pekala, “Deposition of ruthenium nanoparticles on carbon aerogels for high energy density supercapacitor electrodes,” *J. Electrochem. Soc.*, vol. 144, no. 12, pp. L309–L311, Dec. 1997.

[188] H.-J. Oh, J.-H. Lee, H.-J. Ahn, Y. Jeong, Y.-J. Kim, and C.-S. Chi, “Nanoporous activated carbon cloth for capacitive deionization of aqueous solution,” *Thin Solid Films*, vol. 515, no. 1, pp. 220–225, Sep. 2006.

[189] E. Avraham, M. Noked, Y. Bouhadana, A. Soffer, and D. Aurbach, “Limitations of charge efficiency in capacitive deionization processes III: The behavior of surface oxidized activated carbon electrodes,” *Electrochimica Acta*, vol. 56, no. 1, pp. 441–447, Dec. 2010.

[190] S. Stankovich, D. A. Dikin, R. D. Piner, K. A. Kohlhaas, A. Kleinhammes, Y. Jia, Y. Wu, S. T. Nguyen, and R. S. Ruoff, “Synthesis of graphene-based nanosheets via chemical reduction of exfoliated graphite oxide,” *Carbon*, vol. 45, no. 7, pp. 1558–1565, Jun. 2007.

[191] S. Biniak, G. Szymański, J. Siedlewski, and A. Świątkowski, “The characterization of activated carbons with oxygen and nitrogen surface groups,” *Carbon*, vol. 35, no. 12, pp. 1799–1810, 1997.

[192] C.-H. Hou, N.-L. Liu, H.-L. Hsu, and W. Den, “Development of multi-walled carbon nanotube/poly(vinyl alcohol) composite as electrode for capacitive deionization,” *Sep. Purif. Technol.*, vol. 130, pp. 7–14, Jun. 2014.

[193] D. Qu and H. Shi, “Studies of activated carbons used in double-layer capacitors,” *J. Power Sources*, vol. 74, no. 1, pp. 99–107, Jul. 1998.

[194] A. Ghosh and Y. H. Lee, “Carbon-based electrochemical capacitors,” *ChemSusChem*, vol. 5, no. 3, pp. 480–499, 2012.

[195] T. Tay, S. Ucar, and S. Karagöz, “Preparation and characterization of activated carbon from waste biomass,” *J. Hazard. Mater.*, vol. 165, no. 1–3, pp. 481–485, Jun. 2009.

[196] M. A. Lillo-Ródenas, D. Lozano-Castelló, D. Cazorla-Amorós, and A. Linares-Solano, “Preparation of activated carbons from Spanish anthracite: II. Activation by NaOH,” *Carbon*, vol. 39, no. 5, pp. 751–759, Apr. 2001.

[197] D. Lozano-Castelló, M. A. Lillo-Ródenas, D. Cazorla-Amorós, and A. Linares-Solano, “Preparation of activated carbons from Spanish anthracite: I. Activation by KOH,” *Carbon*, vol. 39, no. 5, pp. 741–749, Apr. 2001.

[198] J. ’ichi Hayashi, T. Horikawa, K. Muroyama, and V. G. Gomes, “Activated carbon from chickpea husk by chemical activation with K2CO3: preparation and characterization,” *Microporous Mesoporous Mater.*, vol. 55, no. 1, pp. 63–68, Aug. 2002.

[199] A. Robau-Sánchez, A. Aguilar-Elguézabal, and J. Aguilar-Pliego, “Chemical activation of Quercus agrifolia char using KOH: Evidence of cyanide presence,” *Microporous Mesoporous Mater.*, vol. 85, no. 3, pp. 331–339, Nov. 2005.

[200] Y. Sudaryanto, S. B. Hartono, W. Irawaty, H. Hindarso, and S. Ismadji, “High surface area activated carbon prepared from cassava peel by chemical activation,” *Bioresour. Technol.*, vol. 97, no. 5, pp. 734–739, Mar. 2006.

[201] J. Hayashi, T. Horikawa, I. Takeda, K. Muroyama, and F. Nasir Ani, “Preparing activated carbon from various nutshells by chemical activation with K2CO3,” *Carbon*, vol. 40, no. 13, pp. 2381–2386, 2002.

[202] D. Adinata, W. M. A. Wan Daud, and M. K. Aroua, “Preparation and characterization of activated carbon from palm shell by chemical activation with K2CO3,” *Bioresour. Technol.*, vol. 98, no. 1, pp. 145–149, Jan. 2007.

[203] E. Avraham, B. Yaniv, A. Soffer, and D. Aurbach, “Developing ion electroadsorption stereoselectivity, by pore size adjustment with chemical vapor deposition onto active carbon fiber electrodes. Case of Ca2+/Na+ separation in water capacitive desalination,” *J Phys Chem C*, vol. 112, no. 19, pp. 7385–7389, 2008.

[204] J. Pang, Q. Hu, Z. Wu, J. Eric Hampsey, J. He, and Y. Lu, “Direct synthesis of unimodal and bimodal nanoporous carbon,” *Microporous Mesoporous Mater.*, vol. 74, no. 1–3, pp. 73–78, Sep. 2004.

[205] F. A. Settle, *Handbook of Instrumental Techniques for Analytical Chemistry*. Englewood CLiffs, NJ: Prentice Hall, 1997.

[206] Y. Urabe, T. Ishikura, and K. Kaneko, “Development of porosity in carbons from yeast grains by activation with alkali metal carbonates,” *J. Colloid Interface Sci.*, vol. 319, no. 1, pp. 381–383, Mar. 2008.

[207] J. Guo and A. C. Lua, “Textural and chemical characterizations of adsorbent prepared from palm shell by potassium hydroxide impregnation at different stages,” *J. Colloid Interface Sci.*, vol. 254, no. 2, pp. 227–233, Oct. 2002.

[208] E. Raymundo-Piñero, P. Azaïs, T. Cacciaguerra, D. Cazorla-Amorós, A. Linares-Solano, and F. Béguin, “KOH and NaOH activation mechanisms of multiwalled carbon nanotubes with different structural organisation,” *Carbon*, vol. 43, no. 4, pp. 786–795, 2005.

[209] T. E. P. of C. T. I. of Technology, M. S. P. of P. U. of N. Y. at Binghamton, and M. E. P. of E. E. S. University, *Graphite Intercalation Compounds and Applications*. Oxford University Press, 2003.

[210] M. S. Dresselhaus and G. Dresselhaus, “Intercalation compounds of graphite,” *Adv. Phys.*, vol. 51, no. 1, pp. 1–186, 2002.

[211] D. W. McKee, “Gasification of graphite in carbon dioxide and water vapor—the catalytic effects of alkali metal salts,” *Carbon*, vol. 20, no. 1, pp. 59–66, 1982.

[212] K. Morishige and N. Tarui, “Capillary condensation of nitrogen in ordered mesoporous silica with bicontinuous gyroid structure,” *J. Phys. Chem. C*, vol. 111, no. 1, pp. 280–285, 2006.

[213] M. Thommes, “Physical adsorption characterization of nanoporous materials,” *Chem. Ing. Tech.*, vol. 82, no. 7, pp. 1059–1073, Jul. 2010.

[214] S. Lowell, *Characterization of Porous Solids and Powders: Surface Area, Pore Size and Density*. Springer Science & Business Media, 2004.

[215] J. Rouquerol, F. Rouquerol, P. Llewellyn, G. Maurin, and K. S. W. Sing, *Adsorption by Powders and Porous Solids: Principles, Methodology and Applications*. Academic Press, 2013.

[216] B. N. M. Dolah, M. a. R. Othman, M. Deraman, N. H. Basri, R. Farma, I. A. Talib, and M. M. Ishak, “Supercapacitor electrodes from activated carbon monoliths and carbon nanotubes,” *J. Phys. Conf. Ser.*, vol. 431, no. 1, p. 12015, Apr. 2013.

[217] C. Wu, X. Wang, B. Ju, Y. Bai, L. Jiang, H. Wu, Q. Zhao, J. Gao, X. Wang, and L. Yi, “Supercapacitive behaviors of the nitrogen-enriched activated mesocarbon microbead in aqueous electrolytes,” *J. Solid State Electrochem.*, vol. 17, no. 6, pp. 1693–1700, Feb. 2013.

[218] E. Taer, M. Deraman, I. A. Talib, S. A. Hashmi, and A. A. Umar, “Growth of platinum nanoparticles on stainless steel 316L current collectors to improve carbon-based supercapacitor performance,” *Electrochimica Acta*, vol. 56, no. 27, pp. 10217–10222, Nov. 2011.

[219] A. M. Dehkhoda, N. Ellis, and E. Gyenge, “Electrosorption on activated biochar: effect of thermo-chemical activation treatment on the electric double layer capacitance,” *J. Appl. Electrochem.*, vol. 44, no. 1, pp. 141–157, Jan. 2014.

[220] C. Macías, P. Lavela, G. Rasines, M. C. Zafra, J. L. Tirado, and C. O. Ania, “Improved electro-assisted removal of phosphates and nitrates using mesoporous carbon aerogels with controlled porosity,” *J. Appl. Electrochem.*, vol. 44, no. 8, pp. 963–976, Jul. 2014.

[221] Z. Xu, D. Cai, Z. Hu, and L. Gan, “A combination of porous and crystalline characters in carbon aerogels by a synergistic graphitization,” *Microporous Mesoporous Mater.*, vol. 195, pp. 36–42, Sep. 2014.

[222] J. Yang and L. Zou, “Recycle of calcium waste into mesoporous carbons as sustainable electrode materials for capacitive deionization,” *Microporous Mesoporous Mater.*, vol. 183, pp. 91–98, Jan. 2014.

[223] N. R. Khalili, M. Campbell, G. Sandi, and J. Golaś, “Production of micro- and mesoporous activated carbon from paper mill sludge: I. Effect of zinc chloride activation,” *Carbon*, vol. 38, no. 14, pp. 1905–1915, 2000.

[224] S. B. Y. Minsuk Kim, “Synthesis and characterization of spherical carbon and polymer capsules with hollow macroporous core and mesoporous shell structures,” *Microporous Mesoporous Mater.*, vol. 63, no. 1–3, pp. 1–9, 2003.

[225] J. Lee, S. Yoon, T. Hyeon, S. M. Oh, and K. B. Kim, “Synthesis of a new mesoporous carbon and its application to electrochemical double-layer capacitors,” *Chem. Commun.*, no. 21, pp. 2177–2178, 1999.

[226] H. Marsh, *Activated carbon compendium*. Gulf Professional Publishing, 2001.

[227] E. P. Barrett, L. G. Joyner, and P. P. Halenda, “The determination of pore volume and area distributions in porous substances. I. computations from nitrogen isotherms,” *J. Am. Chem. Soc.*, vol. 73, no. 1, pp. 373–380, Jan. 1951.

[228] K. K. Geza Horvath, “Method for calculation of effective pore size distribution in molecular sieve carbon,” *J. Chem. Eng. Jpn. - J Chem Eng JPN*, vol. 16, no. 6, pp. 470–475, 1983.

[229] D. L. Valladares, F. Rodríguez Reinoso, and G. Zgrablich, “Characterization of active carbons: the influence of the method in the determination of the pore size distribution,” *Carbon*, vol. 36, no. 10, pp. 1491–1499, Oct. 1998.

[230] L. M. Viculis, J. J. Mack, O. M. Mayer, H. T. Hahn, and R. B. Kaner, “Intercalation and exfoliation routes to graphite nanoplatelets,” *J. Mater. Chem.*, vol. 15, no. 9, pp. 974–978, Feb. 2005.

[231] F. Liu, S. Song, D. Xue, and H. Zhang, “Folded structured graphene paper for high performance electrode materials,” *Adv. Mater.*, vol. 24, no. 8, pp. 1089–1094, Feb. 2012.

[232] A. C. Ferrari and J. Robertson, “Interpretation of Raman spectra of disordered and amorphous carbon,” *Phys. Rev. B*, vol. 61, no. 20, pp. 14095–14107, May 2000.

[233] A. C. Ferrari, J. C. Meyer, V. Scardaci, C. Casiraghi, M. Lazzeri, F. Mauri, S. Piscanec, D. Jiang, K. S. Novoselov, S. Roth, and A. K. Geim, “Raman spectrum of graphene and graphene layers,” *Phys. Rev. Lett.*, vol. 97, no. 18, p. 187401, Oct. 2006.

[234] A. C. Ferrari, “Raman spectroscopy of graphene and graphite: Disorder, electron–phonon coupling, doping and nonadiabatic effects,” *Solid State Commun.*, vol. 143, no. 1–2, pp. 47–57, Jul. 2007.

[235] S. Piscanec, M. Lazzeri, J. Robertson, A. C. Ferrari, and F. Mauri, “Optical phonons in carbon nanotubes: Kohn anomalies, Peierls distortions, and dynamic effects,” *Phys. Rev. B*, vol. 75, no. 3, p. 35427, Jan. 2007.

[236] M. S. Dresselhaus, G. Dresselhaus, R. Saito, and A. Jorio, “Raman spectroscopy of carbon nanotubes,” *Phys. Rep.*, vol. 409, no. 2, pp. 47–99, Mar. 2005.

[237] R. K. Kalluri, M. M. Biener, M. E. Suss, M. D. Merrill, M. Stadermann, J. G. Santiago, T. F. Baumann, J. Biener, and A. Striolo, “Unraveling the potential and pore-size dependent capacitance of slit-shaped graphitic carbon pores in aqueous electrolytes,” *Phys. Chem. Chem. Phys.*, vol. 15, no. 7, pp. 2309–2320, Jan. 2013.

[238] S. Porada, D. Borchardt, M. Oschatz, M. Bryjak, J. S. Atchison, K. J. Keesman, S. Kaskel, P. M. Biesheuvel, and V. Presser, “Direct prediction of the desalination performance of porous carbon electrodes for capacitive deionization,” *Energy Environ. Sci.*, vol. 6, pp. 3700–3712, 2013.

[239] E. R. Nightingale, “Phenomenological theory of ion solvation. effective radii of hydrated ions,” *J. Phys. Chem.*, vol. 63, no. 9, pp. 1381–1387, Sep. 1959.

[240] Y.-H. Li, S. Wang, Z. Luan, J. Ding, C. Xu, and D. Wu, “Adsorption of cadmium(II) from aqueous solution by surface oxidized carbon nanotubes,” *Carbon*, vol. 41, no. 5, pp. 1057–1062, 2003.

[241] L. Han, K. G. Karthikeyan, M. A. Anderson, J. J. Wouters, and K. B. Gregory, “Mechanistic insights into the use of oxide nanoparticles coated asymmetric electrodes for capacitive deionization,” *Electrochimica Acta*, vol. 90, pp. 573–581, Feb. 2013.

[242] C.-C. Huang and Y.-J. Su, “Removal of copper ions from wastewater by adsorption/electrosorption on modified activated carbon cloths,” *J. Hazard. Mater.*, vol. 175, no. 1–3, pp. 477–483, Mar. 2010.

[243] G. Rasines, P. Lavela, C. Macías, M. C. Zafra, J. L. Tirado, J. B. Parra, and C. O. Ania, “N-doped monolithic carbon aerogel electrodes with optimized features for the electrosorption of ions,” *Carbon*, vol. 83, pp. 262–274, Mar. 2015.

[244] G. Rasines, P. Lavela, C. Macías, M. C. Zafra, J. L. Tirado, and C. O. Ania, “Mesoporous carbon black-aerogel composites with optimized properties for the electro-assisted

removal of sodium chloride from brackish water," *J. Electroanal. Chem.*, vol. 741, pp. 42–50, Mar. 2015.

[245] J. C. Farmer, D. V. Fix, G. V. Mack, R. W. Pekala, and J. F. Poco, "Capacitive deionization of NaCl and NaNO3 solutions with carbon aerogel electrodes," *J. Electrochem. Soc.*, vol. 143, no. 1, pp. 159–169, Jan. 1996.

Appendices

Appendix A : Electrode preparation

The preparation procedure of electrodes was included in Section 3.1.2. Two different ink solutions were prepared for electrodes:

1. About 40 mg of each carbon sample was mixed with 10 mL of isopropanol (solvent). Then the amount of required Nafion (5 and 30 wt.%) was calculated based on the total mass of coated material on the electrode. For example for preparation of 5 wt.% electrode:

$$5\%\ Nafion\ content = \frac{m_{Nafion}}{m_{Nafion} + m_{carbon}} = \frac{m_{Nafion}}{m_{Nafion} + 40}$$

   The m_{Nafion} from above equation is 2.10 mg. Thus, 42 mg of the diluted Nafion solution (5 wt.% in water and low-molecular alcohol) should be added to the mixture of carbon and solvent. The mixture was then sonicated for 2 h to increase the dispersion of particles for spraying. The ratio of solvent (isopropanol) to solid is 207. This ink solution was used for preparing electrodes investigated in Chapters 4 and 5. The IWATA air brusher (Figure B2) was used for spraying the prepared ink on the Nickel mesh. Figure B1 demonstrates the SEM images of prepared electrodes with increasing Nafion content.

   Prior to spraying, Nickel mesh was washed with acetone and then soaked in 1 mol L^{-1} HNO_3 at 60°C for about 15 min (until the color of the solution turned green). Treated meshes were dried in oven for 2 h.

2. For the electrodes investigated in Chapter 6, the ink solution was prepared similar to ink solution #1 except for increasing the concentration (reducing mass ratio of solvent to solid) of the ink. The amount of carbon sample increased from 40 to 80 mg and the volume of isopropanol reduced from 10 to 5 mL. Amount of required Nafion (10 wt.%) was calculated similarly. Manual spraying with Mastercraft® air-powered gravity-feed spray gun (Figure B2) were conducted. Thus, the material loading on electrodes increased significantly comparing to the ink solution #1. The amount of material coating was increased because the electrodes with material loading between 30 and 100 mg showed negligible amount of ion removal in CDI tests.

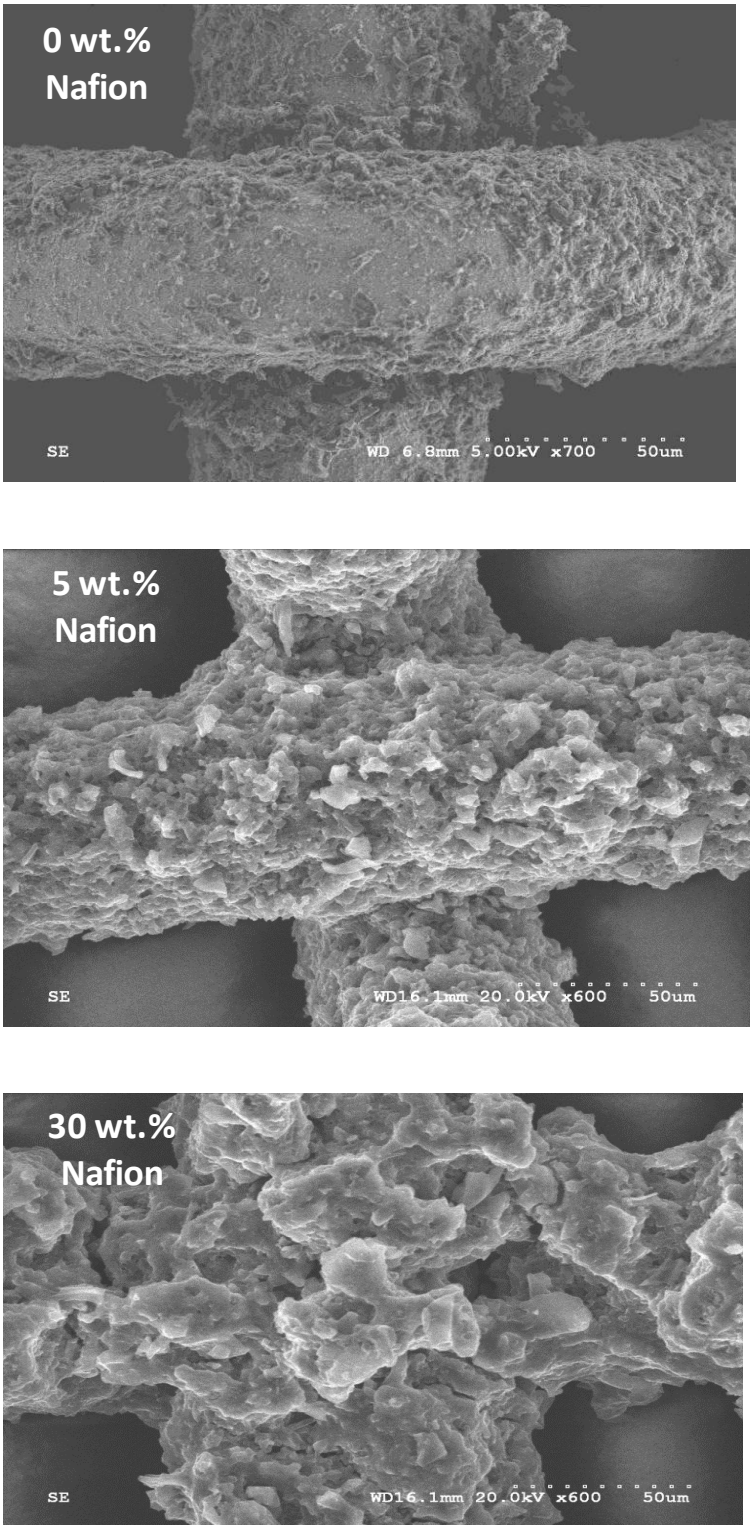

Figure A.1 Biochar electrodes on Ni mesh with 0, 5, and 30 wt.% Nafion.

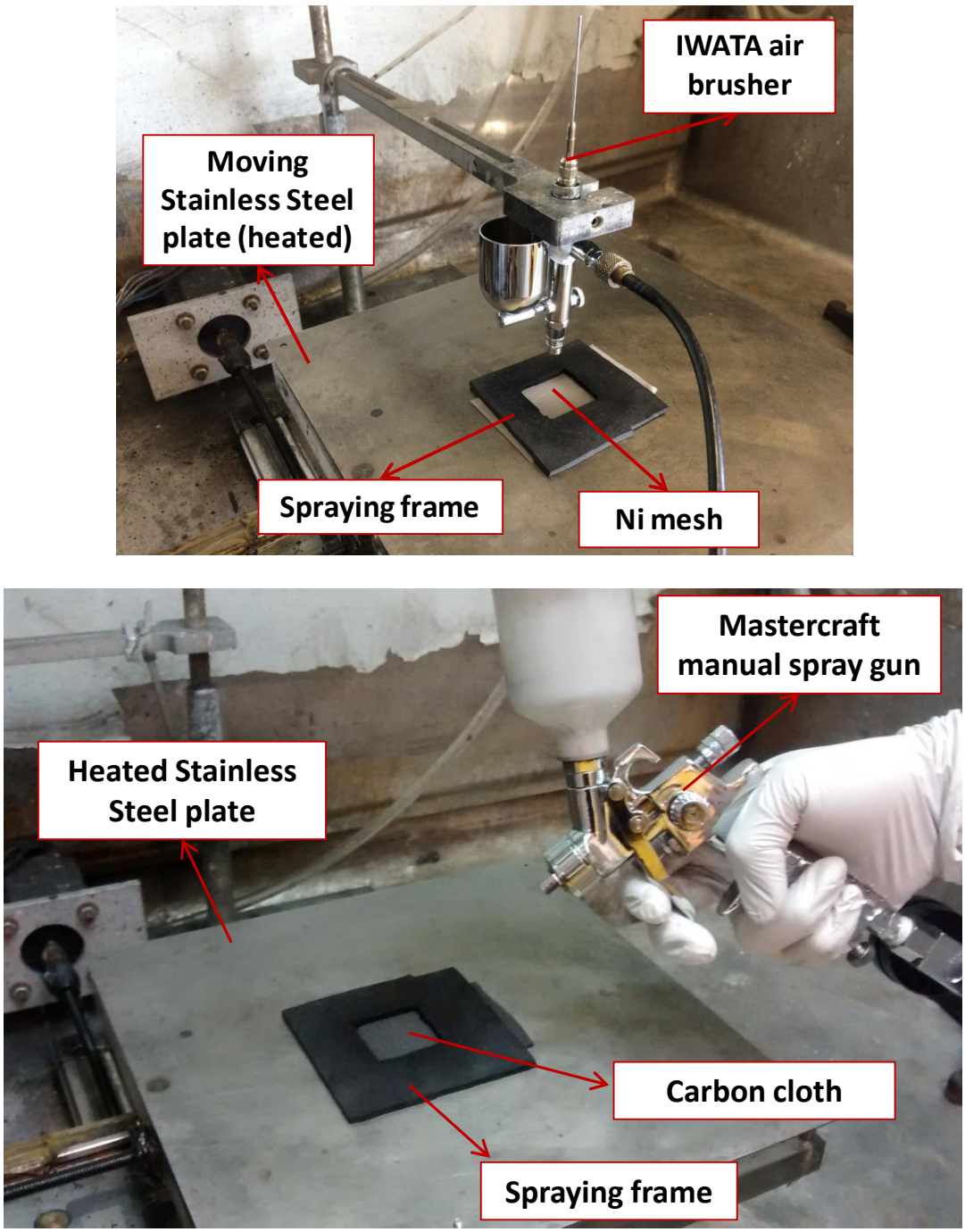

Figure A.2 Automatic (top) and manual (bottom) spraying setups.

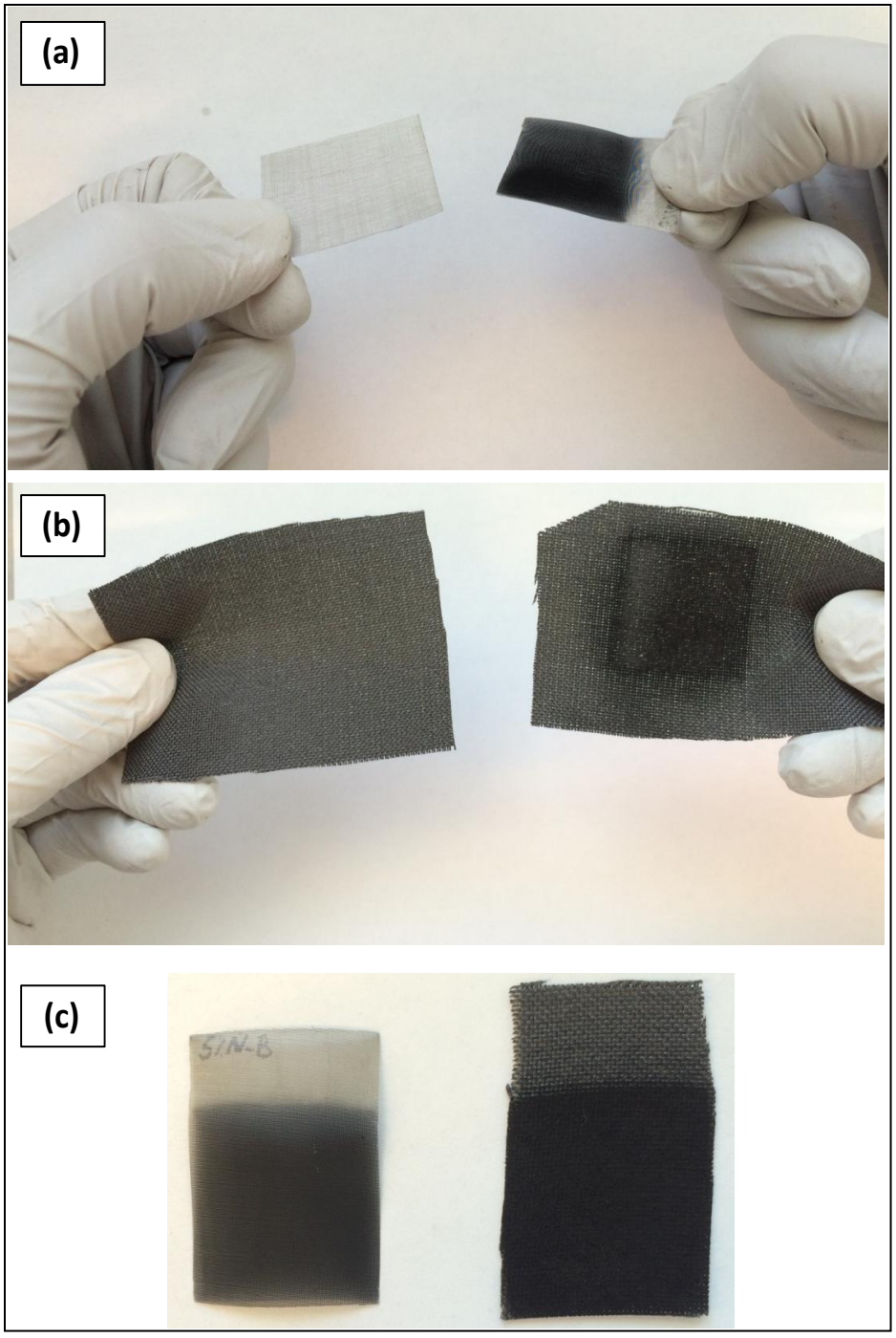

Figure A.3 Mechanically flexible current collectors and corresponding electrodes: (a) Ni mesh; (b) carbon cloth; (c) electrodes on Ni mesh (left) and carbon cloth (right).

Table A.1 Summary of electrodes prepared from biochar activated at 675°C with 5 wt.% Nafion using 0.1 mol L^{-1} NaCl – 0.1 mol L^{-1} NaOH electrolyte.

Electrode	Current collector	Thickness (mm)	Nitric acid soaking time (min)	Total Capacitance (F/g)	Discharge Capacitance (F/g)	IR-drop (V)
CC 1	Carbon Cloth	0.2	15[1]	171	67.4	0.079
CC 2	Carbon Cloth	0.2	75	191	62.1	0.022
GF	Graphite Felt	2.5	75	107[2]	42.7	0.067
Ni mesh	Nickel mesh 150 × 150	~0.1	15	154	55.4	0.016

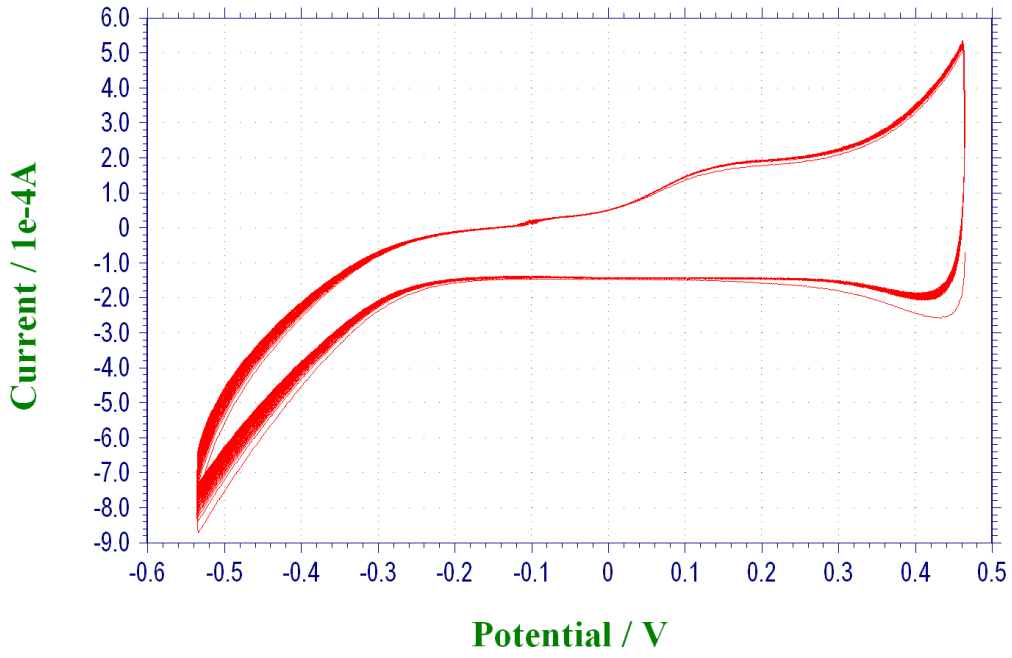

Figure A.4 CV diagram of pure Nickel electrode at 50 mV s^{-1} scanning rate.

[1] Soaked in boiling 1 mol L^{-1} HNO_3 for 15 minutes followed by washing with distilled water and acetone.
[2] Regression coefficient of 0.83 in current difference vs. sweep rate diagram.

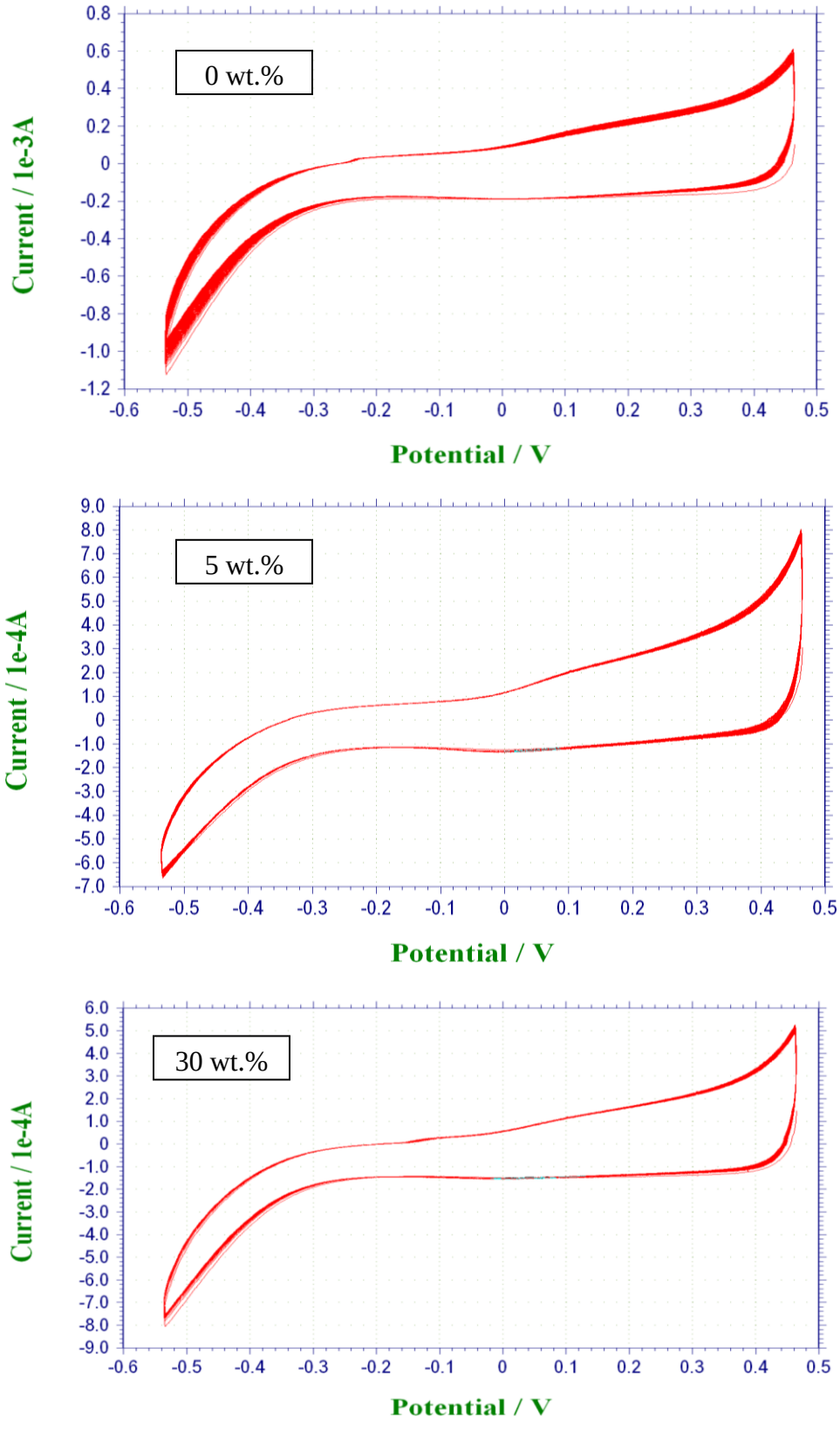

Figure A.5 CV diagram of Biochar-AR electrodes at 50 mV s^{-1} scanning rate.

Appendix B : Elemental composition of ash content

Table B.1 Ash content composition of as received biochar

Analyte	Results	Unit
Aggregate organic constituents		
Loss on ignition at 900°C	86.4	wt.%
Ash content	13.6	wt.%
Metals Total (Fusion)		
Aluminum (Al_2O_3)	1.17	wt.%
Calcium (CaO)	1.03	wt.%
Iron (Fe_2O_3)	0.52	wt.%
Silicon (SiO_2)	7.5	wt.%
Metals (ICP)		
Barium	184	µg/g
Iron	3620	µg/g
Manganese	500	µg/g
Phosphorus	430	µg/g
Titanium	247	µg/g
Zinc	7.85	µg/g
Antimony	3.71	µg/g
Arsenic	<0.99	µg/g
Cadmium	0.3	µg/g
Chromium	13.7	µg/g
Cobalt	1.26	µg/g
Copper	12.4	µg/g
Lead	<1.24	µg/g
Lithium	3	µg/g
Mercury	0.02	µg/g
Molybdenum	1.96	µg/g
Nickel	12.8	µg/g
Selenium	<1.24	µg/g
Strontium	46.3	µg/g
Tellurium	<1.7	µg/g
Thalium	<1.24	µg/g
Vanadium	5.44	µg/g

Appendix C : Electrical conductivity test setup

The electrical conductivity of the dried powders was measured in a test cell shown in Figure C1. The ground and dried samples were placed between two conductive copper plates and connected to a power supply. Further details are provided in Chapter 3.

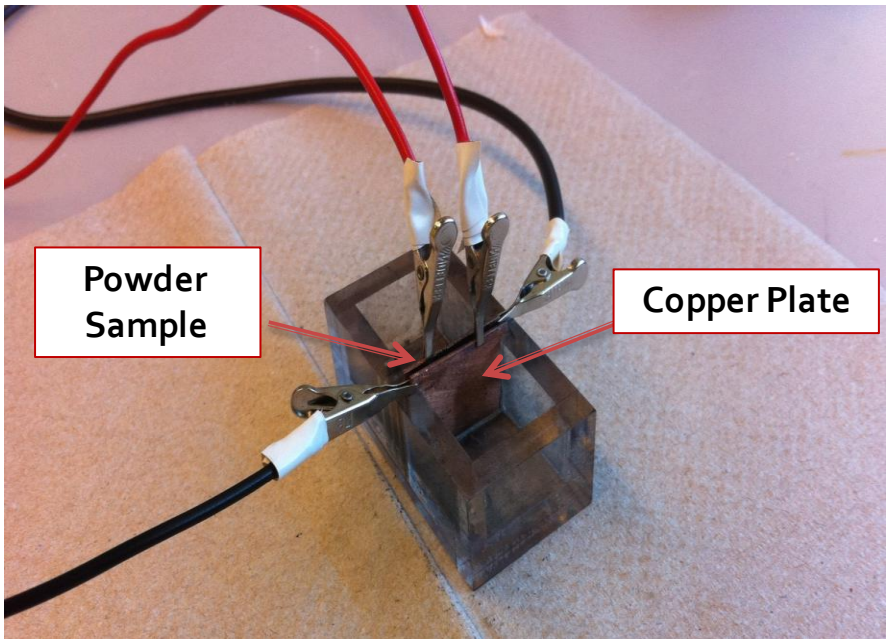

Figure C.1 Electrical conductivity test cell

Appendix D : Correlation between CV scanning rates and produced anodic and cathodic currents

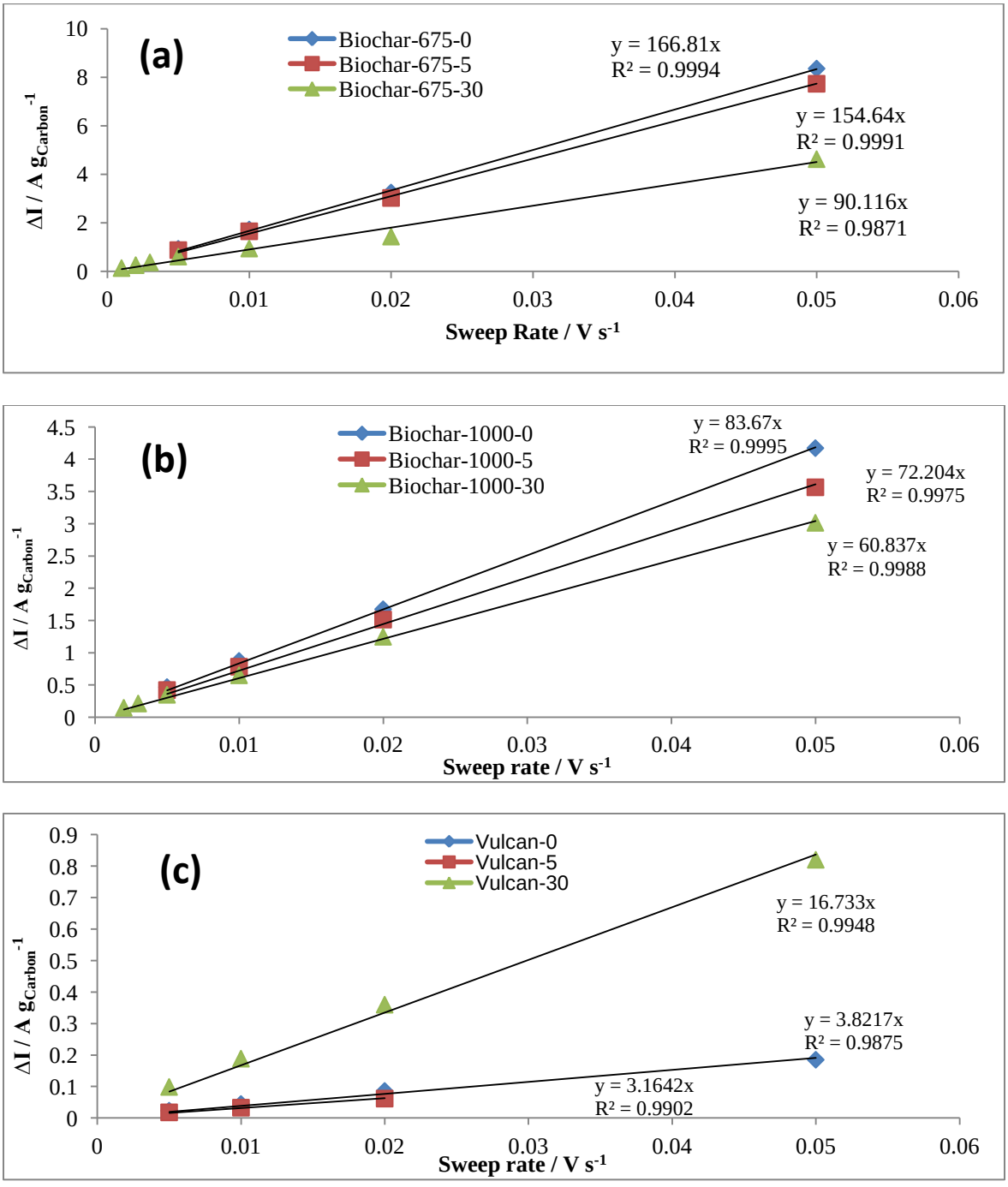

Figure D.1 Current difference ($\Delta I = I_a - |I_c|$) at 0 V vs. Hg/HgO as a function of sweep rates for: (a) Biochar-675; (b) Biochar-1000; and (c) Vulcan electrodes. Electrolyte: 0.1 mol L^{-1} NaCl in 0.1 mol L^{-1} NaOH.

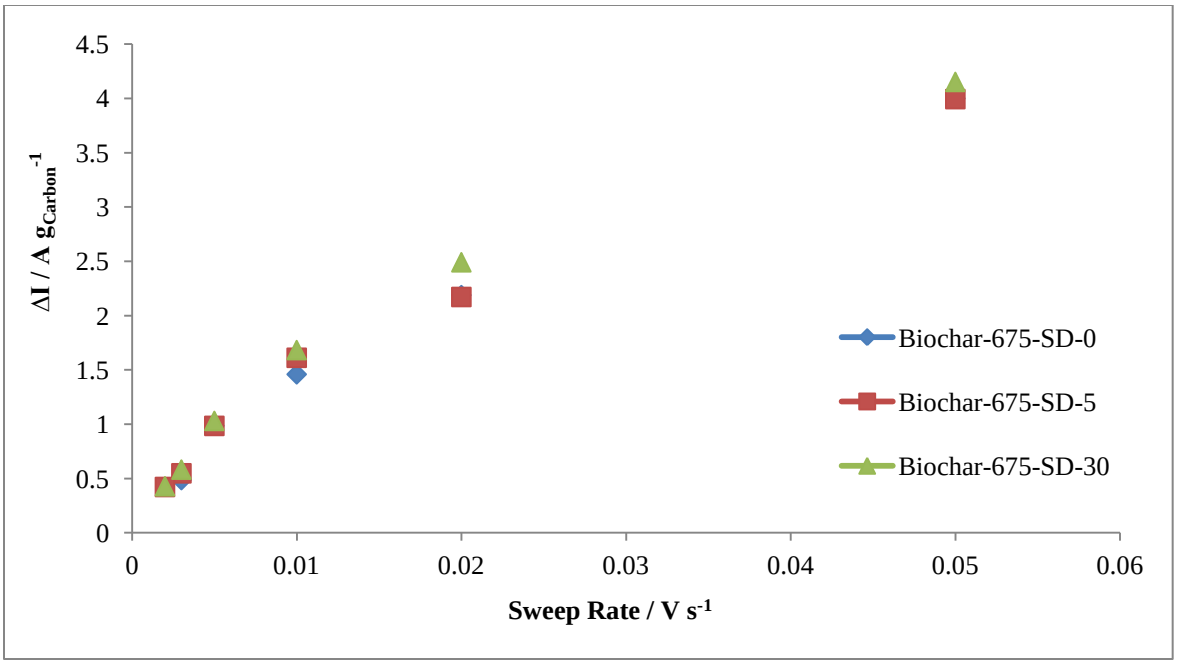

Figure D.2 Current difference ($\Delta I = I_a - |I_c|$) at 0 V vs. Hg/HgO as a function of sweep rates for Biochar-675-SD electrodes. Electrolyte: 0.1 mol L^{-1} NaCl in 0.1 mol L^{-1} NaOH.

Appendix E : Zeta potential and elemental analysis of HNO_3 treated samples

A suspension of 100 ppm was prepared by mixing a representative sample in 0.01 mol L^{-1} NaCl background electrolyte. The suspension was ultrasonicated for 1 min and then mixed with a magnetic stirrer for 10 min at desired pH value. The pH was adjusted using 5% and 1% NaOH solutions. The tests were performed at natural pH (~5) and at pH 11 for each of the samples.

The sample was left to stand for 1 min prior to analysis. An aliquot was then drawn for Zeta potential analysis using a glass syringe and injected into the ZetaView® electrophoresis cell. The results were reported as average Zeta potential calculated from the electrophoretic mobility using the Smoluchowski equation.

Table E.1 Zeta potential of HNO_3-treated samples

Sample	Zeta potential at pH 11 (mV)	Zeta potential at natural pH (mV)
B675-SD	–38.56	—
B675-SD-HNO3	–36.50	–30.27 (pH 4.53)
B675-SD-HNO3-150C	–29.30	–27.54 (pH 4.48)
B675-SD-HNO3-450C	–25.66	–23.77 (pH 5.16)

Table E.2 Reproducibility of Zeta potential analysis (HNO_3-treated samples)

Sample	Zeta potential (pH 11) (mV)
B675-SD-HNO3-150C-1	–29.30
B675-SD-HNO3-150C-2	–30.27
B675-SD-HNO3-150C-3	–30.88

Table E.3 Elemental analysis of HNO_3-treated samples

Sample	C (wt.%)	H (wt.%)	N (wt.%)	O[1] (wt.%)	H/C ratio	O/C ratio
B 675-SD-Plain	82.95	<0.3	<0.3	8.76	0.004	0.11
B675-SD-HNO3	56.67	2.91	0.36	21.66	0.051	0.38
B675-SD-HNO3 150C	57.80	2.80	0.37	20.27	0.048	0.35
4B675-SD-HNO3 450C	63.47	2.10	0.46	9.98	0.033	0.16

[1] Organic content

Appendix F : Comparison between micropore volume measured by Horvath Kawazoe vs. t-plot method

Table F.1 Micropore volume measured by HK vs. t-plot method

Sample	HK Cumulative Micropore Volume ($cm^3 g^{-1}$)	t-plot Micropore Volume ($cm^3 g^{-1}$)
B675-ND	0.63	0.67
B675-MD-Air	0.41	0.38
B875-SD-15h-Air	0.66	0.1
B875-LD-140h-Air	0.68	0.18
B875-LLD-280h-Air	0.70	0.22
B875-SD-15h-N2	0.75	0.08
B875-LD-140h-N2	0.85	0.04
B875-LLD-280h-N2	0.92	0.09

Appendix G : Charge discharge diagrams for CDI of NaCl and $ZnCl_2$

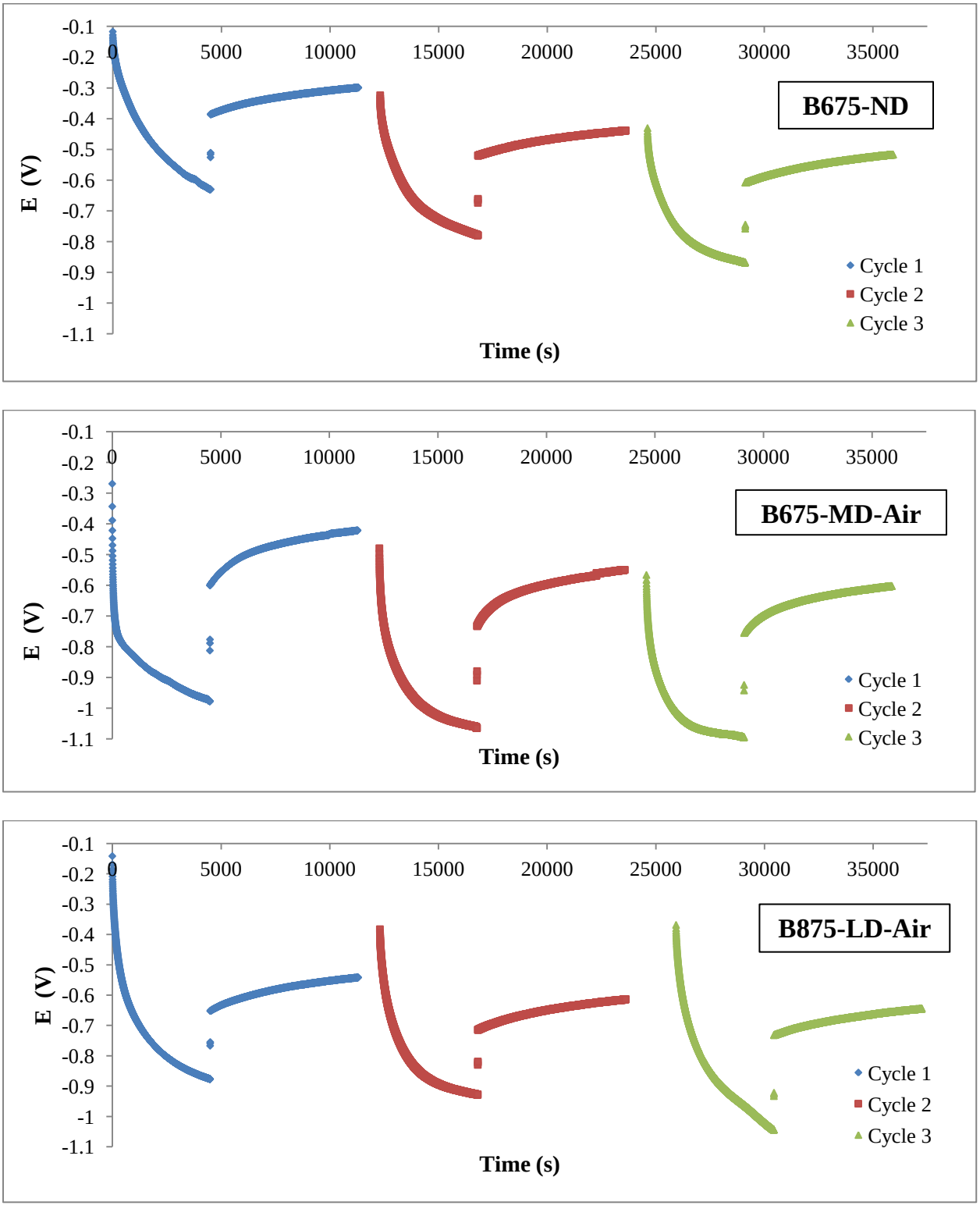

Figure G.1 Charge discharge profiles of tailored biochar electrodes for NaCl desalination.

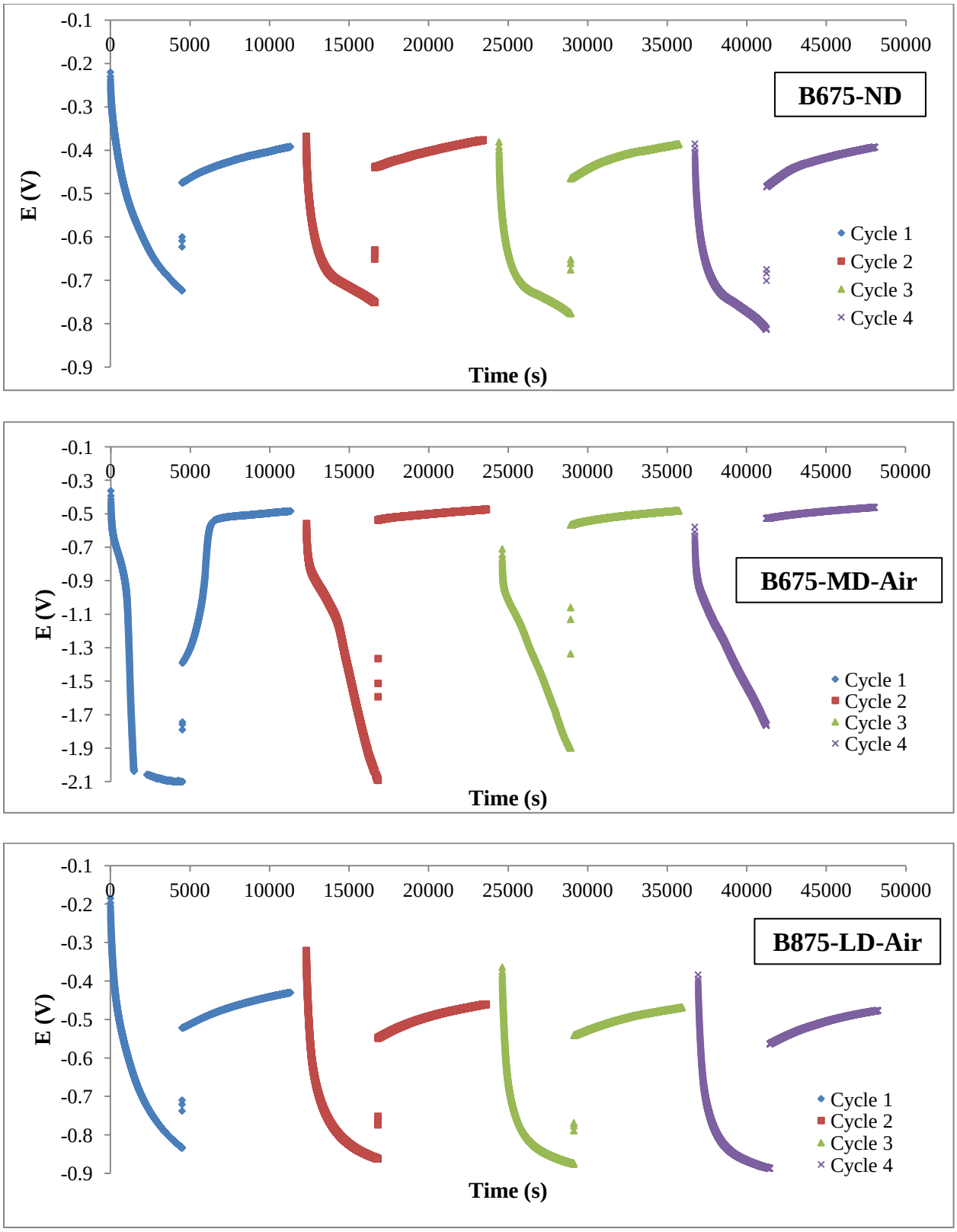

Figure G.2 Charge discharge profiles of tailored biochar electrodes for electrosorption of $ZnCl_2$.

Appendix H Sample calculations of the required amounts of active material and geometric area of electrodes based on desired desalination percentage

Assuming 90% desalination[1] of a 1000 ppm NaCl (i.e., brackish water) solution with desalination percentage defined as follows:

$$[(C_o - C_{final})/C_o] \cdot 100$$

where C_o and C_{final} are initial and final concentrations of NaCl in the test cell. Thus, $C_{final} =$ 100 ppm and the amount of removed NaCl (assuming 1 L treated saline water) is 900 mg.

The amount of required B675-MD-Air sample with removal efficiency of 5.39 mg NaCl g^{-1} (provided in Table 6.5) can be calculated as follows:

$$Required\ amount\ of\ activated\ biochar = \frac{Amount\ of\ NaCl\ removal}{Removal\ efficiency}$$

$$= \frac{900\ mg\ NaCl}{5.39\ mg\ NaCl\ g^{-1}} = 166\ g$$

To calculate the required geometric area of electrodes accommodating 166 g of activated biochar, the material loading per geometric area is measured as:

$$Material\ loading\ per\ geometric\ area = \frac{Amount\ of\ sprayed\ biochar\ on\ each\ electrode}{Geometric\ area\ of\ each\ electrode}$$

$$= \frac{0.25\ g}{9\ cm^2} = 0.027\ g\ cm^{-2}$$

Thus:

$$Total\ geometric\ area\ of\ electrodes = \frac{Required\ amount\ of\ activated\ biochar}{Material\ loading\ per\ geometric\ area} = \frac{166}{0.027}$$

$$= 6148\ cm^2$$

[1] Desalination percentage varied between 60-90 % according to the literature [34], [47], [107].